Trajectory-based methods for the study of ultrafast quantum dynamics

Lidice Cruz Rodriguez

Université Fédérale
Toulouse Midi-Pyrénées

THÈSE

En vue de l'obtention du
DOCTORAT DE L'UNIVERSITÉ DE TOULOUSE

Délivré par l'Université Toulouse 3 - Paul Sabatier

Cotutelle internationale : Université de La Havane

Présentée et soutenue par

Lidice CRUZ RODRIGUEZ

Le 11 décembre 2018

"Méthodes de dynamique quantique ultrarapide basées sur la propagation de trajectoires"

Ecole doctorale : **SDM - SCIENCES DE LA MATIERE - Toulouse**

Spécialité : **Physique**

Unité de recherche :
LCAR-IRSAMC - Laboratoire Collisions Agrégats Réactivité

Thèse dirigée par
Christoph MEIER et Llinersy URANGA-PINA

Jury

M. Yohann SCRIBANO, Rapporteur
M. Pascal LARREGARAY, Rapporteur
Mme Nadine HALBERSTADT, Examinateur
M. Jesus RUBAYO SONEIRA, Examinateur
M. Christoph MEIER, Directeur de thèse
Mme Llinersy URANGA PIñA, Directeur de thèse

DEPARTAMENTO DE FÍSICA GENERAL
FACULTAD DE FÍSICA, UNIVERSIDAD DE LA HABANA
LCAR, IRSAMC, UNIVERSITÉ PAUL SABATIER

THESIS
presented in option to the degree
Doctor in Physics

TRAJECTORY-BASED METHODS FOR THE STUDY OF ULTRAFAST QUANTUM DYNAMICS

Author:
MsC. Lidice Cruz Rodríguez

Supervisors:
Dra. Llinersy Uranga Piña
Dr. Aliezer Martínez Mesa
Dr. Christoph Meier

Havana
September 2018

To my family for their unconditional support.

SYNTHESIS

In this thesis different trajectory-based methods for the study of quantum mechanical phenomena are developed. The first approach is based on a global expansion of the hydrodynamic fields in Chebyshev polynomials. The scheme is used for the study of one-dimensional vibrational dynamics of bound wave packet in harmonic and anharmonic potentials.

Furthermore, a different methodology is developed, which, starting from a parametrization previously proposed for the density, allows the construction of effective interaction potentials between the pseudo-particles representing the density. Within this approach several model problems are studied and important quantum mechanical effects such as, zero point energy, tunneling, barrier scattering and over barrier reflection are founded to be correctly described by the ensemble of interacting trajectories. The same approximation is used for study the laser-driven atom ionization.

A third approach considered in this work consists in the derivation of an approximate many-body quantum potential for cryogenic Ar and Kr matrices with an embedded Na impurity. To this end, a suitable *ansatz* for the ground state wave function of the solid is proposed. This allows to construct an approximate quantum potential which is employed in molecular dynamics simulations to obtain the absorption spectra of the Na impurity isolated in the rare gas matrix.

Contents

CHAPTER 1 GENERAL INTRODUCTION

1 GENERAL INTRODUCTION

The investigation of the real-time dynamics of complex, anharmonic, correlated many-body systems is one of the major challenges in contemporary physics, with implications for reaction dynamics in chemistry and biology. The emergence and the subsequent development of time-resolved spectroscopic techniques have triggered a large number of experimental and theoretical investigations of dynamical processes at the molecular scale [1, 2]. In the last decades, sophisticated numerical techniques have been developed, such as multiconfigurational time-dependent Hartree (MCTDH) [3], thereby increasing our understanding of the microscopic world. In particular, two limiting cases have been extensively studied: on one hand, we have the full quantum dynamics of small systems and, on the other hand, classical molecular dynamics methods (MD) which allow to study large systems of many thousands of particles, such as liquids and biomolecules.

Quantum mechanical phenomena are at the essence of any first-principle description of the microscopic structure of matter. A variety of phenomena such as particle delocalization and interference, tunneling, non-adiabatic transitions, etcetera, are ubiquitous in the theoretical modeling of the structural and dynamical properties of atomic and molecular systems. The methods to perform exact quantum calculations are in continuous development. Typically, those methods are based on spatial grids, basis sets of functions or discrete variable representations [3, 4, 5], and they scale exponentially with the dimensionality of the system. This scaling properties make them very demanding from the computational point of view, and therefore not applicable at present to systems beyond ten degrees of freedom. In contrast, MD methods are based on the propagation of an ensemble of classical trajectories, which allows the study of many-body systems. However, these methods are not capable of describing quantum effects such as tunneling, for example.

It is within this context that we have the **scientific problem** of this thesis, which is the

development of alternatives to standard methods to simulate quantum phenomena, in the perspective to be able to increase the dimensionality of the system under study. We have the **hypothesis** that it is possible to conceive a fully quantum mechanical propagation method, based on trajectories only, which due to the better scalability of trajectory-based methods, could be suitable for the study of high dimensional quantum systems.

A natural way of including quantum effects into a trajectory-based method is to use *quantum trajectories*, a concept that was introduced by de Broglie and Bohm as part of the hydrodynamic formulation of quantum mechanics [6, 7].

The idea of quantum trajectories was developed by Bohm in the following way: he started from the hydrodynamic approach, where we can define a velocity field. Then he introduced the concept of trajectories evolving according to this velocity field, and derived a Hamilton-like Jacobi equation, similar to the classical one, but with an additional potential term. This potential has no classical analog and hence it is known as the *quantum potential*. It depends on the shape of the amplitude of the wave function or, in terms of the quantum trajectories, on the density of the trajectories around the point where we are evaluating the potential. In the following chapter we present the main ideas of Bohm formulation for the particular case of non-relativistic, spin-free particles.

In fact, quantum trajectories could be seen as elements of the probability fluid, associating their speed with that of the quantum flux. However, the philosophical discussions related with Bohm interpretation restrained their use for another thirty years. It was in 1999 that the interest in the hydrodynamic formulation of quantum mechanics started to grow, with the introduction by Robert Wyatt of the Quantum Trajectory Method (QTM) [8]. Within this approach, quantum trajectories are used as a numerical tool to solve the hydrodynamic equations of motion.

As it was proposed by Wyatt, in this method the quantum trajectories are used as a numerical grid which evolves in time, and the phase and amplitude of the wave function are propagated along them. The trajectories are seen as elements of the probability fluid

following the time evolution of the wave function. An extensive review of this method and its applications can be found in Ref. [9]. The QTM has been applied to the study of several model problems [8]−[14]. Furthermore, other approaches allowing the solution of the hydrodynamic equations in the Lagrangian (i.e., *evolving with the fluid*) frame have been proposed [15, 16].

In spite of the theoretical simplicity of the hydrodynamic equations, several factors hinder the solution of the equations of motion for the fluid fields for general anharmonic potentials, e.g., the need to evaluate the fields derivatives on an unstructured grid (as a consequence of each trajectory moving with a different velocity), and the numerical instability introduced by the divergence of the quantum potential at the positions of the nodes of the wave function [17].

To overcome these problems, a variety of techniques have been designed and implemented such as local least square fitting [8]−[12], global polynomial interpolation [18], derivative propagation [19, 20], dynamical adaptive grids [13]−[23] and mixing arbitrary Lagrangian-Eulerian grids [17, 24, 25]. Alternatively, to deal with the node problem caused by interferences, a bipolar decomposition of the wave function has been proposed, to obtain smooth counter propagating wave packets which create interference [26]. Another approach is based on complex trajectories, which are able to directly capture quantum effects such as interference or revivals [27, 28, 29]. However, in the latter approach, the calculation of observables which require knowledge of the information on the real axis remains a challenge. Furthermore, complex quantum trajectories have been also used to study photodissociation dynamics [30].

A different approach has been followed by Chou [31], who modeled a two dimensional chemical reaction by subsequently eliminating the reflected trajectories from the ensemble. With this approach the numerical instabilities associated with nodes and ripples formation are avoided, and the stable propagation of the transmitted trajectories is achieved. As the calculation of the quantum potential is notoriously difficult, another approach has been developed by Garashchuk *et al.* based on an energy conserving approximation of the

quantum potential, to model quantum delocalization in semi-classical systems [32]-[36]. Furthermore, quantum trajectories have been used in mixing quantum/classical methods. Recently, Garashchuk *et al.* studied reactive process in condensed phase by performing molecular dynamics simulations with quantum corrections, using quantum trajectories to incorporate quantum effects into the dynamics of some selected light nuclei [37].

As a promising alternative to the QTM pioneered by Wyatt, a fully wave function-free formulation of quantum mechanics has been developed [38]−[41], and first applications to atomic scattering have only very recently been published [42]. In this approach, the time-dependent quantum mechanical problem is recast into a dynamical problem of a parameterized density. While in principle different parametrizations are possible, for one-dimensional problems a special *ansatz* has been proposed in Ref. [39], which leads to an effective Newton equation with a quantum potential. As it is described in chapter four, a specific choice of the parametrization (which effectively labels the trajectories according to their spatial positions) leads to the form of the quantum potential employed in this thesis [43, 44]. Despite the fact that this discretized version of the density was referred to as "many interacting world" interpretation [43, 45], it can be used for the study of quantum dynamics based on the propagation of an ensemble of trajectories, which evolve under the action of a quantum potential-like quantity, as was already proposed in Ref. [39].

The second main direction in which quantum trajectories have been used is as an interpretative tool, where quantum trajectories are calculated with the aim to visualize and interpret quantum dynamical processes. This can be combined with the wave function-free methods discussed above. However, very often the quantum trajectories are computed from a wave function obtained by the standard solution of the Schrödinger equation using wave packet propagation methods. In this sense, quantum trajectories have been used for example by Sanz *et al.* to describe particle diffraction [46]-[49]. Furthermore, in the context of strong field physics quantum trajectories have been recently employed at descriptive and interpretative levels. In order to gain a deeper insight into the laser-

driven electron dynamics, they have been used in the study of phenomena such as high order harmonic generation, above threshold ionization, among others [50]-[60]. However, if the trajectories are generated *a posteriori* from a pre-computed wave function (calculated from standard wave packet propagation methods) the numerical problems associated with the accurate representation of the wave function, as the number of degrees of freedom increases, are still present.

The **general objective** of this thesis is to develop trajectory-based methods to model quantum mechanical phenomena. **As specific objectives** we aim to use quantum trajectories as a tool to solve the hydrodynamic equations, without pre-computing the wave function, and to exploit the advantage of the trajectories also as a tool to describe and interpret quantum dynamics. Furthermore, we derive approximate expressions for the quantum potential for one-dimensional and multidimensional model systems by using different parametrizations of the density. Several one-dimensional systems will be studied within this approximation. The multidimensional quantum potential will be added to the classical interaction potential to obtain an effective potential, which will be used in MD simulations, in order to simulate the absorption spectra of atomic sodium embebed in argon and krypton matrices.

Then, the **contribution and scientific novelty** of the work we present here is that we have applied a full quantum wave function (grid/basis-set) free methodology based entirely on trajectories, to the study of realistic situations in atomic or molecular physics. It is worth to notice that previous work regarding the specific parametrization of the density used in this thesis involve its application to the description of model systems only [38]−[41]. The method implemented in this thesis gives accurate results, captures well-known quantum effects and is a promising alternative to already existing, standard wave packet methods. Furthermore, we are able to correctly simulate the absorption spectra of atomic sodium embebed in argon and krypton matrices. The same methodology can be applied to study similar systems where quantum effects are relevant and classical molecular dynamics methods fail. The thesis is structured as follows.

In **chapter two**, the main ideas related to the hydrodynamic formulation of quantum mechanics together with the QTM are presented.

In **chapter three**, a method based on a global polynomial expansion of the hydrodynamic fields (here we choose the Chebyshev polynomials) is developed and applied to study the ground state vibrational dynamics in harmonic and anharmonic potentials.

In **chapter four**, a different wave function-free method is presented. It starts from the parametrization for the density proposed by Hall and coworkers [43], from which it is possible to obtain effective interaction potentials between the pseudo-particles representing the density. This allows to model quantum dynamics entirely based on trajectory propagations. This approach is developed and implemented in order to study to which extent it is capable of capturing quantum effects such as zero point energy, tunneling, barrier scattering and over barrier reflection. Furthermore, the same methodology is applied to describe the laser-matter interaction and both the ionization yield and the left-right asymmetry are evaluated as a function of the Carrier Envelope Phase. To assess the validity of our grid-free and wave function free numerical modeling, the results presented all along chapter four, are compared to standard wave packet propagations, and the numerical convergence of the former for progressively larger sets of quantum trajectories is analyzed in detail.

In **chapter five**, a different parametrization of the density is chosen in order to derive an approximate quantum potential for a many-body system. This approximate quantum potential is added to the classical potential to simulate the absorption spectra of atomic sodium embebed in rare gas matrices (i.e., argon and krypton matrices).

These systems have been chosen due to the availability of experimental results [61]. Furthermore, from the theoretical point of view, the absorption spectra of atomic sodium embebed in such matrices has been simulated from MD calculations, which are not able to accurately reproduce the experimental results. Our aim is to evaluate the influence of the quantum corrections, entering into the MD simulations via a model quantum poten-

tial, in the simulated absorption spectra.

The main results of the thesis, together with future perspectives of the methods we have proposed are summarized in the **conclusions**. Finally in the **appendices** we present some technical details regarding the methods used.

CHAPTER 2 ELEMENTS OF THE QUANTUM TRAJECTORY METHOD

2 ELEMENTS OF THE QUANTUM TRAJECTORY METHOD

2.1 The theory of quantum trajectories

The introduction of deterministic trajectories whose position and momentum were assumed to be known at every point in time, was one of Bohm's main contributions [7]. In this chapter we show how to define the new fields in which quantum trajectories evolve directly from the wave function [62]. The main outcome is that the equations of motion determining the time evolution of these fields are completely equivalent to the Schrödinger equation. We will only present the main aspects of the theory related with the introduction of the concept of trajectories in quantum mechanics. The chapter is structured as follows: in the first part it is described how new fields can be derived from the wave function, then the concept of trajectories is introduced and finally, we present the equations that govern the movement of a set of trajectories. For the sake of simplicity, the equations of motion are deduced for the study of a single particle in Cartesian coordinates. At the end of the chapter some partial conclusions are drawn. The reader interested in gaining deeper understanding of the aspects of the theory could consult the work of Peter R. Holland [62].

2.1.1 Hydrodynamic field equations

Reformulation of the Schrödinger equation

The development of the theory underlying the dynamics of quantum trajectories dates from the early years of the 20th century. During the years 1920s, Louis de Broglie introduced the concept of deterministic trajectories into his *pilot wave* theory [6]. Within this viewpoint, de Broglie conceived the wave function as a guiding field acting on the particle that evolves along a deterministic trajectory. During the same period, in 1926, Madelung developed the hydrodynamic formulation of quantum mechanics [63]. In his work, Madelung derived the equation for a velocity field, which governs the evolution of

the probability of localizing the particle at a given position. This probability is given by the square modulus of the wave function. These equations are equivalent to the time-dependent Schrödinger equation and they had lead, for example, to the notion of probability flux.

For around twenty years, de Broglie's ideas were abandoned. It was just at the beginning of the years 1950s, when David Bohm developed a deterministic theory of quantum mechanics based on trajectories [7]. According to Bohm theory, it is the absence of the information of the initial exact position of the particle, what is going to determine the probabilistic character of quantum mechanics. However, it is possible to follow the movement of the particle, evolving along a deterministic *quantum trajectory*.

In this section we follow Madelung's derivation of the hydrodynamic equations. Since we are introducing a special kind of trajectories, which require time-dependent positions, it can be inferred that we are dealing with a time-dependent theory. Thus, this part is devoted to rewrite the Schrödinger equation and to introduce the equations of motion of the new fields.

The starting point is the time-dependent Schrödinger equation (TDSE) for a particle of mass m which evolves in the external potential $V(\mathbf{x}, t)$, where $\mathbf{x}$ stands for the Cartesian coordinates and t, the time,

$$i\hbar\frac{\partial}{\partial t}\Psi(\mathbf{x}, t) = -\frac{\hbar^2}{2m}\nabla^2\Psi(\mathbf{x}, t) + V(\mathbf{x}, t)\Psi(\mathbf{x}, t) \ , \tag{2.1.1}$$

The wave function can be written in its polar form [9, 62]

$$\Psi(\mathbf{x}, t) = R(\mathbf{x}, t)e^{iS(\mathbf{x},t)/\hbar} \ , \tag{2.1.2}$$

where $R(\mathbf{x}, t)$ is the amplitude and $S(\mathbf{x}, t)$ is the phase, both real, and time-position dependent. Then we have,

$$R(\mathbf{x}, t) = (\Psi(\mathbf{x}, t)^*\Psi(\mathbf{x}, t))^{1/2} > 0 \ , \quad S(\mathbf{x}, t) = \hbar/2i \ln(\Psi(\mathbf{x}, t)/\Psi(\mathbf{x}, t)^*) \ . \tag{2.1.3}$$

At each time t, $|\Psi(\mathbf{x},t)| = R(\mathbf{x},t)$, hence $R(\mathbf{x},t)$ is a positive defined magnitude with dimensions $L^{3/2}$, being L a length. The phase $S(\mathbf{x},t)$ carries the units of $\hbar$. The wave function is invariant to a shift of the phase, that is, it takes the same value under the change $S \to S + 2\pi n\hbar$ [9].

Let us note that the polar form of the wave function Ψ is not useful at points were $\Psi = 0$, because S is not well defined as we can see from Eq. (8.0.3). This problem does not appear when using the Schrödinger equation where the propagation of a complex field is performed. However, the former does not present any difficulties for the development of the theory as we will see later. For now, it is important to keep in mind that the upcoming definitions and equations, are only valid in regions where the wave function Ψ is different from zero.

In the derivations shown below, we omit the variables $\mathbf{x}$ and t unless it is necessary to specify them. Substituting the *ansatz* for the wave function (Eq. 8.0.2) into the TDSE (Eq. 8.0.1) and dividing by $e^{iS/\hbar}$ it is obtained,

$$i\hbar\left[\frac{\partial R}{\partial t} + \frac{iR}{\hbar}\frac{\partial S}{\partial t}\right] = -\frac{\hbar^2}{2m}\left[\nabla^2 R - \frac{R}{\hbar^2}(\nabla S)^2 + i\left(\frac{2}{\hbar}(\nabla R)\dot{(}\nabla S) + \frac{R}{\hbar}\nabla^2 S\right)\right] + V \ . \quad (2.1.4)$$

Taking the real and the imaginary part, it is derived for the real part, after dividing by R (notice that these derivations are valid if $R \neq 0$)

$$-\frac{\partial S}{\partial t} = \frac{(\nabla S)^2}{2m} + V - \frac{\hbar^2}{2m}\frac{\nabla^2 R}{R} \ , \quad (2.1.5)$$

and for the imaginary part after dividing by $i\hbar$,

$$\frac{\partial R^2}{\partial t} + \nabla \cdot \left(R^2 \frac{\nabla S}{m}\right) = 0 \ . \quad (2.1.6)$$

So far, it has been replaced an equation for a complex field Ψ (Eq.8.0.1) by two coupled equations for the real fields S and R Eqs. (8.0.4) and (8.0.5). From the mathematical point of view, solving the equation (8.0.1) or equations (8.0.4) and (8.0.5) is equivalent.

By starting from the equations (8.0.2) and (8.0.3) it is possible to build R and S from the wave function Ψ and viceversa. If Ψ is a solution of Eq. (8.0.1) then, by definition, S and R are solutions of equations (8.0.4) and (8.0.5). Furthermore, a given initial condition Ψ_0 defines a unique solution in the same way the initial conditions S_0 and R_0 produce it.

Let us remark that Eq. (8.0.4) has the form of a classical Hamilton-Jacobi (HJ) equation, but it contains and additional potential which is called *quantum potential* Q [62]:

$$Q = -\frac{\hbar^2}{2m}\frac{\nabla^2 R}{R} = -\frac{\hbar^2}{2m}\frac{\nabla^2|\Psi|}{|\Psi|} \ , \tag{2.1.7}$$

or written in terms of the density $\rho(\mathbf{x},t) = R^2(\mathbf{x},t)$

$$Q = -\frac{\hbar^2}{4m}\left(\frac{\nabla^2\rho}{\rho} - \frac{1}{2}\left(\frac{\nabla\rho}{\rho}\right)^2\right) . \tag{2.1.8}$$

The denomination for this potential comes from the fact that it has no analog in classical mechanics. If we disregard the quantum potential, the evolution of S will be determined by the classical HJ equation, independently of the amplitude of the wave function. It is precisely the presence of the quantum potential Q that determines the difference between classical and quantum trajectories. Among other properties, the quantum potential is non-local in the sense that the potential at a given point in space depends not only on the value of the amplitude at that particular point in space, but also on the amplitude at neighboring points. This stems from the fact that it depends on the second derivative of the amplitude. In addition, Q only depends on the shape of the wave function, not on the phase, and any multiplication of R by a constant will yield the same quantum potential.

Hydrodynamic analogy

Due to the analogy with the classical HJ equation, Eq. (8.0.4) is usually known as the quantum Hamilton-Jacobi equation (qHJ). The momentum in classical mechanics is defined as the gradient of the classical action which is the solution of the classical HJ

equation. Similarly, in quantum mechanics, it can be defined a field $\mathbf{p}$ determined by ∇S. Dividing the latter by the mass m, we can define the velocity field $\mathbf{v} = \mathbf{p}/m$. The fields $\mathbf{p}$ and $\mathbf{v}$ are orthogonal to the surface with constant S and they have the dimensions of a momentum and a velocity respectively. Due to the proportionality between these fields, we will refer either to one or the other, but the statements we will make are valid for both of them.

Once we have defined the velocity field, $\mathbf{v}$, we can express its time evolution by taking the gradient in equation (8.0.4). Furthermore, by entering the velocity field in equation (8.0.5) and the density ρ it is obtained,

$$\frac{\partial \mathbf{v}}{\partial t} + (\mathbf{v}\cdot\nabla)\mathbf{v} = -\frac{1}{m}\nabla(V+Q)\ , \tag{2.1.9}$$

$$\frac{\partial \rho}{\partial t} + \nabla\cdot(\rho\mathbf{v}) = 0\ . \tag{2.1.10}$$

Equations (8.0.8) and (8.0.9), were derived by Madelung in 1926 [63] and represent what is known as the hydrodynamic formulation of quantum mechanics. They are identical to the classical hydrodynamic equations if we identify $\mathbf{v}$ with the velocity field and m with the mass of a particle evolving in the fluid. Equation (8.0.9) has the form of a continuity equation.

Let us also note that the equations (8.0.8) and (8.0.9) are equivalent to equations (8.0.4) and (8.0.5) and thereby, they are equivalent to the Schrödinger equation. From the point of view of quantum mechanics we can talk about the fluid probability density ρ which evolves in the velocity field $\mathbf{v}$ given by the gradient of the phase and the wave function. The qHJ equation (8.0.4) gives the time evolution of the phase S, also known as the *quantum action*, hence determining the time evolution of the associate velocity field $\mathbf{v}$ (Eq. 8.0.8), while equation (8.0.5) expresses the conservation of the fluid probability density. The above derivation has a link with the standard formulation of quantum mechanics, where

the current probability density $\mathbf{j}$ is defined as [64],

$$\frac{\mathbf{j}}{|\Psi|^2} = \frac{\hbar}{m}\mathbf{Im}\left(\frac{\nabla\Psi}{\Psi}\right) = \frac{\nabla S}{m} = \mathbf{v} \ . \tag{2.1.11}$$

Equation (8.0.9) expresses the conservation of the probability density with $\mathbf{j} = \rho\mathbf{v}$. Then, to reproduce the results of standard quantum mechanics, we would need that at any time t, R correctly represents the module of the wave function $|\Psi|$ and the velocity field is determined by Eq. (8.0.10), which is directly fulfilled due to the way this theory is built. So far, we have described how the Schrödinger equation can be rewritten in terms of the fields R and S. The fields $\mathbf{p}$ and $\mathbf{v}$ defined from them by analogy with classical mechanics, take a well-defined meaning in quantum mechanics through the probability density current. We are now ready to introduce the notion of *quantum trajectories* that evolve in this velocity field $\mathbf{v}$, in the way they were introduced by Bohm [7].

2.1.2 Quantum trajectories

Until now, we have defined the velocity field which determine the time evolution of the fluid probability density. The existence of trajectories is a postulate, which is added to those usually admitted [62]:

1. a physical system is composed by a wave function propagating in space and time together with a point particle which propagates guided by the wave function.

2. the wave function Ψ is the solution of the Schrödinger equation

3. the time evolution of the particle is obtained as the solution $\mathbf{x}(t)$ of the equation

$$\dot{\mathbf{x}} := \left.\frac{\nabla S(\mathbf{x},t)}{m}\right|_{\mathbf{x}=\mathbf{x}(t)}, \tag{2.1.12}$$

   where S is the phase of Ψ given by Eq.(8.0.3).

To solve equation (8.0.11), it is necessary to give an initial condition $\mathbf{x}(0) = \mathbf{x}_0$. Once this condition is set, all other quantities are uniquely determined by $\Psi(t = 0)$ (the velocity

field is fixed once we know S). It is precisely the time evolution of this particle, governed by equation (8.0.11) and the initial conditions $\mathbf{x}(0)$ and $\Psi(t = 0)$ what determines a *quantum trajectory*. The ensemble of possible motions associated with the wave function Ψ, is obtained by generating a set of initial conditions $\mathbf{x}(0)$, as we will show in the following section.

To guarantee the compatibility between the motion of the ensemble and the results of quantum mechanics, another postulate is necessary, which states that:

4. the probability of finding a particle of the ensemble in the interval $\mathbf{x}$ and $\mathbf{x} + d\mathbf{x}$ is given by $R^2(\mathbf{x}, t)d^3x$, with $R^2 = |\psi|^2$.

Now let us look at some of the fundamental properties of the *quantum trajectories*. If we take two paths that evolve on the same potential V and with the same velocity field, which differ only by their initial position, they can never cross. This property is determined by the fact that ∇S is an single-valued function. So, a single path can pass through that point at that instant. In addition, quantum trajectories cannot pass through the nodes of the wave function. If equation (8.0.9) is evaluated along a trajectory (where it has been introduced the Lagrangian derivative $d/dt = \partial/\partial t + \mathbf{v} \cdot \nabla$),

$$\frac{d}{dt} \ln R^2(\mathbf{x}(t), t) = -\nabla \cdot \mathbf{v}(\mathbf{x}, t)_{|\mathbf{x}=\mathbf{x}(t)} \ , \tag{2.1.13}$$

or integrating

$$R^2(\mathbf{x}(t), t) = R_0^2(\mathbf{x}_0, 0) e^{-\int_0^t \nabla \cdot \mathbf{v}(\mathbf{x}, \tau)_{|\mathbf{x}=\mathbf{x}(\tau)} d\tau} \ , \tag{2.1.14}$$

where $R_0(\mathbf{x}_0, 0)$ is the amplitude of the initial wave function $\Psi(\mathbf{x}_0, 0) = R_0(\mathbf{x}_0, 0) e^{iS_0(\mathbf{x}_0,0)/\hbar}$. Hence, if $R_0^2(\mathbf{x}_0, 0) \neq 0$ then $R^2(\mathbf{x}(t), t) \neq 0$ at any given time t. This is consistent with the deduction of the equations (8.0.4) and (8.0.5), where we have written the wave function in polar form, and we have assumed that $R \neq 0$.

Evaluated along a single trajectory, the qHJ equation (8.0.4) can be interpreted from the point of view of an effective particle associated to this trajectory, as an equation for its

total energy [62] defined as:

$$E(\mathbf{x},t) = -\frac{\partial S(\mathbf{x},t)}{\partial t}\bigg|_{\mathbf{x}=\mathbf{x}(t)} . \tag{2.1.15}$$

This energy is determined by the sum of a kinetic energy term,

$$\frac{(\nabla S)^2}{2m}_{|\mathbf{x}=\mathbf{x}(t)} = m\frac{\dot{\mathbf{x}}^2}{2} , \tag{2.1.16}$$

and a potential energy term, $V(\mathbf{x},t)_{|\mathbf{x}=\mathbf{x}(t)} + Q(\mathbf{x},t)_{|\mathbf{x}=\mathbf{x}(t)} = V(\mathbf{x}(t),t) + Q(\mathbf{x}(t),t)$.

In general, this energy is not conserved along an individual path. Indeed, even when the external field V is time-independent, the quantum potential Q is generally time-dependent as it depends on the wave function $R(\mathbf{x},t)$. However, as we will show later, this energy is conserved if we average by an ensemble of trajectories.

So far, we have shown how new fields can be defined from Ψ, which can be interpreted as the equivalent magnitudes corresponding to those of hydrodynamics and classical mechanics. In principle, by rewriting the Schrödinger equation there are not new elements added to the theory, it only allows to have another point of view. We have presented the concept of trajectory following Bohm's theory. Propagating trajectories in the velocity field derived from the wave function implies to know the wave function beforehand, or at least being able to reproduce it at every time step. Furthermore, this description becomes very appealing at it is possible to obtain complementary information, such as the total energy evaluated along a path (seen as a fluid element). That could give insight information about the process. It is also interesting to see that we can reproduce the results of quantum mechanics with the help of an ensemble of quantum trajectories. We will illustrate this in the following section.

2.1.3 Ensembles of quantum trajectories

As we have already mentioned, it is possible to follow the evolution of the trajectories over time. This evolution is determined by the initial conditions $\mathbf{x}_0$ and Ψ_0. The selection of

these initial conditions is the crucial step to reproduce the results of quantum mechanics from the information contained in the trajectories. In order to reproduce the probability distribution determined by the wave function at $t = 0$, the initial positions $\mathbf{x}_0$ are generated in such a way that they are distributed according to $|\Psi_0|^2$, with an initial velocity $\mathbf{v}_0 = \nabla S_0/m$. Only under these conditions, the evolution of the trajectory ensemble represents the wave function $|\Psi|^2$ at each time t [7, 62]. According to Bohm's theory, it is the lack of precise information on the initial position of trajectories, assumed to be unique, what justifies the introduction of the set of trajectories that we have just defined [62]. It is important to emphasize that this is not an ensemble of material particles. In fact, it represents a set of possible realizations of the trajectories of a single particle. To ensure the correspondence between the distribution of the trajectories and the wave function, an infinite set of trajectories must be chosen $\mathbf{x}_i : i = 1, ..., \infty$. It is only from this ensemble and not from a single trajectory that we can reproduce the results of quantum mechanics.

To obtain the value of any observable in the position representation, it is required to average over all possible positions. This usually translates into averaging over the wave function that represents the probability of finding a particle in a certain region of space. This probability can be also represented by the set of quantum trajectories, which is unique, once the initial wave function Ψ_0 is given.

In order to introduce the averages, let us change the sense of our notation. So far, by definition $R^2 = |\Psi|^2$. However, from now on, R^2 will also represent the density of the quantum trajectories. Let us assume that we have an ensemble of trajectories, uniquely defined by the initial wave function. In general, the mean value of an operator $\hat{O}$ corresponding to a normalized state $|\Psi\rangle$ is expressed as:

$$<\hat{O}>= \langle\Psi|\hat{O}|\Psi\rangle = \int \Psi^* \hat{O} \Psi d^3x. \tag{2.1.17}$$

Evaluating the corresponding mean values of the position, the momentum and the energy

[62], it is obtained

$$\langle \hat{\mathbf{x}} \rangle = \int \Psi^* \mathbf{x} \Psi d^3x = \int R e^{-iS} \mathbf{x} R e^{iS} d^3x = \int R^2 \mathbf{x} d^3x = \langle x \rangle \ , \tag{2.1.18}$$

$$\langle \hat{\mathbf{p}} \rangle = \int \Psi^* (-i\hbar\nabla) \Psi d^3x = \int R^2 \nabla S d^3x = \langle p \rangle \ , \tag{2.1.19}$$

$$\langle \hat{\mathbf{H}} \rangle = \int \Psi^* [(-\hbar^2/2m)\nabla^2 + V]\Psi = \tag{2.1.20}$$

$$\int R^2 [(\nabla S)^2/2m + V + Q] d^3x = \langle E \rangle \ . \tag{2.1.21}$$

Hence, from the quantum trajectory ensemble, we can reproduce the results of quantum mechanics, because the mean values calculated with the trajectory ensemble coincide with those obtained with the wave function. This equality comes from the fact that the initial distribution of the trajectories as well as their initial velocities $\mathbf{v}_0$ have been taken according to the initial wave function Ψ_0. Let us also note that the mean value of the energy is constant for a conservative system, while the energy along any trajectory is not conserved. It can be also noted that the mean value of the quantum force on the trajectory ensemble is zero, which guarantees the conservation of energy and the validity of Ehrenfest's theorem [62].

Up to this point, we have presented the notion of quantum trajectory in quantum mechanics and summarized some of their fundamental properties. We have shown that, by selecting a suitable set of trajectories, the standard results of quantum mechanics can be reproduced. From this point of view, Bohm's formulation is mathematically equivalent to the Schrödinger equation. In the next section we will illustrate how quantum trajectories can be used from a practical point of view to study quantum dynamics.

2.2 Quantum Trajectory Method (QTM)

In practice, there are two ways to study the temporal evolution of quantum trajectories from a computational point of view. A first approach consists in solving the TDSE by the conventional methods (using space-fixed grids or basis set expansions) and computing the trajectories afterwards, and the other one is based in propagating quantum trajectories

evolving in the velocity field determined by Ψ (Eq. (8.0.10)).

The former was actually the main idea in which are based the quantum trajectories introduced by de Broglie, Bohm, and others [6, 7]. Within this approach the goal is not to solve the Schrödinger equation by itself, but to visualize and interpret the quantum dynamics. However, it retains the difficulties of computing the wave function in a fixed grid when the dimensions of the system increase.

On the other hand, there is a different approach in which quantum trajectories are used as a tool to solve the Schrödinger equation, and they are propagated together with the hydrodynamic filed which evolves along them. As we mentioned in the introduction, here we aim to develop methods that allow us to study quantum dynamics of several systems, without facing the problem of the representation of the wave function when the dimensionality of the system grows. In this sense, using quantum trajectories as a numerical tool seems to be very appealing. Hence, we will use the latter approach to propagate the quantum trajectories.

In this section we introduce what is known as the Quantum Trajectory Method (QTM) developed by Wyatt et al. in 1999 [8]. We present the fundamental aspects related to the solution of the equations of motion in the Lagrangian reference frame using the QTM method [8, 9]. Furthermore, we discuss which hydrodynamic fields should be propagated, as well as some of the numerical techniques already developed in order to evolve quantum trajectories.

2.2.1 General aspects

From now on, we limit our derivation to one spatial dimension x and to a single potential energy curve. Here, x will represent a variable and x_i a trajectory.

Thus, suppose that we have an ensemble of trajectories whose distribution represents the density $|\Psi|^2$. For any numerical calculation we will need to discretize the time and the space. Therefore, it is necessary to define a spatial and a temporal grid. In the quantum trajectory method, the initial density is discretized in terms of N fluid elements with mass

m, corresponding to N trajectories x_i, i=1,...,N, each of them carrying its own amplitude $R_i = R(x_i, t)$

Under this strategy, we do not need to propagate the trajectories, but the amplitude R, which means that we have to integrate Eq. (8.0.5). Furthermore, this continuity equation also depends on the phase S, so we also need to integrate Eq. (8.0.4). Hence, if we integrate together equations (8.0.4) and (8.0.5), we will know the wave function. In fact, these equations are independent of the trajectories, they just depend on the grid chosen. This is what is called the Euler reference frame. However, we can also solve these equations along the trajectories, in the Lagrangian reference frame that moves with the fluid. In this case, the positions of the trajectories determine the grid which evolves in time [8, 9].

Let us remark that the choice of the quantum trajectories as a grid is not indispensable. The advantage of the quantum trajectories is that they constitute a grid with the right properties to propagate the probability density, because the amplitude and the phase are directly propagated along them. However, any set of points fulfilling certain properties can be used, i.e. in Ref [25] a fix and a moving grid were mixed, and the grid velocities were chosen to adapt dynamically to the evolution of the hydrodynamic fields. As we already shown, equations (8.0.4) and (8.0.5) can be written in the Lagrangian reference frame. If we introduce the derivative along a trajectory $d/dt = \partial/\partial t + v\partial/\partial x$ and the velocity field $v = \frac{1}{m}\frac{\partial S}{\partial x}$, it can be obtained the following set of coupled equations

$$\frac{dS}{dt} = \frac{1}{2}mv^2 - (V+Q) \ , \tag{2.2.1}$$

$$\frac{d\rho}{dt} = -\rho\frac{\partial v}{\partial x} \ , \tag{2.2.2}$$

$$m\frac{dv}{dt} = -\frac{\partial(V+Q)}{\partial x} \ , \tag{2.2.3}$$

$$\dot{x}_i = v|_{x_i=x_i(t)} \ , \tag{2.2.4}$$

where the equations for the hydrodynamic fields are evaluated along each trajectory. The above set of equation is exact. However, the selection of a finite number of trajecto-

ries needed for the numerical implementation constitute an approximation. The number of trajectories used will be then a crucial parameter to ensure the convergence of the results.

The equations of motion presented above can be combined in different ways in order to evolve the trajectories in time [9]. In order to integrate equation (8.0.20), we need to know the value of the velocity field along a trajectory at each time step. Hence, we can use the Newton-like equation (8.0.19) to integrate the velocity. This requires the evaluation of the quantum force $-\frac{\partial Q}{\partial x}$, which depends on the density ρ, then we also need to integrate Eq. (8.0.18). The above combination has the disadvantage that derivatives of the quantum potential Q are required and this is another source of numerical error in the propagation of quantum trajectories.

Another way of combining the equations to evolve the trajectories is using equation (8.0.17) to integrate S and then evaluate the velocity field as $\nabla S/m$. For this combination we also need to integrate the amplitude R (Eq. (8.0.18)) in order to evaluate Q, but no derivatives of the quantum potential are required. In the next chapter we implement a methodology to integrate the equation of motion of the quantum trajectories which uses this last combination.

For any of the combinations we choose to propagate the trajectories, in general we have the time evolution of the hydrodynamic fields S and R, therefore the wave function can be constructed along the path followed by the quantum trajectories. That is, along a quantum trajectory x_i, from an initial point $x_i(t_0)$ the rate of change of the amplitude is given by equation (8.0.18). This equation can be easily integrated to give the new amplitude R in terms of the initial value

$$R(x_i,t) = R(x_i,t_0)\exp\left(-\frac{1}{2}\int_{t_0}^{t}\left(\frac{\partial v}{\partial x}\right)|_{x_i(\tau)}d\tau\right) . \tag{2.2.5}$$

The derivative of the velocity field in equation (2.2.5) is integrated along a trajectory x_i. Furthermore, the integration of Eq. (8.0.17) allows to write the exponential of the action

at time t in terms of its value at the initial time,

$$e^{\frac{i}{\hbar}S(x_i,t)} = e^{\frac{i}{\hbar}S(x_i,t_0)} \exp\left(\frac{i}{\hbar} \int_{t_0}^{t} \left(\frac{1}{2m} \left(\frac{\partial S}{\partial x} \right)^2 - V - Q \right) \Big|_{x_i(\tau)} d\tau \right) . \tag{2.2.6}$$

Combining equations (2.2.5) and (2.2.6), the value of the wave function along each trajectory can be expressed as [9, 65],

$$\begin{aligned} \Psi(x_i,t) &= \Psi(x_i,t_0) \exp\left(-\frac{1}{2} \int_{t_0}^{t} \left(\frac{\partial v}{\partial x} \right) |_{x_i(\tau)} d\tau \right) \\ &\times \exp\left(\frac{i}{\hbar} \int_{t_0}^{t} \left(\frac{1}{2m} \left(\frac{\partial S}{\partial x} \right)^2 - V - Q \right) \Big|_{x_i(\tau)} d\tau \right) , \end{aligned} \tag{2.2.7}$$

where we have denoted $\Psi(x_i,t_0) = R(x_i,t_0)e^{\frac{i}{\hbar}S(x_i,t_0)}$. The above equation gives the wave function propagator. Hence, within the QTM, by propagating the fields S and R, we can reconstruct the wave function along each trajectory.

So far we have presented the theory underlying the time evolution of the quantum trajectory. In principle, the solution of the equations described above gives the exact solution of the time-dependent Schrödinger equation and therefore it has the same predictive power as standard wave packet propagation methods [16, 66, 67]. However, several factors hinder the solution of the equations of motion (EOM) for the quantum trajectories. The presence of the derivatives of S and R in the equations makes the numerical integration a very difficult task. In order to integrate equations (8.0.17)-(8.0.20) we need to know the derivatives of the hydrodynamic fields at each trajectory. But, even if at the beginning of the propagation the fluid elements form a regular grid, as time evolves, the trajectories will form an unstructured grid. The evaluation of numerical derivatives on such a grid is very challenging. Another intrinsic problem related to the propagation of quantum trajectories is the numerical instabilities at the nodes of the wave function due to the divergence of the quantum potential and force.

As we mentioned in the introduction, several strategies have been implemented in order to overcome the numerical problems associated with the propagation of quantum trajectories,

with relative success [9]. However, the problem is far from being solved and search for new methods to accurately solve the hydrodynamic equations is still an active field of research.

In this work we propose two different alternatives to integrate the equation of motion of the quantum trajectories. The first approach is introduced in the next chapter, and is based on a Chebyshev representation of the hydrodynamic fields. The scheme is subsequently applied to the description of the vibrational dynamics, in particular to the evolution of a wave packet on a harmonic and on a Morse potential.

Then, in chapter four, a different approach is implemented based on a discrete representation of the density, originally proposed by Hall and coworkers [43]. This approach has the advantage that analytical expressions for the quantum potential and force are obtained. The method is used to study some well known quantum phenomena, such as, zero-point energy, tunneling and scattering on a barrier. Furthermore, the one-dimensional electron dynamics under the action of a strong and short laser pulse will be studied within the method. In all cases our calculations are benchmarked with the results from standard wave packet methods, to show how our methodology is capable to reproduce the quantum dynamics.

2.3 Conclusions

Here we have presented the theory underlying the QTM. We have obtained the set of equations we need to solve to propagate the quantum trajectories and we have shown how the solution of the TDSE can be in principle obtained from the propagation of the quantum trajectories. In the next two chapters we introduce two different methods to find the numerical solution of equations (8.0.17)-(8.0.20). The methods are applied to the study of several one-dimensional problems.

CHAPTER 3 CHEBYSHEV EXPANSION OF THE HYDRODYNAMIC FIELDS

3 CHEBYSHEV EXPANSION OF THE HYDRODYNAMIC FIELDS

In this chapter we propose a method for the numerical solution of the equations of motion of the quantum trajectories. The method is based on the representation of the hydrodynamic fields in terms of Chebyshev polynomials. It is applied to study the vibrational dynamics of a Gaussian wave packet on a harmonic and a Morse potential. The main advantages and disadvantages of the method are discussed.

3.1 Introduction

In the previous chapter we presented the main theoretical aspects related to the propagation of quantum trajectories as a numerical tool to solve the TDSE. As we already mentioned, within the QTM, the set of equations (8.0.17)-(8.0.20) are solved by propagating the fields S and R and the trajectories simultaneously. However, the solution of these coupled equations is not straightforward.

One of the main difficulties is the evaluation of the derivatives of the fields in an unstructured grid. Since the development of the QTM by Wyatt and coworkers [8], several techniques has been implemented to overcome this problem. Among them, we can cite local least squares fitting. Within this family of methods, the moving weighted least squares (MWLS) method has been the most extensively used in the Quantum Trajectory Method [8, 12, 17, 68].

As an alternative to those fitting schemes, another techniques have been implemented such as the derivative propagation method along the trajectories [9, 19] as well as methods based on mixed Eulerian and Lagrangian grids [23, 25].

Here we propose a new method to propagate quantum trajectories, based on a global Chebyshev expansion of the hydrodynamic fields [18]. Chebyshev expansions of the wave function propagator have been used extensively in standard wave packet propagation methods [69]-[73], here we use them to the quantum trajectory modeling of the molecu-

lar dynamics. Chebyshev polynomials are chosen because of their property of being the best interpolation polynomials in the minimax sense. In the Chebyshev expansion, the truncation error is smoothly spread out throughout the interpolated interval. As a consequence, the Chebyshev approximation exhibits the smallest maximum deviation from the interpolated function (among all polynomials of the same degree). Likewise, the recurrence relations that satisfied the Chebyshev polynomials allow the direct calculation of the derivatives of the hydrodynamic fields. The main properties of the Chebyshev polynomials are described in the Appendix A. In the next section we show how they can be used to express the hydrodynamic fields and their derivatives in order to propagate the quantum trajectories.

3.2 Methods

In this section we develop an algorithm to propagate quantum trajectories based on the expansion of the hydrodynamic fields in Chebyshev polynomials. We restrict ourself to one dimensional equations and the trajectories are denoted by x_i, with $(i = 1, ..., N)$. Several numerical techniques are combined with the Chebyshev expansion in order to overcome the numerical instabilities inherent to the numerical solution of the hydrodynamic equations.

The C-amplitude

Before we start with the description of the method, we will rewrite the equations (8.0.17)-(8.0.20) in terms of the logarithm of the amplitude $C = \ln R$. This representation in terms of what is known as the C-amplitude has been previously used to solve the EOM of quantum trajectories [9, 12, 17]. It has been shown to be numerically more stable than the representation in terms of R, in particular in regions where R approach to zero, due the fact that near to these points $R \ln R \to 0$. In addition, such representation is particularly useful when working with Gaussian wave packets, in which the logarithm of the density is a quadratic function, which can therefore be accurately represented in any polynomial base.

Thus, in terms of C and S, the previous *ansatz* for the wave function (Eq. 8.0.2) takes the form, $\Psi = Re^{iS/\hbar} = e^{C}e^{iS/\hbar}$. Now we can propagate either R or C. In terms of the C-amplitude the quantum potential (Eq. (8.0.6)) can be written as,

$$Q = -\frac{\hbar^2}{2m}\left[\left(\frac{\partial C}{\partial x}\right)^2 + \left(\frac{\partial^2 C}{\partial x^2}\right)\right] . \tag{3.2.1}$$

The interest in the quantum potential expressed in terms of C, comes from the fact that we do not longer require division by ρ or R to evaluate Q, which suppose a numerical advantage, as has been already shown in Refs. [12, 13].

Then, we can write the set of equations we want to solve in terms of the C-amplitude

$$\frac{dS}{dt} = \frac{1}{2m}\left(\frac{\partial S}{\partial x}\right)^2 - V - Q , \tag{3.2.2}$$

$$\frac{dC}{dt} = -\frac{1}{2m}\frac{\partial^2 S}{\partial x^2} , \tag{3.2.3}$$

evaluated along the trajectories:

$$\dot{x_i} = \frac{1}{m}\frac{\partial S}{\partial x}|_{x_i = x_i(t)} . \tag{3.2.4}$$

To integrate the set of equations (3.2.2)-(3.2.4) we need to evaluate at each time step S, C and their derivatives at the positions of each trajectory x_i. As we already mentioned, this is a very difficult task because the trajectories move with different velocities v_i. Then, an initially uniform mesh, will become an unstructured grid as time evolves. Here we propose a methodology based on expanding the fields in Chebyshev polynomials in order to evaluate their derivatives.

Besides rewriting the equations in terms of C, another step which can improve the numerical stability, is to subtract a conveniently chosen reference function C_0 from C:

$$C = C_0 + \phi . \tag{3.2.5}$$

This transformation is strictly exact and a good reference will reduce the amplitude of the function ϕ to be expanded and the stiffness of the equations of motion.

In this study, C_0 is selected as the logarithm of a Gaussian function ρ_0 which approximates the instantaneous density distribution $\rho(x_i,t) = e^{2C(x_i,t)}$. Consequently, the quantum potential Q (Eq. (3.2.1)) is expressed as the quantum potential Q_0 of the reference Gaussian (which is known analytically) plus an additional contribution which takes into account the deviation of the time-dependent wave packet from the Gaussian shape:

$$Q_0 = -\frac{\hbar^2}{2m}\left(\frac{\partial^2 C_0}{\partial x^2} + \left(\frac{\partial C_0}{\partial x}\right)^2\right) , \tag{3.2.6}$$

$$Q = Q_0 - \frac{\hbar^2}{2m}\left(\frac{\partial^2 \phi}{\partial x^2} + \left(\frac{\partial \phi}{\partial x}\right)^2 + 2\frac{\partial \phi}{\partial x}\frac{\partial C_0}{\partial x}\right) . \tag{3.2.7}$$

Then, we can express only the residual function ϕ as a series of Chebyshev polynomials rather than C. The separation (3.2.5) is well suited for the application of the QTM to the investigation *of ground state* vibrational dynamics, where both the average position and the width of the molecular wave packet remain bound at all times, and a Gaussian profile usually constitutes a reasonable first approximation to the molecular density.

Chebyshev expansion

As we discussed in the appendix A, any continuous function can be expressed as a finite sum of M Chebyshev polynomials [74, 75]. Thus, we can expand the functions S and ϕ at each time step as a sum of Chebyshev polynomials, in particular evaluating them at the trajectories x_i, $i = 1, ..., N$ we can write:

$$\phi(x_i,t) = \sum_{j=0}^{M-1} c_j(t) T_j(\tilde{x}_i) , \quad S(x_i,t) = \sum_{j=0}^{M-1} s_j(t) T_j(\tilde{x}_i) , \tag{3.2.8}$$

where s_j and c_j are the expansion coefficients. In a similar way, we can represent the derivatives with coefficients $s_j^{(1)}$, $s_j^{(2)}$, $c_j^{(1)}$ and $c_j^{(2)}$,

$$\frac{\partial\phi(x_i,t)}{\partial x} = \sum_{j=0}^{M-1} c_j^{(1)}(t)T_j(\tilde{x}_i) \ , \quad \frac{\partial S(x_i,t)}{\partial x} = \sum_{j=0}^{M-1} s_j^{(1)}(t)T_j(\tilde{x}_i) \ , \tag{3.2.9}$$

$$\frac{\partial^2\phi(x_i,t)}{\partial x^2} = \sum_{j=0}^{M-1} c_j^{(2)}(t)T_j(\tilde{x}_i) \ , \quad \frac{\partial^2 S(x_i,t)}{\partial x^2} = \sum_{j=0}^{M-1} s_j^{(2)}(t)T_j(\tilde{x}_i) \ . \tag{3.2.10}$$

The new variable $\tilde{x}_i = (2x_i - a - b)/(b-a)$, maps the real space in which the trajectories evolve $x_i \in [a,b]$ into the space of the Chebyshev polynomials $[-1,1]$.

As we describe in the Appendix A, once we know the Chebyshev expansion coefficients s_j and c_j of S and ϕ, we can obtain the values of the expansion coefficients of their derivatives from the recurrence relations (Eqs. (A.0.12) and (A.0.13)),

$$a_{j-1}s_{j-1}^{(1)} = s_{j+1}^{(1)} + 2js_j \ , \quad j \geq 1 \ , \tag{3.2.11}$$

$$a_{j-1}s_{j-1}^{(2)} = s_{j+1}^{(2)} + 2js_j^{(1)} \ , \quad j \geq 1 \ . \tag{3.2.12}$$

In Eq. (3.2.11) and Eq. (3.2.12), $a_0 = 2$ and $a_j = 1$ for $j \geq 1$ and we need to fix the values for the last two coefficients of the first derivative

$$s_{M-1}^{(1)} = 0 \ , \quad s_{M-2}^{(1)} = 2(M-1)s_{M-1} \ ,$$

and for the second derivative:

$$s_{M-1}^{(2)} = s_{M-2}^{(2)} = 0 \ .$$

Similar equations hold for $c_j^{(1)}$ and $c_j^{(2)}$:

$$a_{j-1}c_{j-1}^{(1)} = c_{j+1}^{(1)} + 2jc_j, \quad j \geq 1 \ , \tag{3.2.13}$$

$$a_{j-1}c_{j-1}^{(2)} = c_{j+1}^{(2)} + 2jc_j^{(1)} \ , \quad j \geq 1 \ . \tag{3.2.14}$$

Usually, the Chebyshev interpolation coefficients of any arbitrary function are evaluated by collocation methods using for example, the zeros of the Chebyshev polynomials as we described in the appendix A. However, here we only know the values of S and ϕ at the instantaneous positions of the trajectories x_i, which do not coincide with the zeros of the Chebyshev polynomials. Therefore, here we propose the following strategy in order to evaluate the expansion coefficients.

We write equation (3.2.8) in a matrix form, given that we know the value of ϕ at each trajectory position:

$$\begin{pmatrix} \phi(x_1,t) \\ \phi(x_2,t) \\ \cdots \\ \phi(x_N,t) \end{pmatrix} = \begin{pmatrix} T_0(\tilde{x}_1),\ldots,T_{M-1}(\tilde{x}_1) \\ T_0(\tilde{x}_2),\ldots,T_{M-1}(\tilde{x}_2) \\ \cdots \\ T_0(\tilde{x}_N),\ldots,T_{M-1}(\tilde{x}_N) \end{pmatrix} \begin{pmatrix} c_0(t) \\ c_1(t) \\ \cdots \\ c_{M-1}(t) \end{pmatrix} , \tag{3.2.15}$$

$$\vec{\phi} = \mathbf{T}\vec{c}\,. \tag{3.2.16}$$

In a similar way we have for S:

$$\begin{pmatrix} S(x_1,t) \\ S(x_2,t) \\ \cdots \\ S(x_N,t) \end{pmatrix} = \begin{pmatrix} T_0(\tilde{x}_1),\ldots,T_{M-1}(\tilde{x}_1) \\ T_0(\tilde{x}_2),\ldots,T_{M-1}(\tilde{x}_2) \\ \cdots \\ T_0(\tilde{x}_N),\ldots,T_{M-1}(\tilde{x}_N) \end{pmatrix} \begin{pmatrix} s_0(t) \\ s_1(t) \\ \cdots \\ s_{M-1}(t) \end{pmatrix} , \tag{3.2.17}$$

$$\vec{S} = \mathbf{T}\vec{s}\,. \tag{3.2.18}$$

In practice, the number of trajectories N used to solve the equations (3.2.2)-(3.2.4) exceeds the number M of polynomials used for the expansion. Therefore, the expansion coefficients are obtained by solving an over-determined system of linear equations. Then, to find the solution to the system of equations (3.2.15) and (3.2.17) we applied the Singular Value Decomposition method (SVD) [76]. This method is based on proposing the following

factorization for the $(N \times M)$ rectangular matrix $\mathbf{T} = \mathbf{U}\Sigma\mathbf{V}^t$ with $N >> M$, where $\mathbf{U}$ is a $N \times M$ matrix with orthogonal columns, $\mathbf{V}$ is a $M \times M$ orthogonal matrix and $\mathbf{\Sigma}$ is a $M \times M$ matrix whose only nonzero elements lie along the main diagonal.

We construct the matrix $\mathbf{\Sigma}$ of the decomposition $\mathbf{T} = \mathbf{U}\Sigma\mathbf{V}^t$, by finding the eigenvalues of the $M \times M$ symmetric matrix $\mathbf{T}^t\mathbf{T}$. These eigenvalues are all non-negative real numbers, and we order them from the largest to the smallest one and we denote them by $\sigma_1^2 \geq \sigma_2^2 \geq \sigma_3^2 \geq ...\sigma_k^2 > \sigma_{k+1} = ... = \sigma_n = 0$. That is, we denote by σ_k^2 the smallest nonzero eigenvalue of $\mathbf{T}^t\mathbf{T}$. The positive square roots of these eigenvalues, which are called the singular values of $\mathbf{T}$, gives the diagonal entries of $\mathbf{\Sigma}$. Then, once we have found the factorization for $\mathbf{T}$, the values for the coefficients s_j and c_j can be calculated as

$$\vec{c} = \mathbf{V}\mathbf{diag}[\sigma_1^{-1}, \sigma_2^{-1}, ..., \sigma_n^{-1}]\mathbf{U}^t\vec{C} \ , \quad \vec{s} = \mathbf{V}\mathbf{diag}[\sigma_1^{-1}, \sigma_2^{-1}, ..., \sigma_n^{-1}]\mathbf{U}^t\vec{S} \ , \tag{3.2.19}$$

where for each singular value σ_j, such $\sigma_j = 0$, then σ_j^{-1} is replaced by 0.

The coefficients, $s_j^{(1)}$, $s_j^{(2)}$,$c_j^{(1)}$ and $c_j^{(2)}$, $j = 0, ..., M-1$, for the first and the second derivatives of S and ϕ can now be evaluated from Eq. (3.2.11)-(3.2.14).

Another step forward in order to increase numerical stability is the regularization of the density ρ, in order to avoid singularities in the evaluation of the quantum potential. Thus, at each time step after the new value of C is obtained, the density is evaluated $\rho(x_i, t) = e^{2C(x_i,t)}$, and then regularized, using the form given in Ref. [77]

$$\rho_{reg}(x_i, t) = \rho(x_i, t) + \epsilon \exp\left(-\rho(x_i, t)/\epsilon\right) \ , \ \epsilon \ll 1 \ . \tag{3.2.20}$$

Here we have used $\epsilon = 10^{-6}$.

In order to build the reference Gaussian $\rho_0 = e^{2C_0}$ for the separation introduced in Eq. (3.2.5), the center $\langle x \rangle$ and the width σ are chosen as the average and the root mean square deviation of the positions of the fluid particles, respectively. They are computed using

the simple quadrature

$$\langle x\rangle = \sum_{i=1}^{N} x_i \rho_{reg}(x_i,t)\Delta_i \ , \tag{3.2.21}$$

$$\sigma = \sum_{i} (x_i - \langle x\rangle)^2 \rho_{reg}(x_i,t)\Delta_i \ , \tag{3.2.22}$$

where

$$\Delta_i \equiv (x_i - x_{i-1}) \ , \quad i = 1, ..., N \ . \tag{3.2.23}$$

Then, once those parameters are found we express the reference Gaussian as

$$\rho_0(x_i,t) = \frac{1}{\sqrt{2\pi}\sigma} e^{-\frac{-(x_i-\langle x\rangle)^2}{2\sigma^2}} \ , \tag{3.2.24}$$

and then

$$C_0(x_i,t) = \ln \rho_0(x_i,t)/2 \ . \tag{3.2.25}$$

With the interpolation using Chebyshev polynomials we no longer require an equally spaced mesh to interpolate the hydrodynamic fields at each time step. A further important improvement of the present scheme is the application of the SVD/Chebyshev interpolation to the *residual* density, i.e., to the function ϕ in Eq. (3.2.5). This function is in general small and can present both positive and negative signs, allowing the full potential of Chebyshev polynomial interpolation to be exploited.

The proposed scheme to solve the EOM (3.2.2)-(3.2.4) is summarized in Figure 3.1. The starting point is the initialization, setting the trajectories positions, as well as the values of the fields and their derivatives at each trajectory. Then, the trajectories positions and the fields are updated using a four order Runge-Kutta integrator and it is performed the Chebyshev expansion of the fields at the new positions. Afterwards, observables can be computed and the new integration step is taken. Further details of the numerical algorithm can be found in the appendix B. In the following section we show the application of the scheme proposed above to study the vibrational dynamics of a Gaussian wave packet in two one-dimensional models: a quadratic potential and a Morse potential.

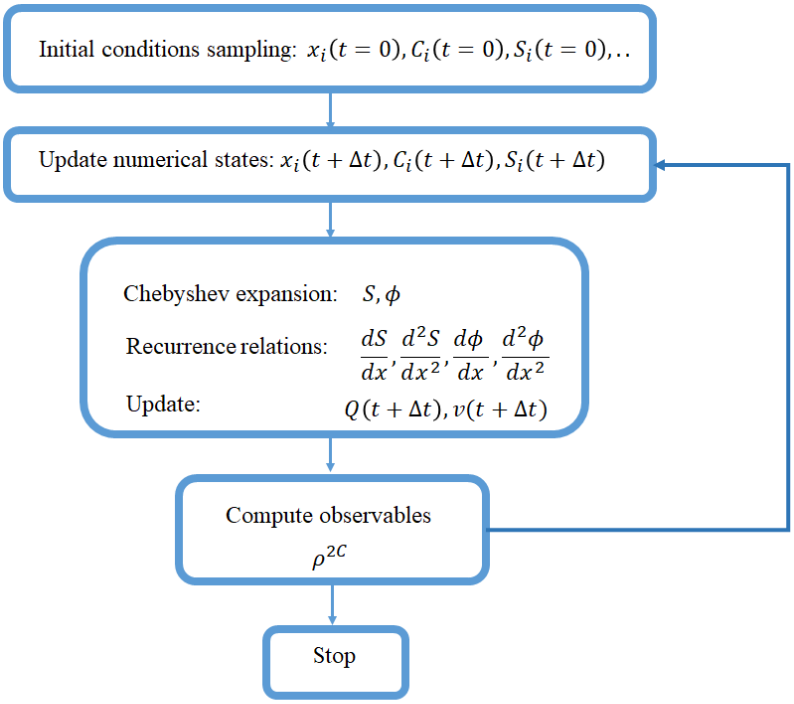

Figure 3.1: Schematic representation of the numerical algorithm proposed to integrate the hydrodynamic equations.

In the harmonic case, the outcome of the simulation using the QTM is compared with the analytical solution of the quantum mechanical equations of motion [62, 78]. On the other hand, the QTM results on the anharmonic potential are compared with a benchmark provided by the quantum wave packet propagation approach using the Cranck-Nicholson scheme [75]. The latter is based on the decomposition of the time evolution operator according to the Trotter expansion [79, 80], combined with a finite-difference representation of the molecular Hamiltonian on a uniform mesh containing 4096 points. The election of this value of the grid density, together with the time step of $\Delta t = 2.489 \times 10^{-2}$ fs, was found to yield an accurate representation of the effect of the kinetic energy operator and of the interaction potential on the evolution of the molecular wave function. The wave packet is evolved in time by recursively applying the free-particle propagator and the exponential of the potential energy matrix on the state vector.

The equations of motion for the quantum trajectories are solved using the algorithm described in the appendix B. The simulations were carried out up to 50 fs, (i.e., the total

propagation time is several vibrational periods long). At every time step, the coefficients of the Chebyshev expansion of the functions S and ϕ are computed using $M = 10$ Chebyshev polynomials and we have used $N = 100$ trajectories unless specified otherwise. For these parameters selection we ensure norm conservation up to 1%.

3.3 Results

3.3.1 Gaussian wave packet on a quadratic potential

As a first example of the implementation of the quantum trajectory method using Chebyshev polynomials we will study the vibrational dynamics of a one-dimensional Gaussian wave packet in a harmonic potential. The results of these simulations are compared with the analytical solutions of the TDSE, thus providing an accurate assessment of our results. The upcoming equations of this chapter will be written in atomic units (a.u.), unless specified ($\hbar = 1, |e| = 1$ and $m_e = 1$, being e and m_e the electron charge and mass respectively). In the presentation of our results, we use femtoseconds (fs) as the unit of time while for the rest of the magnitudes we employ atomic units (a.u.). In particular for the energy and length units we use the symbols E_h and a_0, respectively ($1\,E_h = 4.3597 \times 10^{-18}$ J and 1 a.u.=0.5291 Å).

We choose the harmonic potential:

$$V(x) = \frac{1}{2} m\omega^2 (x - x_c)^2 \ , \tag{3.3.1}$$

centered at $x_c = 0\,a_0$ with a frequency $\omega = 1.25 \times 10^{-2}\,E_h$ and a mass $m = 10000$ a.u. For the particular case of the evolution of a Gaussian wave packet in a harmonic potential, the analytical solutions of the time-dependent and time-independent Schrödinger equation are known. The ground state is a Gaussian wave packet centered at $x_c = 0\,a_0$

$$\rho(x_i, 0) = Ae^{-2a(x_i - x_c)^2} \ , \tag{3.3.2}$$

as is shown in Figure 3.2 together with the harmonic potential. The constant $A =$

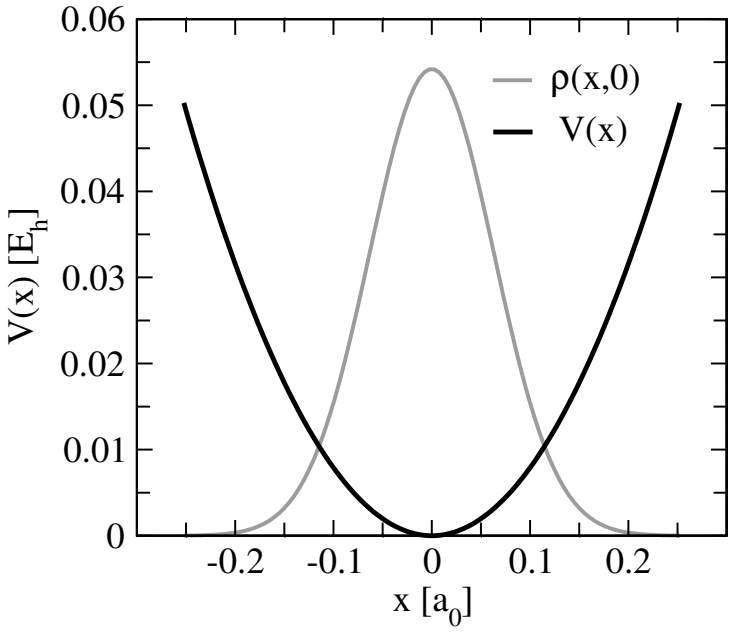

Figure 3.2: Quadratic potential (Eq.(3.3.1)) and ground state density built evaluating the analytical solution (Eq. (3.3.2)) at the initial positions of the trajectories x_i, $i = 1, ..., 100$.

$(2a/\pi)^{1/2}$ accounts for normalization of the initial density ρ, and $a = m\omega/2 = 62.8\ a_0^{-2}$. If the center of the initial wave packet is shifted with respect to the minimum of the potential, we can study the vibrational dynamics. A Gaussian wave packet in a harmonic potential retains its form. However, depending on the initial conditions, the width of the wave packet can change periodically in time, which is known as the "breathing of the wave packet" [78]. In general, the solution of the TDSE can be written as:

$$\rho(x_i, t) = Ae^{-2\beta_t(x_i - x_t)^2} = Ae^{-\frac{(x_i - x_t)^2}{2\sigma_t^2}} , \tag{3.3.3}$$

where σ_t and x_t represent the time-dependent width and center of the wave packet respectively, and its analytical solutions are given by [78]:

$$x_t = x_o \cos(\omega t) , \tag{3.3.4}$$

$$\beta_t = a\left(\frac{\beta_0 \cos(\omega t) + ia \sin(\omega t)}{i\beta_0 \sin(\omega t) + a \cos(\omega t)}\right) , \tag{3.3.5}$$

$$\sigma_t^2 = \frac{1}{4Re[\beta_t]} = \frac{a^2 \cos^2(\omega t) + \beta_0^2 \sin^2(\omega t)}{4a^2 \beta_0} . \tag{3.3.6}$$

where at $t = 0$, $x_t = x_o$ and $\beta_t = \beta_0$. For the particular case of $\beta_0 = a$ we obtain

$\beta_t = a$ for all the propagation time. The width of the wave packet does not change, this is called a "coherent state". On the other hand if $\beta_0 \neq a$ we have an "squeezed state": the width of the wave packet spreads and contracts ($\beta_0 > a$) (contracts and spreads ($\beta_0 < a$)) periodically in time.

To illustrate the results of the method, the initial wave packet is shifted to $x_o = 4\,a_0$. The trajectories are initially selected forming an equally spaced grid around x_o between the values $x_{min} = x_o - 2/\sqrt{\beta_0}$ and $x_{max} = x_o + 2/\sqrt{\beta_0}$. The initial wave packet is then evaluated at each trajectory

$$\rho(x_i, 0) = (2\beta_0/\pi)^{(1/2)} e^{-2\beta_0 (x_i - 4)^2} \ , \quad i = 1, ..., N \ , \tag{3.3.7}$$

and the hydrodynamic fields are propagated using the algorithm described above. Calculations are performed for three different values of the initial width of the wave packet: $\beta_0 = a$, and two squeezed states ($\beta_0 = a/3$ and $\beta_0 = 4a$).

In Figure 3.3, the results for the time evolution of the mean value $\langle x \rangle$ (left panel), and the width of the wave packet σ (Eq. (3.2.22)) (right column), for the three cases considered here are plotted. In both cases the comparison with the analytical results are shown. For the three initial values of the width of the wave packet, the numerical results obtained using the implementation of the QTM based on the Chebyshev expansion of the hydrodynamic fields exactly match the analytical solutions of the time-dependent Schrödinger equation. From figures 3.3 and 3.4, it can be noticed that for $\beta_0 < a$ the wave packet contracts first (as the centre of the distribution approaches the equilibrium position). Beyond this point, the wave packet gradually spreads until it reaches the inner turning point. The opposite behaviour is observed for $\beta_0 > a$ (that is, during its motion inwards, the wave packet initially broadens and it gets contracted afterwards). The sequential narrowing and spreading of the squeezed states happens twice every period, as expected from Eq. (3.3.5).

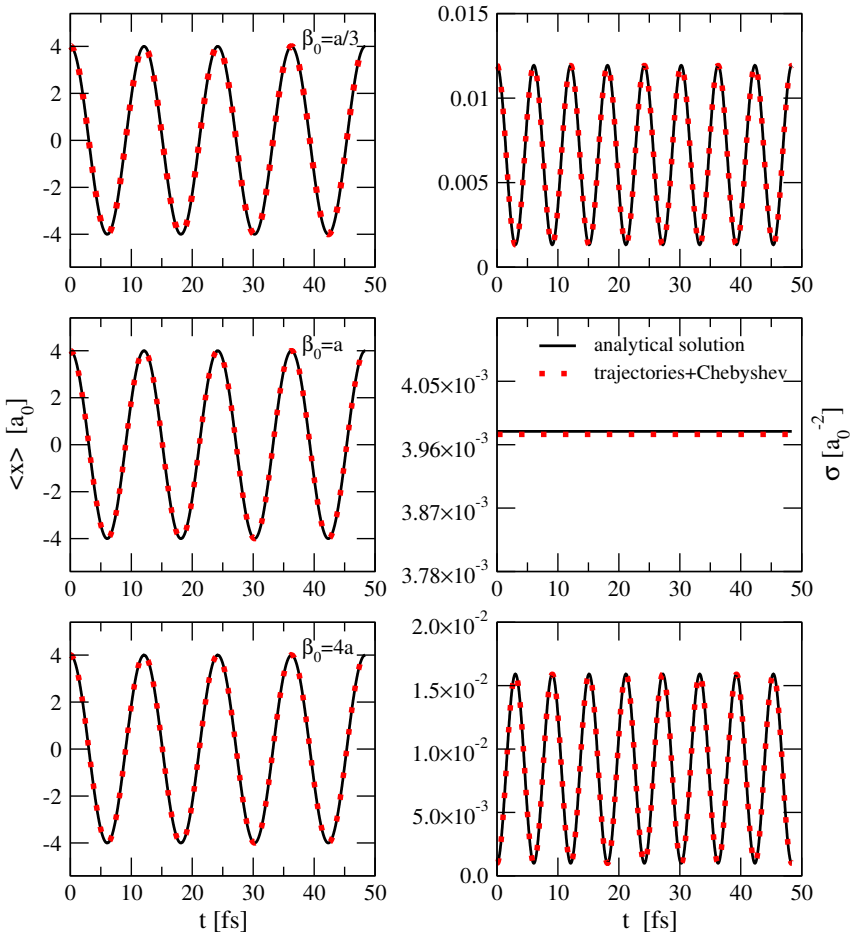

Figure 3.3: Time evolution of the mean value $\langle x \rangle$ (left column) and the width σ (right column) of the Gaussian wave packet in the quadratic potential (Eq. (3.3.1)). Three different values of the initial width are considered: $\beta_0 = a/3$, (top panel), $\beta_0 = a$ (central panel) and $\beta_0 = 4a$ (bottom panel). In all cases the comparison between the analytical results (solid line) and the averaged values are shown for $N = 100$ trajectories (points).

3.3.2 Non-Gaussian densities: time-independent analysis

As a preliminary analysis, in this section we discuss the performance of the present implementation of the QTM for structured wave packets from a time-independent perspective.

We choose three different analytical forms to represent the initial density. The densities are constructed in order to have the desired structure. The behavior of the quantum potential and the quantum force for different orders of the Chebyshev expansion are studied. As a first example we choose a Gaussian wave packet,

$$\rho_0(x_i, 0) = e^{-2a(x_i - 0.5)^2} \ , \tag{3.3.8}$$

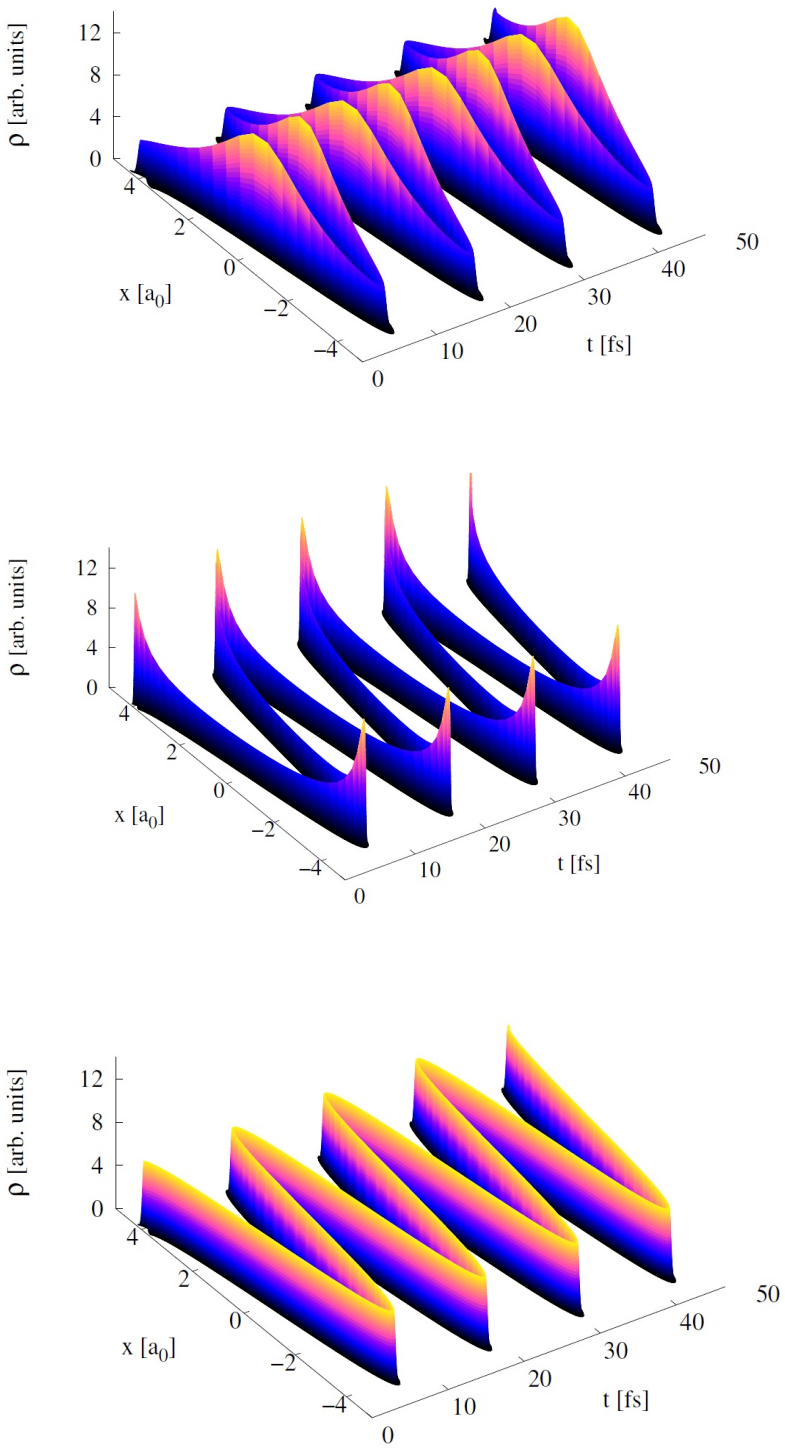

Figure 3.4: Time evolution of ρ for the three initial values of β considered: $\beta_0 = a/3$ (top panel), $\beta_0 = 4a$ (central panel) and $\beta_0 = a$ (bottom panel). The density ρ is evaluated as it is described in step 2.2 of the algorithm described in the appendix B.

with $a = 1\, a_0^{-2}$.

The second case corresponds to a density that has a well-defined node, whose analytical expression is given by:

$$\rho_1(x_i, 0) = e^{-2a_1(x_i-0.5)^2} e^{-a_2 x_i} (0.15 + \cos(\pi a_3 x_i))^2 \ . \tag{3.3.9}$$

and the third form for the density is a more structured function, but without well-defined nodes,

$$\rho_5(x_i, 0) = \frac{e^{-20a_1(x_i+1.25)^2} (1 + 0.5(1 + \cos[10\pi a_2 x_i]))^2}{(1 + e^{a_3 x_i/5})^2} \ , \tag{3.3.10}$$

with $a_1 = 1\, a_0^{-2}$ and $a_2 = a_3 = 1\, a_0^{-1}$.

We restrict our analysis to a maximal basis size of $M = 20$ Chebyshev polynomials for the expansion of the hydrodynamic fields. Setting this upper bound for the number of polynomials in the truncated expansion is motivated by the possibility to extend this algorithm to the modeling of the quantum dynamics in three- or higher-dimensional systems.

In the left column of Figure 3.5 the three analytical densities are shown with continuous lines and with points we have plotted the results of the Chebyshev expansion using $M = 10$ polynomials. In the central column we show the quantum potential for the three densities, using different orders of the Chebyshev expansion with our SVD/Chebyshev scheme described in the previous section. In order to test the accuracy of these results, we calculate the quantum potential derived from each analytical density using the collocation method described in the appendix A.0.1. In this case, as we know each density analytically, we can evaluate them at the zeros of the Chebyshev polynomials and calculate the expansion coefficients from equation (A.0.16). The coefficients used to expand the derivatives are then calculated from the recurrence relations given in the previous section. In this case we have used $M = 50$ polynomials and we have referred to the quantum potential obtained by this method as the exact quantum potential.

As a general trend, all numerically computed Q slowly converge to their exact values

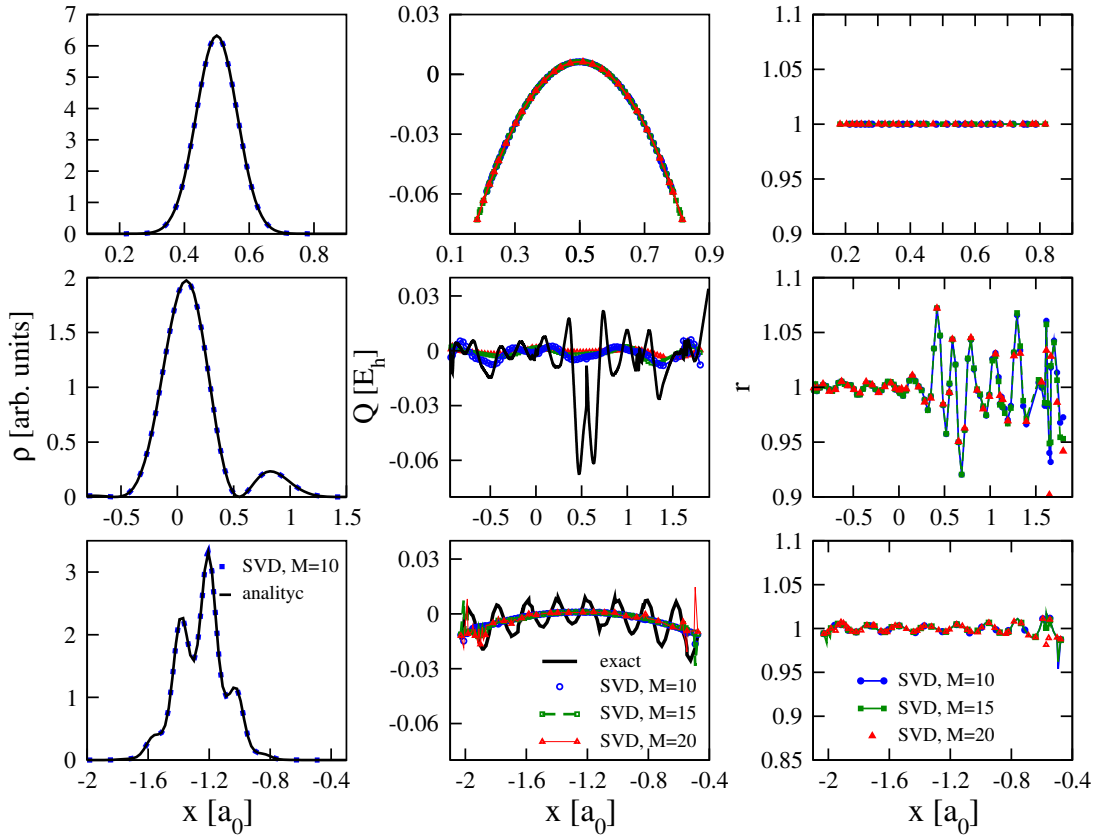

Figure 3.5: Left panel: Analytical densities (Eqs. (3.3.8)-(3.3.10)) (solid line) compared with its representation in Chebyshev polynomials for M=10. Central panel: Quantum potential calculated after representing the three analytical densities on the left using different orders of the Chebyshev expansion with the SVD/Chebyshev scheme. With the black continuous line we have represented the exact quantum potential calculated using the collocation method described in the Appendix A.0.1. Finally, in the right panel we show the results of evaluating the relative error of the force (Eq. (3.3.11)) for several orders of the expansion.

as the order of the Chebyshev series is increased. Considering only 20 Chebyshev polynomials in the expansion, the function Q reproduces the overall behaviour of the exact quantum potential but it averages the rapid spatial oscillations of the latter. The quantum potential obtained for the quantum trajectory representation of the Gaussian profile (top central panel) is perfectly reproduced, as can be expected from the results in the previous section. The oversmoothing of the quantum potential for the more structured density patterns is larger for the density with a resolved node (central panel). Due to their global interpolation properties, the Chebyshev polynomials flatten the large oscillations in the region of the node. Although the third density exhibits more structure, the unresolved character of the nodes provoke a better overall performance of the density

smoothing.

This trend can be better observed from the analysis of the error in the forces. The dynamics of the quantum trajectories is governed by the quantum and the classical forces, hence we could evaluate the relative error we make in the evaluation of the forces by evaluating the following ratio

$$r(x) = \frac{f_{cl}(x) + f_{qc}(x)}{f_{cl}(x) + f_{qe}(x)} \ . \tag{3.3.11}$$

We have identified with f_{qc} the quantum force evaluated using our Chebyshev/SVD scheme and with f_{qe} the force derived from the exact quantum potential. To calculate the force we need to evaluate the gradient of the quantum potential and then the third derivatives of the amplitude are required. In fact, from Eq. (3.2.1) we obtain the quantum force expressed in terms of C,

$$f_q = -\frac{1}{2m}\left(\frac{\partial^3 C}{\partial x^3} + 2\frac{\partial C}{\partial x}\frac{\partial^2 C}{\partial x^2}\right) \ . \tag{3.3.12}$$

To obtain the expansion coefficients, we can use the recurrence relations given in the appendix A (i.e. Eq. (A.0.14) for $p = 3$). With f_{qe} we have identified the reference quantum force calculated using the collocation method. Finally, f_{cl} is the classical force derived from the potential $V(x)$ (Eq. (3.3.1)),

$$f_{cl} = -m\omega(x - x_c). \tag{3.3.13}$$

A ratio of 1 implies a perfect fit to the density, quantum potential, and quantum force. As it can be seen, the error in the force calculation increases when the density is more structured, especially where strict nodes exist (central right panel of Figure 3.5). Increasing the number of Chebyshev polynomials only improves the convergence to the numerical exact functions marginally, but the errors still remain modest in all cases. Again, the density with unresolved nodes (bottom right panel) behaves better than the one with an

explicit node.

These results indicate that the error associated to the calculation of the quantum potential depends on the topology of the density distribution: the truncated series produce very accurate quantum potentials for nearly Gaussian shapes, but the agreement of the SVD-based and the exact quantum potentials degrades as the number of nodes or ripples increases.

3.3.3 Non-Gaussian densities: time-evolution

As a more realistic model of molecular vibrations, the method is also tested for the time evolution of a Gaussian wave packet on a Morse potential. The Morse function

$$V(x) = D(e^{-2\alpha(x-r_0)} - 2e^{-\alpha(x-r_0)}) \ , \tag{3.3.14}$$

provides a reasonable description of intra-molecular interactions for a wide range of di-atomic molecules. The results presented in this subsection correspond to the following choice of the interaction potential parameters: $\alpha = 0.27\, a_0^{-1}$, $r_0 = 3.5\, a_0$ and $D = 10\, E_h$. Following the methodology described in section 3.2, we consider the propagation of a Gaussian wave packet of the form (3.3.7) for several choices of the initial width.

As in the previous subsection, the equations of motion (3.2.2)-(3.2.4) are solved on the anharmonic potential energy curve using a fourth order Runge-Kutta integrator (Step 2 of the algorithm described in the appendix B), but employing an adaptive time step. The value of the time step Δt is adjusted to keep the maximum change in the positions of the fluid particles below a pre-defined fraction δ of the minimal spacing between adjacent trajectories. In this study, δ is set to be 0.5 so that, at every time step, Δt is chosen as half the minimum value of $(x_{i+1} - x_i)/v_i$, where v_i is the value of the velocity field at the position x_i, as in Ref. [17]. In Figure 3.6, a comparison between the results of the quantum trajectory simulations and those of the wave packet propagation is shown for the case of a Gaussian initial wave function of width $\beta_0 = 62.8 a_0^{-2}$ in Eq. (3.3.7).

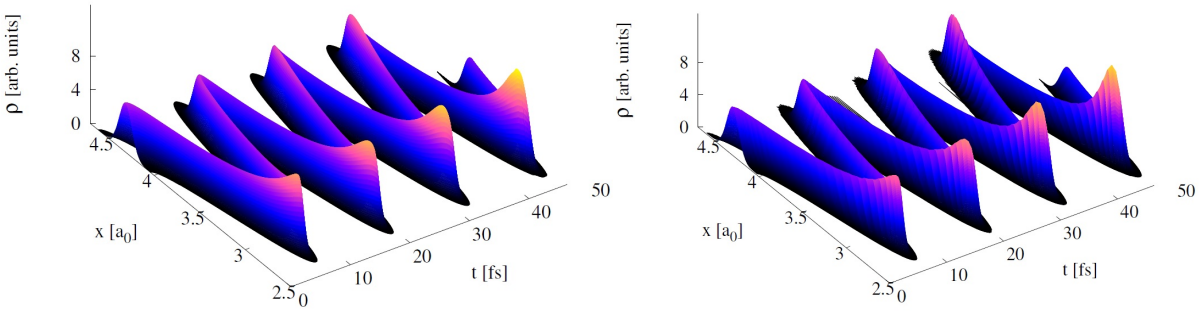

Figura 3.6: Time evolution of a Gaussian wave packet with $\beta_0 = 62.8a_0^{-2}$ in a Morse potential. Comparison between the results of the SVD/Chebyshev scheme (left panel) and the benchmark calculations using Crank-Nicholson method (right panel).

It can be observed that there is a good agreement between both methods. In order to evaluate the correspondence between the wave packet and the quantum trajectory simulations, we calculated the mean value of the relative error r_e at different time steps

$$\langle r_e(t) \rangle = \frac{1}{N} \sum_{i=1}^{N} \frac{|\rho_{wp}(x_i, t) - \rho_c(x_i, t)|}{\rho_{wp}(x_i, t)}, \tag{3.3.15}$$

where ρ_{wp} represents the results from standard wave packet propagation methods, and ρ_c accounts for the results from our SVD/Chebyshev method. We obtained that up to 46 fs the mean value of the relative error remains smaller than 11%. The correspondence of our method and the full quantum mechanical wave packet propagation supports the validity of the numerical approach proposed in this work, at least in the case of the one-dimensional quantum dynamics on anharmonic potentials for short time propagation (i.e., for several vibrational periods). As time evolves the wave packet gets more structured and the method (in particular, the use of a Gaussian reference function C_0) is no longer accurate.

3.4 Conclusions

In this chapter we have investigated the ultrafast vibrational dynamics on model one-dimensional potentials within the framework of the Quantum Trajectory Method in the Lagrangian frame. We have integrated the equations for the fields S and C along the

quantum trajectories, by computing the spatial derivatives of those fields via the recurrence relations obeyed by global interpolating (Chebyshev) polynomials. A key advantage of the present approach is that a relatively small number of polynomials are required in the truncated expansions to attain a reasonably accurate representation of the hydrodynamic fields. Numerical instabilities in the calculation of the quantum potential and, as a consequence, in the integration of the equation of motion, are surmounted by a combination of several numerical techniques:

- First, the density is regularized to avoid strict nodes and it is recasted in logarithm form.
- Second, the logarithm of the density is split into two contributions: that of a reference Gaussian which approximates the density distribution, and a residual function ϕ. This partition have shown to improve the description of the quantum effects and it is expected to improve convergence in other applications of the QTM to the treatment of molecular vibrations, especially for localized wave packets.

The comparison between the quantum potential computed using the Chebyshev expansion coefficients of the density retrieved from the singular value decomposition, and the exact quantum potential for various distributions suggests that the accuracy of the SVD procedure decreases as the topology of the density distribution gets more structured. The truncation of the Chebyshev series leads to a slight oversmoothing of the spatial dependence of the quantum potential. Nevertheless, the error remains small and it does not affect significantly the corresponding forces exerted on the fluid particles.

In general, the proposed methodology allows to propagate quantum trajectories and to study the full quantum dynamics from a wave function free perspective. Several numerical strategies were implemented all together with the SVD/Chebyshev scheme for the derivatives evaluation in order to improve the numerical accuracy. However, by using the SVD method to calculate the expansion coefficients, we are gaining in numerical accuracy, but we are limited in the future extension of the method to describe higher dimensional

systems. Indeed, in the multidimensional case, the Singular Value Decomposition needs to be applied to matrices of order M^d (d being the number of spatial dimensions). Retrieving the expansion coefficients using the SVD would become impractical for matrices with order M^d exceeding several thousands. Furthermore, the proposed scheme is not suitable for applications where the wave packet is delocalized. For example, to study phenomena such as scattering on a barrier, where the wave packet splits into a transmitted and a reflected part, or during the interaction of an atom with a strong laser field. In this case, the electronic wave packet can spread over a wide region in space while the field is driving the electron far form the core. Therefore, new algorithms are required in order to describe these phenomena, within a quantum trajectory perspective. The next chapter is devoted to the development of a new methodology to study the dynamics of the quantum trajectories, which will allow the study of such kind of problems.

CHAPTER 4 QUANTUM DYNAMICS MODELED BY INTERACTING TRAJECTORIES

4 QUANTUM DYNAMICS MODELED BY INTERACTING TRAJECTORIES

In this chapter we present a new method to perform quantum dynamical simulations based on the propagation of interacting trajectories where the effect of the quantum potential is mimicked by effective pseudo-particle interactions. The method is applied to several quantum systems, both for bound and scattering problems. Furthermore, the methodology is applied to ultrashort laser ionization of a model hydrogen atom. The pulses are chosen to be sufficiently short so the relative phase between the carrier wave and the pulse envelope becomes important.

4.1 Introduction

In the second chapter we presented the theoretical aspects of the quantum hydrodynamic equations that govern the dynamics of the quantum trajectories. Together with this theoretical background, we introduced the QTM, as the numerical implementation of the equation of motion of the quantum trajectories. As a promising alternative to the QTM pioneered by Wyatt, a fully wave function-free formulation of quantum mechanics has been proposed [38]−[41].

In this approach, the time-dependent quantum mechanical problem is recast into a dynamical problem of a parameterized density. While in principle different parametrizations are possible, for one-dimensional problems a special parametrization has been proposed in [39], which leads to an effective Newton equation with a quantum potential. For a specific choice of the parametrization, which effectively labels the trajectories according to their spatial positions, one is lead to the form of the quantum trajectories equations of motion proposed by Hall and collaborators [43]. The discretized version of the density was referred by Hall and coworkers as "many interacting world" interpretation [43, 45]. However, apart from the interpretative aspects of the formulation, it can be used for

the study of quantum dynamics based on the propagation of an ensemble of trajectories, which evolve under the action of a quantum potential-like quantity. In Ref. [43], the model quantum potential was chosen as one of the terms of the full quantum potential, since it contains only the energy conserving term depending only on the first derivative of the probability density (second term of Eq. (8.0.7) in chapter two). Consequently, using this approach, it is not straightforward to generate the phase of the wave function. In contrast, by working with the complete expression of the quantum potential, as proposed in Ref. [38] and [39], the phase becomes equal to the action and it can easily be computed via a simple integral (see i.e. Eq. 8.0.21 in chapter two).

Therefore, our objective in this chapter is to derive the full form of the quantum-like potential considering the same *ansatz* for the density proposed in Ref. [43]. In order to evaluate the influence of the term neglected in Ref. [43] on the trajectory dynamics, we derive the model quantum force and calculate the correlation function and spectra, as examples of observables where the phase of the wave function is relevant.

Thus, to evaluate the performance of these model quantum potentials and forces, i.e., their capacity to capture some essential quantum mechanical phenomena (such as the zero-point energy, tunneling and scattering from a barrier), in the first part of this chapter the method is applied to several one dimensional test problems for time-independent potentials. Namely, the determination of the ground state on harmonic and anharmonic potentials, the propagation of wave packets in the presence of an Eckart barrier and of an uphill ramp, tunneling dynamics in a double minimum potential and in a potential with a local minimum and a finite barrier. Moreover, the calculation of correlation functions and spectra are performed from the quantum trajectory simulations.

Then, in the second part of this chapter we study the laser-driven electron dynamics within the interacting trajectory formalism. This is precisely, one of the fields where the use of quantum trajectories arise as a promising alternative. Even for one-dimensional model systems, as the one we study here, the solution of the Schrödinger equation with the standard methods is very difficult. This is due to the fact that during the interaction

with the field, the electron wave packet expands over a wide region in space, and huge grids are required in order to accurately represent the wave function. Here, we show the performance of our trajectory-based method in the description of the laser-driven atomic ionization. As model system we choose a soft-core Coulomb potential to model the electron-nucleus interaction. An interesting aspect of the dynamical process triggered by intense and short laser pulses is that for extremely short pulses, comprising only a few optical cycles, the Carrier Envelope Phase (CEP) has a strong influence on the laser induced dynamics. This dependence can be used as an additional parameter to experimentally control the ionization dynamics of atomic or molecular systems. A particularly relevant example of the influence of the CEP on the electron dynamics is found in the photo-electron emission, where the CEP allows to control the forward-backward asymmetry (also called the left-right asymmetry) in the photo-electron spectra [81]-[84]. To assess the performance of our trajectory-based dynamics, observables like the total ionization yield are calculated and the CEP effects on the photo-electron spectra are analyzed.

The chapter is structured as follows. In the next section we shortly come back to the EOM of the quantum trajectories presented in chapter two, in order to introduce the model quantum potential and force. Afterwards we present our main results divided in two parts. A first part, where the method is applied to simulate quantum dynamics in the time-independent potentials mentioned above. Then, in the second group of our results we model the laser driven electron dynamics as an example of the performance of the method for time-dependent potentials. Finally, some partial conclusions are drawn.

4.2 Methods

In this section, we start from the *ansatz* for the density proposed by Hall and coworkers [43] and follow their derivation, but including both terms in the quantum potential, in order to evaluate the full quantum potential and force.

4.2.1 Model quantum potential and force

First we will come back to some of the results presented at the end of chapter two concerning the equations to propagate quantum trajectories. The one-dimensional version of the hydrodynamic equations is used and all equations are written in atomic units unless specified. As we mentioned in chapter two, one of the possible combinations of the hydrodynamic equations which allows to propagate quantum trajectories is the following,

$$\frac{d\rho}{dt} = -\rho\frac{\partial v}{\partial x} , \tag{4.2.1}$$

$$m\frac{dv}{dt} = -\frac{\partial}{\partial x}(V+Q) , \tag{4.2.2}$$

$$\frac{dS}{dt} = \frac{1}{2}mv^2 - (V+Q) . \tag{4.2.3}$$

In principle, the solutions of equations (4.2.1)-(4.2.3) correspond to the exact time evolution of the quantum mechanical state of the system. In chapter three, we have proposed a method to propagate the trajectories based on Chebyshev expansion of the hydrodynamic fields, which were used to study the ground state vibrational dynamics of bounded systems. Here we follow a different approach, starting from the *anstaz* for the density proposed by Hall and coworkers [43], we derive approximate expressions for the quantum potential and force. Then, we propagate a set of interacting trajectories with the model quantum potential and force. We show that in the limit where the number of paths goes to infinity they resemble the quantum trajectories and the predictions of our model approach the quantum mechanical results. Following Hall's derivation [43], given that the initial set of N trajectories is ordered and labeling them as $x_1 < x_2 < ... < x_N$. Then, if $\rho(x)$ is any smooth interpolation of the density, the mean value $\langle A \rangle$ of certain function $A(x)$ is given by

$$\langle A\rangle = \frac{1}{N}\sum_{n=1}^{N} A(x_n) \approx \int \rho(x)A(x)dx$$
$$\approx \sum_{n=1}^{N}\int_{x_{n-1}}^{x_n} \rho(x_n)A(x_n)dx \approx \sum_{n=1}^{N}(x_n - x_{n-1})\rho(x_n)A(x_n)\ . \quad (4.2.4)$$

It suggests the following *ansatz* for the smoothed density at $x = x_n$, as was proposed in Ref. [43],

$$\rho(x_n) = \frac{1}{N(x_n - x_{n-1})} \approx \frac{1}{N(x_{n+1} - x_n)}\ , \quad (4.2.5)$$

where x_n represents the position of the trajectories at each time step. Under the assumption that the separation between the trajectories is a smooth function of the index n, the discrete sampling at the points $x_1, x_2, ..., x_N$ approaches the density in the limit when the number of trajectories N tends to infinity.

Now from Eq. (4.2.5) we can derive an approximate expression for the quantum potential. If we return to equation (8.0.7) the quantum potential for a one-dimensional system, written in terms of the density ρ has the form

$$Q(x,t) = -\frac{1}{4m}\left[\frac{\rho''(x,t)}{\rho(x,t)} - \frac{1}{2}\left(\frac{\rho'(x,t)}{\rho(x,t)}\right)^2\right]\ , \quad (4.2.6)$$

where ρ' and ρ'' denote the first and second spatial derivatives of the density. In the derivation presented in Ref. [43], only the second term in 4.2.6 was considered in the model quantum potential. Here we follow the same idea, but including both terms in Q. In our notation we assume that the time dependence is implicitly included, given that x_n represents the trajectory position at a given time.

The first and second derivatives in equation (4.2.6) can be evaluated using finite differences. Asymptotically, for a large number of trajectories, the first derivatives of the

function $\rho(x)$ at the point $x = x_n$ can be approximated as:

$$\rho'(x_n) \approx \frac{\rho(x_{n+1}) - \rho(x_n)}{x_{n+1} - x_n} \ , \tag{4.2.7}$$

using Eq. (4.2.5),

$$\rho'(x_n) \approx \frac{1}{x_{n+1} - x_n}\left(\frac{1}{x_{n+2} - x_{n+1}} - \frac{1}{x_{n+1} - x_n}\right)\frac{1}{N} \ , \tag{4.2.8}$$

From Eqs. (4.2.5) and (4.2.8) the ratio $\rho^{'}(x_n)/\rho(x_n)$ can be written as

$$\frac{\rho'(x_n)}{\rho(x_n)} \approx \frac{1}{x_{n+2} - x_{n+1}} - \frac{1}{x_{n+1} - x_n} \approx \frac{1}{x_{n+1} - x_n} - \frac{1}{x_n - x_{n-1}} \ . \tag{4.2.9}$$

In Ref. [43], this formula was used to approximate the second term in expression (4.2.6), which was subsequently used to propagate the trajectories. This procedure accounts for the time evolution of the trajectories under the influence of a purely repulsive quantum-like potential Q_0 [43],

$$Q_0(x_n) = \frac{1}{8m}\left(\frac{1}{x_{n+1} - x_n} - \frac{1}{x_n - x_{n-1}}\right)^2 \ . \tag{4.2.10}$$

However, we can use the same procedure to approximate the second derivative $\rho^{''}(x_n)$

$$\rho''(x_n) \approx \frac{\rho'(x_{n+1}) - \rho'(x_n)}{x_{n+1} - x_n} \ , \tag{4.2.11}$$

$$\rho''(x_n) \approx \frac{1}{x_{n+1} - x_n}\left(\frac{1}{(x_{n+3} - x_{n+2})(x_{n+2} - x_{n+1})} - \frac{1}{(x_{n+2} - x_{n+1})^2} - \frac{1}{(x_{n+1} - x_n)(x_{n+2} - x_{n+1})} + \frac{1}{(x_{n+1} - x_n)^2}\right) \ , \tag{4.2.12}$$

and the ratio $\rho^{''}(x_n)/\rho(x_n)$

$$\frac{\rho''(x_n)}{\rho(x_n)} \approx \frac{1}{x_{n+2}-x_{n+1}}\left(\frac{1}{x_{n+3}-x_{n+2}}-\frac{1}{x_{n+2}-x_{n+1}}-\frac{1}{x_{n+1}-x_n}\right)+\frac{1}{(x_{n+1}-x_n)^2}$$
$$\approx \frac{1}{x_{n+1}-x_n}\left(\frac{1}{x_{n+2}-x_{n+1}}-\frac{1}{x_{n+1}-x_n}-\frac{1}{x_n-x_{n-1}}\right)+\frac{1}{(x_n-x_{n-1})^2}\ . \quad (4.2.13)$$

Therefore, after substituting equations (4.2.9) and (4.2.13) into Eq. (4.2.6), we derive the following expression for the quantum potential

$$Q(x_n)=-\frac{1}{4m}\left[\frac{1}{(x_{n+2}-x_{n+1})(x_{n+1}-x_n)}-\frac{1}{(x_{n+1}-x_n)^2}-\frac{1}{(x_{n+1}-x_n)(x_n-x_{n-1})}\right.$$
$$\left.+\frac{1}{(x_n-x_{n-1})^2}-\frac{1}{2}\left(\frac{1}{x_{n+1}-x_n}-\frac{1}{x_n-x_{n-1}}\right)^2\right]\ . \quad (4.2.14)$$

In this expression, the last term in parenthesis coincides with the quantum-like potential proposed by Hall and coworkers, Q_0 (Eq. 4.2.10), and it can also be obtained from a more general one proposed earlier [39]. In what follows we want to analyze to which extent the quantum potential Q is capable to account for quantum effects, and to evaluate the influence of the additional terms, as compared with Q_0, on the dynamics of the quantum trajectories.

As we mentioned in the introduction, the quantum force is obtained as the gradient of the quantum potential. For our one-dimensional model, the quantum force acting on the nth particle, is computed using this quantum potential as $f_q = \frac{-\partial \sum_{i=1}^{N} Q(x_i)}{\partial x_n}$.

The approximate quantum force depends on the four nearest neighbors, the first two particles to the left and to the right, and it reads

$$f_q(x_{n-2},x_{n-1},x_n,x_{n+1},x_{n+2}) = \frac{1}{4m}\left[\frac{1}{(x_{n+1}-x_n)^2}\times\left(\frac{1}{x_{n+2}-x_{n+1}}-\frac{2}{x_{n+1}-x_n}+\frac{1}{x_n-x_{n-1}}\right)\right.$$
$$\left.-\frac{1}{(x_n-x_{n-1})^2}\times\left(\frac{1}{x_{n+1}-x_n}-\frac{2}{x_n-x_{n-1}}+\frac{1}{x_{n-1}-x_{n-2}}\right)\right]\ , \quad (4.2.15)$$

leading to the same expression for the quantum force as the one obtained in Ref.[43] from Q_0.

Because of this equivalence, propagating the trajectories employing the present form for the quantum potential Eq. (4.2.14) or Q_0 yields identical results. However, differences arise in the computation of observables which depend on the phase of the wave function, for instance, in the evaluation of correlation functions, as shall be shown below.

Equation (4.2.14), together with the relations (4.2.1) to (4.2.3), maps the original problem of a quantum particle moving in one dimension into an equivalent problem of N particles interacting with their first and second nearest neighbours. Noteworthy, the paths obtained using this procedure, strictly obey the non-crossing rule for the quantum trajectories, because of the divergence of the model quantum potential if trajectories become infinitely close. Furthermore, if we assume that the initial set of particles is distributed according to some known initial density, and we define their velocity as $v_i = \nabla S(x_i)/m$ as N approach to infinity our set of interacting trajectories will approach the quantum trajectories.

Here we finally solve the following set of equations

$$\dot{x}_n = v_n \ , \tag{4.2.16}$$

$$m\frac{dv_n}{dt} = f_c(x_n) + f_q(x_n) \ , \quad n = 1, ..., N \ , \tag{4.2.17}$$

$$\tag{4.2.18}$$

which represent the equation of motion for the interacting particles evolving under the action of the external force $f_c = -\partial V/\partial x$, evaluated as the gradient of the classical interaction potential, and the approximate quantum force f_q, Eq. (4.2.15).

Furthermore, equations (4.2.1) and (4.2.3) can be integrated to reconstruct the wave function along each trajectory, as it was shown in chapter two (Eq. (8.0.21)).

4.2.2 Calculation of observables and wave packet analysis

In sections 4.3 and 4.4, we show the results of using the aforementioned form for the quantum force (Eq. (4.2.15)) to study a variety of model dynamical problems. Our aim is to test how the time evolution of these trajectories reproduce the emergence of well known quantum effects, such as zero-point energy, tunneling, wave packet spreading, over-barrier reflection, etc. In particular, in section 4.3 we perform ground state calculations for a harmonic and a Morse potential. As for the quantum dynamics, we study the wave packet scattering on an Eckart barrier. To illustrate the over-barrier reflection we show the example of an uphill ramp. As the last examples of this part we study the tunneling dynamics in a double minimum potential as well as the dynamics in a potential with a local minimum and a finite barrier. Therefore, now we define some of the observables we will need in order to evaluate the information coming out from the trajectory dynamics.

From the *ansatz* proposed in the previous section for the density distribution (Eq. (4.2.5)), the expectation values of an arbitrary function $\phi(x,t)$ can be computed as:

$$\langle \phi(x,t) \rangle = \int dx\, \rho(x,t)\phi(x,t) \approx \frac{1}{N}\sum_{n=1}^{N} \phi(x_n) \ . \tag{4.2.19}$$

The expectation value of the energy is then evaluated from equation (4.2.19),

$$\langle E \rangle = \frac{1}{N}\sum_{n=1}^{N} E(x_n) = \frac{1}{N}\sum_{n=1}^{N}\left[\frac{p_n^2}{2m} + V(x_n) + Q(x_n)\right] \ . \tag{4.2.20}$$

Another magnitude of interest is the transmission probability. Let us suppose that we have the barrier located at x_b, then the transmission probability as a function of time $P(t)$ can be evaluated as

$$P(t) = \int_{x_b}^{\infty} \rho(x,t)dx \ . \tag{4.2.21}$$

From the *ansatz* proposed for the density, this equation translates into a summation over

all the trajectories with positions x_n such that $x_i \geq x_b$

$$P(t) = \frac{1}{N} \sum_{n=1, x_n \geq x_b}^{N} 1 \ . \tag{4.2.22}$$

Let us remark that $P(t)$ is the time-dependent transmission probability, in the sense that it is evaluated from the trajectory distribution at each time.

Furthermore, in the study of wave packet dynamics and of reactive scattering it is often useful to evaluate the time-dependent autocorrelation function,

$$C(t) = \langle \Psi(x,0) | \Psi(x,t) \rangle \ , \tag{4.2.23}$$

and its Fourier transform, the energy spectrum [78]

$$F(\omega) = \frac{1}{2\pi} \int_{-\infty}^{\infty} dt \langle \Psi(x,0) | \Psi(x,t) \rangle e^{i\omega t} \ . \tag{4.2.24}$$

In equations (4.2.23) and (4.2.24), the brackets denote the integration over the spatial coordinate. In order to compute the correlation function, the time evolution of the wave function along each trajectory is required, which can be formally evaluated starting from the initial wave function given at the sampling points $x_i(t_0)$ as it was shown in chapter two:

$$\Psi(x_i(t)) = \Psi(x_i(t_0)) \exp\left(-\frac{1}{2} \int_{t_0}^{t} \left(\frac{\partial v}{\partial x} \right)_{x_i(\tau)} d\tau \right) \times \exp\left(i \int_{t_0}^{t} \left[\frac{1}{2m} \left(\frac{\partial S}{\partial x} \right)^2 - V - Q \right]_{x_i(\tau)} d\tau \right) . \tag{4.2.25}$$

From this relation, it can be seen that the synthesis of the wave function along each trajectory relies on the time integration of the quantum potential Q. Hence, the evaluation of the auto-correlation function provides a suitable test to evaluate the importance of considering the quantum potential in Eq. (4.2.14), as compared to the one proposed in Ref.[43]. Although in principle, the correct wave function phase can be generated from either Q or Q_0, only the complete quantum potential Q generates the phase via the

simple wave function synthesis given in Eq. (4.2.25). This will be documented in Sec. 4.3 below.

4.2.3 Details of the numerical implementation

In the next section, the methodology presented above using the approximate form of the quantum potential Q (Eq. (4.2.14)) is applied to a variety of one dimensional model problems. Moreover, we evaluate the influence of the term $\nabla^2\rho/\rho$ of the quantum potential, in the calculation of observables such as the energy spectrum and the correlation function.

For each model system, we analyze the numerical convergence properties as the number of trajectories is increased. For a large number of propagating trajectories, large quantum forces are encountered, which yields the numerical integration difficult and requires automatic step size control. Hence, the equation of motion for the quantum trajectories are solved using a fourth order Runge-Kutta integrator with adaptive time step [85]. The time step required for the integration varies over several orders of magnitude, since the quantum force shows strong variations, in particular when trajectories come close together. This is shown below for the example of the Eckart barrier (see Figure 4.6). The integration with an absolute error of 10^{-12}, leads to a relative energy conservation of 10^{-7} over the full propagation time. Furthermore, left and right boundaries need to be specified. In the examples presented below, we follow Ref. [43] and assume x_{-2} and $x_{-1} \to -\infty$ as well as x_{N+1} and $x_{N+2} \to \infty$.

In the ground state, the total force (i.e., the gradient of the interaction potential plus the quantum potential) acting on each trajectory should vanish, that is $f_c(x_n) + f_q(x_n) = 0$, for $n = 1, .., N$. Therefore, following a procedure proposed in Ref. [43], in order to find the stationary distribution of the trajectories, equations (4.2.16)-(4.2.17) are solved, but the velocities of the trajectories are set to zero after each time step. The final distribution obtained via this relaxation process approaches the ground state density distribution in the limit $N \to \infty$. In the next section we will show the results of the ground state calculation

for the harmonic and the Morse potential. However, the ground state distribution of trajectories of an arbitrary potential can be calculated using the same methodology. In fact, all the initial conditions we use in the examples presented below, are generated with this relaxation process.

The results derived from the trajectory dynamics are compared with the exact solution of the TDSE using the split operator Fast Fourier Transform Method (FFT) developed by Feit et al. [80]. Within this method, the ground state densities of each model potential are calculated by a relaxation method, propagating the wave function in imaginary time.

4.3 Results. Part I: time-independent potentials

4.3.1 Ground state calculations

Harmonic potential

As a first example, we will study the ground state of a particle in a parabolic potential, $V(x) = \frac{1}{2}m\omega^2(x - x_0)^2$. Using atomic units, we choose the parameters of the harmonic potential as $m = 1\,a.u.$, $x_0 = 10\,a_0$, $\omega = 1\,E_h$. The initial condition is taken as a Gaussian wave packet with the same width as the ground state wave function and displaced to the left (i.e., centered at $9.5\,a_0$).

The stationary distribution of the trajectories is obtained, after solving the equations (4.2.16)-(4.2.17), setting to zero the velocities of the trajectories after each integration step, we build the density using the *ansatz* proposed in Eq. (4.2.5). We also calculate the mean value of the total energy $\langle E \rangle$.

In Figure 4.1, we show the convergence of the energy estimator (Eq. (4.2.20)) and of the density distribution (Eq. (4.2.5)) towards the ground state energy and probability density, respectively, as a function of the number of trajectories. It can be seen that the quantum mechanical probability distribution of the ground state is qualitatively well reproduced already for the smallest number of trajectories ($N = 31$). As the number of sampling points gets larger, the description of the tails of the density distribution improves progressively, and it becomes very accurate for an ensemble of $N = 601$ trajectories.

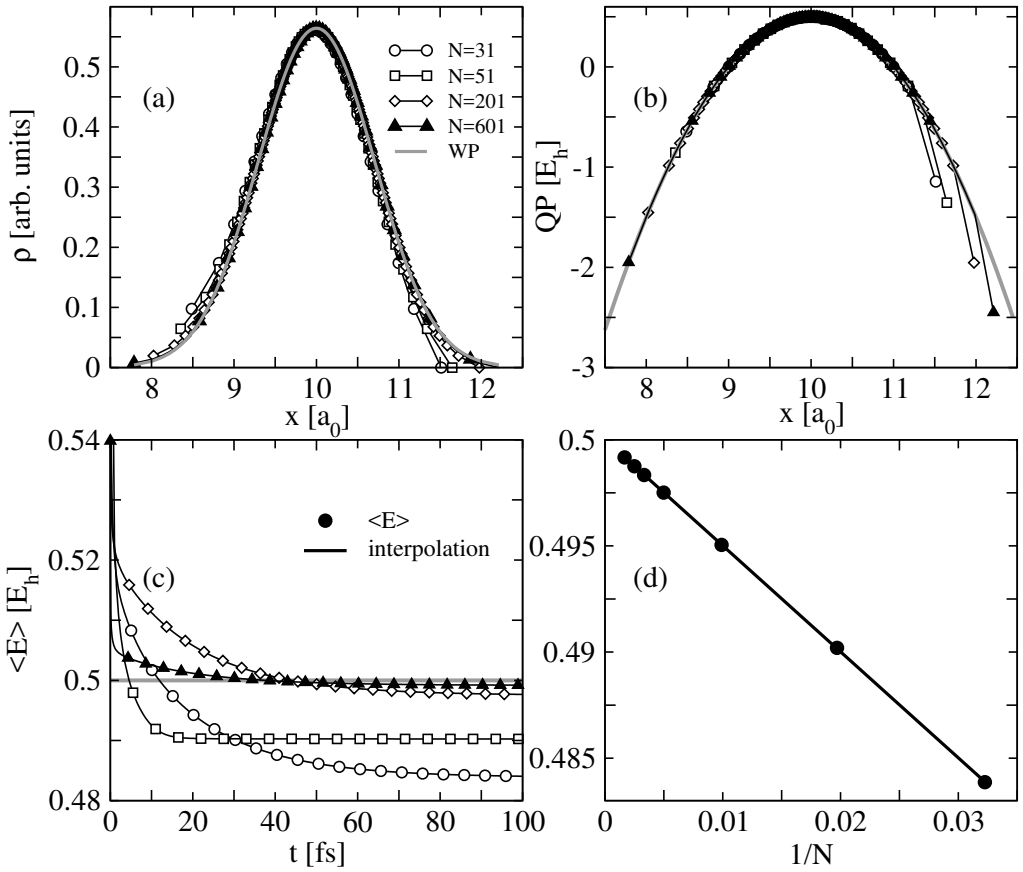

Figura 4.1: (a) Convergence of the asymptotic density distribution to the probability density of the ground state of a harmonic oscillator, for an increasing number of trajectories. (b) Convergence of the quantum potential to the known analytical form of the quantum potential of a harmonic oscillator, for an increasing number of trajectories. (c) Average energy $\langle E \rangle$ for an ensemble of N quantum trajectories as a function of time. The horizontal line indicates the exact value of the zero-point energy. (d) Linear interpolation of the dependence of the asymptotic energies E as a function of the inverse of the number of trajectories N.

In panel b) of Figure 4.1, the convergence of the quantum potential towards the analytical solution is shown. Moreover, for every size of the ensemble the average energy reaches its asymptotic value after a propagation time $\lesssim$100 fs. These limiting values quickly approach the zero-point energy as $N \to \infty$. The linear extrapolation of the estimated energy to the limit of $1/N \to 0$ is plotted in the bottom right panel of Figure 4.1. Indeed, the relative error decreases below 10^{-3} already for $N = 100$ trajectories.

Morse oscillator

As an illustration of the performance of the method for the determination of the vibrational ground state in anharmonic potentials, we analyze the case of a Morse oscilla-

tor

$$V(x) = D\left[1 - e^{-\alpha(x-x_0)}\right]^2 \ , \tag{4.3.1}$$

with the same mass ($m = 1\,a.u.$), equilibrium position ($x_0 = 10\,a_0$) and the frequency in the harmonic approximation ($\omega = 1\,E_h$) as in the previous example. The stiffness parameter α is varied in the range from $\alpha = 0.01\,a_0^{-1}$ to $\alpha = 0.5\,a_0^{-1}$, while the well depth $D = m\omega^2/2\alpha^2$ is adjusted to keep the vibrational frequency ω constant. For this choice of parameters, the number of supported bound states decreases from $N_b = 10^4$ ($\alpha = 0.01$) down to $N_b = 3$ ($\alpha = 0.5$). The eigenvalues of the Morse oscillator are given analytically (atomic units are used) [86],

$$E_n = \left(n + \frac{1}{2}\right)\omega - \left(n + \frac{1}{2}\right)^2 \frac{\omega^2}{4D} \ . \tag{4.3.2}$$

The computed density distribution and energies are depicted in Figure 4.2, for $\alpha = 0.1\,a_0^{-1}$. On the one hand, the slight shift of the probability density to larger distances is accurately described in the interacting trajectories representation, for ensembles larger than $N = 200$, whereas the convergence to the exact density distribution (for progressively larger sizes of the ensemble) happens faster than for the harmonic case.

On the other hand, the average energy (Eq. (4.2.20)) is initially larger than that of the harmonic oscillator, for the same initial wave packet. This reflects the larger steepness of the Morse function in the region sampled by the initial wave function, compared to the parabolic potential. The difference in the slopes of the potential energy curves is also the cause of the faster convergence rate (to the ground state energy, as a function of the propagation time) observed in Figure 4.2b, in comparison with the corresponding plots in Figure 4.1c. These variations in the rate of convergence depend on the specific shape of the anharmonic potential considered, and on the particular distribution chosen as initial condition for the relaxation process.

In Figure 4.3, it is shown how the error in the determination of the ground state energy depends on the anharmonicity, for the range of values of the stiffness parameter considered

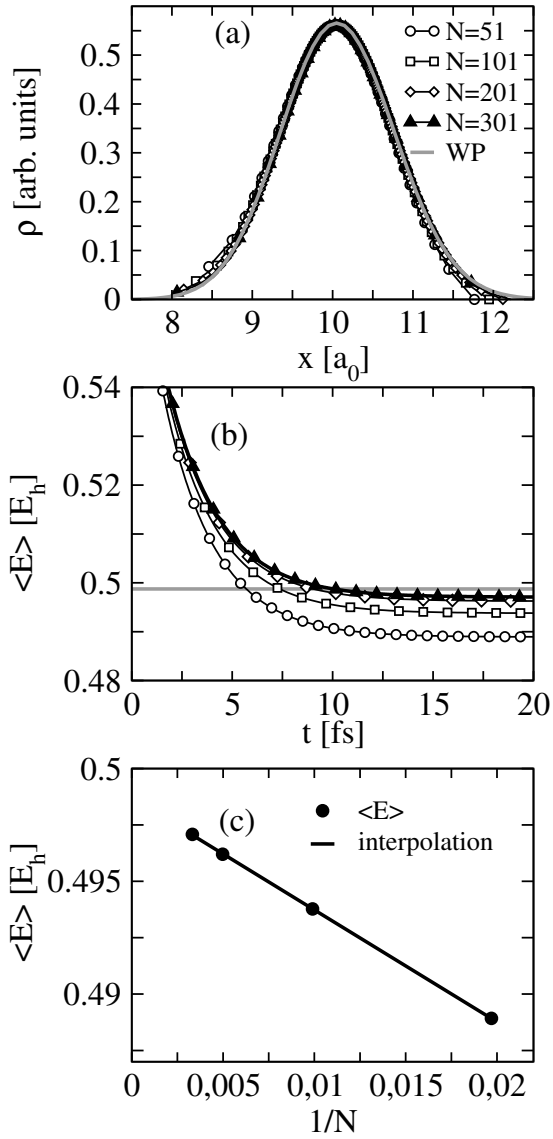

Figure 4.2: (a) Convergence of the asymptotic density distribution to the probability density of the ground state of a Morse oscillator ($\alpha = 0.1a_0^{-1}$), for an increasing number of trajectories. (b) Average energy $\langle E \rangle$ for an ensemble of N quantum trajectories as a function of time. The horizontal line indicates the exact value of the zero-point energy $\langle E \rangle = 0.4987E_h$ evaluated from Eq.4.3.2 for the given parameters. (c) Linear interpolation of the dependence of the asymptotic energies E as a function of the inverse of the number of trajectories N.

in this work. It is striking, that the relative error remains small (below 5%), even for strongly anharmonic potentials.

4.3.2 Quantum dynamics

The scattering from uphill ramps and Eckart barriers, as well as tunneling in a double well potential, constitute typical examples of phenomena where numerical difficulties may arise

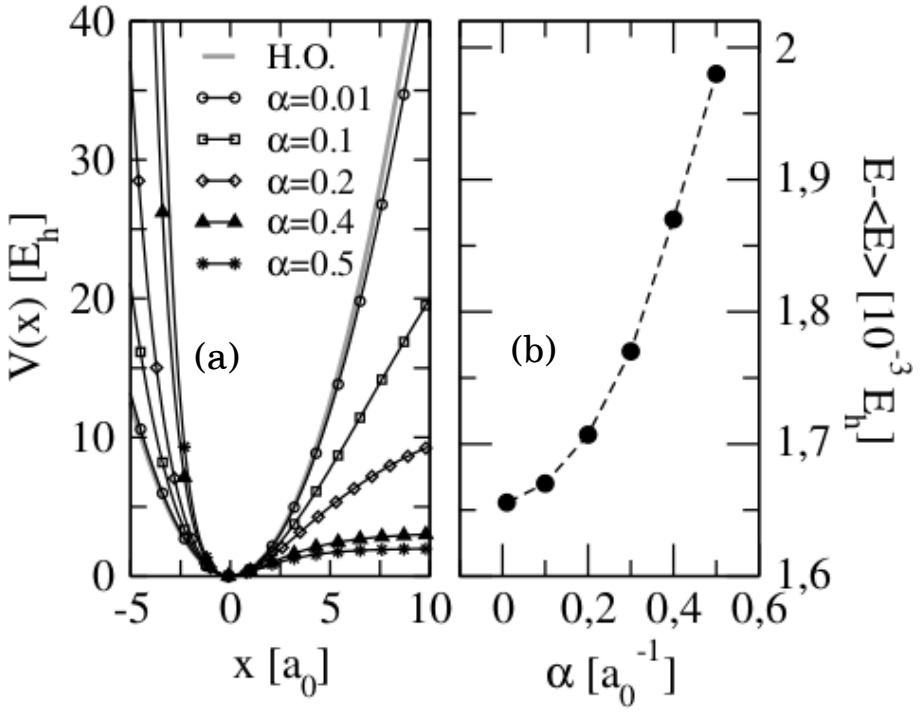

Figure 4.3: (a) Morse potential (Eq. (4.3.1)) for different values of the stiffness parameter α. The corresponding number of supported bound states is in the range from $N_b = 3$ ($\alpha = 0.5$) to $N_b = 10^4$ ($\alpha = 0.01$). (b) Deviation between the asymptotic value of the average energy $\langle E \rangle$, obtained via the relaxation of the quantum trajectories, and the energy E of the ground state, calculated by solving the time-independent Schrödinger equation.

in the propagation of quantum trajectories. These systems have been considered before as test cases for several previous numerical studies in the QTM [8, 9, 12, 17, 13, 23, 28, 38, 68]. In these problems, the wave packet is squeezed against the barrier, part of the wave packet is reflected and ripples appear in the tail of the density distribution. The accurate description of these rapid spatial oscillations is essential to account for quantum interference effects, but these oscillations are associated with strong repulsion between the quantum trajectories which subsequently leads to a breakdown of the integration. These problems have been addressed before giving rise to a variety of numerical techniques, like the integration of the equation of motion using arbitrary Lagrangian-Eulerian grids, which allowed to extend markedly the total propagation time [24, 25].

Here we show how the trajectories interacting via the approximate quantum force Eq. (4.2.15) are able to reproduce the scattering and tunneling through the barrier and a potential ramp. Four test cases are chosen: Eckart barrier, uphill barrier, double minimum potential and a potential composed of a local minimum and a finite barrier.

Eckart barrier

First, we will study the scattering of a one-dimensional Gaussian wave packet from a repulsive Eckart barrier [44],

$$V(x) = V_0 \frac{1}{\cosh^2[a(x - x_b)]} \ , \tag{4.3.3}$$

where V_0 is the barrier height, the parameter a controls the barrier width and x_b is the position of the potential maximum. The parameters determining the form of the initial wave packet and of the potential barrier were chosen as in Ref. [23], that is, $V_0 = 3.65 \times 10^{-2}\, E_h$, $a = 0.5\, a_0$ and $x_b = 6\, a_0$. As the initial condition we choose a Gaussian wave packet

$$\psi(x, 0) = (2\beta/\pi)^{1/4} \exp[-\beta(x - x_0)^2 + ikx] \ , \tag{4.3.4}$$

centered at $x_0 = 0\, a_0$ and the width parameter $\beta = 10\, a_0^{-1}$. The wave vector k is connected to the initial kinetic energy E by the relation $k = \sqrt{2mE}$. The initial situation is sketched in Figure 4.4.

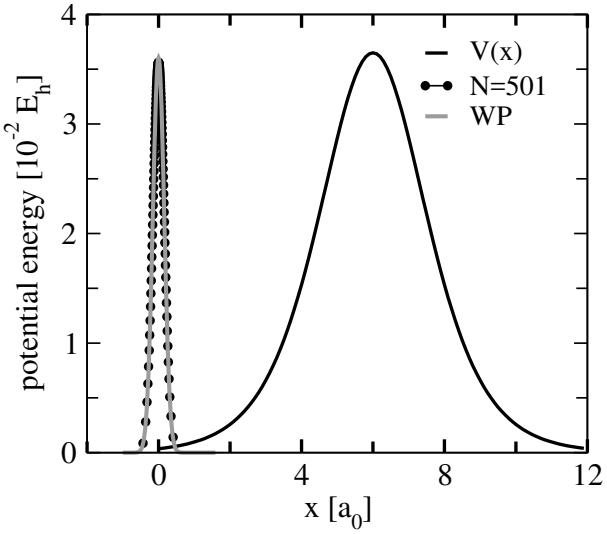

Figure 4.4: Eckart barrier (Eq. (4.3.3)) and initial wave packet (WP) ρ calculated using the stationary distribution of the trajectories with Eq. (4.2.5), for $N = 501$ trajectories, plotted with points. The exact density is represented with a solid line, it has been plotted using the Gaussian function given in Eq. (4.3.4) with $x_0 = 0\ a_0$ and $\beta = 10\ a_0^{-1}$.

The initial set of trajectories are generated from the initial density Eq. (4.3.4) $\rho = |\psi|^2$. All the trajectories are chosen with the same initial velocity $v_n = \sqrt{2E/m}$, $n = 1, ..., N$. We are interested in study the transmission probability of the wave packet as a function of the initial kinetic energy E. Hence, Eqs. (4.2.16)-(4.2.17) are solved considering different initial kinetic energies of the incident wave packet.

In Figure 4.5, we show the transmission probability as a function of the kinetic energy $P(E)$ of the incoming wave packet, for collision energies between $1.14 \times 10^{-2}\, E_h$ to $4.56 \times 10^{-2}\, E_h$. The transmission probability was calculated integrating the density using equation (4.2.22) with $x_b = 6\, a_0$. In order to evaluate $P(E)$ using equation (4.2.22), the sum was performed only for the distribution of trajectories at the end of the propagation time, for all the initial kinetic energies considered. It can be noticed, that a remarkably good agreement is achieved between the integration of the interacting quantum trajectories and the results from standard wave packet propagation, which are denoted by WP in Figure 4.5. In particular, the tunneling through the barrier (for energies below the barrier height, $E < 3.65 \times 10^{-2}\, E_h$) is reproduced with great accuracy.

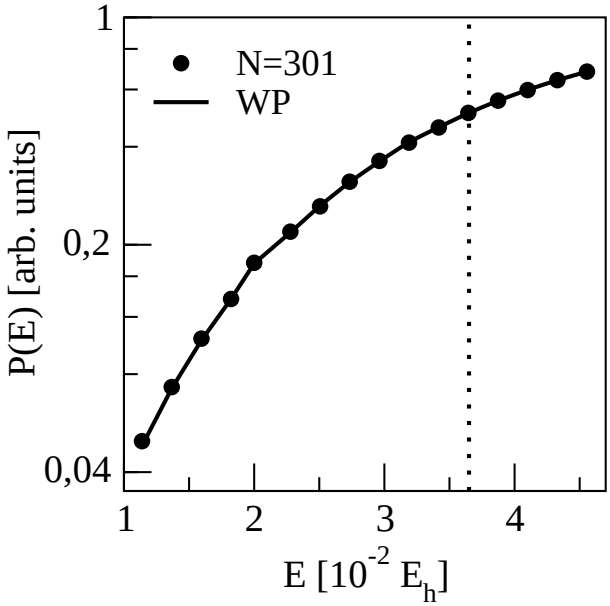

Figure 4.5: Transmission probability for a particle impinging on an Eckart barrier (in logarithmic scale), as a function of the initial energy of the wave packet. The circles represent the transmission probability calculated using the quantum trajectories (with $N = 301$), the solid line is the exact quantum result. The dashed line indicates the height of the barrier.

In Figure 4.6 (a), the time evolution of a representative set of the quantum trajectories is depicted for an incoming particle with an initial kinetic energy $E = 3.42 \times 10^{-2}\, E_h$. It can be noticed, that the region sampled by the trajectories spreads steadily until the first ones hit the barrier, after approximately 15 fs. From this point in time, and until $t = 30$ fs, the trajectories in the early part of the wave packet get decelerated, and considerable strain is accumulated as a consequence of the piling up of these quasi-stationary points in the region immediately before the barrier. As a result of this stress, a fraction of the trajectories crosses the barrier at different times between 15 fs and 65 fs.

There is a second group of trajectories which are scattered back from the barrier. On their way leftwards, they encounter the trajectories in the late portion of the incoming wave packet, and after the collision taking place between 50 and 60 fs, both groups continue to move apart from the barrier (due to the repulsion among them and the transmitted points, and once the majority of the scattered paths have drifted sufficiently away from the obstacle).

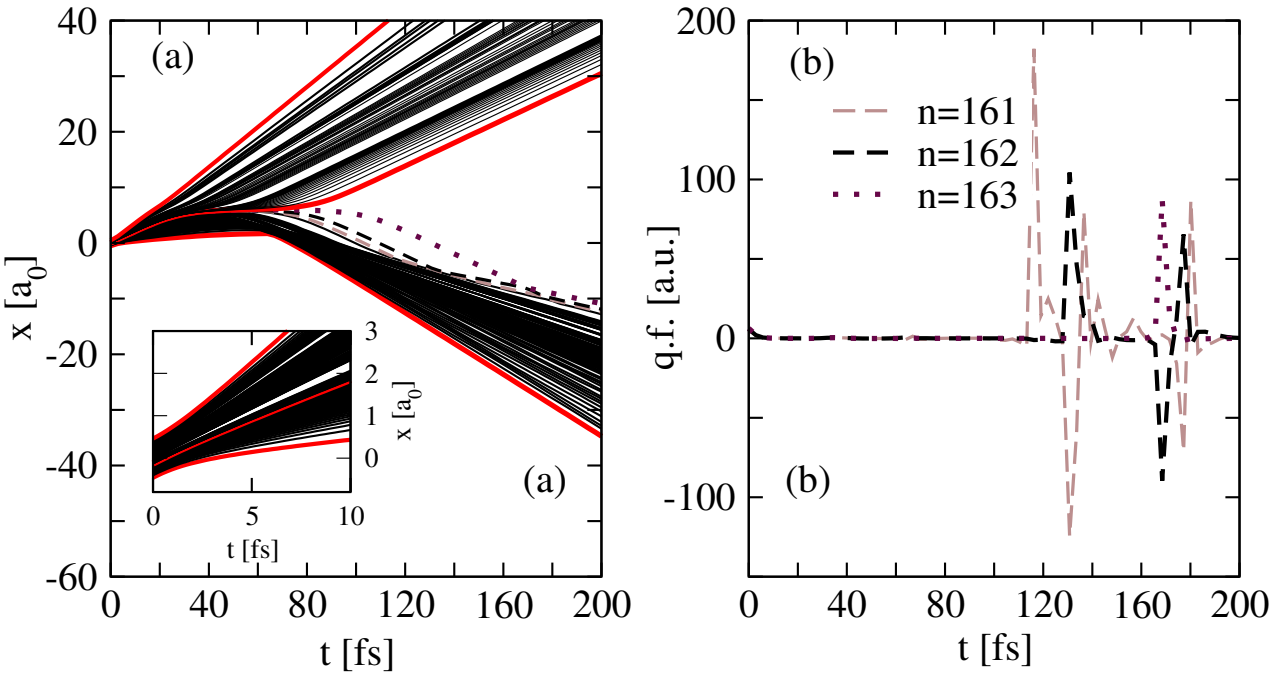

Figure 4.6: (a) Swarm of $N = 301$ trajectories representing the evolution of the wave packet associated with a particle, with an initial energy $E = 3.42 \times 10^{-2}\, E_h$, impinging on an Eckart barrier centered at $x_b = 6\, a_0$, as a function of time. The inset shows how the wave packet spreads during the first 10 fs of the dynamics. (b) Quantum force acting on selected trajectories, indicated in (a) by dashed and dotted lines.

To illustrate the quantum effects, we show in Figure 4.6 (b) the quantum force acting on three of inner trajectories, as an example. During the initial phase of the dynamics, the quantum force acting on the trajectories is relatively small, however once the reflected trajectories encounter the trailing ones on their way back, the non-crossing rule leads to very strong, peaked quantum forces. The dynamics induced by this strong forces leads to the nodes in the density, as shown in Figure 4.7. In passing, we want to note that these very peaked quantum forces make the system of equations very hard to integrate, and a numerical method with automatic step size control is required to account for these strong variations happening on a very short timescale.

From the trajectories, the time-dependent density distribution can be evaluated at any point in time from equation (4.2.5). In Figure 4.7, two snapshots of the particle density are shown after $t = 24\,\mathrm{fs}$ and $t = 56\,\mathrm{fs}$.

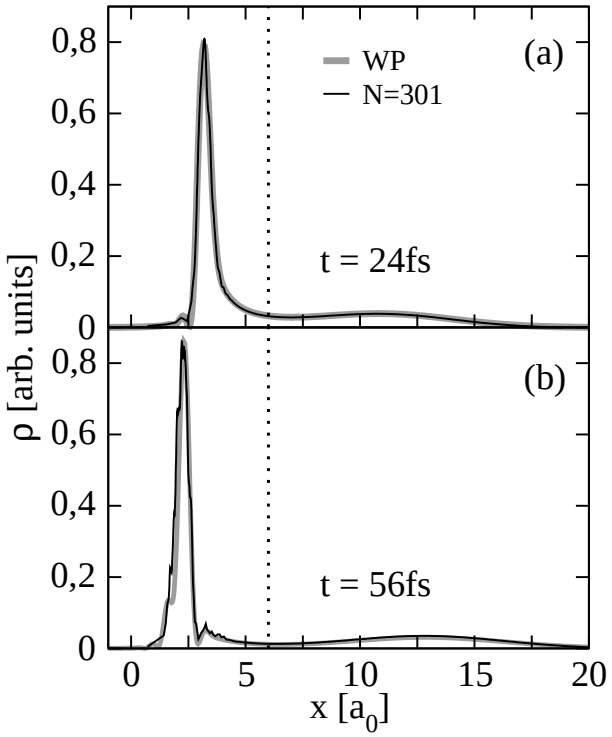

Figure 4.7: Time evolution of a Gaussian wave packet impinging on a Eckart-like potential centered at $x_b = 6\,a_0$. The wave packet is initially centered at $x = 0\,a_0$, and the collision energy $E = 3.42 \times 10^{-2}\,E_h$. (a) density distribution after 24 fs and (b) $t = 56\,\mathrm{fs}$. These results correspond to a swarm of $N = 301$ trajectories, and they reflect the splitting of the wave packet upon collision with the barrier and the subsequent formation of density ripples due to the quantum interference between the different components of the wave packet. The vertical dotted line indicates the position of the center of the barrier.

The overall agreement with the probability density computed via wave packet propagation (designed as WP in Figure 4.7) is very good over the entire spatial domain. In Figure 4.7a, one can see the onset of the interference between the late portion of the incident wave packet and the scattered density. The bottom panel 4.7(b) shows two main peaks on the scattered density, consistently with the two sets of paths previously identified in the trajectory representation (c.f. Figure 4.6), which get reflected at different times. This plot captures the instant of maximum squeezing of the main portion of the reflected density, which interferes mildly with the trajectories scattered later.

Uphill barrier

A similar analysis was performed for the case of a Gaussian wave packet impinging on an uphill ramp [44]. The solution of this problem employing arbitrary Lagrangian-Eulerian grids revealed instabilities in the numerical integration of trajectories due to bifurcations in the wave packet, even for energies above the ramp height. The potential has the form of a smoothed step function,

$$V(x) = \frac{\lambda}{1 + e^{-b(x-x_b)}} \ . \tag{4.3.5}$$

The parameters, $\lambda = 3.65 \times 10^{-2}\, E_h$, $b = 1.5\, a_0^{-1}$ and $x_b = 1\, a_0$ were taken from the literature [25]. The initial wave function has the same form as the one used for the Eckart barrier (cf. Eq. (4.3.4)), with the width parameter $\beta = 10\, a_0^{-2}$, the mass $m = 2000\, a.u.$ and $x_0 = 1\, a_0$. In this case the initial kinetic energy E of the incoming wave packet is fixed and set to be equal to the ramp height $\lambda = 3.65 \times 10^{-2}\, E_h$. The initial condition is represented in Figure 4.8.

In Figure 4.9, a representative set of trajectories propagated using the proposed form of the model quantum potential is depicted. Clearly, the quantum trajectories can be grouped in two distinct sets: those at the fore-front of the wave packet, which overcome the barrier and undergo a change in their momenta at the crossing region, and the trajectories whose motion is reversed upon collision with the barrier. For illustration purposes, the trajectories defining the limits between these two classifications are highlighted in Figure 4.9. The set of transmitted trajectories, after surpassing the potential step, spreads in a way

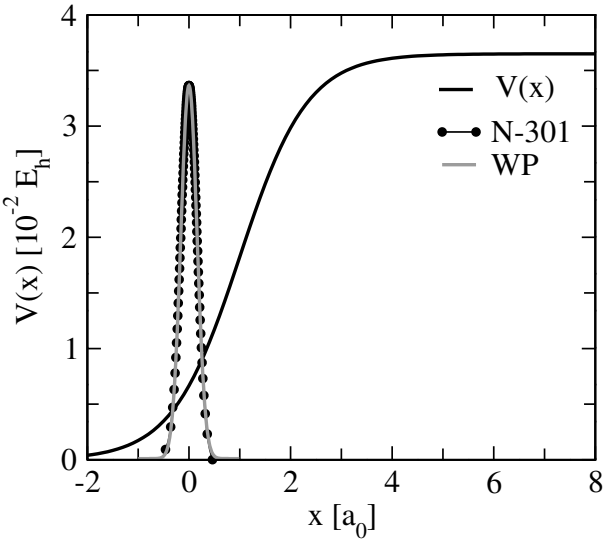

Figure 4.8: Uphill ramp potential (Eq. (4.3.5)) and initial wave packet ρ calculated for a stationary distribution of $N = 301$ trajectories, plotted with points. The exact density $\rho = |\psi|^2$ is represented with a solid line (WP), it has been plotted using the Gaussian function given in Eq. (4.3.4) with $x_0 = 0\,a_0$ and $\beta = 10\,a_0^{-1}$.

similar to a wave packet evolving in free space. Alternatively, the scattered trajectories experience a cascade of collisions among them, which propagates outwards.

Compared with the time evolution of the trajectories for the scattering on an Eckart barrier, it can be seen that the trajectories defining the left-most boundaries of the reflected wave packet have similar velocities for both model problems (for example, the corresponding trajectories reach the position $x = -20\,a_0$ after $t \approx 115\,\text{fs}$ for the Eckart and for the uphill barriers).

Conversely, the boundary of the transmitted wave packet moves more slowly for the smooth step compared with the transmission through the Eckart barrier although the initial kinetic energy is approximately 7% larger in the former case (i.e., the right-most trajectory crosses $x = 40\,a_0$ after $t \approx 125\,\text{fs}$, while the corresponding point for the Eckart barrier reaches this position at $t \approx 100\,\text{fs}$). This behaviour reflects the differences between the asymptotic kinetic energies (i.e., for $x \to \infty$) of the transmitted wave packets for each potential function.

The time evolution of the density distribution as a result of the wave packet scattering by the ramp is plotted in Figure 4.10 at three different points in time. These density

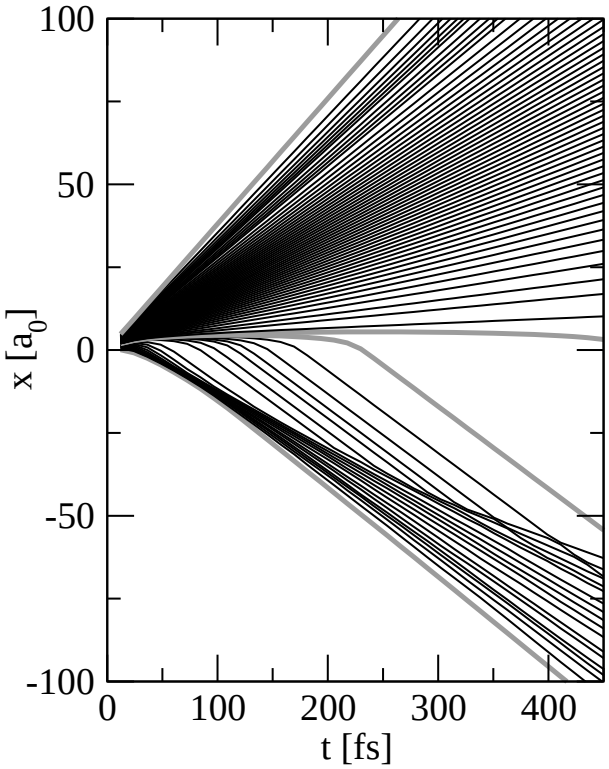

Figure 4.9: Swarm of trajectories representing the evolution of the wave packet associated with a particle, with an initial energy $E = 3.65 \times 10^{-2}\, E_h$, impinging on an uphill barrier, as a function of time.

profiles were reconstructed from the distribution of trajectories according to Eq. (4.2.5), and they are shown to correspond nicely with the exact ones obtained from the wave packet propagation (denoted as WP in Figure 4.10). The wave packet gets split into two components: at $t = 24\,\mathrm{fs}$, a wide distribution (approximately $10\,a_0$ of full width at half maximum) continues to move forward, while a much more localized portion of the wave packet propagates backwards after colliding with the ramp. After 72 fs, the formation of density ripples in the reflected wave packet becomes apparent, which develops into a highly oscillatory density profile for the late wing of the scattered portion of the wave packet (see Figure 4.10, panel (c)).

Interestingly, at least for the presented example, the description of the quantum dynamics by trajectories interacting via a model quantum potential of the form (4.2.14), results in an averaging of the density field in the region where large-amplitude, spatially-localised oscillations take place. Although such averaging implies that the interference between the different components of the wave packet is treated only approximately, this feature has a

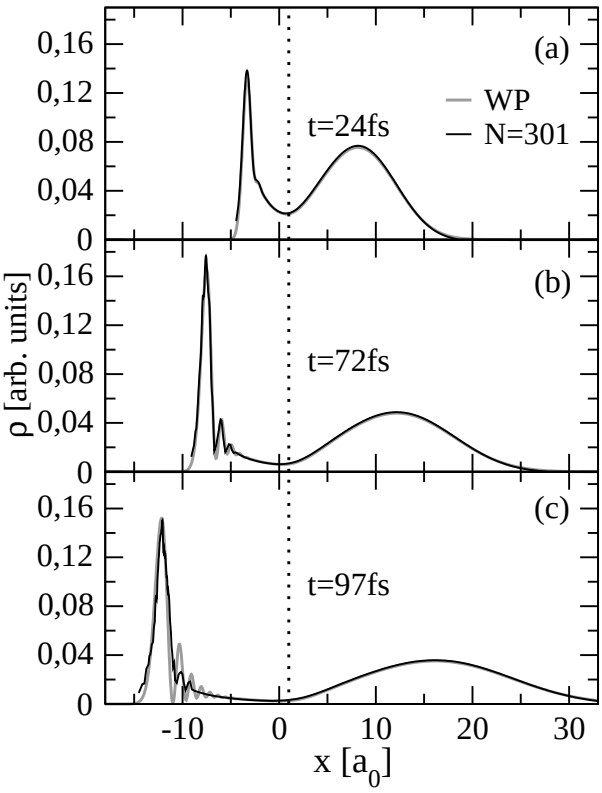

Figure 4.10: Time evolution of a Gaussian wave packet impinging on a ramp-like potential. The wave packet is initially centered at $x = 0\,a_0$ and the collision energy is $E = 3.65 \times 10^{-2}\,E_h$. (a) density distribution after 24 fs, (b) 72 fs and (c) 97 fs. These results correspond to a swarm of $N = 301$ trajectories, and they reflect the splitting of the wave packet upon collision with the potential step and the subsequent formation of density ripples due to the quantum interference between the different components of the wave packet. The vertical dotted line indicates the position of the center of the barrier.

positive impact on the numerical stability of the algorithm. This level of correspondence between the results obtained using wave packet propagation and in the interacting trajectories picture is found to be preserved even for highly structured density profiles and for a relatively long times (for this problem, the simulations were stopped after 250 fs). For the ramp case we study the transmission probabilities for several heights of the ramp. The corresponding transmission probabilities $P(t)$ were calculated using equation (4.2.22) with $x_b = 5\,a_0$. The computed transmission probabilities yield accurate results for different values of the ramp heights, $\lambda = 2.73 \times 10^{-2}\,E_h$, $3.65 \times 10^{-2}\,E_h$, $4.56 \times 10^{-2}\,E_h$, $5.47 \times 10^{-2}\,E_h$ as is shown in Figure 4.11. In all cases with a continuous line we show the results for the transmission probability obtained from standard wave packet propagation.

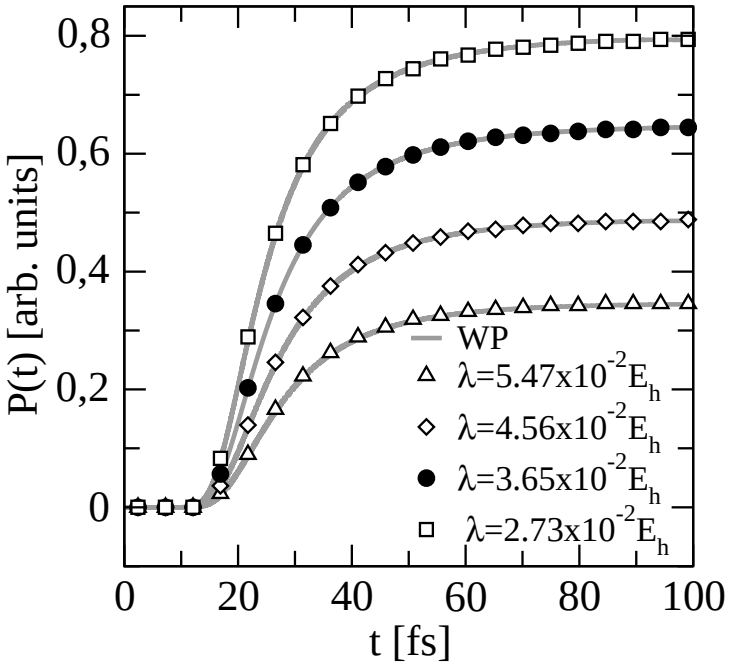

Figure 4.11: Transmission probability $P(t)$ Eq. (4.2.22) as a function of time for four different heights of the uphill ramp (symbols) compared with the standard wave packet calculation (straight lines, WP).

Double well minimum

As the next example we will study the tunneling dynamics in a double minimum potential. This problem has been addressed before within the quantum trajectories formalism in Ref.[68]. There, in order to propagate the quantum trajectories, the moving least square algorithm was combined with the logarithmic form of the density, in order to represent the derivatives required to propagate the quantum trajectories.

However, in spite of the numerical strategies implemented in Ref.[68], severe numerical difficulties arise after some trajectories cross the barrier region and encounter the repulsive potential wall. As soon as the first trajectories hits the wall and some reflections occur, the integration of the equations of motion, due to the very picky quantum force, become extremely difficult. As they report, the trajectories start to cross after $t = 16\,\mathrm{fs}$ and their numerical calculations are meaningless beyond this point.

Here we choose the same model potential as in Ref.[68], and we study the tunnelling dynamics by propagating the trajectories with the approximate quantum force (Eq. (4.2.15)).

The model potential is chosen as

$$V(x) = ax^4 - bx^2 \ , \tag{4.3.6}$$

with $a = 0.007$ and $b = 0.01$ (in atomic units) as in Ref.[68], and the potential height $V_b = 3.5810^{-3} E_h$. As the initial condition we chose the distribution of trajectories obtained after the relaxation process described above, for the harmonic approximation to a state centered in the right hand-side well. That is, after the relaxation the trajectories are distributed according to a Gaussian wave packet centered at $x_0 = \sqrt{b/2a}$ and with a width $\beta = \sqrt{4bm}$, which corresponds to the ground state of the second order expansion of $V(x)$ around the minimum, as is shown in Figure 4.12. The density is reconstructed after the relaxation using equation (4.2.5) employing $N = 201$ trajectories and is compared with the exact density.

As the initial state is not an eigenstate of the potential $V(x)$, a net force due to the non-compensate contributions of $f_c = -dV(x)/dx$ and f_q sets the trajectories in motion at $t = 0$. In the top panel of Figure 4.13, a swarm of $N = 201$ trajectories is shown. As we can see, already at 10 fs some trajectories start to cross the barrier, and continue their time evolution on the left-hand side well.

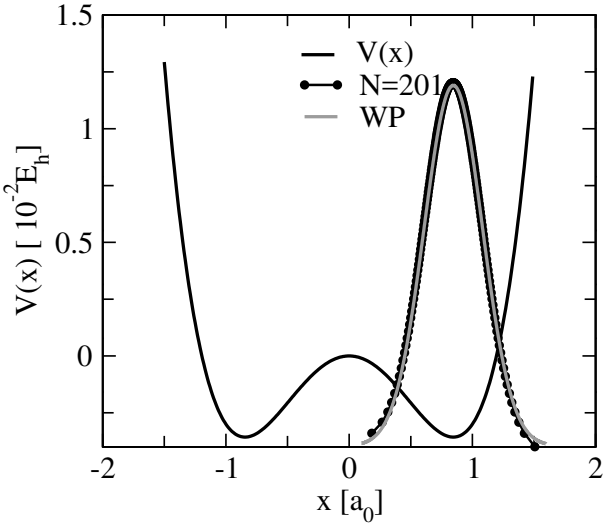

Figure 4.12: Double minimum potential defined in Eq. (4.3.6). The initial wave packet calculated using Eq. (4.2.5) from the stationary distribution of the trajectories for $N = 201$ is plotted with points. The exact density is plotted with a solid line (WP).

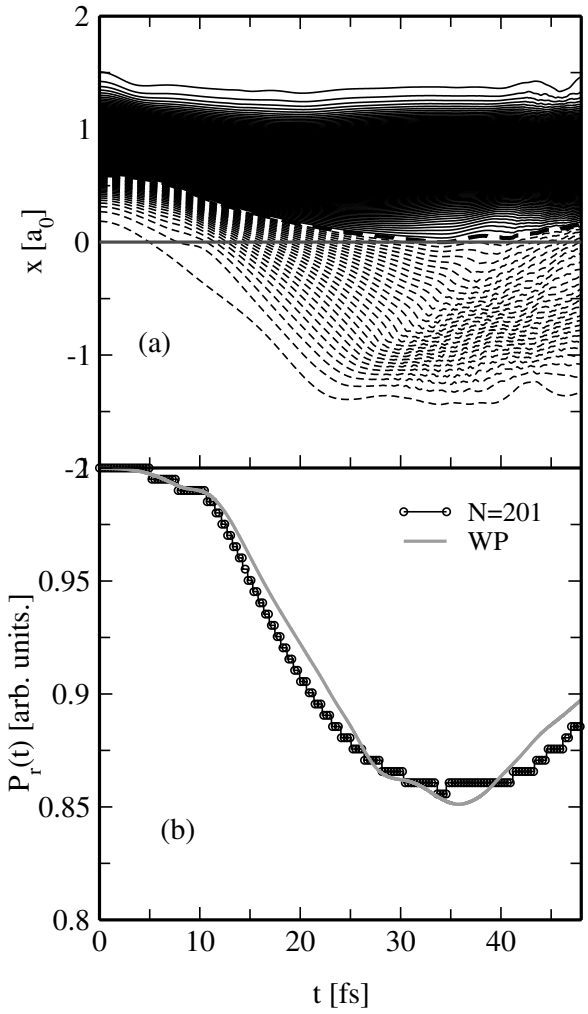

Figure 4.13: (a) A swarm of $N = 201$ trajectories is shown. As we can see, already at $10\,\mathrm{fs}$ some trajectories start to cross the barrier, and continue the dynamics on the left had side well. (b) The probability of finding the particle on the right hand side well $Pr(t)$ calculated from Eq. (4.3.7) is plotted. With solid line we plotted the results from the standard wave packet propagation (WP).

The probability of having the particle on the right hand side well as a function of time $P_r(t)$ can be evaluated from equation (4.2.22) as

$$P_r(t) = \frac{1}{N} \sum_{n=1, x_n \geq 0}^{N} 1 \ . \tag{4.3.7}$$

In the bottom panel of Figure 4.13, $P_r(t)$ is plotted. With a solid line we show the results from standard wave packet propagation. After $t = 30\,\mathrm{fs}$, already the first trajectories that hit the repulsive potential wall on the left get reflected and they start the collisions with those in the incoming portion of the wave packet. This makes the equations of motion very difficult to integrate and numerical errors start to accumulate, as it can be seen if we

compare the value of $P_r(t)$ computed from the trajectories with the wave packet results. Beyond 48 fs the agreement between the trajectory dynamics and the results obtained from wave packet calculations start to deteriorate. However, it is worth to notice that the present approach extends the validity of the quantum trajectory representation of the dynamics to longer times compared with the methodology employed in [68].

In Figure 4.14, snapshots of the density are shown to illustrate the splitting of the wave packet when the trajectories start to cross the barrier. The vertical line represent the position of the barrier. Around $t = 12$ fs, some trajectories have already started to cross the barrier and they keep crossing up to $t = 29$ fs, as can be seen from Figure 4.13. At this point in time, due to the reflections with the repulsive wall on the left hand side well, some of the trajectories cross back to the right hand side well. We have again represented the density calculated using Eq. (4.2.5) evaluated at the trajectories together with the results from wave packet propagation.

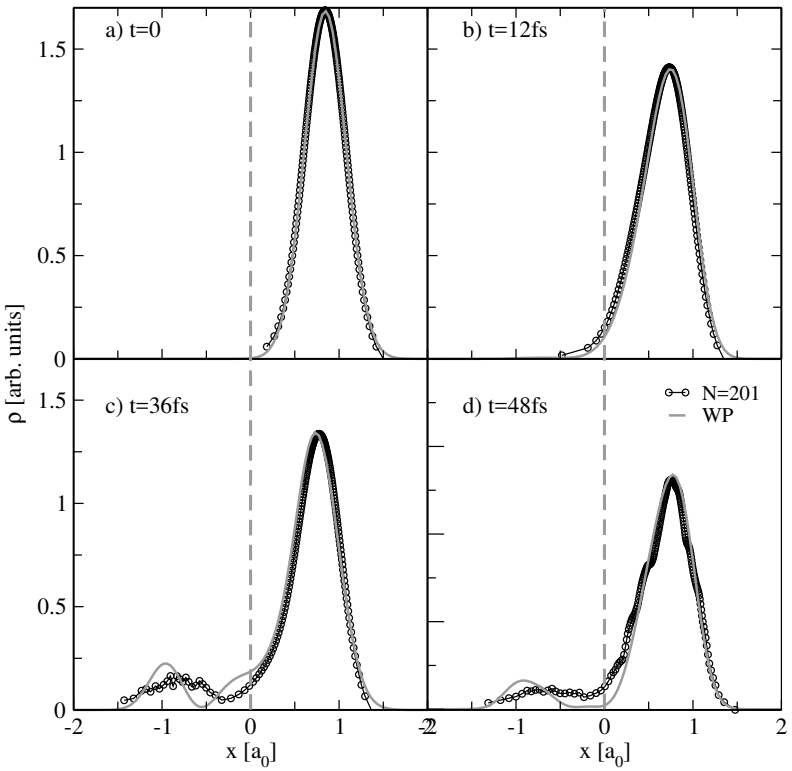

Figure 4.14: Snapshots of the density. With points we have represented the density calculated using Eq. (4.2.5) evaluated at the trajectories using $N = 201$ trajectories. The solid line correspond to the results from wave packet propagation (WP). The vertical dotted line indicates de maximum of the potential barrier.

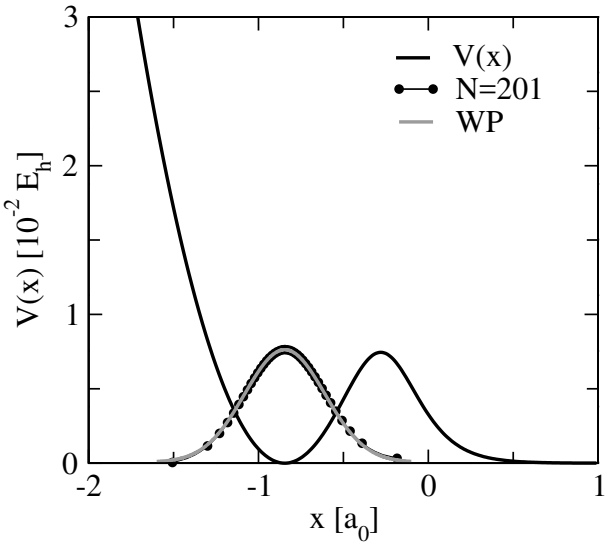

Figure 4.15: Potential defined in Eq. (4.3.8). The initial wave packet is calculated using the relaxation mechanism described above for the harmonic approximation of the given potential and then is reconstructed using Eq. (4.2.5) for a set of $N = 201$ trajectories.

Shape resonances

As a qualitatively different example of time-independent potentials we study the quantum dynamics on a potential with a local minimum and a finite barrier. This type of potentials can support a finite number of shape resonant states. In this case, the dynamics is slightly different because (after tunneling through the barrier) the particle move to the continuum, and the effects of reflections observed in the double minimum potential disappear. The one dimensional potential is built as follows,

$$V(x) = \frac{a(x + x_0)^2}{be^{d(x-cx_0)} + 1} \ . \tag{4.3.8}$$

The parameters of the potential are adjusted in such a way that the potential well resembles one of the wells of the double minimum potential we have shown before. The minimum of the potential is located at $x_0 = -\sqrt{b/2a}$, the rest of the values for the parameters in atomic units are $a = 0.04$, $b = 8$, $c = 0.005$ and $d = 8.5$. The initial situation is represented in Figure 4.15.

The time evolution of the probability of having the particle on the potential well $P_l(t)$,

can be defined from Eq. (4.3.7) as

$$P_l(t) = \frac{1}{N} \sum_{n=1, x_n \leq -0.3}^{N} 1 \ , \tag{4.3.9}$$

(where $x_b = -0.3\, a_0$ is the position of the barrier maximum), is plotted in the left panel in Figure 4.16 for an increasing number of trajectories. The results from standard wave packet propagation is also shown. As it can be seen, the results derived from the trajectories dynamics converge to the exact quantum result as the number of trajectories increases.

Furthermore, the exponential decay of the excited states can be described within the trajectory formalism. The decay of the population of the initially excited bound state $P_l(t)$ can be model as an exponential function $P_l(t) = e^{-t/\tau}$, where τ, identified as the lifetime of the excited state is defined by $P_l(\tau) = 1/e$ [87]. Then, we can calculate the lifetime of the excited state as a function of the number of trajectories and see how it converges to the exact quantum result. In order to evaluate the lifetime we have fitted an exponential function to each curve in the left panel of Figure 4.16. The values of

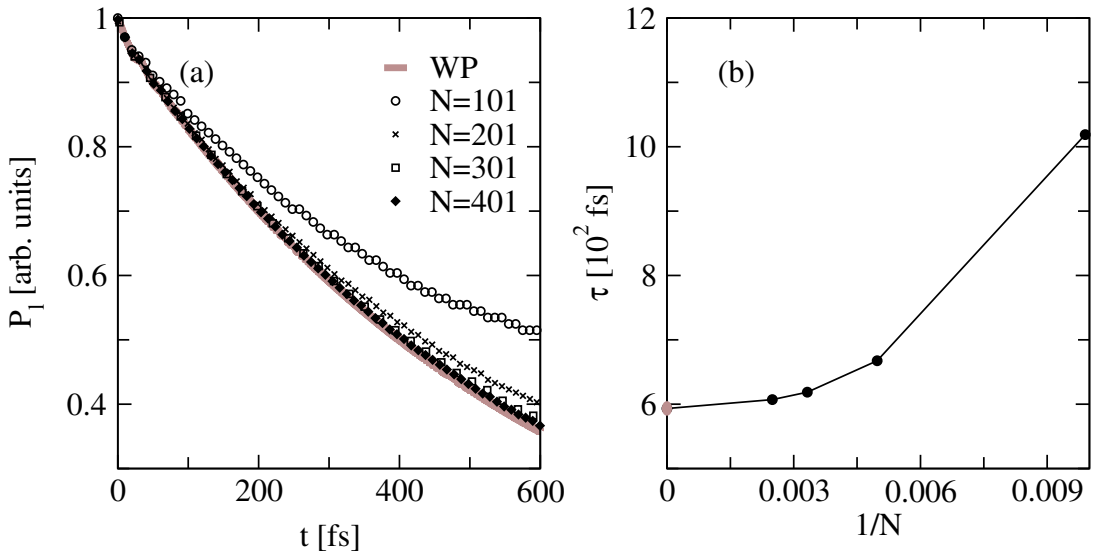

Figure 4.16: (a) The time evolution of the probability of having the particle in the well $P_l(t)$ from Eq. (4.3.9) is plotted for an increasing number of trajectories. The wave packet results are also shown. As the number of trajectories increases, the results converge towards the wave packet results (WP). (b) The values of τ obtained as the result of the fitting are plotted, in the x-axis we have $1/N$ and in the y-axis, the life time, τ. The point just on top of the y-axis represents the lifetime obtained from the wave packet population probability.

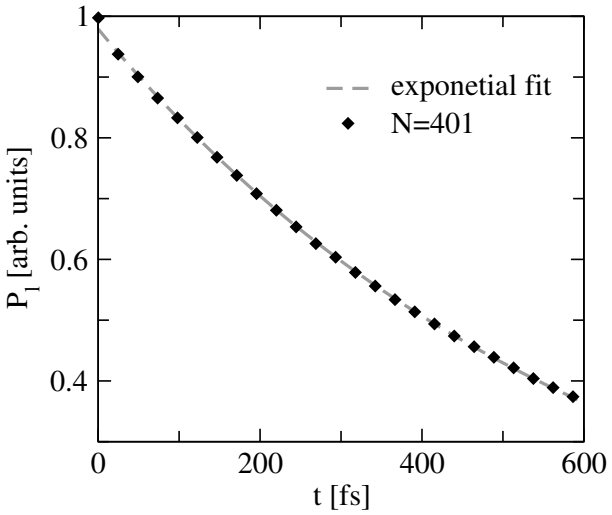

Figure 4.17: The time evolution of the probability of having the particle in the well $P_l(t)$ calculated from Eq. (4.3.9) is plotted for $N = 410$ trajectories. The exponential curve fitted to $P_l(t)$ is plotted with a dashed line.

τ derived as a result of the fitting are plotted in the right panel of Figure 4.16, in the x-axis we have $1/N$ and in the y-axis, the life time, τ. The point just on top of the y-axis represents the lifetime obtained from the wave packet population probability. As we can see by extrapolating the curve we approach the wave packet result as the number of trajectories approach to infinity. The exponential curve fitted to P_l calculated with $N = 401$ trajectories is plotted with a dashed line in Figure 4.17.

4.3.3 Correlation functions and spectra

Of particular interest in the time-dependent formulation of absorption and dissociation processes is the time-dependent autocorrelation function, whose Fourier transform is proportional to the absorption spectrum. It also provides a very intuitive representation of the time evolution of the system, since it allows the identification of the modes chiefly involved in the dynamics.

In this section, the final distribution of trajectories obtained in section 4.3.1 after the relaxation procedure is now used as the initial condition for the study of the vibrational dynamics of a Gaussian wave packet on a shifted harmonic potential (centred at $x_0 = 8.5\, a_0$, the minimum of the potential is centered at $10\, a_0$) [44]. The time-dependent correlation function is evaluated via the integration of the wave function along each trajectory using

(Eq.(4.2.25)). In order to update the Lagrangian, the quantum-like potential Q_0 and the full quantum potential Q were used. In the appendix C are given further details related to the calculation of the correlation functions. In Figure 4.18, the real part of the correlation functions computed using Q_0 and Q, are compared with the exact quantum mechanical result. It can be noticed that using the quantum potential Q in eq. (4.2.14) correctly reproduces the quantum time-dependent correlation functions.

One can see that using Q_0 in Eq. (4.2.10) for the wave function reconstruction fails to reproduce the right amplitudes of the peaks of the correlation function centered at times $t = 2\pi n/\omega$ ($2\pi/\omega \approx 12.5\,\text{fs}$). Moreover, the correlation function computed with Q_0 takes opposite signs, compared to the quantum mechanical benchmark, at times equal to half-integer number of vibrational periods.

On the contrary, using the quantum potential Q of Eq.(4.2.14), comprising both repulsive and attractive terms, correctly reproduces the positive and negative peaks in the quantum correlation function. The agreement is less perfect for the region between the mean peaks, where the small amplitude oscillations in the quantum correlation function are averaged out in the interacting trajectories representation.

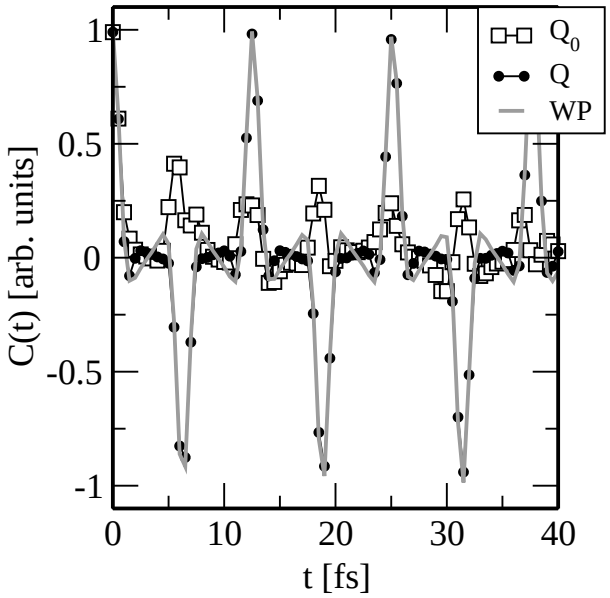

Figure 4.18: Real part of the correlation function of a Gaussian wave packet on a parabolic potential, computed from the time evolution of $N = 201$ interacting trajectories using the full form of the quantum potential (Q eq. (4.2.14)) and the one introduced in Ref. [43] (Q_0). The solid lines represents the exact solution, obtained via wave packet propagation.

Augmenting the size of the ensemble of trajectories allows to diminish this smoothing effect, bringing the results of trajectory and wave packet propagation in closer correspondence. In Figure 4.19, the real part of the correlation function is plotted for a varying number of trajectories. The quantum mechanical result is recovered in the limit $N \to \infty$.

It is worth to mention that the small deviations from the exact quantum correlation function, that appear due to insufficient sampling of the probability density distribution, has minimal impact on the overall structure of the energy spectrum.

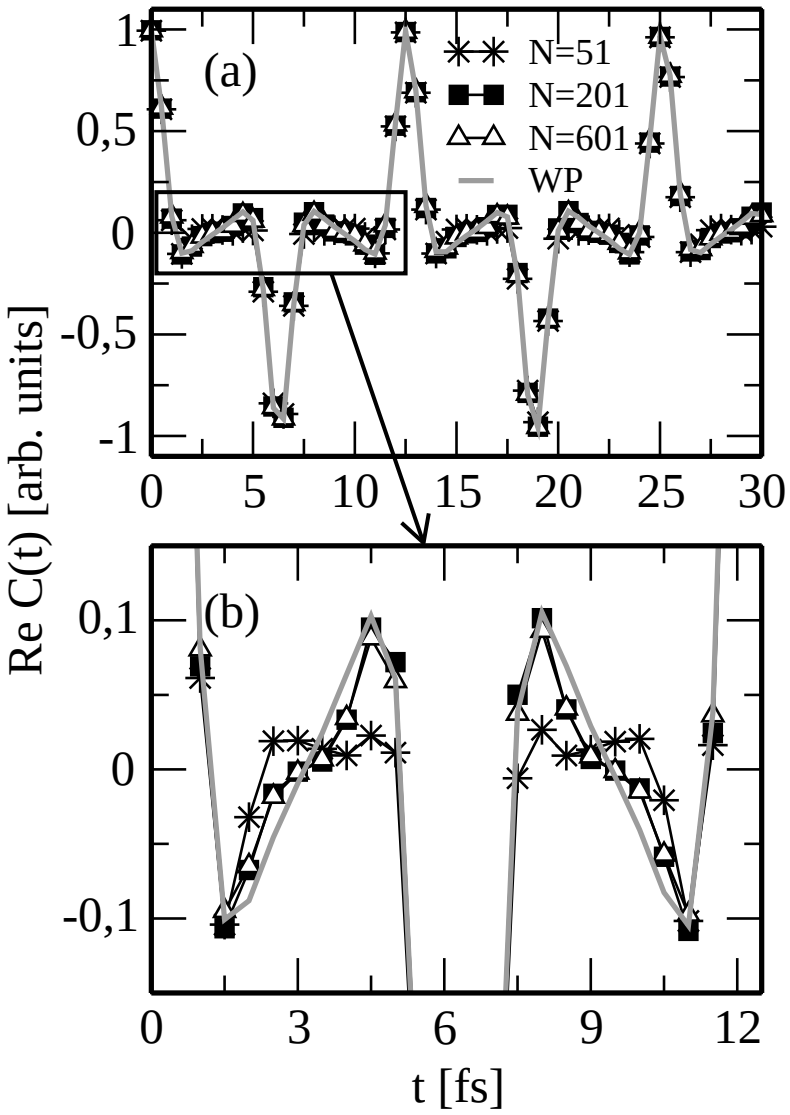

Figure 4.19: (a) Real part of the correlation function of a Gaussian wave packet on a parabolic potential calculated for an increasing number of trajectories. The results are compared with the quantum correlation function calculated using standard wave packet (WP) propagation techniques. (b) Amplification of the highlighted region in panel (a), it shows how the convergence is reached as the number of trajectories is increased.

From the plots in Figure 4.20, it becomes apparent that the qualitative agreement between the trajectory-based and the quantum mechanical correlation function is very good, even for a small number of quantum trajectories (i.e., $N = 51$). However, a closer look reveals the emergence of spurious peaks in the energy spectrum (Figure 4.20 (b)) originated by the deviations in the calculated autocorrelation function. They become largely depleted as N increases, eventually converging to the exact result.

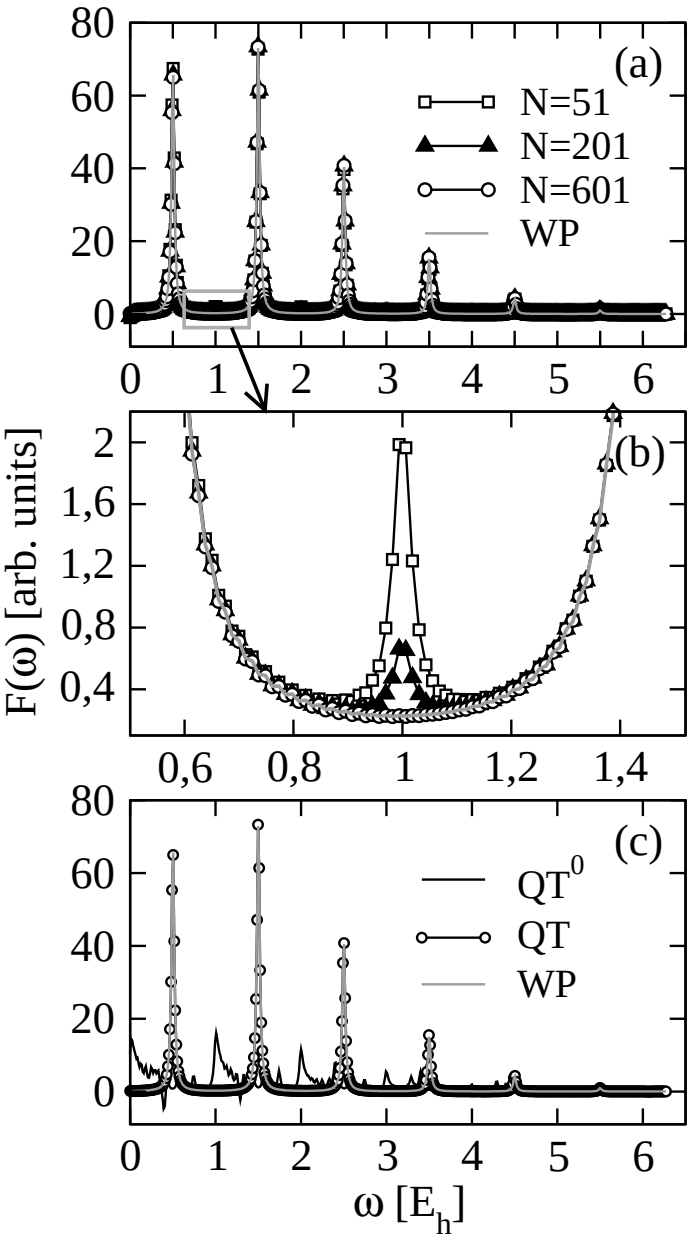

Figure 4.20: Energy spectrum obtained from the Fourier transform of the correlation function: (a) increasing the number of trajectories and comparing with the exact solution. (b) Amplification of the highlighted region in panel (a), showing the presence of spurious peaks in the spectrum, as well as the convergence to the exact solution as the number of trajectories gets larger. (c) Comparison between spectra using the model quantum potential and the approximation introduced in Ref.[43].

Let us notice in passing that the number of trajectories in the ensemble can not be augmented arbitrarily. Although, in principle, the exact quantum mechanical result is recovered in the limit $N \to \infty$, increasing the density of quantum trajectories makes the numerical integration more difficult due to the increase of the quantum forces. As a consequence, the model (4.2.14) employed to approximate the interaction between neighbouring trajectories is more conveniently used in calculation of observables for a large but finite value of N. This convergence problem is analog to the problems arising in the treatment of the inter-bead interaction in numerical implementation of the path integral formulation of quantum mechanics, i.e., the path integral Monte Carlo and molecular dynamics methods [88, 89].

In general, the results obtained for the correlation function and the energy spectrum reveal that these observables are very sensitive to the term in the quantum potential which is proportional to the curvature of the density profile $\nabla^2\rho/\rho$, as it can be seen in Figure 4.20 (bottom panel) and in Figure 4.21. Taking into account this contribution causes the larger deviations in the computed correlation function to become one order of magnitude smaller than the corresponding errors for purely repulsive quantum-like potential Q_0. Likewise, the removal of this term from the equations of motion can lead to incorrect spectral densities.

4.4 Results. Part II: laser-driven electron dynamics

4.4.1 Brief introduction

This part is devoted to illustrate the performance of the proposed methodology in a different area: we study the laser-driven atomic ionization within our trajectory, wave function-free methodology. As we mentioned in the introduction, the study of laser-matter interactions is one of the areas where the development of trajectory-based methods seems to be one of the most appealing alternatives to wave packet propagation techniques.

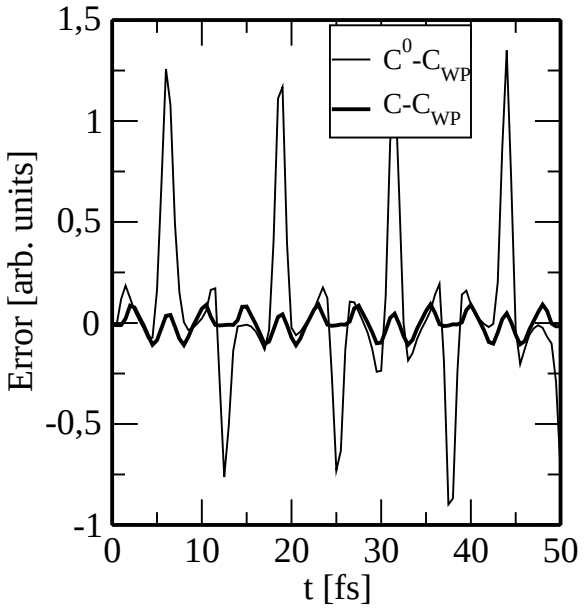

Figure 4.21: Error in the computed correlation functions, using the model quantum potential of Eq. (8.0.6) $(Re[S] - Re[S_{WP}])$ **and the approximation introduced in Ref. [43]** $(Re[S^0] - Re[S_{WP}])$**.**

Here, we study the electron dynamics and its interaction with a strong laser field, via the direct solution of the equation of motion for the ensemble of interacting trajectories we have obtained above Eqs. (4.2.16)-(4.2.17).

An interesting aspect of the dynamical process triggered by intense and short laser pulses is that (for extremely short pulses, comprising only a few optical cycles) the Carrier Envelope Phase (CEP) has a strong influence on the laser induced dynamics. Here we address this problem from a quantum trajectory perspective, and evaluate both, the ionization yield and the left-right asymmetry as a function of the CEP parameter. The results are compared to standard wave packet propagations, and the numerical convergence of the former for progressively larger sets of quantum trajectories is analyzed in detail [90].

4.4.2 Theoretical methods and numerical details

As some new aspects are studied in this part, we will give more details on the methods and numerical calculations corresponding to the results we present below. In all the equations atomic units are used, being the electron mass $m = 1\,a.u$ and $e = -1\,a.u$. Coming back to the Newton-like equation (4.2.17), now concerning the classical part of the potential we

have two contributions. The interaction between the electron and the core is modeled by a soft-core Coulomb potential $V_c(x) = -1/\sqrt{x^2+1}$. We also have the laser atom interaction modeled as $V(x,t) = xE(t)$ in the dipole approximation. The coordinate x denotes the electron position and $E(t)$ is the intensity of the electric field of the laser pulse, which is polarized along the x-axis. Then, Eq. (4.2.17), evaluated along each trajectory takes the form,

$$m\frac{dv_n}{dt} = f_c(x_n) + f_q(x_n) - E(t) \ , \quad n = 1, ..., N \ , \tag{4.4.1}$$

where we have identified $f_c = -dV_c/dx$.

In this section, the trajectory-only propagation method is applied to study the electron dynamics in interaction with a strong laser field, given by

$$E(t) = E_0 sin^2\left(\frac{\pi t}{T_{pulse}}\right) cos\left(\omega\left(t - \frac{T_{pulse}}{2} + \phi_{CEP}\right)\right) \ , \tag{4.4.2}$$

for $0 \leq t \leq T_{pulse}$. In equation (4.4.2), E_0 denotes the pulse amplitude, T_{pulse} is the pulse duration and the CEP parameter denoted by ϕ_{CEP} defines the phase difference between the maxima of the field oscillations with frequency ω and the maximum of the pulse envelope. In Figure 4.22, the time dependence of the laser field is plotted for selected values of the parameter ϕ_{CEP} and for two different durations of the pulse. We employ a high intensity near-infrared (NIR) laser pulse with a wavelength of $800nm$ ($\omega = 0.057\, E_h$), an intensity of $I = 3.51 \times 10^{14} W/cm^2$ and a pulse duration of 1.5 and 2.5 cycles ($T_{pulse} = 4.0$ fs and 6.6 fs), respectively. In this regime of ultrashort and intense laser pulses, CEP-effects occur [81]-[84] and the experimentally accessible quantities are the total ionization and the right/left (forward/backward) asymmetry of the ejected electrons [81], [82]. In this context we refer to "right" for the direction of positive "x", and "left" for the direction of negative "x".

One of the main advantages of the trajectory description of these atomic processes is that the trajectory dynamics (albeit being fully quantum) provides an intuitive picture of the ionization process.

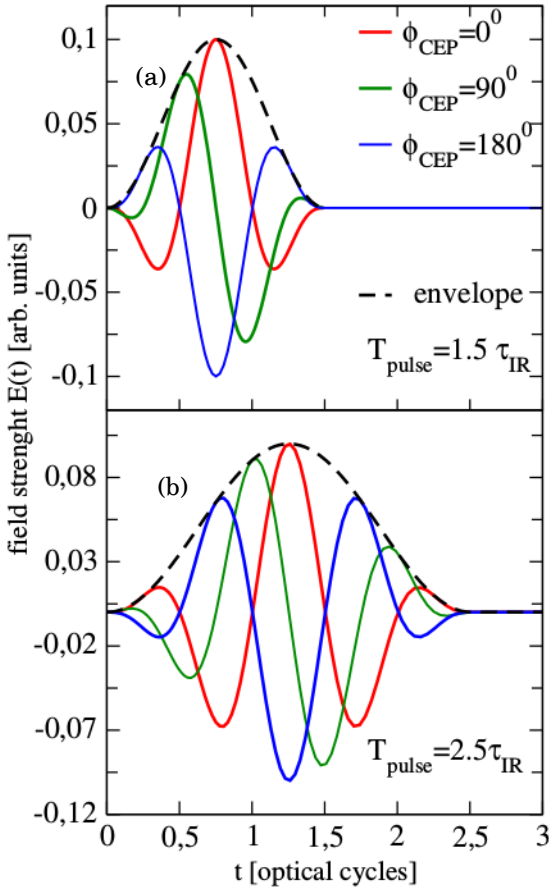

Figure 4.22: Shape of the laser pulse for (a) $T_{pulse} = 4.0$ fs and (b) $T_{pulse} = 6.6$ fs. In both cases three values of the CEP parameter are represented $\phi_{CEP} = 0^0, 90^0, 180^0$, the envelope is plotted with a thin dashed line.

Hence, the right (left) ionization yield is simply calculated from the number of trajectories with $x_n > x_c$ ($x_n < -x_c$), with $x_c = 250\ \ a.u$:

$$P_r = \frac{1}{N} \sum_{i=1, x_i > x_c}^{N} 1 \ , \quad P_l = \frac{1}{N} \sum_{i=1, x_i < -x_c}^{N} 1 \ . \tag{4.4.3}$$

This value for x_c was chosen to ensure that for the laser and Coulomb potential parameters we have used, once the trajectories have reached this point, they will move to the continuum. The total ionization is

$$P_I = P_r + P_l \ , \tag{4.4.4}$$

and the asymmetry is given by

$$\eta = \frac{P_r - P_l}{P_r + P_l} \ , \tag{4.4.5}$$

as in previous studies in this field [82]-[84]. To gain access to the energy-resolution of these quantities, a binning is performed with a bin size in energy of $5 \times 10^{-3} E_h$ to calculate $P_l(E_{kin})$ and $P_r(E_{kin})$. We have found this value to be a good compromise between energy resolution and statistical significance, for an ensemble of 500 trajectories.

The equations of motion for the quantum trajectories are solved using a fourth order Runge-Kutta integrator with an adaptive time step [85] and an absolute error of 10^{-12}.

To assess the quality of our trajectory-only approach we have also performed benchmark calculations based on quantum wave packet propagations. To this end, we have used the split-operator approach on a grid ranging from $-2000\,a_0$ to $2000\,a_0$. To avoid grid boundary reflections, and to calculate the spectra of emitted electrons in the right and left direction, as well as the anisotropy and the ionization, the splitting methodology of Metiu et al. [91] is employed.

4.4.3 Results and discussion

The ground state of the soft-core Coulomb potential is chosen as the initial condition for the trajectory propagation. It is obtained after the same relaxation procedure as in the previous examples. The ground state distribution obtained for a swarm of $N = 501$ trajectories is shown in Figure 4.23. Compared to the results of standard wave packet calculations (i.e using imaginary-time propagation), there is a very good agreement between the quantum trajectory and the wave packet representation of the ground state.

As a first application of the interacting trajectory formalism to the study of atomic ionization, we consider the case of the laser-driven ionization for a ϕ_{CEP} of 150^o. The time evolution of the quantum trajectories is plotted in Figure 4.24 (top panel), for a set of $N = 301$ trajectories and in Figure 4.24 (central panel), for $N = 501$, whereas the colour scale plot of the density obtained via wave packet propagation is shown in Figure 4.24 (bottom panel) for comparison. For the sake of clarity, with a brown color we represent dissociative and in black bound trajectories. It can be noticed that no ionization occurs

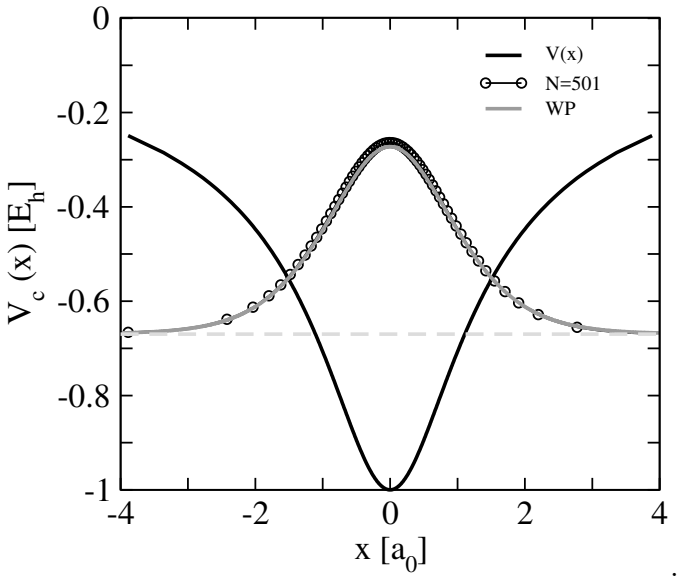

Figure 4.23: Model soft-core Coulomb potential and ground state density evaluated from Eq. (4.2.5) using $N = 501$ trajectories after the relaxation, compared with the exact quantum density (WP). The zero point energy is also plotted, the mean energy for $N = 501$ is $< E_{traj} >= -0.6698$ which is in good agreement with the value reported from wave packet calculation for the model potential ($< E >= -0.6697$) [92].

during the first half period of the driving pulse.

During this interval of time, the net effect of the electromagnetic field is the increase in the kinetic energy of the electron wave packet, which undergoes half an oscillation in the potential well. During the second half of the cycle, a set of trajectories are driven away from the confining region of the Coulomb potential (in the half plane $x > 0$), and the wave packet gets split into a portion that continues the propagation outwards (thereby contributing to the ionization yield) and a fraction of pathways that reverse their motion and re-collides with the bound part of the wave packet. This inward motion of the returning portion of the wave packet extends beyond the duration of the laser pulse. While the top panel of Figure 4.24 shows only direct ionization events, a more dense sampling of the time-dependent density distribution reveals that the electron may also get detached as consequence of the re-collision process (cf. central panel of Figure 4.24). For the specific choice of the laser field employed in the present calculations, the latter mechanism is however less frequent than direct ionization.

This picture is confirmed by the results of the wave packet propagation (depicted in the bottom panel of Figure 4.24), which corroborates the accuracy of the interacting trajectory

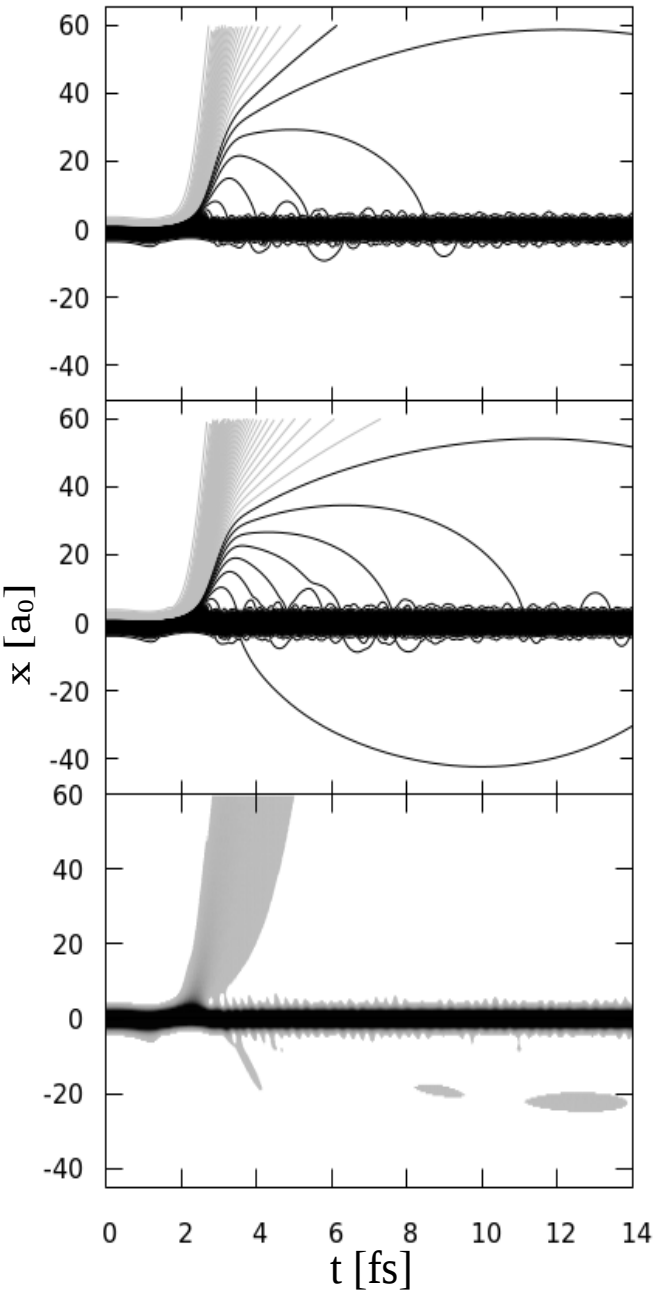

Figure 4.24: Time evolution of the quantum trajectories under the influence of a short and strong laser pulse, for $N = 301$ (top panel) and $N = 501$ (central) trajectories. The parameters of the laser field are $\phi_{CEP} = 150^o$, pulse intensity $E_0 = 0.1a.u$ and $T_{pulse} = 1.5$ pulse cycles. In the bottom panel, the time-dependent probability density evaluated via wave packet propagation is plotted.

treatment for the present problem.

The total ionization P_I (Eq. (4.4.4)) is plotted as a function of time in Figure 4.25, as the number of trajectories increase, the total ionization calculated from the trajectories approaches the results derived from standard wave packet propagation.

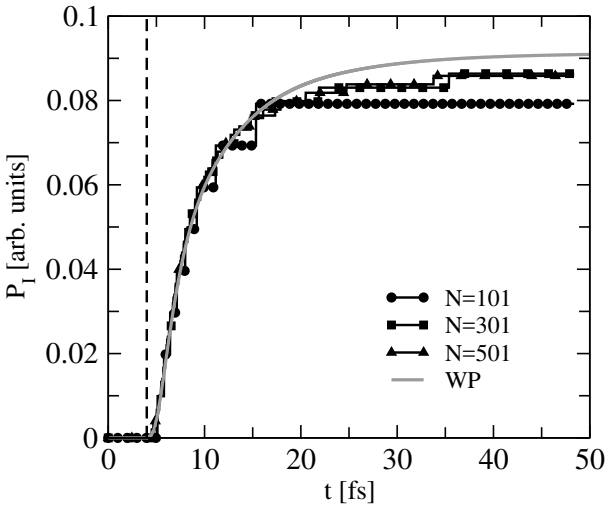

Figure 4.25: Total ionization yield (P_I, Eq. 4.4.4) as a function of time for an increasing number of trajectories N, compared with the exact quantum result (WP). The dashed vertical line represents the end of the laser pulse.

4.4.4 Carrier Envelope Phase analysis

One of the new aspects related to the dynamics under the action of strong and short laser fields is the impact of the Carrier Envelope Phase on the laser induced reaction [81]-[84]. As it can be seen in Figure 4.22, a small change in ϕ_{CEP} affects the shape of the laser pulse, so it may have a large impact on the overall dynamics. In this section we will focus on the influence of the CEP parameter on the atom ionization yield and on the aforementioned asymmetry of the photo-electron emission.

In Figure 4.26 the total ionization probability Eq.(4.4.4), (top panels) and the asymmetry parameter Eq.(4.4.5), (bottom panels) are plotted as function of ϕ_{CEP} for a pulse duration of $T_{pulse} = 1.5$ cycles (left columns) and $T_{pulse} = 2.5$ cycles (right columns). The total ionization yield is a periodic function of the carrier envelope phase. For $\phi_{CEP} = 180^o$, the direction of the driving force is reversed, hence the trajectories are emitted in the opposite direction with respect to the emission for $\phi_{CEP} = 0^o$. As a consequence, we only show ϕ_{CEP} between 0° and 180°. The asymmetry, a more detailed quantity, depends more sensitively upon details of the collisional dynamics, and in particular onto an extremely precise initial distribution of the trajectories. Since the initial distribution should be strictly symmetric with respect to the central point at $x = 0$ (see Figure 4.23), we have improved the numerical precision by averaging over a second run with x_i replaced by $-x_i$

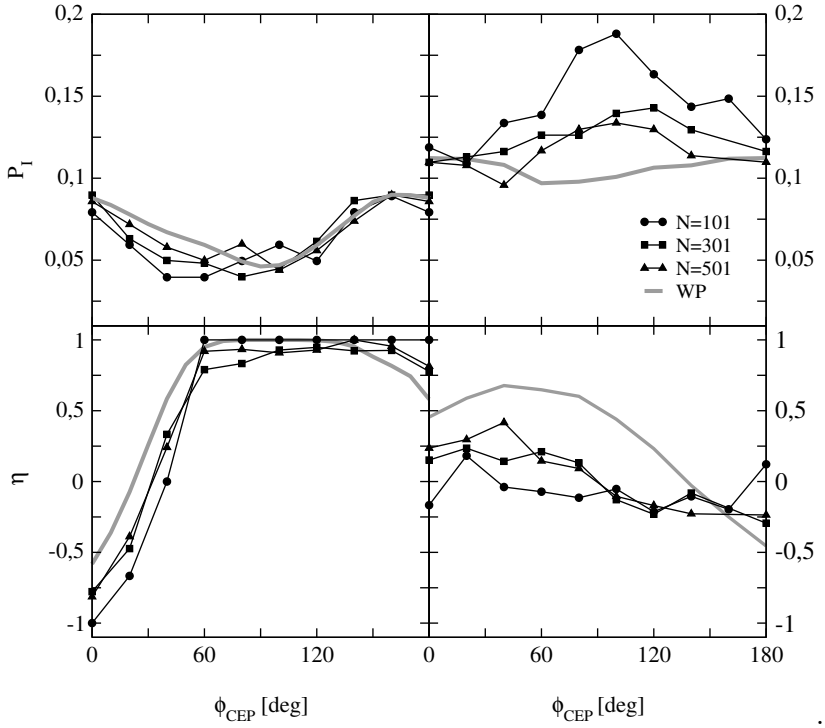

Figure 4.26: Total ionization yield P_I (Eq.(4.4.4)) and left/right asymmetry η (Eq.(4.4.5)), as a function of the ϕ_{CEP} for two different pulse durations: $T_{pulse} = 1.5$ cycles (left panels) and $T_{pulse} = 2.5$ cycles (right panels). The observables computed using $N = 101$, $N = 301$ and $N = 501$ trajectories are shown, together with the results of wave packet calculations (WP).

for each value of ϕ_{CEP}. For the short pulses (left columns), we see that already a small number of $N = 101$ trajectories yields a qualitative agreement with te exact quantum results. As expected, when increasing the number of trajectories the results converge to the exact quantum values (indicated as brown line). For the longer pulses, we find a significantly slower convergence towards the exact values. Increasing the number of trajectories, also implies stronger values and variations in the quantum force, leading to an increased numerical challenge. In particular, the required time step for a precise integration becomes prohibitively small. As a consequence, in practice, it is not always possible to increase the number of trajectories. In particular, for longer pulses, the back and forth driving of the electron leads to significant more collisions between trajectories, and thus to a much higher numerical effort.

From Figure 4.26 it can also be noticed that in the region from $\phi_{CEP} = 80^o$ to $\phi_{CEP} = 180^o$ the agreement between the interacting trajectories formalism and the wave packet calculations is better, compared to the region from $\phi_{CEP} = 0^o$ to $\phi_{CEP} = 80^o$. This

difference can be understood from the trajectory dynamics as it will be shown below.

In Figure 4.27, the time evolution of the trajectories is represented for four different values of ϕ_{CEP}. For $\phi_{CEP} = 0^o$, the ionization burst occurs at the same time that the maximum of the laser field, when a large fraction of the trajectories are ionized into the region $x < 0$. Upon the change of the direction of the field, some of the trajectories are driven back and a second, less intense ionization event occurs due to the recollisions with the core (bound) portion of the wave packet, which gives some of the trajectories enough energy to leave the core towards the region $x > 0$.

However, a different ionization mechanism takes place for $\phi_{CEP} = 50^o$. In this case, at the maximum of the field, a bunch of trajectories is driven to the right, but they do not get enough energy to leave the nucleus and they are driven back by the field and recollide with the core ones. The energy is then transmitted through the core trajectories to the outer ones on the right side, and they are emitted to the region $x > 0$. During this ionization process, many collisions occur which make the integration of the equations of motion for the trajectories very challenging, therefore it is more difficult to reproduce the wave packet calculations.

For $\phi_{CEP} = 100^o$, the field only drives a few trajectories to the right, hence less collisions with the core occur when they are driven back, and finally they get ionized to the left when the force reaches the maximum in the other direction. A different situation is obtained for $\phi_{CEP} = 150^o$, where a bunch of trajectories is ionized at once to the left at the maximum of the field, and no recollision mechanism is involved in the ionization process. For these CEP values, where a direct ionization occurs and fewer collisions with the core are involved in the ionization process, the integration of the equation of motion is less difficult and a good agreement with the wave packet calculations is obtained.

In the right panel of Figure 4.26, the results for a longer laser pulse are shown. In this case, the total ionization increases and no strong dependence with the CEP parameter is seen. Furthermore, the left-right asymmetry is markedly depleted. This disappearance

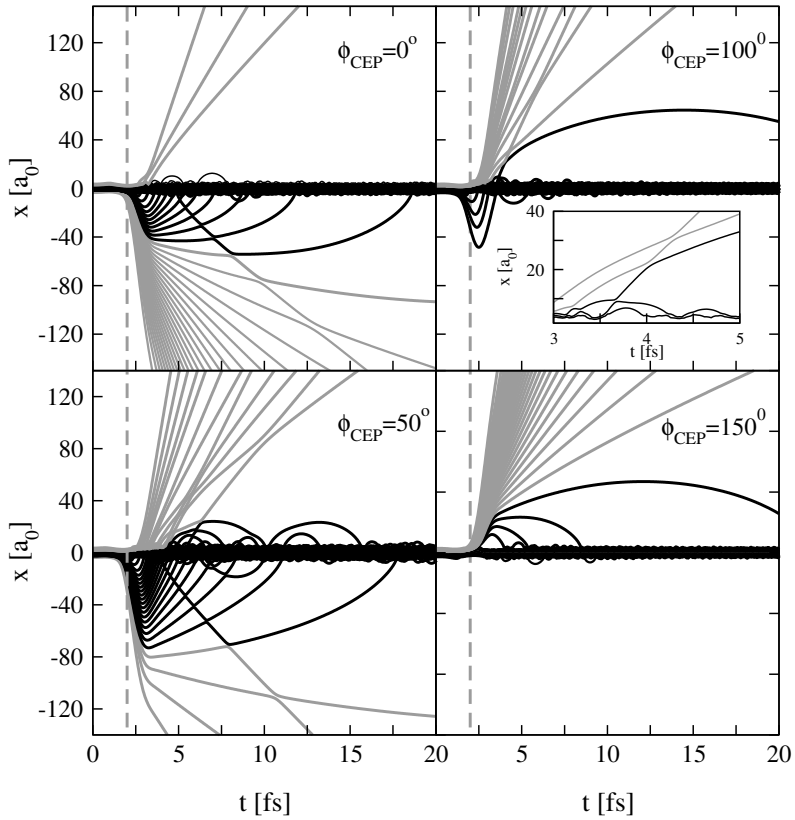

Figure 4.27: Trajectory dynamics for different values of ϕ_{CEP}. They illustrate the different electron dynamics depending on ϕ_{CEP}. The remaining laser parameters are: $\lambda = 800nm$, an intensity of $I = 3.51 \times 10^{14} W/cm^2$ and a pulse duration of 1.5 cycles. Brown color indicates trajectories ending up as free at 2000 a.u., whereas black trajectories end up bound to the nucleus. The vertical dashed line indicates the center of the laser pulse. The inset gives a detail of the trajectory dynamics to illustrate the non-crossing of the trajectories.

on the dependence of the CEP on the asymmetry parameter (when the length of the laser pulse increases) was already discussed in Ref. [84]. For very short laser pulses, only one or two field peaks exist and different values of the CEP lead to completely different time-dependent electric fields (see Figure 4.22). Conversely, when the length of the pulse increases the dependence on the shape of the laser pulse disappears. For $T_{pulse} = 2.5$ cycles, more oscillations of the field take place and the trajectories are emitted to the left and to the right with every oscillation of the field.

In the left panel of Figure 4.28, $P_l(E_{kin})$ (top) and $P_r(E_{kin})$ (bottom) are plotted as a function of the ϕ_{CEP} value and the kinetic energy E_{kin} of the outgoing electron. In the right panel, the density plot obtained from the trajectories dynamics is shown, and in the left panel, the same quantity for the benchmark quantum calculation is represented. We can see that the trajectory-only calculations qualitatively and quantitatively reproduce

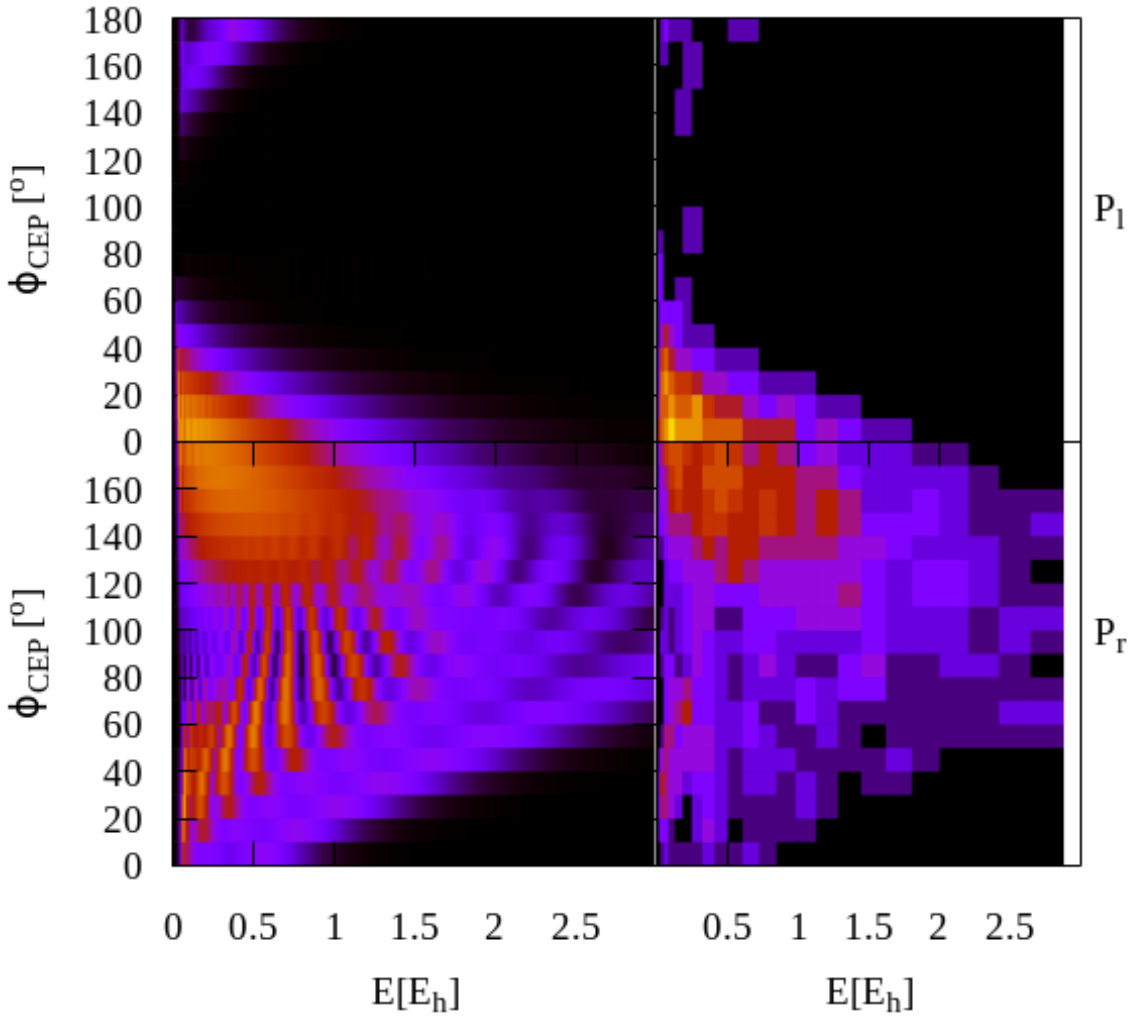

Figure 4.28: Density map of the left/right photo-electron spectra P_l (upper part) and P_r (lower part) as a function of energy and ϕ_{CEP}. Left panel: wave packet calculations, right panel: quantum trajectory results. The maps are plotted one on top of the other to show the symmetry of the electron emission.

the benchmark calculations, thereby confirming the validity of the present approach.

From the analysis of Figure 4.28, we can notice that when $\phi_{CEP} = 0^o$ (top left panel) the trajectories are mainly emitted to the left ($x < 0$) and only low energy trajectories are emitted ($0 < E_{kin} < 2E_h$). As the CEP value is changing from 0^o to 90^o, η is changing from negative to positive and around $\phi_{CEP} = 90^o$ they are all emitted to the region $x > 0$ ($\eta = 1$) and higher energy trajectories are emitted. This high energy trajectories are the first bunch of trajectories which are emitted at the maximum of the field, and the

lower energy ones are emitted after several collisions of the ones that are driven back by the field with those in the core. Another important feature is that in the region from $\phi_{CEP} = 20^o$ to $\phi_{CEP} = 100^o$ interferences are seen in the photo-electron spectra, which is related to the existence of several bunches of ejected trajectories. On the other hand, from $\phi_{CEP} = 120^o$ to $\phi_{CEP} = 180^o$, the ionization is due to the burst of trajectories which are emitted at once at the peak of the field. Hence, the main features of the right or left emitted electrons as a function of both energy and CEP can be rationalized on the basis of the trajectories dynamics, as depicted in Figure 4.27. This is one of the main advantages of the proposed trajectory approach to model quantum mechanics, in particular for the analysis of ultrafast time-dependent electron dynamics.

4.5 Conclusions

In this chapter, we have proposed a method based on propagation of a swarm of interacting trajectories using model quantum potentials, which emerges as a promising alternative for quantum dynamics studies. We use an approximate expression for the quantum potential, obtained by discretizing the quantum probability density. The expression for the resulting quantum potential contains both, attractive and repulsive parts. It yields the same expression for the quantum force as in Ref. [43], but it allows (in addition) to reconstruct the wave function through integration of the Lagrangian along the trajectories.

The methodology is applied to a variety of one-dimensional model systems, and the scheme is found to reproduce important quantum-mechanical phenomena such as the zero-point energy in harmonic and anharmonic potentials, the tunnelling /transmission probabilities for different barrier shapes, and autocorrelation functions and energy spectra. Furthermore, the proposed methodology is applied to simulate the laser-driven electron dynamics and accurate results are also obtained. It is not only capable of reproducing quantitatively total ionization yields, but also subtle CEP effects such as left/right asymmetries in the ionization as a function of the carrier envelope phase.

In every case, numerical convergence was achieved for a few hundreds of interacting tra-

jectories. Besides its numerical performance, the present approach has the advantage to yield a detailed picture of the dynamical process, since it is based on trajectories. Care must be taken in the numerical implementation of the present approach, since the use of very dense trajectory arrangements leads to the appearance of large local peaks in the quantum potential, which may hinder the stability of the algorithm. However, provided the desired observables can be computed accurately with a moderately number of trajectories, the method exhibits high potential regarding its generalization to multidimensional systems, due to the fact that the computed paths strictly abide the non-crossing rule for quantum trajectories.

In the next chapter we develop a different approach. Based on the idea of deriving approximations for the quantum potential from a given parametrization of the density, a many-body system is studied within the molecular dynamics framework, but including the quantum potential and performing the molecular dynamics simulations with the resulting effective potential. As model systems we study the absorption spectra of Na embebed in rare gas matrices, in particular, Ar and Kr matrices.

CHAPTER 5 STUDY OF THE ABSORPTION SPECTRA OF ATOMIC Na ISOLATED IN Ar AND Kr MATRICES

5 STUDY OF THE ABSORPTION SPECTRA OF ATOMIC Na ISOLATED IN Ar AND Kr MATRICES

In this chapter, an approximate quantum potential is derived from a suitable parametrization of the ground state wave function of a rare gas matrix. The proposed *ansatz* takes into account the physical properties of the target system. We use the Car-Parrinello minimization scheme to find the parameters that minimize the variational estimate of the ground state energy. Molecular dynamics simulations are carried out on the total effective potential, comprising both, the classical pair interaction potential and the approximate quantum potential. We applied the method to the study the absorption spectra of atomic Na trapped in Ar and Kr matrices.

5.1 Introduction to matrix isolation spectroscopy of alkali atoms

The study of photo-induced processes in molecular systems has attracted the interest of the scientific community in the last decades. The understanding of the main mechanisms of processes such as photo-dissociation, isomerization, among others, has increased the possibility of developing technological applications such as obtention of solar energy, opto-electronics, among others. The isolation of metal atoms in rare gas matrices is one of the most spread techniques to study the spectroscopy of atoms and molecules [61], [93]-[98]. In particular, alkali atoms are very attractive, because its electronic configuration makes them very suitable for the study of the matrix embedding.

In the past decades, multiple experiments have been done to study the absorption and luminescence of alkali atoms in rare gas matrices. The studies performed by Balling et al. [99]-[101] on Li, Na and K-doped Argon matrices have shown that there may be multiple sites where the impurity atom can be trapped in the matrix, which are all characterized by

a rather well defined triplet structure. For those three alkali metals, two sets of maxima in the absorption spectrum were identified, which are typically referred to as the red and blue triplets. In addition to these bands, Tam and Fajardo [102] investigated Li and Na atoms trapped in rare gas matrix using a new experimental technique based on laser ablation. They found, for both atoms, a new well resolved triplet structure on the high-energy side of the blue band, which is referred to as the violet triplet.

More recently, Ryan and collaborators [61] conducted an experimental and theoretical work in order to study the absorption and the luminescence of atomic Na in Ar and Kr matrices. They also reported the three sets of maxima in the absorption band. Furthermore, they found that the violet band does not produce any characteristic emission for energies above $12500 cm^{-1}$.

From the theoretical point of view, many studies have been conducted to identify the crystal structure responsible for the experimentally observed absorption bands. According to the theoretical studies performed in Refs. [61] and [103], it seems that the smallest trapping sites in the matrix are the responsible of the violet absorption band.

The simulations of the absorption and emission bands of the Na atom embebed in the matrix performed by Ryan and coworkers [61], were based on molecular dynamics methods. In particular, to simulate the absorption bands they used the method known as diatomics-in-molecule (DIM). The potential energy surfaces were obtained from spectroscopic data, and different isolation sites for the Na atom were considered. However, while qualitative information on the absorption bands was obtained, their spectral position turned out to be completely different from those reported experimentally. In Ref. [61], an artificial modification of the shape of the potential correlating to the second excited state of sodium was performed in order to match the measured spectra. Simulations employing the new potential shifted the absorption bands towards the correct spectral positions, but there remains the ambiguity about which is the physical origin of the proposed shift of the excited state potential (which was obtained empirically), and if the rest of the potential energy curves do not change as well.

A different study, using more precise potentials, was carried out by Boatz and collaborators [93] based on first-order perturbation theory analysis of the excited p state of the alkali atom. However, although some qualitative information was extracted from them, the absorption spectra obtained as a result of the simulations do not reproduce the experimental results.

Recently Gervais and collaborators [103] carried out a study based on pseudo-potentials, that take into account the polarization of the nuclei, and modeled the absorption and emission bands of alkali atoms in Ar matrices. Their model allowed to identify the displacements of the sodium spectrum in gaseous state with respect to the sodium trapped in the matrix and to identify certain sites where sodium can be trapped.

It is important to note that the simulations performed by Ryan *et al.* [61] were purely classical simulations, which may give correct results if heavy atoms and relatively high temperatures (i.e., corresponding to liquid and gas phases of rare gas systems) are considered, but for the noble gas atoms in the matrix the intrinsically quantum character of the systems becomes relevant.

Thus, the aim of this chapter is to derive a many-body quantum potential to evaluate the influence of quantum effects onto the simulated absorption spectra of alkali atoms in rare gas matrices. The approximate quantum potential is derived from a given ansatz for the ground state wave function. As the extension of the *ansatz* introduced in the previous chapter to multi-dimensional systems is not straightforward, here we propose a different parametrization that takes into account the physical properties of the noble gas matrix. The parameters to minimize the density are derived by minimizing the variational estimate of the energy using the Car-Parrinello scheme.

Therefore, MD simulations are performed to simulate the absorption spectra, with an effective potential comprising both the classical pair interaction and the quantum potentials. As a model system, we study the absorption spectra of Na trapped in a single vacancy site (sv) in Ar and Kr matrices. This trapping site has been identified as the

responsible for the violet absorption band [61, 103]. In order to evaluate the influence of the quantum corrections on the simulated absorption spectra, we perform molecular dynamics simulations with and without the quantum potential.

The chapter is structured as follows. As in the simulation of the absorption bands of the Na atom in the matrix requires some of the standards techniques of classical MD simulations, the next section is dedicated to present the fundamental aspects related to them. In Section 5.3 we introduce the *ansatz* for the ground state wave function and we obtain the approximate many-body quantum potential. Then, the Car-Parrinello minimization scheme is used to minimize the variational estimate of the energy and to find the parameters to evaluate the quantum potential. Afterwards, in Section 5.4 we discuss the results of the MD simulations with an effective potential. Finally, in Section 5.5 we draw some partial conclusions.

5.2 Methods

In this section the main aspects of classical molecular dynamics simulations are summarized. Furthermore, we present the pair-interaction potentials between the noble gas atoms and between them and the Na atom. We describe how the absorption and emission bands can be evaluated from MD simulations and we define the pair radial distribution function.

5.2.1 Classical Molecular Dynamics

In the study of the time evolution of many-body systems, the use of classical Molecular Dynamics (MD) has been widely spread. Within this method, the dynamics of a microscopic system is studied by the numerical solution of the classical equations of motion, which are usually expressed in the Newton formulation, but the method is also consistent with the Lagrangian and Hamiltonian formulations [104].

To perform a classical molecular dynamic simulation, a set of N classical particles with coordinates $\mathbf{r}_i$ and velocities $\mathbf{v}_i$, $i = 1, ..., N$, is chosen and they evolve on a potential

energy surface $V(\mathbf{r}_1, ..., \mathbf{r}_N)$:

$$V(\mathbf{r}_1, ..., \mathbf{r}_N) = \sum_{i,j(i\neq j)}^{N-1} V^{(2)}(\mathbf{r}_i, \mathbf{r}_j) + \sum_{i,j,k(i\neq j\neq k)}^{N-1} V^{(3)}(\mathbf{r}_i, \mathbf{r}_j, \mathbf{r}_k) + V^N(\mathbf{r}_1, ..., \mathbf{r}_N) \ , \quad (5.2.1)$$

where $V^{(2)}(\mathbf{r}_i, \mathbf{r}_j) = V(r_{ij})$, with $r_{ij} = |\mathbf{r}_i - \mathbf{r}_j|$, represent the two-body interaction potential, $V^{(3)}(\mathbf{r}_i, \mathbf{r}_j, \mathbf{r}_k)$ is the three-body potential and $V^N(\mathbf{r}_1, ..., \mathbf{r}_N)$ denotes the difference between the total interaction potential V and the two-body and three-body contribution. It comprises contributions to the interaction energy involving four or more particles. The two-body contribution to the interaction potential is the most commonly used, since this term is usually the dominant one and the higher order terms constitute progressively smaller corrections to the total energy of the system. Furthermore, the pair potentials employed in computer simulations are generally regarded as effective pair potentials comprising all the many-body effects (e.g., they are obtained by fitting experimental values for the thermochemical properties of the system). In the simulations described below only pairwise interactions are considered.

Hence, the classical equations of motion for each particle read as,

$$m_i \frac{d^2\mathbf{r}_i}{dt^2} = -\nabla_i V_i = \mathbf{f}_i \quad i = 1, ..., N \ , \quad (5.2.2)$$

where

$$V_i = \sum_{j=1(j\neq i)}^{N} V(r_{ij}) \ , \quad \nabla_i = \left(\frac{\partial}{\partial x_i}, \frac{\partial}{\partial y_i}, \frac{\partial}{\partial z_i} \right) . \quad (5.2.3)$$

The standard methods to solve ordinary differential equations like equation (5.2.2) are based on finite difference schemes. The starting point of the solution is the set of initial positions and velocities from which all the other dynamical information at time t (including the new positions and velocities) at the later time $t + \Delta t$ are evaluated. The election of finite-size elementary time interval Δt depends on the specific problem, in general it should be small compared with the characteristic time scale of the dynamics. Among the methods usually employed, we can mention the Verlet algorithm [105] and its variants:

the leap-frog [106] and the velocity Verlet [107] algorithms, and the predictor-corrector methods [104]. In general, Verlet algorithms have good properties for energy conservation, but the predictor-corrector methods can be up to three orders more precise. On the other hand, the latest family of methods is rather slow and requires twice the storage capacity of Verlet algorithms. In the simulations presented below, the velocity Verlet algorithm is used.

An important practical aspect in the computer simulation of a many-body system is the number of particles included in the simulations, which is usually limited by the available storage capacity and, most importantly, by the speed of the calculation. This means that the number of atoms in the simulation is restricted, bringing undesirable surface effects into the simulations. The particles located close to the surface experience quite difference forces, with respect to the inner ones. To tackle this problem, it is customary to introduce periodic boundary conditions [104]. These are obtained by replication of the original simulation cell (which contains the N particles) throughout space to form an infinite lattice. Then, in the course of a simulation, as a particle move in the original box, its periodic image in each neighboring box performs the same movement. Hence, once a particle leaves the original box, one of its images will enter through the opposite face. A two-dimensional example of such periodic system is shown in Figure 5.1. A further step to speed up the simulations is related to the calculation of the forces acting on each molecule. In general, we must include the interaction between each particle with the rest, this means a summation over $N - 1$ terms. Furthermore, in principle we must include all the interactions between the particles and their images, this is an infinite number of terms, which is impossible to evaluate in practice. For short-range potentials the following approximation, known as the minimum image convention, results in a marked reduction of the computational cost while providing accurate results: consider the particle 1 (see Fig. 5.1), in the centre of a region which has the same dimension and shape of the simulation box, then this molecule will interact with all the molecules whose centres lie within this region [104] and its interaction with all the particles and replicas lying outside

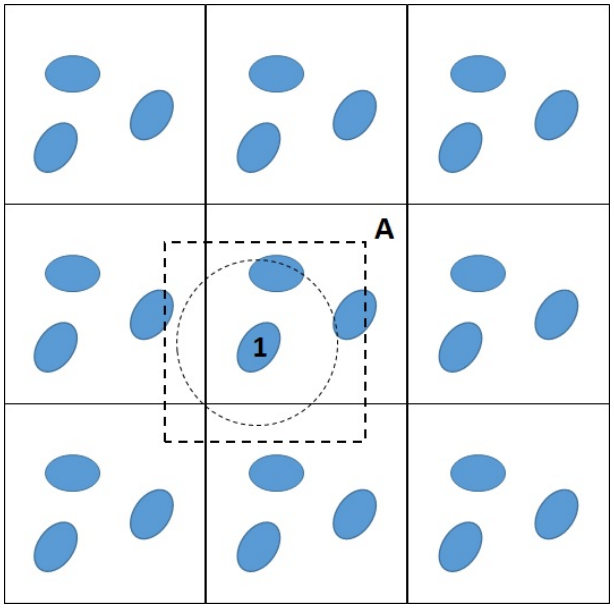

Figure 5.1: Illustration of the application of periodic boundary conditions, the original cell is labeled with the letter A. Reproduced from Ref. [104].

is neglected.

Another approximation which substantially decrease the amount of calculations, which is also valid for short range potentials, is the application of a spherical cutoff, this means, setting the pair potential $V(r_{ij})$ to zero for $r_{ij} > r_c$, being r_c the cutoff distance. This is represented by a dashed circle in Figure 5.1. The cutoff distance must not exceed $\frac{1}{2}L$, (L is the size of the simulation box), to be consistent with the minimum image convention. In our calculations we fix $r_c = 23.24\, a_0$ (for the Na doped Ar matrix) and $r_c = 23.67\ a_0$ (for the Na doped Kr solid), which is 2.5 times longer than the equilibrium distances of the respective $Rg - Rg$ pair potentials.

The experience shows that the method in general does not converge for molecular dynamics simulations starting from arbitrary initial conditions, even if the system is initially close to equilibrium. Hence, thermalization techniques are applied in order to equilibrate the average kinetic energy in the simulations to match a given temperature. Here we use velocity rescaling as it is described in Ref. [108]. From the energy equipartition principle the temperature T is calculated from the kinetic energy of the system at the instant

t,

$$T = \frac{1}{3Nk_b} \sum_{i=1}^{N} m_i v_i^2 \ . \tag{5.2.4}$$

Here, m_i are the particles masses and $\mathbf{v}_i$ their velocities, while k_b denotes the Boltzman constant. Then, if T^* is the temperature at which we want to perform the simulations and $\mathbf{v}_i^*$ are the values of the rescaled velocities corresponding to this temperature, they obey a similar relation

$$T^* = \frac{1}{3Nk_b} \sum_{i=1}^{N} m_i v_i^{*2} \ . \tag{5.2.5}$$

We can transform the velocities of the particles from their values $\mathbf{v}_i$ to the desired ones $\mathbf{v}_i^*$ with the relation

$$\mathbf{v}_i^* = \mathbf{v}_i \sqrt{\frac{T^*}{T}} \ . \tag{5.2.6}$$

In addition to this correction to the velocities, the molecular dynamics simulations may be performed at an effective temperature T^* to mimic zero-point energy effects. As it is well known, when a classical system is in equilibrium, the energy coincides with the minimum of the potential energy, and the kinetic part is zero. However, when a quantum system is in its ground state, the average potential energy is larger than the classical one and the kinetic energy is not zero. An approximation to correct the zero-point energy effect in the classical simulations was proposed by Bergsma and collaborators [109] and has been extensively used in MD simulations to include zero-point energy effects [110]-[113]. The approximation is based on the modeling of the particles motion as harmonic oscillators. Since crystal site oscillations in the Ar and Kr solids are nearly harmonic, the approximation seems adequate for these systems. The effective temperature T^* in the Bergsma scheme is evaluated as (more details are given in the Appendix D):

$$T^* = \frac{\hbar\omega}{2k_b} \tanh^{-1}\left(\frac{\hbar\omega}{2k_b T}\right) \ . \tag{5.2.7}$$

5.2.2 Pair-interaction potentials

In the study of the dynamics of atomic and molecular systems, the representation of the force fields describing their interaction is of fundamental interest. The interaction potentials allow to establish the most stable configurations, as well as to study the dynamics of the system. In general, the calculation of these potentials is a complicated task, and on the basis of theoretical and experimental results, various analytical forms have been proposed for their description but they do not always accurately characterize the real physical situation. As it was previously explained, in the representation of these potentials we can take into account the N-body contributions effectively in the pairwise interactions. Therefore, here we only consider two-body interactions between all pairs of particles.

Here, our model system is a matrix composed of N atoms of noble gas, whose positions are denoted by $\mathbf{r}_i$ (with $i = 1, ..., N$) containing a sodium impurity, whose position is identified with $\mathbf{r}_0$. In particular, we consider Argon and Krypton matrices. The interaction between the noble gas atoms, which we will denote by V_{gg} are modeled by a Lennard-Jones potential (LJ),

$$V_{gg}(r_{ij}) = 4\varepsilon\left[\left(\frac{\sigma}{r_{ij}}\right)^{12} - \left(\frac{\sigma}{r_{ij}}\right)^{6}\right] , \quad r_{ij} = |\mathbf{r}_i - \mathbf{r}_j| , \quad i, j = 1, ..., N . \tag{5.2.8}$$

where r_{ij} is the inter-nuclear distance between the pair of atoms i, j. The potential parameters ε and σ characterize the depth of the potential well and the intercept with the distance axis, respectively. The σ values were taken as $6.35\,a_0$ and $6.76\,a_0$ for Ar and Kr respectively, and ε as $4.5 \times 10^{-4}\,E_h$ (for the Ar-Ar potential energy curve) and $3.8 \times 10^{-4}\,E_h$ (for the Kr-Kr energy curve) [61]. In addition to the interactions between the pairs of noble gas atoms, it is necessary to describe the interaction between them and the sodium atom, V_{ag}. For the sake of simplicity we have identified a with the alkali atom and g with the noble gas atom. The latter depends on the specific electronic state of the dimer. Here we consider the ground and the first two excited states, correlating to the

Table 5.1: Parameters reported in [61] as a result of fitting the analytical expressions given in Eq. (5.2.9) for the interaction potentials, to the experimental results. For the NaKr pair, the parameters of the $V_{ag}^{(3)}$ interaction were derived by us in order to correctly reproduce the shape of the potential energy curve. The values of the parameters are given in Kelvin.

NaAr	$V_{ag}^{(1)}$ K	$V_{ag}^{(2)}$ K	$V_{ag}^{(3)}$ K	NaKr	$V_{ag}^{(1)}$ K	$V_{ag}^{(2)}$ K	$V_{ag}^{(3)}$ K
$R_o\,(a_0)$	**9.441**	**5.486**	**12.773**	$R_o\,(a_0)$	**9.444**	**5.815**	**12.121**
a_6	-44.45	-7089.54	-39.71	a_6	-118.19	-6657.94	-12.25
a_8	-617.14	18559.25	-471.68	a_8	-979.40	10824.88	-841.91
a_{10}	1223.85	-27224.38	966.04	a_{10}	2222.37	-9537.86	1513.94
a_{12}	-901.07	22797.57	-738.82	a_{12}	-1852.37	5541.58	-1054.72
a_{14}	342.28	-9355.03	307.39	a_{14}	799.96	-1426.44	396.59
a_{16}	-71.78	1481.51	-77.84	a_{16}	-191.12	137.52	-89.23
a_{18}	7.91	0	12.36	a_{18}	24.01	0	12.24
a_{20}	-0.35	0	-1.20	a_{20}	-1.24	0	-0.97
a_{22}			0.06	a_{22}	0	0	0.039
a_{24}			-0.0015	a_{24}	0	0	-0.00054

atomic states $^2S_{1/2}$, $^2P_{1/2}$ and $^3P_{1/2}$ of the alkali atoms. In the presence of a noble gas atom, these excited states are modified to produce a strongly bound state: $A^2\Pi$, hereafter referred to as $V_{ag}^{(2)}$, and a repulsive one: $B^2\Sigma$ ($V_{ag}^{(3)}$), while the ground state is a weakly bound state: $X^2\Sigma$ (denoted as $V_{ag}^{(1)}$).

In the work done by Ryan and collaborators [61], the following analytical form was proposed to describe the ground $V_{ag}^{(1)}$ and the excited states $V_{ag}^{(2,3)}$ of the diatomic pairs $Na-Rg$, depending on the distances between the impurity and each rare gas atom,

$$V_{ag}^{(\alpha)}(r_{i0}) = \sum_{k=1}^{n} a_{2(k+2)} \left(\frac{r_{i0}}{R_0}\right)^{(2(k+2))} , \quad r_{i0} = |\mathbf{r}_i - \mathbf{r}_0| , \quad (\alpha = 1, 2, 3) . \tag{5.2.9}$$

The values of the expansion coefficients reported in Ref. [61] (which are obtained as a result of fitting the analytical expressions for the potentials given in equation (5.2.9) to the experimental results) are listed in Table 5.1, except for the $B^2\Sigma$ state of the diatomic pair $Na-Ar$. The expansion coefficients reported in Ref. [61] do not reproduce this higher energy excited estate potential ($V_{ag}^{(3)}$). To solve this problem, we fitted the potential values given by Saxon et al [114] to the analytical form given in Eq. (5.2.9), and the fitting parameters are reported on the fourth column of Table 5.1. This final set

of parameters are the one we use in our MD simulations.

The potential energy curves corresponding to the three states $V_{ag}^{(\alpha)}$ ($\alpha = 1, 2, 3$) are depicted in Figure 5.2, for the diatomic pairs NaAr (Figure 5.2 (left panel)) and NaKr (Figure 5.2 (right panel)). With the aim of comparing the shape of the three potentials, each curve is plotted with a common asymptotic value of zero. However, in reality the $V_{ag}^{(2)}$ (A) and $V_{ag}^{(3)}$ (B) states dissociate to the ^2P asymptote, $16956 cm^{-1}$ above the ground state. In the description of the interaction potentials presented so far, we have only included the pairwise interaction, to describe both, the ground and the excited states of the Na atom in its interaction with the rare gas atoms in the matrix. However, although this description is correct for modeling the ground state, given that both, the ground state of the Na and the rare gas atoms present spherical symmetry, in the description of the excited states this symmetry disappears and therefore a summation of the two-body terms, without taking into account the angles, is no longer correct. In order to tackle this problem we will use a correction for the excited state potentials, based on first-order perturbation theory. This correction, first proposed by Boatz and coworkers [93], is based on using

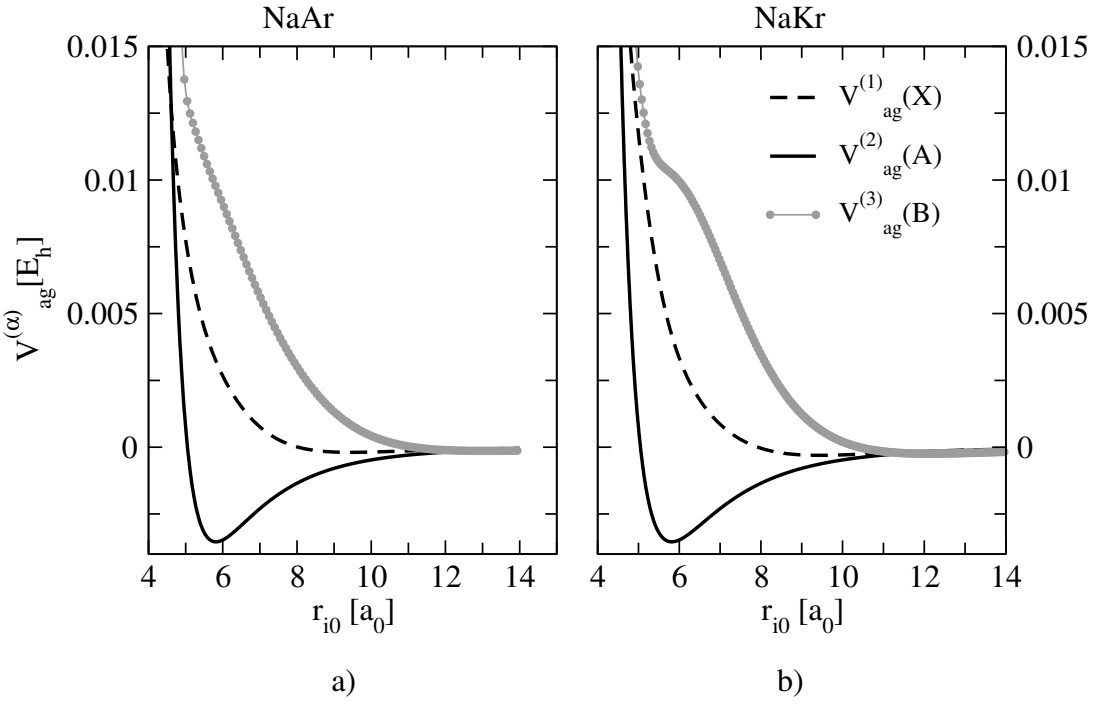

Figure 5.2: Interaction potentials $V_{ag}^{(\alpha)}(r_{i0})$ (see Eq.(5.2.9)) of the diatomic pairs NaAr (left panel) and NaKr (right panel) for the three states $\alpha = 1, 2, 3$ considered in this study.

the Born-Oppenheimer approach to separate the electronic structure of the atoms from the vibrational motion of the matrix. It assumes that the electrons in the closed shells of the alkali atom are not affected by the interactions with the noble gas atoms, the latter only affect the optically active electron. Then, the Hamiltonian H of the optically active electron can be separated in two contributions, $H_A(\mathbf{r}_e)$ which is the Hamiltonian for the free valence electron, and a perturbation caused by the rare gas atoms. Identifying ϵ_i and ψ_i with the eigenvalues and eigenvectors of the unperturbed Hamiltonian H_A, the eigenvalues E of H, can be derived by solving,

$$det|V_{ij} - (\epsilon_i - E)\delta_{ij}| = 0 \ , \tag{5.2.10}$$

where,

$$V_{ij} = \sum_{k=1}^{N} \langle \psi_i | V(\mathbf{r}_e, \mathbf{r}_k) | \psi_j \rangle \ , \tag{5.2.11}$$

with $\mathbf{r}_e$ and $\mathbf{r}_k$ being the electron and rare gas atoms position vectors, respectively. More details related to this approach are described in the Appendix E. This correction in the excited state potential is taken into account in our simulations of the absorption and emission bands.

5.2.3 Calculation of the absorption and emission bands

As discussed at the beginning of this chapter, our aim here is to study the quantum effects on the absorption bands of sodium trapped in rare gas matrices. In general, the transition energies between the different levels of the sodium atom are given by the energy difference between the final and the initial states of the system. If we assume that the system is initially in the ground state, the total energy E_i can be written as the contribution of the interaction between the rare gas atoms $V_{gg}(r_{ij})$ given in Eq.(5.2.8) and the interaction of the Na atom in the ground state with the rare gas surrounding $V_{ag}^{(1)}(r_{i0})$ in Eq.(5.2.9),

$$E_i(\mathbf{r}_0, \mathbf{r}_1, ..., \mathbf{r}_N) = \sum_{i=1}^{N} V_{ag}^{(1)}(r_{i0}) + \sum_{i=1}^{N-1} \sum_{j>i} V_{gg}(r_{ij}) = U_{ag}^{(1)} + U_{gg} \ , \tag{5.2.12}$$

where to simplify the notation we have defined

$$\sum_{i=1}^{N} V_{ag}^{(\alpha)}(r_{i0}) = U_{ag}^{(\alpha)} \ , \quad \alpha = 1,2,3 \ , \tag{5.2.13}$$

and

$$\sum_{i=1}^{N-1} \sum_{j>i} V_{gg}(r_{ij}) = U_{gg} \ . \tag{5.2.14}$$

According to the modifications introduced in the corresponding potentials for the excited states described in the Appendix E, after solving equation (5.2.10), three different values of the energy $E^{(\beta)}$ with $(\beta = 1,2,3)$ are obtained which represent the total contribution to the energy due to the electronic excitation and to the interaction of the noble gas atoms with sodium in the excited states. Hence the energy in the final state can be written as

$$E_f^{(\beta)}(\mathbf{r}_0, \mathbf{r}_1, .., \mathbf{r}_N) = E^{(\beta)} + U_{gg} \ , \quad \beta = 1,2,3 \ . \tag{5.2.15}$$

Then, the transition energies $\Delta E^{(\beta)}$ are calculated as the differences between the energies of the final state Eq.(5.2.15) and the initial state Eq.(5.2.12), therefore the terms U_{gg} cancelled,

$$\Delta E^{(\beta)} = E^{(\beta)} - U_{ag}^{(1)} \ , \quad \beta = 1,2,3 \ . \tag{5.2.16}$$

Hence, to simulate the absorption spectra from the MD calculations, the dynamics of the system is followed along a trajectory with the Na atom evolving in the potential energy surface corresponding to the ground state. At each time step the total energy of the system, determined by the atomic positions is calculated, in the ground state $E_i(\mathbf{r}_0^0, \mathbf{r}_1^0, ..., \mathbf{r}_N^0)$, as well as in the excited states $E_f^{(\beta)}(\mathbf{r}_0^0, \mathbf{r}_1^0, ..., \mathbf{r}_N^0)$,

$$\Delta E^{(\beta)} = E_f^{(\beta)}(\mathbf{r}_0^0, \mathbf{r}_1^0, ..., \mathbf{r}_N^0) - E_i(\mathbf{r}_0^0, \mathbf{r}_1^0, ..., \mathbf{r}_N^0) \ , \quad \beta = 1,2,3 \ , \tag{5.2.17}$$

where the superscript in the atomic coordinates indicates that the positions of the atoms are evaluated from the evolution on the ground state energy surface, and the same po-

sitions are used to evaluate the final energy state as if the Na atom were in the excited state manifold, assuming that the Franck-Condon principle holds. Finally an histogram is built with these energy differences, which represents the absorption spectra for transitions between the ground state and the excited states.

To simulate the emission spectra, we let the system evolve along a trajectory in the electronic excited states. It is important to note, that while the ^2P state of the Na atom trapped in the matrix, is described by three potential energy surfaces, the simulations were carried out on the lowest energy excited state. Following the previous results obtained by Ryan et al. [61], which showed that after a few picoseconds only the lowest energy state is populated and therefore to simulate the emission spectra it is reasonable to run the simulations on the lowest energy excited state $\beta = 1$. Similar conclusions were drawn previously by Rojas-Lorenzo et al. [111] in the study of Hg doped Ar solid.

Finally, for the calculation of the emission spectra, the equation (5.2.16) is evaluated at each time step. Now only the lowest energy excited state is considered, the energies of the final $E_f^{(1)}(\mathbf{r}_0^e, \mathbf{r}_1^e, ..., \mathbf{r}_N^e)$ and initial $E_i(\mathbf{r}_0^e, \mathbf{r}_1^e, ..., \mathbf{r}_N^e)$ states, are evaluated from a trajectory with the impurity on the lowest energy excited state,

$$\Delta E^{(1)} = E_f^{(1)}(\mathbf{r}_0^e, \mathbf{r}_1^e, ..., \mathbf{r}_N^e) - E_i(\mathbf{r}_0^e, \mathbf{r}_1^e, ..., \mathbf{r}_N^e) \ . \tag{5.2.18}$$

The histogram obtained at the end of the propagation represents the emission spectra.

5.2.4 Radial distribution function

The analysis of the structure of the solid around the sites accommodating the Na atom is made through the radial pair-distribution function $G(r)$. It is evaluated by determining the Na atom-rare gas atom pair distance, r_{i0}, $i = 1, ..., N$. The histogram $h(r)$ of all the pair distances is built with a binning width $\Delta r = 2.02\, a_0$. Once all the configurations have been taken into account, the histogram must be normalized by dividing it by the total number of iterations over time and the total number N of atoms considered. The

results are presented in the form of the function $G(r)$ [104]

$$G(r) = \frac{h(r)}{Nt_{steps}} \ . \tag{5.2.19}$$

5.3 Molecular dynamics with approximate quantum potentials

In this section, starting from an *ansatz* for the ground state wave function we derive an expression for the effective potential which is used in MD simulations to calculate the absorption and emission spectra in doped rare gas matrices. This effective potential contains the contribution of classical pairwise interaction potentials Eq.(5.2.8) and Eq.(5.2.9), as well as an additional contribution that can be identified as the *quantum potential*.

To derive the approximate quantum potential, we use the following *ansatz* for the wave function, based on the fact that we are modeling the ground state of the noble gas matrix,

$$\Psi(\mathbf{r}_0, \mathbf{r}_1, ..., \mathbf{r}_N) = exp\left(\sum_{i=1}^{N-1}\sum_{j>i} u_{gg}(r_{ij}) + \sum_{i=1}^{N} u_{ag}(r_{i0})\right), \quad r_{i0} = |\mathbf{r}_i - \mathbf{r}_0| \ , \quad i, j = 1, .., N, \tag{5.3.1}$$

In general, due to the bosonic character of the rare gas atoms in the matrix, the ground state wave function must be invariant under translations, rotations and particle permutations. This restriction is satisfied if the interatomic distances r_{ij} are selected as arguments rather than the particle positions. Furthermore, the wave function must be positive define. In general, correlations between all particles must be present in the proposed form, however these many-body effects must be less and less important as the number of particles increases.

The *ansatz* proposed here in Eq.(5.3.1), only includes pair-interactions terms [115, 116] and we have distinguished the Rg-Rg interaction (u_{gg}) from the Na-Rg interaction (u_{ag}).

The Hamiltonian of a system composed of the N rare gas atoms and a Na impurity can

be written as follows (we will use atomic units otherwise indicated, $\hbar = 1$)

$$\hat{H} = -\frac{1}{2}\sum_{k=0}^{N}\frac{1}{m_k}\nabla_k^2 + U_{gg} + U_{ag}^{(1)} \ , \tag{5.3.2}$$

$U_{ag}^{(1)}$ accounts for the Na-Rg interaction and U_{gg} is the contribution due to the Rg-Rg interactions. From Eq. (5.3.2) we can evaluate the local energy

$$\Psi(\mathbf{r}_0, \mathbf{r}_1, ..., \mathbf{r}_N)E_L = \hat{H}\Psi(\mathbf{r}_0, \mathbf{r}_1, ..., \mathbf{r}_N) \ , \tag{5.3.3}$$

which transforms into the following expression

$$E_L = -\frac{1}{2}\sum_{k=0}^{N}\frac{1}{m_k}[\nabla_k^2 \log\Psi + (\nabla_k \log\Psi)^2] + U_{gg} + U_{ag}^{(1)} \ . \tag{5.3.4}$$

In expression (5.3.4), we can identify the term under the summation symbol as the *quantum potential*. Substituting the *ansatz* for the wave function $\Psi(\mathbf{r}_0, \mathbf{r}_1, ..., \mathbf{r}_N)$ given in Eq.(5.3.1) in Eq.(5.3.4) we obtain

$$E_L = -\frac{1}{2}\sum_{k=0}^{N}\frac{1}{m_k}\Bigg[\nabla_k^2\Bigg(\sum_{i=1}^{N-1}\sum_{j>i}^{N}u_{gg}(r_{ij}) + \sum_{i=1}^{N}u_{ag}(r_{i0})\Bigg) + \Bigg(\nabla_k\Bigg(\sum_{i=1}^{N-1}\sum_{j>i}^{N}u_{gg}(r_{ij}) + \sum_{i=1}^{N}u_{ag}(r_{i0})\Bigg)\Bigg)^2\Bigg] + U_{gg} + U_{ag}^{(1)} \ . \tag{5.3.5}$$

As it can be seen in equation (5.3.5), there are multiple crossed terms. These terms contains scalar product of unit vectors with origin on each pair of particles, and pointing to each one of the atoms in the system. Their contribution is expected to vanish for a sufficiently large number of particles. Here we completely neglect them, as a first approximation in the evaluation of the local energy. Hence, including only the two-body terms, the ground state energy can be approximated as (more details related with this derivation are given in the appendix F)

$$E^* \approx U_{gg}^{eff} + U_{ag}^{eff} \ , \tag{5.3.6}$$

where

$$U_{ag}^{eff} = -\frac{\mu}{2}\sum_{k=1}^{N}\left(u_{ag}^{''}(r_{k0}) + 2\frac{u_{ag}^{'}(r_{k0})}{r_{k0}} + u_{ag}^{'2}(r_{k0})\right) + U_{ag}^{(1)} = Q + U_{ag}^{(1)} \ , \quad (5.3.7)$$

$$U_{gg}^{eff} = -\frac{1}{m_g}\sum_{k=1}^{N}\sum_{j>k}^{N}\left(u_{gg}^{''}(r_{jk}) + 2\frac{u_{gg}^{'}(r_{kj})}{r_{kj}} + u_{gg}^{'2}(r_{kj})\right) + U_{gg} = Q + U_{gg} \ . (5.3.8)$$

We have identified $\mu = \frac{m_a+m_g}{m_g m_a}$ with the reduced mass, being m_a the Na mass and m_g the Rg atom mass.

Therefore, the molecular dynamics simulations can be carried out with an effective potential (5.3.6)) which includes the classical pair-interaction potential, as well as a quantum correction, which we have also approximated to consider only the two-body terms. The quantum correction in equations (F.0.10) and (F.0.11) have the same form as the second order approximation to the Feynman-Hibbs potential [117], except for the pre-factor, which reflects the fact that it has been derived for an isolated system instead of one in thermal equilibrium. When solving the equations of motion, we must distinguish whether we are solving them for the impurity, for which the effective potential is given by equation Eq.(F.0.10) or for the Rg atoms (Eq. (F.0.11)). Finally, the equation of motion for the particles has the form

$$m_g\frac{d^2\mathbf{r}_i}{dt^2} = -\nabla_i U_{gg}^{eff} \ , \quad i = 1, .., N \ , \quad (5.3.9)$$

$$m_a\frac{d^2\mathbf{r}_0}{dt^2} = -\nabla_0 U_{ag}^{eff} \ , \quad (5.3.10)$$

with $V^{eff} = U_{ag}^{eff}$ if $i = 0$ or $V^{eff} = U_{gg}^{eff}$ for $i = 1, ..., N$.

The form for the trial functions u_{gg} and u_{ag} in equation (5.3.1) remains to be specified. For the selection of these functions, we must analyze the asymptotic behavior of the wave function for long and short inter-particle distances. Based on previous studies on Ar

clusters [115],[118], here we propose the following functional form

$$u(r) = b\log r + ar + \frac{a_4}{r^4} + \frac{a_9}{r^9} + \sum_p c_p \hat{r}^p \ , \tag{5.3.11}$$

where we have written generically $u(r)$, i.e., without explicit reference to the specific chemical elements involved, being r the pairs distance r_{ij} between any pair of atoms i, j and all the parameters entering in Eq. (5.3.11) are in atomic units. We will have two different sets of coefficients for the u_{gg} and u_{ag} functions, respectively.

The first two terms in Eq.(5.3.11) are included to ensure that the particles remain bound. The terms a_4/r^4 and a_9/r^9 account for short distance repulsion [118]. Finally, the terms $\sum_p c_p \hat{r}^p$ are included to describe the behavior of the system at intermediate distances, which is usually described in the form of polynomials. To avoid that higher order polynomials dominate the behavior of the test function $u(r)$ at infinity, we introduce a new variable $\hat{r}$ mapping the distance into a finite-range interval (which approaches a constant when $r \to \infty$) [118],

$$\hat{r} = w(1 - e^{(r_0 - r)/w}) \ . \tag{5.3.12}$$

In principle, r_0 and w are also variational parameters, however in practice, the quality of the wave function depends weakly on their values [115]. Hence, to simplify the minimization process we chose them constant and equal to unity.

Now the problem is to find the values of the coefficients which minimize the variational estimate of the ground state energy, which is given in terms of the local energy as:

$$E^* = \int \rho(\mathbf{r}_0, \mathbf{r}_1, ..., \mathbf{r}_N) E_L(\mathbf{r}_0, \mathbf{r}_1, ..., \mathbf{r}_N) d\mathbf{r}_0 \mathbf{r}_1 ... \mathbf{r}_N \ . \tag{5.3.13}$$

In Ref. [115], small clusters of noble gas atoms were studied, and the corresponding wave function parameters were evaluated by minimizing the local energy using the Variational Monte Carlo (VMC) method. However, for systems composed of many atoms, the minimization using VMC is extremely expensive, so here we use the Car-Parrinello

(CP) minimization strategy [119],[120], to find the coefficients which minimize the energy estimate E^*. Although, the Car-Parrinello method was initially conceived to perform molecular dynamics simulations based on first principles, it can be used in general to minimize any functional [121], as we show below.

Car-Parrinello minimization

Similar to the Car-Parinello (CP) strategy, we introduce an artificial kinetic energy term for each of the coefficients whose value we wish to find, and we write the CP Lagrangian for each set of coefficients,

$$L_g = \frac{m_g}{2}\sum_{i=1}^{N}\dot{\mathbf{r}}_i + \frac{\dot{a}_g M_{a_g}}{2} + \frac{\dot{b}_g M_{b_g}}{2} + \frac{\dot{a}_{4g} M_{a_{4g}}}{2} + \frac{\dot{a}_{9g} M_{a_{9g}}}{2} + \sum_p \frac{\dot{c}_{pg} M_{c_{pg}}}{2} + U_{gg}^{eff}, \quad (5.3.14)$$

$$L_a = \frac{m_a \dot{\mathbf{r}}_0}{2} + \frac{\dot{a}_s M_{a_s}}{2} + \frac{\dot{b}_s M_{b_s}}{2} + \frac{\dot{a}_{4s} M_{a_{4s}}}{2} + \frac{\dot{a}_{9s} M_{a_{9s}}}{2} + \sum_p \frac{\dot{c}_{ps} M_{c_{ps}}}{2} + U_{ag}^{eff} \ . \quad (5.3.15)$$

In equations (5.3.14) and (5.3.15), m_g and m_a denote the masses of the noble gas atoms and the Na, respectively. The first term in each of these equations accounts for the kinetic energy of the rare gas atoms and the Na respectively, while the last terms U_{gg}^{eff} and U_{ag}^{eff} are the effective potentials. The other terms are the artificial kinetic energy contributions corresponding to the coefficients.

The artificial masses of the coefficients are chosen to be orders of magnitude larger than the masses of the atoms, so the time evolution of the coefficients is slower than the real system dynamics. Here we have chosen the masses of the coefficients to be 10^4 times larger than the mass of the noble gas atoms or the sodium for the coefficients of the functions u_{gg} and u_{ag}, respectively.

The Euler-Lagrange equations of motion for each set of coefficients are given as,

$$M_{a_g}\frac{d^2a_g}{dt^2} = -\frac{\partial U_{gg}^{eff}}{\partial a_g} - M_{a_g}\eta\dot{a}_g \tag{5.3.16}$$

$$M_{b_g}\frac{d^2b_g}{dt^2} = -\frac{\partial U_{gg}^{eff}}{\partial b_g} - M_{b_g}\eta\dot{b}_g \tag{5.3.17}$$

$$M_{a_{4g}}\frac{d^2a_{4g}}{dt^2} = -\frac{\partial U_{gg}^{eff}}{\partial a_{4g}} - M_{a_{4g}}\eta\dot{a}_{4g} \tag{5.3.18}$$

$$M_{a_{9g}}\frac{d^2a_{9g}}{dt^2} = -\frac{\partial U_{gg}^{eff}}{\partial a_{9g}} - M_{a_{9g}}\eta\dot{a}_{9g} \tag{5.3.19}$$

$$M_{c_{pg}}\frac{d^2c_{pg}}{dt^2} = -\frac{\partial U_{gg}^{eff}}{\partial c_{pg}} - M_{c_{pg}}\eta\dot{c}_{pg} \quad p=(1,...,5)\ . \tag{5.3.20}$$

Furthermore, we have added an artificial viscosity term η to ensure the convergence [121]. The subindex g refers to the Rg-Rg interactions. A similar set of equations is obtained for the Na-Rg coefficients, starting from the Lagrangian in Eq.(5.3.15),

$$M_{a_s}\frac{d^2a_s}{dt^2} = -\frac{\partial U_{ag}^{eff}}{\partial a_s} - M_{a_s}\eta\dot{a}_s \tag{5.3.21}$$

$$M_{b_s}\frac{d^2b_s}{dt^2} = -\frac{\partial U_{ag}^{eff}}{\partial b_s} - M_{b_s}\eta\dot{b}_s \tag{5.3.22}$$

$$M_{a_{4s}}\frac{d^2a_{4s}}{dt^2} = -\frac{\partial U_{ag}^{eff}}{\partial a_{4s}} - M_{a_{4s}}\eta\dot{a}_{4s} \tag{5.3.23}$$

$$M_{a_{9s}}\frac{d^2a_{9s}}{dt^2} = -\frac{\partial U_{ag}^{eff}}{\partial a_{9s}} - M_{a_{9s}}\eta\dot{a}_{9s} \tag{5.3.24}$$

$$M_{c_{ps}}\frac{d^2c_{ps}}{dt^2} = -\frac{\partial U_{ag}^{eff}}{\partial c_{ps}} - M_{c_{ps}}\eta\dot{c}_{ps} \quad p=(1,...,5)\ . \tag{5.3.25}$$

In general, the minimization process is complex because, depending on the initial conditions the system can be trapped in local minima. Hence, it is necessary to make an initial estimate of the coefficients that allows to generate a set of initial conditions for them, such that the convergence to the global minimum of the system can be achieved.

The system of equations (5.3.16)-(5.3.20), together with the system (5.3.21)-(5.3.25), and the atomic equations of motion (5.3.9) and (5.3.10), are solved using the velocity Verlet

algorithm. We can summarize the minimization process as follows:

1. The initial positions and velocities of the atoms are set, as it is usually done in standard molecular dynamics simulations.

2. The initial values for the coefficients are generated, as well as the initial velocities, the latest are chosen within the same order of magnitude as those chosen for the atoms.

3. Hence, the system of equations (5.3.16)-(5.3.20), (5.3.21)-(5.3.25) are solved together with the equations of motion for the atoms Eq.(5.3.10) and Eq.(5.3.9), using the velocity Verlet algorithm.

4. At each time step the total energy of the system is calculated according to Eq.(5.3.6).

5. The system is allowed to evolve until the fluctuations in the energy are small. Here we considered that the energy has converged when its relative fluctuations were of the order of 10^{-2}.

6. Once the energy has converged, we have the final set of coefficients which are used in the molecular dynamics simulations with the effective potential given by Eq.(5.3.6).

In the Table 5.2, the final values obtained for the wave function coefficients after the Car-Parrinello minimization are listed. These parameters are used to calculate the ground state wave function given in Eq.(5.3.1) and the effective potential in Eq.(5.3.6), which will be used in the MD simulations.

In Figure 5.3 we show an example of the time evolution of the coefficients, in this case a_s (left panel) and b_s (right panel), obtained by solving equations (5.3.21) and (5.3.22), respectively.

The time evolution of the energy (Eq.(5.3.6)) calculated in the step 4 of the algorithm described above, is illustrated in Figure 5.4. It can be seen that after a few femtoseconds this magnitude does not seem to change significantly.

Table 5.2: Final set of values for the coefficients of the functions u_{gg} and u_{ag} (Eq. (5.3.1)) after the minimization of the variational energy with the Car-Parrinello scheme.

Kr-Kr	a.u.
a_g	-1.80
b_g	2.21
a_{4g}	3.368×10^3
a_{9g}	-1.979×10^6
c_{1g}	0.22
c_{2g}	0.22
c_{3g}	0.22
c_{4g}	0.22
c_{5g}	0.22

Na-Kr	a.u.
a_s	-1.78
b_s	2.22
a_{4s}	3.367×10^3
a_{9s}	-1.979×10^6
c_{1s}	0.23
c_{2s}	0.23
c_{3s}	0.23
c_{4s}	0.23
c_{5s}	0.23

Ar-Ar	a.u.
a_g	-0.82
b_g	3.20
a_{4g}	2.341×10^3
a_{9g}	-8.72×10^5
c_{1g}	1.20
c_{2g}	1.20
c_{3g}	1.20
c_{4g}	1.20
c_{5g}	1.20

Na-Ar	a.u.
a_s	-1.78
b_s	3.22
a_{4s}	2.350×10^3
a_{9s}	-8.72×10^5
c_{1s}	1.22
c_{2s}	1.22
c_{3s}	1.22
c_{4s}	1.22
c_{5s}	1.22

5.4 Results

In this section, we discuss the results of the classical molecular dynamics simulations with effective potentials. Simulations are initially run without the quantum potential but with the system equilibrated at the effective temperature (Eq. (5.2.7)) and, afterwards, adding the quantum potential. We analyze the effect of the quantum correction to the potential energy on the absorption spectra, as well as in the positions of the Na trapping sites in the matrix.

5.4.1 Molecular dynamic simulations of Na doped rare gas matrices with approximate quantum potentials

In the simulations we have employed a cubic cell composed by $N = 863$ atoms of rare gas (Ar or Kr), with a face centered cubic structure (fcc) and the Na atom placed on

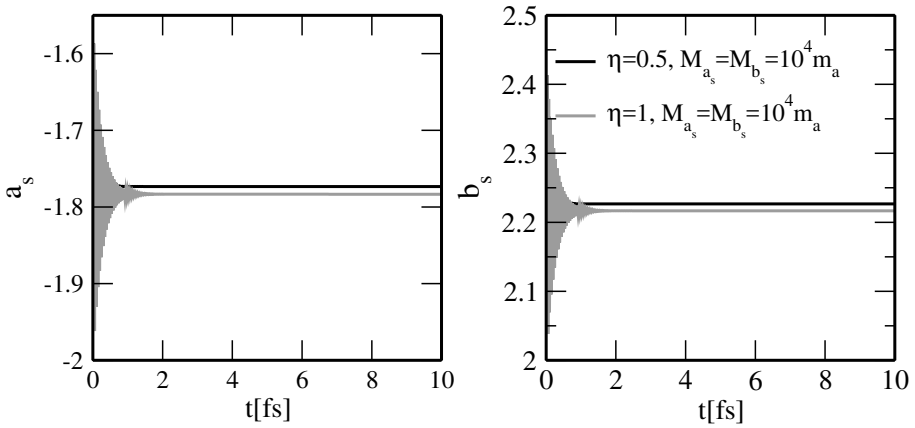

Figure 5.3 Time evolution of the parameters a_s (right panel) and b_s (left panel) obtained via the integration of the equations of motion (5.3.16) and (5.3.21), for two different values of the artificial viscosity η. The artificial masses are $M_{a_s} = 10^4 m_a$, $M_{b_s} = 10^4 m_a$.

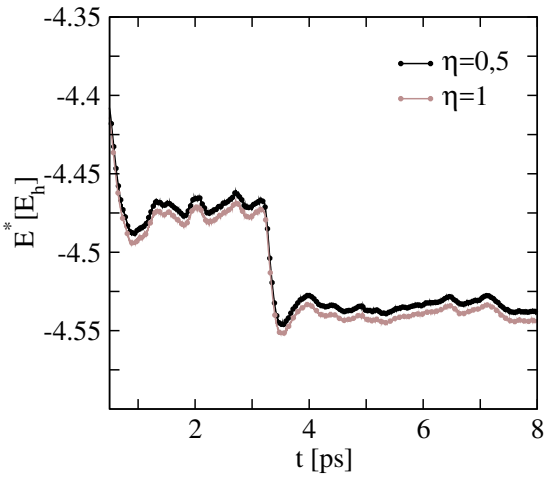

Figure 5.4: Time evolution of the average energy E^* (Eq.(5.3.6)) for two different values of the viscosity parameter η. The artificial masses of the coefficients are chosen to be 10^4 times larger than the mass of the noble gas atoms or the sodium for the coefficients of the functions u_{gg} and u_{ag}, respectively.

a substitutional site of the cell (single vacancy site, sv). We apply periodic boundary conditions to minimize the surface effects, and to simulate an infinite crystal. The initial velocities are generated randomly according to a Gaussian distribution, with variance chosen to match the desired temperature. The molecular dynamics simulations (without the quantum potential) are performed at the effective temperatures $T^* = 35K$ for the Kr matrix and $T^* = 45K$ for the Ar matrix. The values for the effective temperature of each system are calculated from Eq.(5.2.7), in order to simulate the amplitude of the zero-point motions at the physical temperature at which experiments are conducted ($T = 10K$) [109].

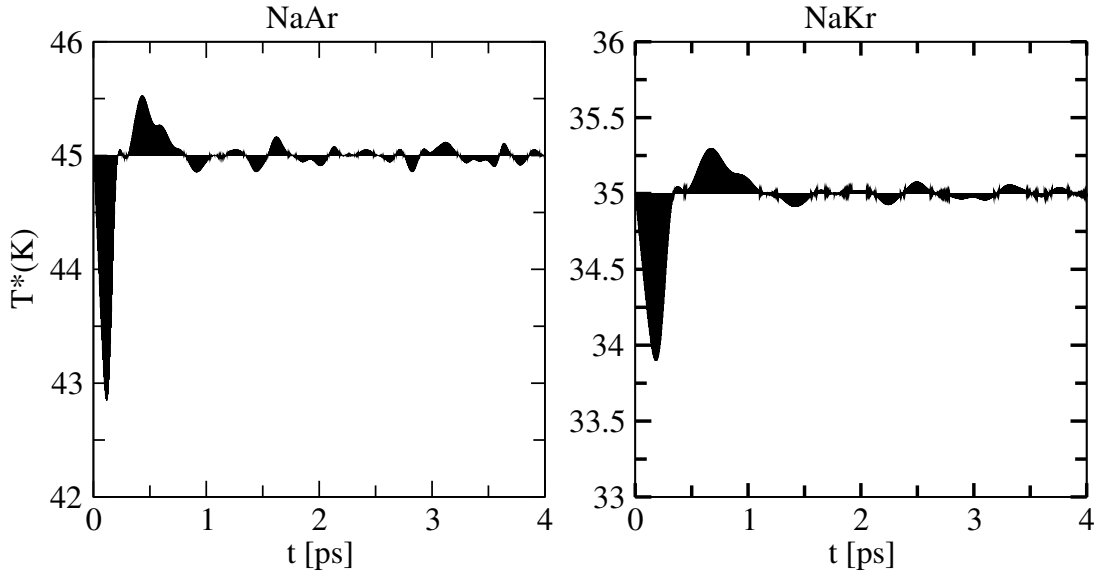

Figure 5.5: Time evolution of the effective temperature T^* (Eq. 5.2.7) along a MD simulation for both systems, in the left panel for the Ar matrix and in the right panel for the Kr matrix.

The time evolution of the effective temperature T^* given Eq.(5.2.7) during a MD simulation for both systems is shown in Figure 5.5. The molecular dynamics simulations including the quantum potential are performed at the physical temperature $T = 10K$. In this way, we compare two different approaches to incorporate the zero-point energy effects in the MD simulations: via the effective temperature and by adding an approximate form of the quantum potential. In all cases, the system is thermalized using the velocity rescaling scheme explained above (see Eq.(5.2.6) in section 5.2.1).

Radial distribution function (RDF)

In order to analyze how the presence of the impurity, located in a substitutional site of the matrix, affects the distribution of the Kr and Ar atoms in the solid, we compute the radial distribution function *G(r)* defined in Eq. (5.2.19). Two different kinds of radial distribution functions are calculated, one centered at a Rg atom and the other one centered at the Na atom. In Figure 5.6, we present the radial distribution functions for the ArAr (left panel) and the NaAr (right panel) pairs.

As we can see, adding the quantum contribution to the ground state interaction potential does not shift the relative distances between the argon atoms, compared to the results of

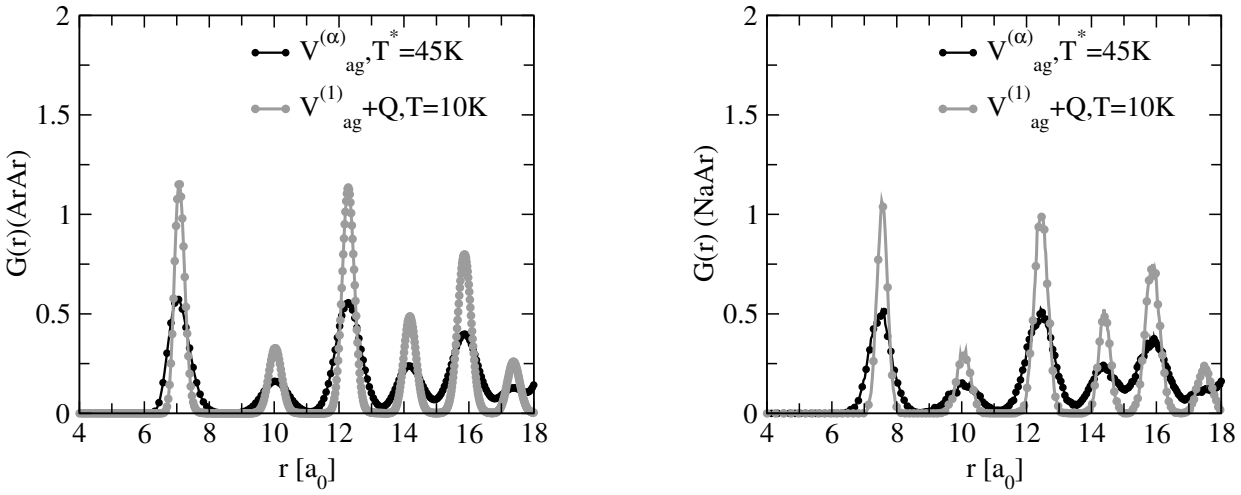

Figure 5.6 Radial distribution function $G(r)$ defined in Eq.(5.2.19) of the ArAr pairs (left panel) and of the NaAr (right panels) pairs. The comparison between the simulations with the interaction potential $V_{ag}^{(\alpha)}$ at the effective temperature $T^* = 45K$ and the simulations with the quantum potential added to the ground state potential $V_{ag}^{(1)} + Q$ at $T = 10K$ are shown.

the effective temperature MD simulations (the main peaks of the ArAr distribution are localized at positions corresponding to the relative separations of the atoms in the pure Ar solid). The peaks of the RDF calculated at the physical temperature $T = 10$ K (and including the quantum potential) are narrower with respect to the ones at the effective temperature.

This result shows the advantages of employing the quantum potential to simulate zero-point energy effects in rare gas solids, over the use of effective temperature of Eq. 5.2.7. Since the impurity perturbs the lattice only locally, the ArAr RDF computed for the doped matrix closely resembles that of the pure solid. The widths of the peaks in Figure 5.6 correspond to an amplitude of Ar atoms oscillations which accounts to 5% of the nearest neighbor distance in the crystal, in good agreement with experimental observations [61]. Likewise, the use of the effective temperature approach cause the overestimation of the oscillation amplitude of Ar atoms. In the right panel, the analysis of $G(r)$ (NaAr) shows that the inclusion of a Na atom cause a small displacement of the first nearest neighbors, ($Ar \approx 0.47\, a_0$), in order to accommodate the impurity, while the positions of the rest of the atoms do not change because of the substitution.

In Figure 5.7 a similar behaviour is observed for the Na doped Kr matrix.

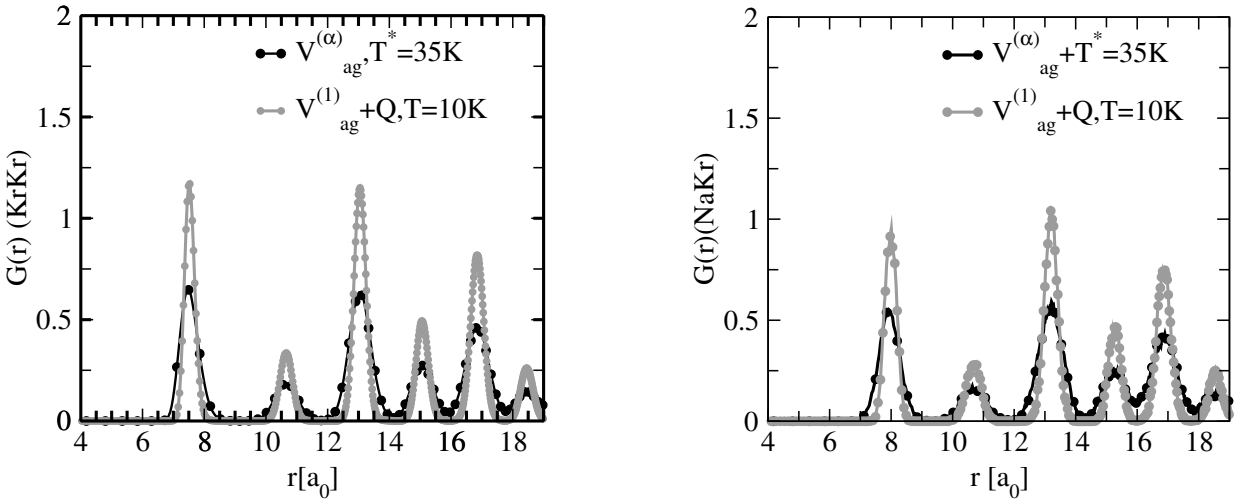

Figure 5.7 Radial distribution function $G(r)$ defined in Eq.(5.2.19) of the KrKr pairs (left panel) and of the NaKr pairs (right panel). The comparison between the simulations with the interaction potential $V_{ag}^{(\alpha)}$ at the effective temperature $T^* = 35K$ and the simulations with the quantum potential added to the ground state potential $V_{ag}^{(1)} + Q$ at $T = 10K$ are shown.

Simulation of the absorption spectra

To simulate the absorption spectra, the equations of motion are solved, first including only the classical potential and then adding the quantum potential to the ground state pair interaction potential Eq.(5.3.9) and Eq.(5.3.10). In both cases, the system evolves along a trajectory with the atoms in the ground electronic state. Once the system has reached the equilibrium, the energy differences $\Delta E^{(\beta)}$ between the ground and the excited electronic states (Eq.(5.2.17)) are computed at each time step, and at the end of the simulations the histogram of these energy differences is built. The energy resolution used to build the histograms we present here is $dE = 20cm^{-1}$ and in all of them we have plotted the superposition of the three energy differences. In the histograms we have used cm^{-1} as units of energy because these are the usual units in which the spectra are reported.

In Figure 5.8 we show the results for the three simulated spectra for both systems, NaKr on the left and NaAr on the right. With discontinuos vertical lines we represent the experimental values reported for the maxima of the triplet [61].

As it can be seen, the spectra obtained from the simulations with the classical interaction potential (shown in blue), captures the triplet structure of the experimental spectra, but

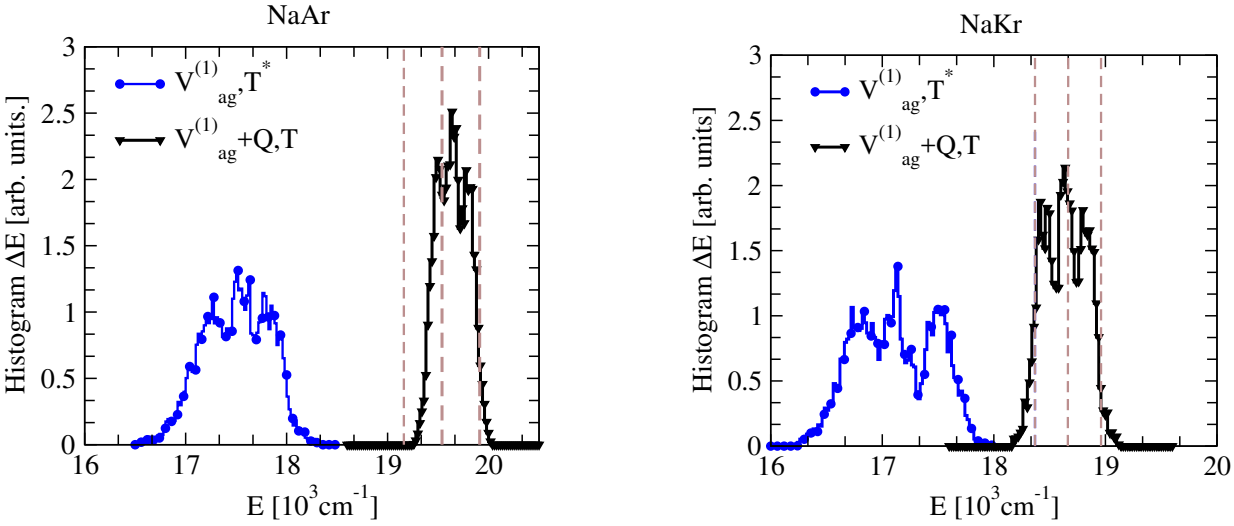

Figure 5.8: Simulated absorption spectra obtained as the histogram of the superposition of the energy differences $\Delta E^{(\beta)}$ between the ground and the excited electronic states for $\beta = 1, 2, 3$ (Eq.(5.2.17). In the left panel, the results for the NaAr matrix are shown and in the right panel we present the results for the NaKr matrix. In blue it is plotted the spectra obtained from the MD simulations with the interaction potential only, at the effective temperatures $T^* = 35K$ and $T^* = 45K$ calculated from Eq.(5.2.7) for the NaKr and the NaAr system, respectively. In black, the spectra from the MD simulations with the quantum potential and at the physical temperature T=10K is plotted. With discontinuos vertical lines we represent the experimental values reported for the maximum of the triplet [61].

is shifted to a lower energy region with respect to the experimental results. This red shift of the absorption spectra matches the behaviour observed by Ryan and coworkers [61] for the different trapping sites for the Na atom in rare gas matrices, the simulated spectra was located in the red part of the experimental profile. As we already mentioned, in order to improve the correspondence between the simulated and the experimental spectra, in their work they empirically modified the repulsive excited state potential (referred here as $V_{ag}^{(3)}$) to have a more repulsive potential.

Here, we show that adding an approximate expression for the quantum potential (obtained by minimizing the ground state energy) to the interaction potential shifts the simulated absorption band to the right energy region (for both Na doped Ar and Kr matrices). These results support the conclusion that the discrepancies between the effective temperature MD simulations and the experiment are a consequence of the inability of the effective temperature approach to mimic quantum effects in the vicinity of the impurity, rather than to a modification of the interaction potential due to matrix effects. The agreement

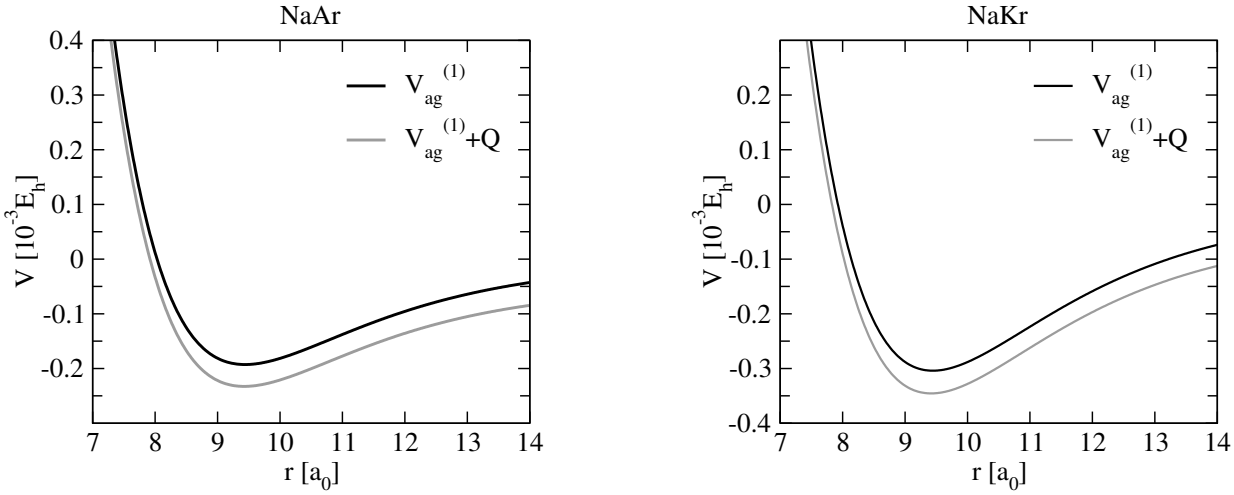

Figure 5.9 Comparison between the classical interaction potentials $V_{ag}^{(1)}$ (left) defined in Eq.(5.2.9) and V_{gg} (right) given in Eq.(5.2.8) with the effective potentials U_{ag}^{eff} Eq.(F.0.10) and U_{gg}^{eff} Eq.(F.0.11).

between our simulated spectra and the experimental ones is only qualitative, because of the approximations introduced, mainly in the perturbative evaluation of the energies of the electronic excited states and the constrains imposed to the functions $u(r)$.

In Figure 5.9 we show the classical pairwise interaction potential $V_{ag}^{(1)}$ (Eq.(5.2.9)) and the effective potential obtained as a result of adding the quantum potential. As we can see, by adding the quantum correction the resulting potential gets slightly more attractive around the minimum zone of the well and beyond the equilibrium distance of the alkali-rare gas interaction. This energy shift can explain why the absorption band move towards a higher energy region when the quantum correction is added. This effect is reproduced in Ref. [61] by artificially increasing the B-state potential.

Simulated emission

As we described in the previos section, the emission spectra can be simulated from an equilibrium configuration in the excited state. The simulations are run on the lower energy excited state. A strong rearrangement of the matrix in the neighborhood of the Na atom is observed upon photoexcitation. When evolving the trajectories in the excited energy surface, the Na atom, which is initially in the sv site (with twelve nearest neighbors), moves closer to four of them.

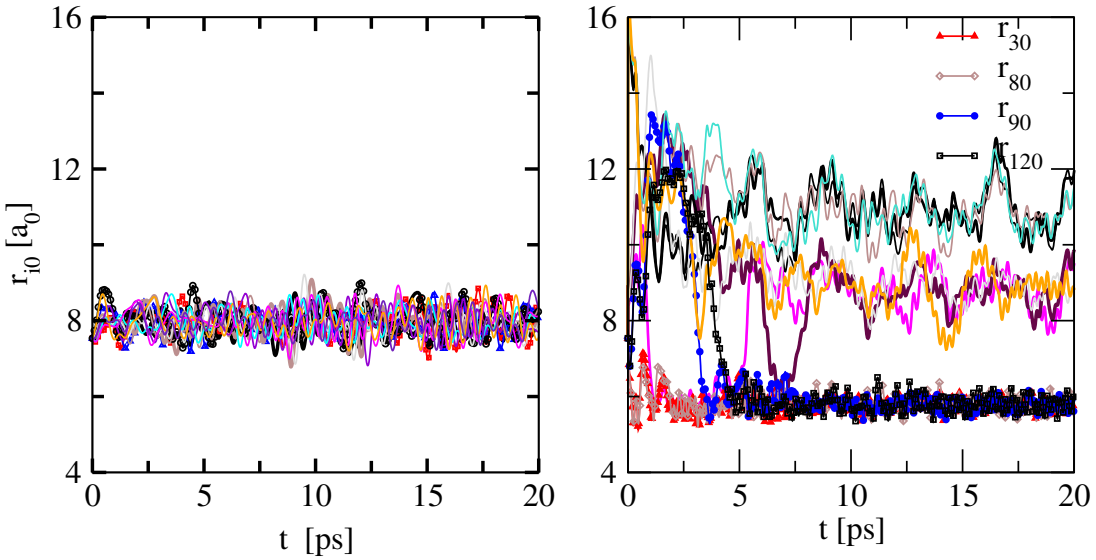

Figure 5.10: Pair distances (r_{i0}) between the Na atom and its nearest neighbors in the lattice. In the left panel, we show the results for the MD simulations with the system evolving in the ground state potential energy surface. In the right panel are plotted the results of the MD simulations with the system evolving in the lower energy excited state. As we can see, in the excited state the Na atom has four well defined nearest neighbors.

We can see this motion in Figure 5.10, where we have plotted the time evolution of the pair distances r_{i0} between the Na atom and its initially twelve nearest neighbors (specifically we have plotted the results for the NaKr matrix). In the left panel, we show the results for the Na atom evolving on the ground state energy surface. Initially the Na atom is placed in the matrix in a sv site and its distance to the nearest neighbors is around $7.56\,a_0$. As the system evolves, the expansion of the matrix occurs, and at equilibrium, the Na is still in a sv site with twelve nearest neighbors. The only effect is hat the matrix has expanded to accommodate the guest atom. Oscillations around the equilibrium configuration are observed for the twelve nearest neighbors pair distances. However, when the MD simulations are performed on the lower energy excited state, the Na atom moves closer to four of the initially nearest Kr atoms, as it is shown in the right panel of Figure 5.10.

Furthermore, in the left panel of Figure 5.11, the z-coordinate of the Na atom and of the four Kr atoms already identified as the ones the Na gets closer, are plotted. In the right panel, the time evolution in the x and y coordinates is shown. From these plots we can see that the Na atom approaches the Kr atoms by moving in the z direction. This can also

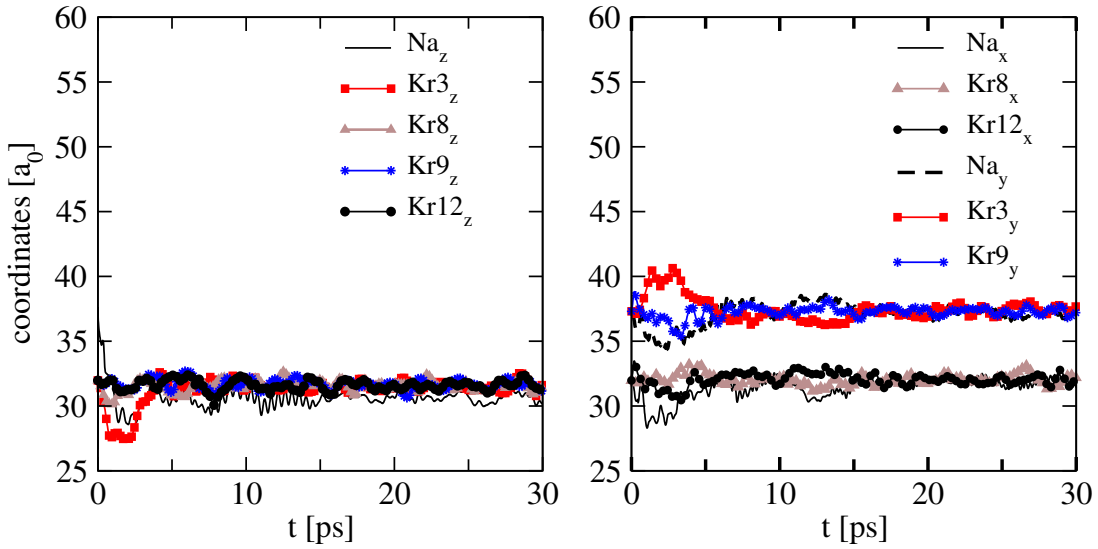

Figure 5.11: Time evolution of the z-coordinates of the Na atom and its four nearest neighbors in the excited state (left panel) and in the right panel the time evolution of the x-coordinate and the y-coordinate of two of these four nearest neighbors.

be seen in the snapshots of Figure 5.12, where the initial positions of the Na atom and its twelve nearest neighbors at the initial configuration (sv) are shown on the left panel. The snapshot of the atoms distribution at the final state is shown in the right panel, we can see how the Na atom has moved towards the upper plane.

Finally, we can calculate the radial distribution function $G(r)$ of the excited system and compare it with the one for the ground state for both matrices. The results for $G(r)$ are plotted in Figure 5.13 for the NaAr pairs on the left and for the NaKr pairs on the right.

As we described in the Appendix E, for the MD simulations we used a modified excited state potential (Eq. (E.0.4)).

Hence, as the first term in Eq. (E.0.4) is the one which depends on the pair distances, we added the quantum potential to this part of the excited state potential to simulate the dynamics of the photoexcited system.

As we can see, for all the calculated RDF, a first peak around $5.66\,a_0$ is obtained in the excited state for both solids. This is in agreement with the results plotted in the right panel of Figure 5.10. There, we can appreciate that the equilibrium distance between the

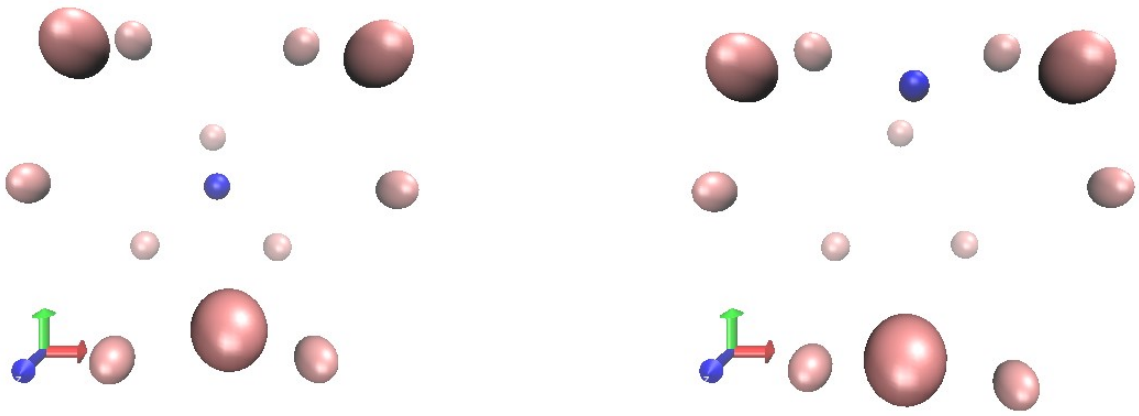

Figure 5.12 Snapshot of the positions of the Na atom and its twelve nearest neighbors (Kr atoms). The initial configuration with the Na in sv site is shown in the left panel. The atoms positions at the end of the time evolution is shown in the right panel. We can see how the Na atom has moved towards the positive z direction.

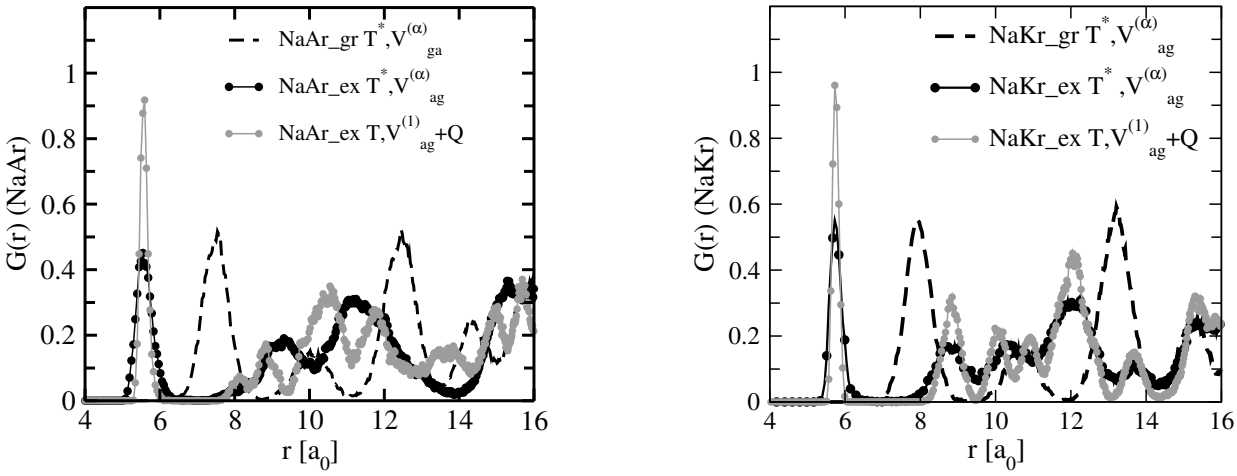

Figure 5.13 Left panel(Right panel): NaAr(NaKr) radial distribution function of the Na doped Ar(Kr) matrix in the equilibrated excited state, for effective temperature and potential variants of the algorithm, compared with the function $G(r)$ around the Na atom in the ground state .

Na and the closest Kr atoms in the excited state is around $5.66\,a_0$. We can see how in the excited state, the Na atom moves to a smaller space with respect to the ground state position. The influence of the quantum correction into the system structure and dynamics in the excited state was found to be minor. This can be attributed to the fact that the four Rg atoms which get closer to the impurity end up in a highly excited vibrational state in the deep well of the A-state potential, while the rest of the matrix atoms are located at longer distances from the alkali atom, where the role of the impurity-rare gas

interactions is less relevant.

As for the emission spectra, the simulated emission bands are obtained at negative energies. This counter-intuitive result is consistent with those reported by other research groups [93]. It points to the inadequacy of the perturbation theory scheme employed to evaluate the interaction energies at the equilibrium configurations in the excited electronic states. Since the atoms are closer, the total energy can not be evaluated from atomic energies using first order perturbation theory.

Let us notice that for the structure of the matrix we have chosen, with the Na atom placed in a sv site, we have obtained the absorption band on the "violet" site. This result is in agreement with previous works [61], [103], that have identified the sv trapping site with the violet absorption band. On the other hand, among the experimental results available, no emission has been reported for this absorption band, at least within the energy range explored (above 12500 cm^{-1} [61]). Our results are in agreement with this, however, as in the excited state the atom explores the repulsive part of the potential, which is the less well represented, further theoretical and experimental studies need to be performed in order to have final conclusions on this subject.

5.5 Conclusions

In this chapter, we have proposed a methodology to simulate structural changes and the absorption spectra of doped rare gas matrices, based on the inclusion of quantum corrections into molecular dynamics simulations. The scheme is based on proposing a specific functional form for the ground state wave function, and deriving from it an approximate quantum potential, which is afterwards included as an additional potential into the molecular dynamic simulations.

As a model system to test our methodology, we have chosen Ar and Kr matrices with a Na impurity located at the substitutional site of the matrix. The parametrization of the wave function have been chosen to reproduce basic properties of rare gas systems. The Car-Parrinello minimization scheme have been used to minimize the variational estimate

of the ground state energy of the doped matrix, and to obtain the parameters to model the ground state wave function and therefore the quantum potential.

Then, we carried out molecular dynamic simulations with an effective potential, comprising both the interaction potential and the approximate quantum potential. We simulated the absorption spectra of atomic Na embebed in the Ar and Kr matrices by performing molecular dynamics simulations with and without the quantum potential. The comparison between the two simulated spectra clearly shows how, by adding the quantum potential, a better agreement between the theoretical and the experimental results is obtained. Our calculations were restricted to the case where the Na atom was located at a single vacancy site. For this particular structure, the experimental studies reveal that the absorption spectra is located at the violet region of the energy spectra, and no emission band has been reported, at least in the energy range explored by the experiments. The present knowledge of the energies of the first excited electronic states in the solid is not accurate enough, which prevent us to provide additional insight around this point. Furthermore, we also studied the structural modifications of the system and we found that the quantum correction to the potential energy improves the description of the vibrational amplitudes of Ar atoms in the matrix.

The presented scheme can be applied to similar many-body systems where quantum effects are relevant, and pure classical molecular dynamics methods fail to accurately model the system. Furthermore, even though we have not studied the photoinduced dynamics, by modeling the quantum potential we are taking the first step in order to study the dynamics of the structural modification of the system upon photoexcitation of the alkali atom, using approximate quantum potentials.

GENERAL CONCLUSIONS

6 GENERAL CONCLUSIONS

The main topic of this work, essentially methodological, is to develop trajectory-based numerical alternatives to model quantum phenomena. We have shown that a fully quantum-mechanical method, wave function-free (i.e., grid and basis-set free), based entirely on trajectories, is possible and it has been implemented and tested along the thesis. The methodology is applied to a variety of one dimensional model systems, and the scheme is found to reproduce quantum phenomena such as the zero point energy in harmonic and anharmonic potentials, as well as tunneling/transmission probabilities for different barrier shapes. The expression for the resulting quantum potential contains both attractive and repulsive parts. While yielding the same expression for the quantum force as in Ref. [43], it is only using the full quantum potential that correlations functions and energy spectra can be calculated, by integrating the Lagrangian along the trajectories.

Furthermore, the same methodology is applied to another kind of problems, using time-dependent potentials (in particular to study the laser-driven electron dynamics). It is not only capable of reproducing quantitatively the total ionization yields, but also CEP effects such as left/right asymmetries in the ionization as a function of the carrier envelope phase. For all the examples shown here, a moderate number of trajectories was necessary to accurately compute the observables, this also shows the potential of the method regarding its generalization to higher dimensions.

In addition to the interacting trajectory approach, we have proposed a method to propagate quantum trajectories by expanding the hydrodynamic fields in Chebyshev polynomials.

Moreover, we have derived an approximate quantum potential for a many-body system. We have used this quantum potential to build an effective potential to the molecular dynamics simulations. Within this method, we have studied the absorption bands of

atomic sodium isolated in a rare gas matrix. In particular we have studied two systems, an Argon and a Krypton matrix with the Sodium atom located in a substitutional site of the matrix. By adding the quantum potential to the MD simulations, a better agreement with the experimental results have been obtained. In particular, the absorption spectra of atomic sodium in the matrix have been qualitatively reproduced. This opens the possibility of applying the same methodology to study other many-body systems.

7 RECOMMENDATIONS

- Possible extension to higher dimensions should in principle be possible, and presents an interesting aspect for future developments. The challenge is to develop a parametrisation of the quantum density which allows to rapidly identify neighbouring trajectories as they evolve in time.

- The use of trajectories for quantum dynamics naturally opens the way to mix quantum and classical dynamics. In particular, different regions in configuration space can be defined to be treated either by quantum mechanics or by classical mechanics, and a smooth transition from a quantum region to a classical one can be achieved by simply neglecting the quantum force in the latter. For example, scattering problems with significantly different short and long range potentials, or large amplitude motion as encountered in laser driven electron dynamics, are situations where such an approach can be promising.

- As far as the results presented in chapter five are concerned, it will be interesting to apply the presented methodology to other many body systems exhibiting quantum effects. In particular, the wide field of matrix isolation spectroscopy with a large range of chromophores could be modelled based on the quantum corrections presented in this work.

RESUMÉ EN FRANÇAIS

8 RÉSUMÉ EN FRANÇAIS

Chapitre1: Introduction

La modélisation de la dynamique de systèmes complexes quantiques comprenant un grand nombre de degrés de liberté et impliquant des effets anharmoniques, présente un grand défi en physique contemporaine. Le développement de méthodes de spectroscopie résolue en temps a permis de réaliser un grand nombre d'études expérimentales et théoriques de processus dynamiques à l'échelle atomique et moléculaire. Dans ce contexte, des phénomènes quantiques comme la délocalisation, les interférences, l'effet tunnel ou la discrétisation des énergies vibrationnelles, sont au coeur des modélisations de la structure et de la dynamique des systèmes moléculaires. Malgré le succès de méthodes sophistiquées de dynamique quantique et des ressources informatiques de plus en plus performantes, il n'est en général pas possible de décrire la dynamique quantique de systèmes comportant plus que quelques degrés de liberté. La complexité réside non seulement dans le nombre de particules impliquées, mais aussi dans la diversité des interactions mises en jeu ainsi que dans la réponse à l'excitation par des sources lumineuses externes. Par conséquent, le développement de nouvelles méthodes est un domaine de recherche de grande actualité, avec des implications bien au delà de la physique moléculaire.

Le travail présenté est consacré au développement, à l'implémentation et au test de nouvelles méthodes de dynamique quantique, qui ont pour spécificité d'être basées entièrement sur des trajectoires. En effet, un ensemble de trajectoires est capable de décrire des phénomènes quantiques, à condition de rajouter un potentiel supplémentaire, appelé potentiel quantique. Dans ce travail de thèse, plusieurs approches pour effectuer des modélisations quantiques sont présentées, basées sur des trajectoires et sans calcul explicite de la fonction d'onde. La première consiste à utiliser des polynômes de Tchebycheff pour décrire la densité quantique, ce qui permet de construire de façon efficace le potentiel

quantique, et ainsi simuler une dynamique quantique. Une deuxième méthode, alternative à la première, est basée sur la représentation de la densité quantique par un ensemble de pseudo-particules, soumises à des interactions construites de telle sorte que leur évolution temporelle reproduise une dynamique quantique. Il est montré qu'une telle méthode est en effet capable de décrire correctement des effets quantiques, tel que l'effet tunnel, l'énergie de point zéro et des niveaux discrets d'énergie d'une vibration moléculaire. Cette méthodologie est aussi utilisée pour étudier la dynamique d'un électron lors de l'ionisation avec des champs laser intenses et ultrabrefs. En généralisant cette idée à des systèmes à haute dimensionnalité, une troisième approche est proposée, pour décrire la spectroscopie d'atomes d'alcalins incrustés dans des matrices de gaz rares cryogéniques. L'importance d'inclure des effets quantiques est mise en évidence par un meilleur accord avec des données expérimentales, montrant ainsi l'utilité de la nouvelle méthodologie pour la description des effets quantiques dans des systèmes étendus. En résumé, le travail présente différentes nouvelles méthodes basées entièrement sur la propagation de trajectoires, leur implémentation et test numérique pour la modélisation de la dynamique quantique.

L'idee de base d'utiliser des trajectoires pour décrire la dynamique quantique a été developpée par David Bohm de la manière suivante: en commencent de la description hydrodynamique de la mécanique quantique, il est possible de définir un champs de vitesses, et ainsi des trajectoires associées à ce champs de vitesses. En suivant ce développement, on est naturellement mené à une équation de Newton, mais avec un potentiel supplémentaire, appelé potentiel quantique. Ce potentiel supplémentaire n'a pas d'équivalent classique, et est entièrement responsable d'induire toutes les effets quantiques de la dynamique. Ce potentiel dépend de la forme de la densité quantique, et son evaluation numérique pose d'énormes problèmes. C'était seulement en 1999 par les travaux de B. Wyatt qu'une approche numérique a été proposée (appelée 'Quantum trajectory method, QTM). Dans cette méthode, la densité quantique requise pour l'évaluation du potentiel quantique est déduit de l'ensemble des trajectoires par des méthodes d'interpolation non-equidistantes.

Les trajectoires peuvent être considérées comme éléments du fluide de probabilité quantique. Malgré la clarté du concept d'exprimer l'équation de Schrödinger par des équations hydrodynamiques, leur implémentation numérique reste un grand défi. La raison principale est que pour l'utilisation de cette approche, il faut évaluer la densité et sa dérivé jusqu'à l'ordre trois a partir des schéma d'interpolations. Ceci demande une très grande précision, y compris dans des régions de faible densité. En particulier, des noeuds de la fonction d'onde présentent un problème, car dans leur proximité la densité de trajectoires est très faible, ce qui rend des schémas d'interpolation précise très difficile. Dans ce contexte, plusieurs méthodes numériques ont été proposées pour contourner ce problème, nommé le 'node problem'. Notamment, citons l'interpolation par polynômes d'ordre élevé [18], la propagation simultanée des dérivées [19,20] ou l'utilisation de grilles adaptives. Une autre approche est basé sur l'utilisation d'une décomposition en fonctions d'ondes propageant dans des sens opposés pour décrire des structures d'interférences quantiques. En outre, des trajectoires dans le plan complexe ont été proposées par Koch et Tannor, et appliqués à des problèmes de dissociation moléculaire. Une autre approche consiste à utiliser une approximation semiclassique pour modéliser le potentiel quantique et ses dérivées. Toutes ces approches ont comme point commun d'obtenir une expression de la densité a partir de l'ensemble des trajectoires. Une alternative prometteur a été proposée très récemment par Poirier et al, qui proposent une méthode de propagation de trajectoires quantiques sans interpolation, mais d'inclure les effets quantiques en considérant des potentiels supplémentaires entre les trajectoires. Cet approche consiste donc a propager des trajectoires quantiques, sans faire référence à la fonction d'onde quantique.

L'objective scientifique est de développer, implémenter et appliquer de tes méthodes pour les études de processus dynamiques quantiques, pour évaluer leur potentiel futur dans des simulations à plus grandes échelles.

Le thèse comporte six chapitres, et est structurée de la manière suivante : En chapitre deux, les concepts principales de la formulation hydrodynamique est développée, et les bases de la méthode QTM sont présentées.

En chapitre trois, une nouvelle méthode est présentée, qui consiste à utiliser des polynômes de Chebycheff pour exprimer la densité quantique, pour ainsi pouvoir évaluer numériquement le potentiel quantique et ses dérivées à une très haute précision.

En chapitre quatre, une méthode alternative est développée. Cette méthode est basée sur l'ansatz présenté par Hall et al, et consiste à exprimer la densité d'une façon discrétisée. Ceci mène à une forme du potentiel quantique et les forces associées qui permettent leur prise en compte par un potentiel d'interaction entre les trajectoires. Dans une première partie, cette approche est développée et testée dans des systèmes quantiques modèles, pour étudier sa capacité de décrire correctement des effets quantiques comme l'effet tunnel ou des interférences. Dans une deuxième partie, cette méthodologie est étendu pour inclure des champs laser externes, et appliquée pour des études de l'ionisation ultrarapide de l atome d'hydrogène avec des impulsions ultrabrèves, comprenant seulement quelques oscillations optiques.

En chapitre cinq, une troisième approche est présentée, qui permet d'inclure des effets quantiques dans des systèmes a très haute dimensionnalité. Cette approche est basée sur un ansatz particulier de la densité quantique multidimensionnelle, permettant ainsi d'inclure des effets quantiques dans des simulations de dynamique moléculaire. Cette méthode est appliquée à la spectroscopie de chromophores incrustés dans des matrices cryogéniques. Ces systèmes ont été choisis à cause des données expérimentaux disponibles, qui ne sont pas reproduit d'une façon satisfaisante par des simulations classiques à cause des effets quantiques présents. Ces systèmes forment donc des exemples idéaux pour évaluer la nouvelle méthodologie développée.

Chapitre six comprend une conclusion avec des perspectives du travail présenté.

Comme résultat principal de la thèse, il est montré que de telles méthodes sont capables de décrire des effets quantiques comme l'énergie de point zéro, la discrétisation de l'énergie ou l'effet tunnel. Ainsi, elles présentent des alternatives prometteuses aux méthodes standard, avec comme perspective d'être avantageuses pour la modélisation de systèmes

à haute dimensionnalité.

Chapitre 2: La théorie des trajectoires quantiques

Dans ce chapitre, nous montrons comment définir les nouveaux champs dans lesquels les trajectoires quantiques évoluent directement à partir de la fonction onde [62]. Le résultat principal est que les équations de mouvement déterminant l'évolution temporelle de ces champs sont complètement équivalentes à l'équation de Schrödinger.

Équations de champ hydrodynamiques

Reformulation de l'équation de Schrödinger

Dans cette section, nous suivons la dérivation de Madelung des équations hydrodynamiques. Puisque nous introduisons un type particulier de trajectoires, qui nécessitent des positions dépendantes du temps, on peut en déduire qu'il s'agit d'une théorie dépendant du temps. Ainsi, cette partie est consacrée à réécrire l'équation Schrödinger et à introduire les équations de mouvement des nouveaux champs.

Le point de départ est l'équation de Schrödinger (ESDT) pour une particule de masse m qui évolue dans le potentiel externe $V(\mathbf{x},t)$, $\mathbf{x}$ représente les coordonnées cartésiennes et t, le temps,

$$i\hbar\frac{\partial}{\partial t}\Psi(\mathbf{x},t) = -\frac{\hbar^2}{2m}\nabla^2\Psi(\mathbf{x},t) + V(\mathbf{x},t)\Psi(\mathbf{x},t)\ . \tag{8.0.1}$$

La fonction d'onde peut être écrite sous sa forme polaire [9, 62]

$$\Psi(\mathbf{x},t) = R(\mathbf{x},t)e^{iS(\mathbf{x},t)/\hbar}\ , \tag{8.0.2}$$

$R(\mathbf{x},t)$ est l'amplitude et $S(\mathbf{x},t)$ est la phase, à la fois réelle et dépendante de la position et du temps. On peut donc écrire:

$$R(\mathbf{x},t) = (\Psi(\mathbf{x},t)^*\Psi(\mathbf{x},t))^{1/2} > 0\ , \quad S(\mathbf{x},t) = \hbar/2i\ln(\Psi(\mathbf{x},t)/\Psi(\mathbf{x},t)^*)\ . \tag{8.0.3}$$

Notons que la forme polaire de la fonction d'onde Ψ n'est pas utile aux points où $\Psi = 0$, car S n'est pas bien défini comme on peut le voir de Eq. (8.0.3). Pour l'instant, il est

important de garder à l'esprit que les définitions et équations à venir ne sont valables que dans les régions où la fonction d'onde Ψ est différente de zéro.

Dans les dérivations montrées ci-dessous, nous omettons les variables $\mathbf{x}$ et t sauf s'il est nécessaire de les spécifier. Remplacer la fonction d'onde par la fonction *ansatz* (Eq. 8.0.2) dans l'ESDT (Eq. 8.0.1), séparant la partie réelle et la partie imaginaire, on obtient pour la partie réelle

$$-\frac{\partial S}{\partial t} = \frac{(\nabla S)^2}{2m} + V - \frac{\hbar^2}{2m}\frac{\nabla^2 R}{R} \ , \tag{8.0.4}$$

et pour la partie imaginaire,

$$\frac{\partial R^2}{\partial t} + \nabla \cdot \left(R^2 \frac{\nabla S}{m} \right) = 0 \ . \tag{8.0.5}$$

Eq. (8.0.4) a la forme d'une équation de Hamilton-Jacobi (HJ) classique avec un potentiel supplémentaire qui est appelé *potentiel quantique* Q [62]:

$$Q = -\frac{\hbar^2}{2m}\frac{\nabla^2 R}{R} = -\frac{\hbar^2}{2m}\frac{\nabla^2 |\Psi|}{|\Psi|} \ , \tag{8.0.6}$$

ou, écrit en termes de la densité $\rho(\mathbf{x}, t) = R^2(\mathbf{x}, t)$

$$Q = -\frac{\hbar^2}{4m}\left(\frac{\nabla^2 \rho}{\rho} - \frac{1}{2}\left(\frac{\nabla \rho}{\rho} \right)^2 \right) \ . \tag{8.0.7}$$

C'est précisément la présence du potentiel quantique Q qui détermine la différence entre les trajectoires classiques et quantiques. Le potentiel quantique est non local, c-à-d. le potentiel à un point de l'espace donné dépend non seulement de la valeur de l'amplitude à ce point particulier de l'espace, mais aussi de l'amplitude aux points voisins. Par analogie avec la mécanique classique, en mécanique quantique, on peut définir un champ $\mathbf{p}$ déterminé par ∇S. En divisant ce dernier par la masse m, nous pouvons définir le champ de vitesse $\mathbf{v} = \mathbf{p}/m$.

Une fois que nous aurons défini le champ de vitesse, $\mathbf{v}$, on peut exprimer son évolution

temporelle en prenant le gradient dans l'équation (8.0.4). De plus, en entrant le champ de vitesse dans l'équation (8.0.5) et la densité ρ on l'obtient,

$$\frac{\partial \mathbf{v}}{\partial t} + (\mathbf{v}\cdot\nabla)\mathbf{v} = -\frac{1}{m}\nabla(V+Q)\ , \tag{8.0.8}$$

$$\frac{\partial \rho}{\partial t} + \nabla\cdot(\rho\mathbf{v}) = 0\ . \tag{8.0.9}$$

Équations (8.0.8) et (8.0.9) représentent la formulation hydrodynamique de la mécanique quantique.

Notons également que les équations (8.0.8) et (8.0.9) sont équivalentes à des équations (8.0.4) et (8.0.5) et par conséquent, ils sont équivalents à l'équation de Schrödinger. La dérivation ci-dessus a un lien avec la formulation standard de la mécanique quantique, où la densité de probabilité actuelle $\mathbf{j}$ est définie comme suit [64],

$$\frac{\mathbf{j}}{|\Psi|^2} = \frac{\hbar}{m}\mathbf{Im}\left(\frac{\nabla\Psi}{\Psi}\right) = \frac{\nabla S}{m} = \mathbf{v}\ . \tag{8.0.10}$$

L'équation (8.0.9) exprime la conservation de la densité de probabilité avec $\mathbf{j} = \rho\mathbf{v}$. Ensuite, pour reproduire les résultats de la mécanique quantique standard, nous avons besoin qu'à tout moment t, R représente correctement le module de la fonction d'onde $|\Psi|$ et le champ de vitesse est déterminé par Eq. (8.0.10), ce qui est directement réalisé grâce à la façon dont cette théorie est construite.

Trajectoires quantiques

Jusqu'à présent, nous avons défini le champ de vitesse qui détermine l'évolution temporelle de la densité de probabilité du fluide. L'existence de trajectoires est un postulat, qui s'ajoute à ceux habituellement admis [62]:

1. un système physique est composé d'une fonction d'onde se propageant dans l'espace et dans le temps avec une particule ponctuelle qui se propage guidée par la fonction d'onde.

2. la fonction d'onde Ψ est la solution de l'équation de Schrödinger

3. l'évolution temporelle de la particule est obtenue comme la solution $\mathbf{x}(t)$ de l'équation

$$\dot{\mathbf{x}} := \left.\frac{\nabla S(\mathbf{x},t)}{m}\right|_{\mathbf{x}=\mathbf{x}(t)}, \tag{8.0.11}$$

là où S est la phase de Ψ donnée par Eq.(8.0.3).

Pour résoudre l'équation (8.0.11), il est nécessaire de donner une condition initiale $\mathbf{x}(0) = \mathbf{x}_0$. Une fois cette condition fixée, toutes les autres quantités sont déterminées de manière univoque par $\Psi(t=0)$. C'est précisément l'évolution temporelle de cette particule, régie par l'équation (8.0.11) et les conditions initiales $\mathbf{x}(0)$ et $\Psi(t=0)$ ce qui détermine une *trajectoire quantique*. L'ensemble des mouvements possibles associés à la fonction d'onde Ψ, est obtenu en générant un ensemble de conditions initiales $\mathbf{x}(0)$, comme nous le montrerons dans la section suivante.

Pour garantir la compatibilité entre le mouvement de l'ensemble et les résultats de la mécanique quantique, un autre postulat est nécessaire, qui dit que:

4. la probabilité de trouver une particule de l'ensemble dans l'intervalle $\mathbf{x}$ et $\mathbf{x} + d\mathbf{x}$ est donnée par $R^2(\mathbf{x},t)d^3x$, avec $R^2 = |\psi|^2$.

Ensembles de trajectoires quantiques

Pour obtenir la valeur de toute observable en représentation de position, il faut faire la moyenne sur toutes les positions possibles. Cela se traduit habituellement par un calcul de la moyenne sur la fonction d'onde qui représente la probabilité de trouver une particule dans une certaine région de l'espace. Cette probabilité peut également être représentée par l'ensemble des trajectoires quantiques, qui est unique, une fois que la fonction d'onde initiale Ψ_0 est donnée.

Supposons que nous avons un ensemble de trajectoires, définies uniquement par la fonction d'onde initiale. La valeur moyenne d'un opérateur $\hat{O}$ correspondant à un état normalisé

$|\Psi\rangle$ s'exprime par:

$$<\hat{O}>=\langle\Psi|\hat{O}|\Psi\rangle=\int\Psi^{*}\hat{O}\Psi d^{3}x. \tag{8.0.12}$$

En évaluant les valeurs moyennes correspondantes de la position, de la dynamique et de l'énergie [62], on obtient

$$\langle\hat{\mathbf{x}}\rangle=\int\Psi^{*}\mathbf{x}\Psi d^{3}x=\int Re^{-iS}\mathbf{x}Re^{iS}d^{3}x=\int R^{2}\mathbf{x}d^{3}x=\langle x\rangle\ , \tag{8.0.13}$$

$$\langle\hat{\mathbf{p}}\rangle=\int\Psi^{*}(-i\hbar\nabla)\Psi d^{3}x=\int R^{2}\nabla Sd^{3}x=\langle p\rangle\ , \tag{8.0.14}$$

$$\langle\hat{\mathbf{H}}\rangle=\int\Psi^{*}[(-\hbar^{2}/2m)\nabla^{2}+V]\Psi= \tag{8.0.15}$$

$$\int R^{2}[(\nabla S)^{2}/2m+V+Q]d^{3}x=\langle E\rangle\ . \tag{8.0.16}$$

On peut donc, à partir de l'ensemble de trajectoires quantiques, reproduire les résultats de la mécanique quantique, car les valeurs moyennes calculées avec l'ensemble de trajectoires coïncident avec celles obtenues avec la fonction onde. Cette égalité vient du fait que la distribution initiale des trajectoires et leurs vitesses initiales $\mathbf{v}_0$ ont été prises selon la fonction d'onde initiale Ψ_0.

La Méthode des Trajectoires Quantique (QTM)

En pratique, il y a deux façons d'étudier l'évolution temporelle des trajectoires quantiques d'un point de vue numerique. Une première approche consiste à résoudre l'ESDT par les méthodes conventionnelles et à calculer les trajectoires par la suite.

D'autre part, il existe une approche différente dans laquelle les trajectoires quantiques sont utilisées comme outil pour résoudre l'équation de Schrödinger, et elles se propagent avec le champ hydrodynamique qui évolue avec elles. C'est précisément l'approche qui nous intéresse. L'utilisation des trajectoires quantiques comme outil numérique pour résoudre l'ESDT a suscité un intérêt particulier aprés le développement de la méthode de trajectoire quantique (QTM) par Wyatt et al. en 1999 [8]. Désormais, nous limitons notre dérivation à une dimension spatiale x et à une seule courbe énergétique potentielle.

Ici, x représentera une variable et x_i une trajectoire. Dans la méthode des trajectoires quantiques, la densité initiale est discrétisée en termes d'éléments fluides N avec une masse m, correspondant aux trajectoires x_i, i=1,...,N, chacun d'entre eux ayant sa propre amplitude $R_i = R(x_i, t)$.

Le choix des trajectoires quantiques comme grille n'est pas indispensable. L'avantage des trajectoires quantiques est qu'elles constituent une grille avec les bonnes propriétés pour propager la densité de probabilité, car l'amplitude et la phase sont directement propagées le long de celles-ci. Les équations (8.0.4) et (8.0.5) peuvent être écrites dans le système de référence Lagrangien. Si nous introduisons la dérivée le long d'une trajectoire $d/dt = \partial/\partial t + v\partial/\partial x$ et le champ de vitesse $v = \frac{1}{m}\frac{\partial S}{\partial x}$, on peut obtenir l'ensemble suivant des équations couplées

$$\frac{dS}{dt} = \frac{1}{2}mv^2 - (V+Q) \ , \tag{8.0.17}$$

$$\frac{d\rho}{dt} = -\rho\frac{\partial v}{\partial x} \ , \tag{8.0.18}$$

$$m\frac{dv}{dt} = -\frac{\partial(V+Q)}{\partial x} \ , \tag{8.0.19}$$

$$\dot{x}_i = v|_{x_i=x_i(t)} \ , \tag{8.0.20}$$

où les équations des champs hydrodynamiques sont évaluées le long de chaque trajectoire. L'équation ci-dessus est exacte. Toutefois, la sélection d'un nombre fini de trajectoires nécessaires à la mise en oeuvre numérique constitue une approximation. Le nombre de trajectoires utilisées sera alors un paramètre crucial pour assurer la convergence des résultats.

Les équations de mouvement présentées ci-dessus peuvent être combinées de différentes manières pour faire évoluer les trajectoires dans le temps [9]. Parmi toutes les combinaisons que nous choisissons pour propager les trajectoires, nous avons en général l'évolution temporelle des champs hydrodynamiques S et R, donc la fonction d'onde peut être construite le long du chemin suivi par les trajectoires quantiques comme suit

[9, 65],

$$\begin{aligned}\Psi(x_i,t) &= \Psi(x_i,t_0)\exp\left(-\frac{1}{2}\int_{t_0}^{t}\left(\frac{\partial v}{\partial x}\right)|_{x_i(\tau)}d\tau\right)\\ &\times \exp\left(\frac{i}{\hbar}\int_{t_0}^{t}\left(\frac{1}{2m}\left(\frac{\partial S}{\partial x}\right)^2 - V - Q\right)\Big|_{x_i(\tau)} d\tau\right), \end{aligned} \tag{8.0.21}$$

où nous avons dénoté $\Psi(x_i,t_0) = R(x_i,t_0)e^{\frac{i}{\hbar}S(x_i,t_0)}$. L'équation ci-dessus donne le propagateur de fonction d'onde. Par conséquent, dans le QTM, en propageant les champs S et R, nous pouvons reconstruire la fonction d'onde le long de chaque trajectoire.

Jusqu'à présent, nous avons présenté la théorie qui donne l'évolution temporelle de la trajectoire quantique. En principe, la solution des équations décrites ci-dessus donne la solution exacte de l'équation de Schrödinger dépendant du temps et a donc la même puissance prédictive que les méthodes standard de propagation de paquets d'ondes [16, 66, 67]. Cependant, plusieurs facteurs entravent la solution des équations du mouvement (EOM) pour les trajectoires quantiques.

Plusieurs stratégies ont été mises en place afin de surmonter les problèmes numériques associés à la propagation des trajectoires quantiques, avec un succés relatif [9]. Cependant, le probléme est loin d'être résolu et la recherche de nouvelles méthodes pour résoudre les équations hydrodynamiques avec précision reste un domaine de recherche actuel.

Dans ce travail, nous proposons deux alternatives différentes pour intégrer l'équation du mouvement des trajectoires quantiques. La première approche est présentée dans le chapitre suivant et est basée sur une représentation de Chebychev des champs hydrodynamiques. Le schéma est ensuite appliqué à la description de la dynamique vibratoinnelle, en particulier à l'évolution d'un paquet d'ondes sur un potentiel harmonique et sur un potentiel de Morse. Une approche différente est suivie dans les chapitres quatre et cinq, où des potentiels quantiques approximatifs sont dérivés de différentes paramétrisations de la densité.

Nous avons présenté ici la théorie de la méthode QTM. Nous avons obtenu l'ensemble des équations qu'il nous faut résoudre pour propager les trajectoires quantiques et nous avons montré comment la solution de l'ESDT peut en principe être obtenue par la propagation des trajectoires quantiques. Dans les deux chapitres suivants, nous présentons deux méthodes différentes pour trouver la solution numérique des équations (8.0.17)-(8.0.20). Les méthodes sont appliquées à l'étude de plusieurs problèmes unidimensionnels.

Chapitre 3: Chebyshev expansion des champs hydrodynamiques

Dans le QTM, les équations (8.0.17)-(8.0.20) sont résolus en propageant les champs S et R et les trajectoires simultanément. Cependant, la solution de ces équations couplées n'est pas simple.

L'une des principales difficultés est l'évaluation des dérivées des champs dans une grille non structurée. Depuis le développement du QTM par Wyatt et ses collaborateurs [8], plusieurs techniques ont été mises en avant pour surmonter ce problème. Parmi eux, on peut citer l'ajustement local des moindres carrés. Dans cette famille de méthodes, les moindres carrés pondérés mobiles (MWLS) a été la méthode la plus largement utilisée dans la méthode de trajectoire quantique [8, 12, 17, 68]. Comme alternative à ces schémas d'ajustement, d'autres techniques ont été mises en place comme la méthode de propagation des dérivées le long des trajectoires [9, 19] ainsi que des méthodes basées sur les grilles mixtes eulériennes et lagrangiennes [23, 25].

Nous proposons ici une nouvelle méthode de propagation des trajectoires quantiques, basée sur une expansion globale de Chebychev des champs hydrodynamiques [18]. Des expansions dans une base de polynomes de Chebyshev du propagateur de la fonction d'onde ont été largement utilisés dans les méthodes de propagation de paquets d'ondes standard [69]-[73], nous les utilisons ici pour la modélisation quantique sur la base de trajectoires. Les polynômes de Chebychev sont choisis en raison de leur propriété d'être les meilleurs polynômes d'interpolation dans le sens minimax. Dans l'expansion de Chebychev, l'erreur est répartie sur l'intervalle interpolé. Par conséquent, l'approximation de

Chebychev présente le plus petit écart maximal par rapport à la fonction interpolée (parmi tous les polynômes du même degré). De même, les relations de récurrence des polynômes de Chebyshev permettent le calcul direct des dérivées des champs hydrodynamiques.

La méthodologie que nous proposons ici, consiste à résoudre l'ensemble des équations (8.0.17)-(8.0.20), à developper les champs S et C dans une base de polynômes de Chebyshev à chaque pas de temps et à utiliser les relations de récurrence pour calculer les dérivés nécessaires. L'amplitude C est définie comme le logarithme de la densité. Cette représentation en termes de C a déjà été utilisée pour résoudre les équations du mouvement des trajectoires quantiques [9, 12, 17] et elle s'est aussi montrée plus stable numériquement que la représentation en termes de R. Pour évaluer les coefficients de l'expansion de Chebyshev des champs hydrodynamiques, nous utilisons la méthode SVD (Single Value Decomposition).

Comme premier exemple, nous étudions la dynamique vibrationnelle d'un paquet d'ondes Gaussiennes dans un potentiel quadratique, dont les solutions analytiques sont connues [78]. Trois largeurs différentes du paquet d'onde initial sont prises en compte.

Dans la figure 8.1, les résultats de l'évolution dans le temps de la valeur moyenne $\langle x \rangle$ (panneau gauche), et la largeur du paquet d'ondes σ (panneau droite), pour les trois cas considérés ici sont tracés. Dans les deux cas, la comparaison avec les résultats analytiques est présentée. Pour les trois valeurs initiales de la largeur du paquet d'ondes, les résultats numériques obtenus en utilisant la mise en application du QTM basé sur l'expansion Chebyshev des champs hydrodynamiques correspondent exactement aux solutions analytiques de l'équation Schrödinger, qui dépend du temps. Nous discutons également de la performance de l'implémentation actuelle du QTM pour les paquets d'ondes structurés d'un point de vue indépendant du temps. Nous choisissons trois formes analytiques différentes pour représenter la densité initiale. Les densités sont construites de manière à avoir la structure désirée. Le comportement du potentiel quantique et la force quantique pour les différents ordres de l'expansion de Chebychev sont étudiés.

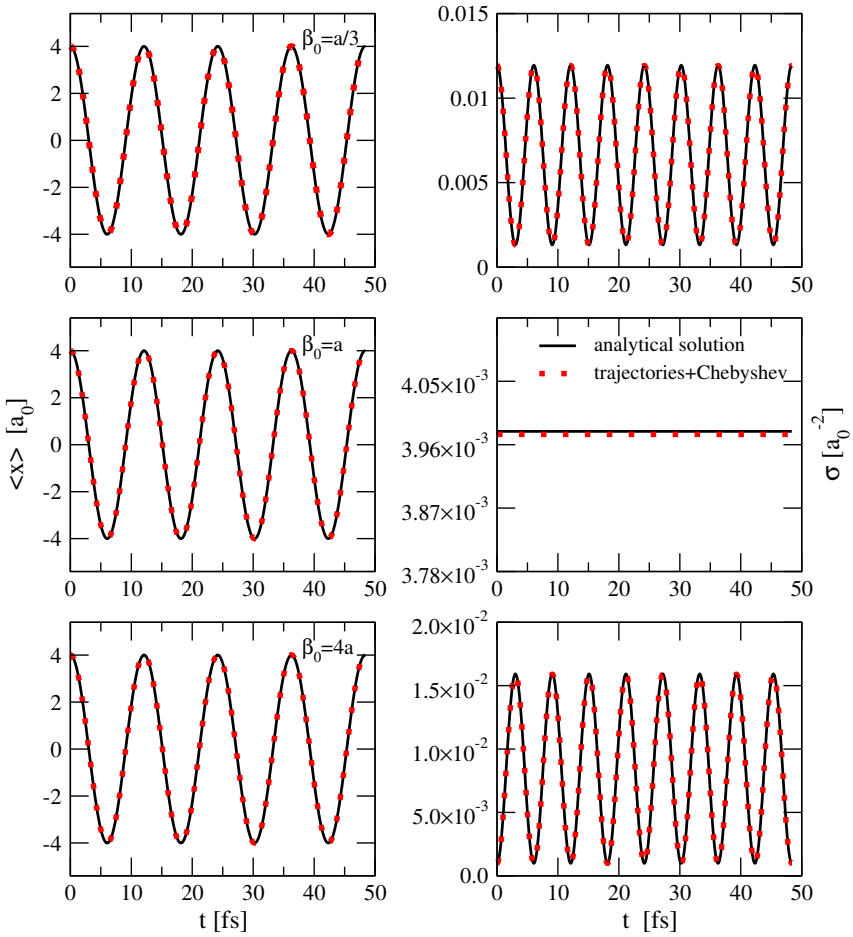

Figure 8.1: **Evolution temporelle de la valeur moyenne $\langle x \rangle$ (panneau gauche) et la largeur σ (panneau droite) du paquet d'ondes gaussiennes dans le potentiel quadratique. Dans tous les cas, la comparaison entre les résultats analytiques (ligne continue) et les valeurs moyennes est indiquée pour $N = 100$ trajectories (points).**

Dans la colonne de gauche de la figure 8.2 les trois densités analytiques sont représentées par des lignes continues et avec des points, nous avons tracé les résultats de l'expansion de Chebychev en utilisant des polynômes avec $M = 10$. Dans la colonne centrale, nous montrons le potentiel quantique pour les trois densités, en utilisant différents ordres de l'expansion de Chebychev avec SVD comparé au potentiel quantique exact.

Dans le panneau de droite de la Figure 8.2 l'erreur dans le calcul des forces est donnée. Comme on peut le voir, l'erreur augmente lorsque la densité est plus structurée, en particulier lorsque des nœuds stricts existent (panneau central droit). L'augmentation du nombre de polynômes de Chebychev n'améliore que marginalement la convergence vers les fonctions exactes numériques, mais les erreurs restent encore modestes dans tous les

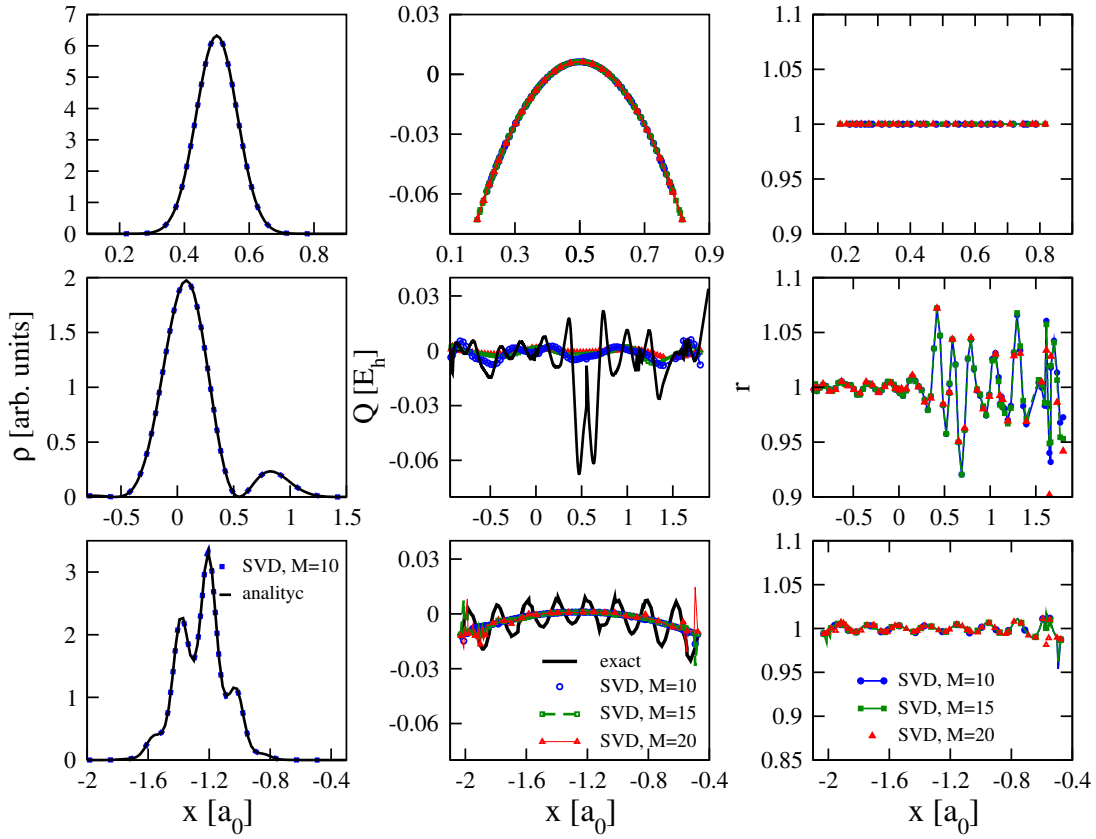

Figure 8.2: **Panneau de gauche: Densités analytiques (ligne continue) comparées à sa représentation dans les polynômes de Chebychev pour M=10. Panneau central: Potentiel quantique calculé après avoir représenté les trois densités analytiques à gauche en utilisant différents ordres de l'expansion de Chebyshev avec le schéma SVD/Chebyshev. Enfin, dans le panneau de droite, nous montrons les résultats de l'évaluation de l'erreur relative de la force.**

cas. Encore une fois, la densité avec des nœuds non résolus (panneau inférieur droit) se comporte mieux que celle avec un nœud explicite.

Le principal avantage de l'approche actuelle est qu'un nombre relativement faible de polynômes est nécessaire dans les expansions tronquées pour obtenir une représentation raisonnablement précise des champs hydrodynamiques. Les instabilités numériques dans le calcul du potentiel quantique et, par conséquent, dans l'intégration de l'équation du mouvement, sont surmontées par une combinaison de plusieurs techniques numériques.

La comparaison entre le potentiel quantique calculé à l'aide des coefficients d'expansion de Chebychev de la densité extraite de la SVD, et le potentiel quantique exact pour diverses distributions suggère que la précision de la procédure SVD diminue au fur et à mesure que la topologie de la distribution de la densité devient plus structuré. La troncation de

la série de Chebyshev conduit à un léger lissage de la dépendance spatiale du potentiel quantique. Néanmoins, l'erreur reste faible et n'affecte pas significativement les forces correspondantes exercées sur les particules.

Chapitre 4: Dynamique quantique modélisée par des trajectories en interaction

Récemment, une formulation de la mécanique quantique sans faire référence à la fonction d'onde, a été proposée [38]−[41], comme une alternative prometteuse au QTM mis au point par Wyatt. Dans cette approche, le problème de mécanique quantique dépendant du temps est transformé en un problème dynamique d'une densité paramétrée. Alors qu'en principe différents paramétrages sont possibles, pour des problèmes unidimensionnels, une paramétrisation spéciale a été proposée dans [39], qui conduit à une équation de Newton avec un potentiel supplémemtaire. Pour un choix spécifique de la paramétrisation, qui marque les trajectoires en fonction de leurs positions spatiales, on est conduit à la forme des équations quantiques de trajectoires de mouvement proposées par Hall et ses collaborateurs [43].

La version discrétisée de la densité a été qualifiée par Hall et ses collègues de travail d'interprétation de "monde en interaction", [43, 45]. Cependant, outre les aspects interprétatifs de la formulation, elle peut être utilisée pour l'étude de la dynamique quantique basée sur la propagation d'un ensemble de trajectoires, qui évoluent sous l'action du potentiel quantique. Dans la Réf. [43], le potentiel quantique a été choisi comme l'un des termes du potentiel quantique total, puisqu'il ne contient que le terme de conservation d'énergie dépendant que de la dérivée première de la densité de probabilité (deuxième terme de l'équation (8.0.7) au chapitre deux). Par conséquent, en utilisant cette approche, il n'est pas simple de générer la phase de la fonction d'onde. En revanche, en travaillant avec l'expression complète du potentiel quantique, comme le propose la Réf. [38] et [39], la phase devient égale à l'action et elle peut être calculée par une intégrale du Langrangien le long de la trajectroire (voir par exemple Eq. 8.0.21 au chapitre deux).

Dans ce chapitre, nous dérivons la forme complète du potentiel quantique en considérant le même *ansatz* pour la densité proposée dans la Réf. [43]. De plus, nous dérivons la force quantique du modèle et nous obtenons la même forme pour la force quantique que celle obtenue dans la Réf. [43]. Par conséquent, afin d'évaluer l'influence du terme négligé par Hall et ses collaborateurs, nous calculons la fonction de corrélation et les spectres, comme exemples d'observables où la phase de la fonction des ondes est pertinente.

Pour évaluer la performance de ces potentiels et forces quantiques modélisés, c'est-à-dire leur capacité à réproduire des phénomènes de mécanique quantique essentiels, tels que l'énergie de point zéro ou l'effet tunnel. Dans la première partie de ce chapitre, la méthode est appliquée à plusieurs problèmes de test unidimensionnel pour les potentiels indépendants du temps. A savoir, la détermination de l'état fondamental sur les potentiels harmoniques et anharmoniques, la propagation de paquets d'ondes en présence d'une barrière Eckart et d'une rampe ascendante, la dynamique de tunnel dans un double potentiel minimum et dans un potentiel avec un minimum local et une barrière finie [44].

Pour chaque système modèle, nous analysons les propriétés de convergence numérique à mesure que le nombre de trajectoires augmente. Pour un grand nombre de trajectoires de propagation, des forces quantiques importantes sont rencontrées, ce qui rend l'intégration numérique difficile et nécessite un contrôle automatique du pas d'intégration. Par conséquent, l'équation de mouvement pour les trajectoires quantiques est résolue en utilisant un intégrateur Runge-Kutta de quatrième ordre avec pas de temps adaptatif [85]. Les résultats obtenus par la dynamique de trajectoire sont comparés à la solution de référence à l'aide de la méthode FFT (Fast Fourier Transform Method) développée par Feit et al. [80]. Pour tous les exemples considérés, on obtient une convergence numérique vers le résultat quantique exact au fur et à mesure que le nombre de trajectoires augmente.

Comme exemple, nous montrons les résultats obtenus pour la fonction de corrélation en utilisant le potentiel quantique complet Q que nous dérivons ici, et le potentiel quantique

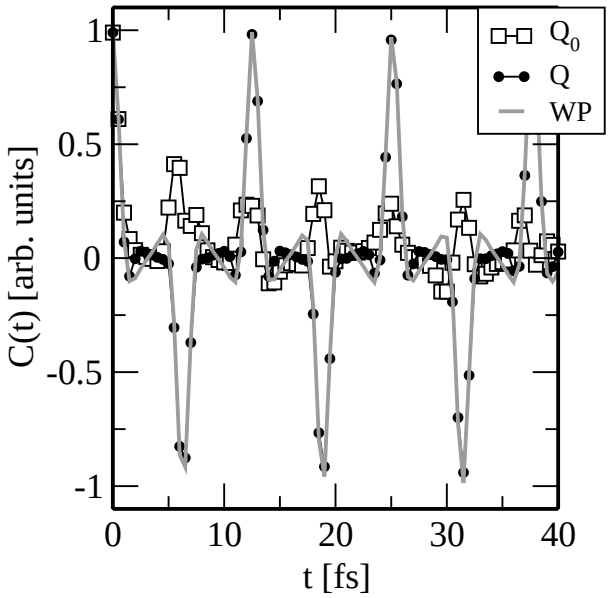

Figure 8.3: **Partie réelle de la fonction de corrélation d'un paquet d'ondes gaussiennes sur un potentiel parabolique, calculée à partir de l'évolution temporelle des trajectoires en interaction $N = 201$ en utilisant la forme complète du potentiel quantique Q et celle introduite dans Ref. [43] (Q_0). Les lignes pleines représentent la solution exacte, obtenue par propagation de paquets d'ondes.**

approximatif de Ref. [43] identifié comme Q_0 dans la Figure 8.3. Ces résultats sont comparés au résultat quantique exact. On peut remarquer que l'utilisation du potentiel quantique Q comprenant à la fois des termes répulsifs et attractifs, reproduit correctement les pics positifs et négatifs de la fonction de corrélation quantique. L'accord est moins parfait pour la région entre les pics moyens, où l'on fait la moyenne des petites oscillations d'amplitude de la fonction de corrélation quantique dans la représentation des trajectoires en interaction.

Augmenter la taille de l'ensemble des trajectoires permet de diminuer cet effet de lissage en rapprochant les résultats de la propagation des trajectoires et des paquets d'ondes.

Dans la deuxième partie de ce chapitre, nous étudions l'ionisation atomique induite par laser dans le cadre de notre méthodologie sans fonction d'onde. Un aspect intéressant du processus dynamique déclenché par des impulsions laser intenses et courtes est que (pour des impulsions extrêmement courtes, comprenant seulement quelques cycles optiques) la phase entre l'enveloppe et la porteuse (CEP) a une forte influence sur la dynamique induite par laser. Nous abordons ici ce problème dans une perspective des tra-

jectoires quantiques et évaluons le rendement d'ionisation et l'asymétrie gauche-droite en fonction du paramètre CEP. Les résultats sont comparés à des propagations par paquets d'ondes standard, et la convergence numérique des premiers pour des trajectoires quantiques progressivement plus grandes est analysée en détail [90]. Nous utilisons une impulsion laser dans l'infrarouge proche (NIR) de haute intensité d'une longueur d'onde de $800nm$ ($\omega = 0.057\,E_h$), une intensité de $I = 3.51 \times 10^{14} W/cm^2$ et une durée d'impulsion de 1.5 and 2.5 cycles ($T_{pulse} = 4.0$ fs et 6.6 fs), respectivement. Dans ce régime d'impulsions laser ultra-courtes et intenses, les effets CEP se produisent [81]-[84] et les quantités expérimentalement accessibles sont l'ionisation totale et l'asymétrie droite/gauche (avant/arrière) des électrons éjectés [81], [82].

Dans la figure 8.4 le rendement d'ionisation total P_I et l'asymétrie totale η sont tracés en fonction du paramètre CEP pour une durée d'impulsion de $T_{pulse} = 1.5$ cycles (colonnes de gauche) et $T_{pulse} = 2.5$ cycles (colonne de droite).

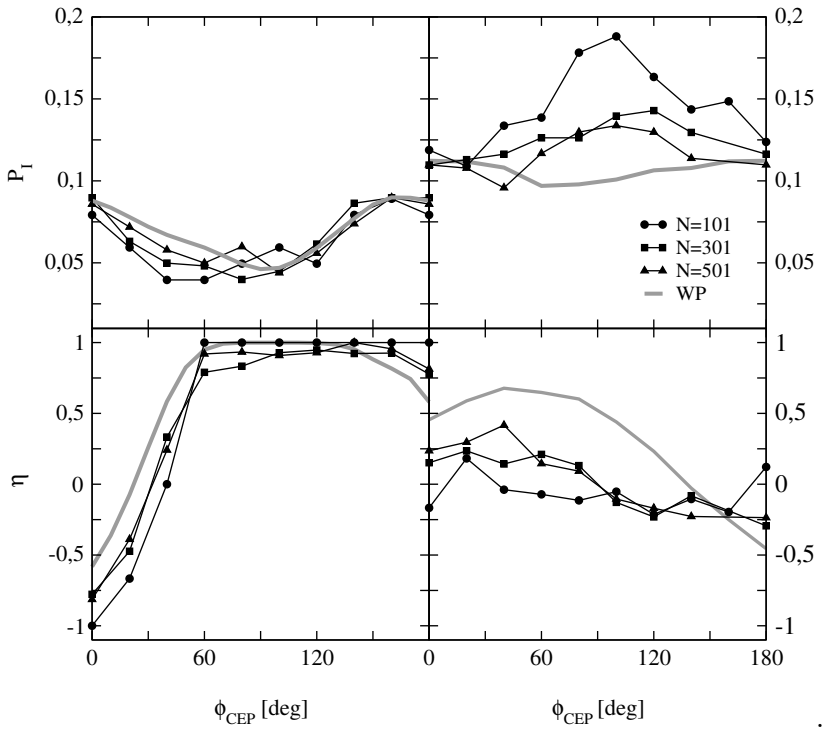

Figure 8.4: **Rendement d'ionisation total P_I et asymétrie gauche/droite η (Eq.(4.4.5)), en fonction du paramètre CEP pour deux durées d'impulsion différentes: $T_{pulse} = 1.5$ cycles (panneaux de gauche) et $T_{pulse} = 2.5$ cycles (panneaux de droite). Les variables observables calculées à l'aide des trajectoires $N = 101$, $N = 301$ et $N = 501$, ainsi que les résultats des calculs des paquets d'ondes (WP) sont présentés.**

Dans le panneau de droite de la figure 8.4, les résultats pour une impulsion laser plus longue sont affichés. Dans ce cas, l'ionisation totale augmente et aucune forte dépendance avec le paramètre CEP n'est observée. De plus, l'asymétrie gauche-droite est nettement réduite. Cette disparition de la dépendance de la CEP par rapport au paramètre d'asymétrie (lorsque la longueur de l'impulsion laser augmente) a déjà été discutée dans la Réf. [84].

Pour avoir une image plus détaillé , nous avons effectué une analyse approfondi des spectres d'ionisation en fonction de ϕ_{CEP}. Le résultat est donné en Fig. 8.5, avec à gauche, les spectres issus des calculs de trajectoires, et a droite les spectres obtenus par le calculs de référence. On voit l'asymétrie de l'émission de l'électron pour toutes les phases ϕ_{CEP}. En plus, l'énergie de l'électron émis dépend aussi de la phase CEP. En particulier, une phase de ϕ_{CEP} de 140^o mène à des électrons d'haute énergie émises dans une seule direction, tandis qu'une valeur de ϕ_{CEP} d'environ 30^o à une probabilité d'émission équilibré dans les deux directions spatiales, avec des énergies plus faibles. En comparant les résultats des trajectoires (à droite) avec les résultats de référence (à gauche), on voit que tous ces caractéristiques sont parfaitement reproduit par la nouvelle méthode développée.

Dans ce chapitre, nous avons proposé une méthode basée sur la propagation d'un ensemble de trajectoires en interaction à l'aide de potentiels quantiques modèles, qui apparaît comme une alternative prometteuse pour les études de dynamique quantique. Nous utilisons une expression approximative du potentiel quantique, obtenue en discrétisant la densité de probabilité quantique. L'expression du potentiel quantique qui en résulte contient à la fois des parties attractives et répulsives. Elle donne la même expression pour la force quantique que dans la Réf. [43], mais il permet (en plus) de reconstruire la fonction de l'onde grâce à l'intégration du Lagrangien le long des trajectoires.

La méthodologie est appliquée à différents systèmes unidimensionnels et le schéma reproduit des phénomènes quantiques importants tels que l'énergie du point zéro dans les potentiels harmoniques et anharmoniques, l'effet tunnel pour différentes formes de barrière, les fonctions d'autocorrélation et le spectre énergétique. De plus, la méthodologie proposée

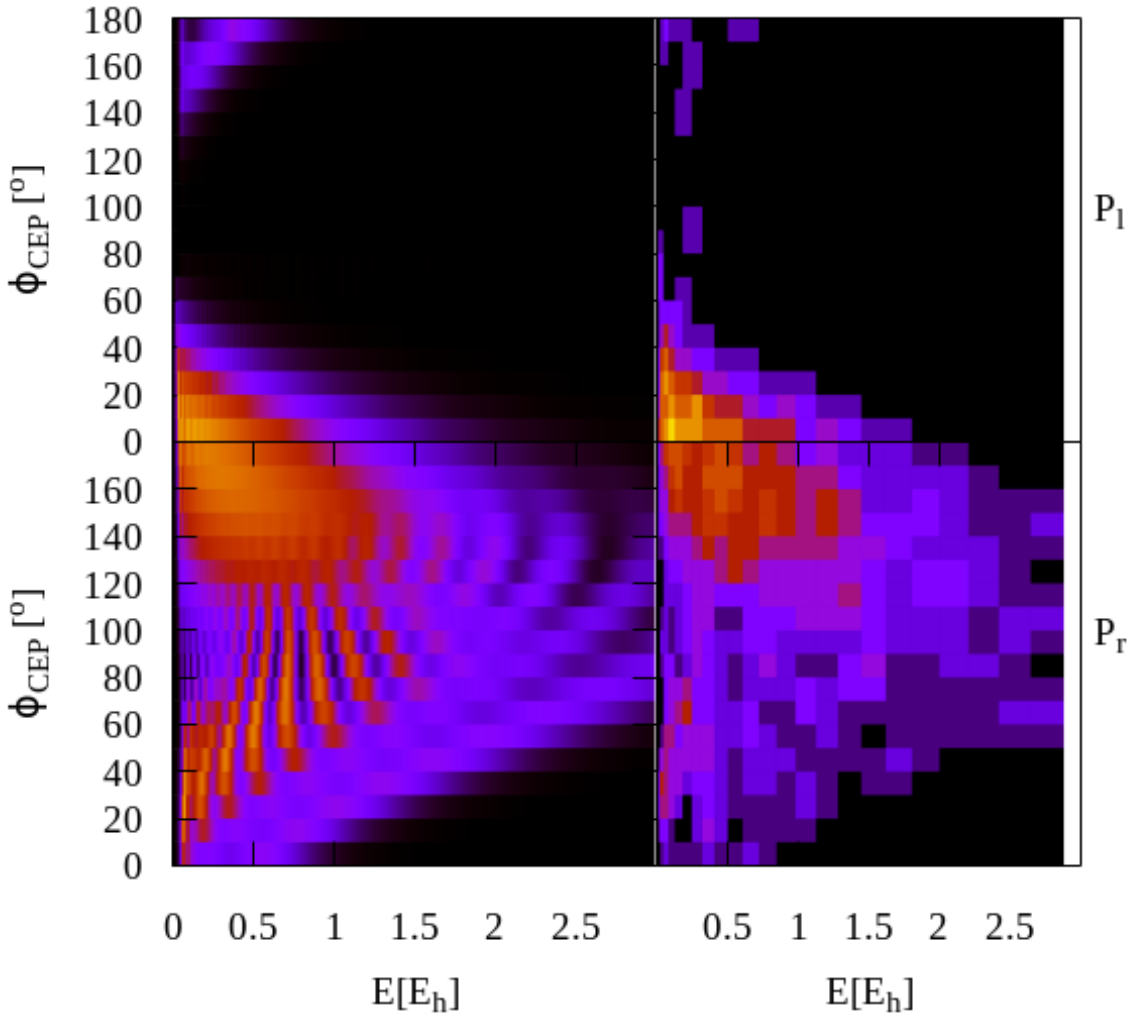

Figure 8.5: **Carte de densité des spectres photo-électroniques gauche/droite en fonction de l'énergie et ϕ_{CEP}. Panneau de gauche: calcul des paquets d'ondes, panneau de droite: résultats des trajectoires quantiques. Les cartes sont tracées les unes sur les autres pour montrer la symétrie de l'émission d'électrons.**

est appliquée pour simuler la dynamique des électrons pilotée par laser et des résultats précis sont également obtenus. Il est non seulement capable de reproduire quantitativement les rendements d'ionisation totale, mais aussi des effets CEP subtils tels que des asymétries gauche/droite dans l'ionisation en fonction de la phase entre l'enveloppe et la porteuse.

Chapitre 5: Étude de spectres d'absorption de l'atome de Na incrustée dans des matrices de gaz rares

Au cours des dernières décennies, de multiples expériences ont été réalisées pour étudier l'absorption et la luminescence d'atomes alcalins dans des matrices de gaz rares. Les études réalisées par Balling et al. [99]-[101] sur des matrices d'argon avec Li, Na et K ont montrées qu'il peut y avoir plusieurs sites où les atomes d'impureté peuvent être piégées dans la matrice. Pour ces trois atomes d'alcalins, deux ensembles de maxima dans le spectre d'absorption ont été identifiés, que l'on appelle généralement les triplets rouge et bleu. En plus de ces bandes, Tam et Fajardo [102] ont étudié les atomes de Li et de Na piégées dans une matrice de gaz rare en utilisant une nouvelle technique expérimentale basée sur l'ablation laser. Ils ont trouvé, pour les deux atomes, une nouvelle structure de triplet bien résolue du côté haute énergie de la bande bleue, qu'on appelle le triplet violet.

Plus récemment, Ryan et ses collaborateurs [61] ont mené un travail expérimental et théorique afin d'étudier l'absorption et la luminescence du Na atomique dans les matrices Ar et Kr. Les simulations des bandes d'absorption et d'émission de l'atome de Na dans la matrice, réalisées par Ryan et ses collègues [61], étaient basées sur des méthodes de dynamique moléculaire. Les surfaces énergétiques potentielles ont été obtenues à partir de données spectroscopiques et différents sites d'isolation de l'atome de Na ont été considérés. Cependant, bien que des informations qualitatives sur les bandes d'absorption ont été obtenues, leur position spectrale s'est avérée complètement différente de celles rapportées expérimentalement. Dans la Réf. [61], une modification artificielle de la forme du potentiel en corrélation avec le second état excité du sodium a été effectuée afin de faire correspondre les spectres mesurés. Les simulations utilisant le nouveau potentiel ont déplacé les bandes d'absorption vers les positions spectrales correctes, mais il reste l'ambiguïté quant à l'origine physique du déplacement proposé du potentiel d'état excité (qui a été obtenu empiriquement), et si les autres courbes d'énergie potentielle ne

changent pas aussi.

Une autre étude, utilisant des potentiels plus précis, a été réalisée par Boatz et ses collaborateurs [93] basée sur une analyse théorique de premier ordre de la perturbation de l'état p excité de l'atome alcalin. Cependant, bien que certaines informations qualitatives en aient été extraites, les spectres d'absorption obtenus à la suite des simulations ne reproduisent pas les résultats expérimentaux.

Il est important de noter que les simulations effectuées par Ryan [61] étaient des simulations purement classiques, qui peuvent donner des résultats corrects si l'on considère les atomes lourds et des températures élevées (correspondant aux phases liquide et gazeuse des systèmes de gaz rares). Néanmoins, pour des atomes de gaz rares dans des matrices cryogénique, le caractère quantique devient pertinent.

Ainsi, dans ce chapitre, nous dérivons un potentiel quantique à plusieurs corps pour évaluer l'influence des effets quantiques sur les spectres d'absorption d'atomes alcalins dans les matrices de gaz rares. Le potentiel quantique approximatif est dérivé d'un ansatz donné pour la fonction d'onde de l'état fondamental. Comme l'extension de l'*ansatz* introduite dans le chapitre précédent aux systèmes multidimensionnels n'est pas simple, nous proposons ici un paramétrage différent qui prend en compte les propriétés physiques de la matrice du gaz rare. Les paramètres pour minimiser la densité sont dérivés en minimisant l'estimation variationnelle de l'énergie à l'aide du schéma Car-Parrinello.

Par conséquent, des simulations MD sont effectuées pour simuler les spectres d'absorption, avec un potentiel effectif comprenant à la fois l'interaction de paires classique et les potentiels quantiques. Comme système modèle, nous étudions les spectres d'absorption du Na incrustée dans un seul site de vacance (sv) dans les matrices Ar et Kr. Ce site de piégeage a été identifié comme responsable de la bande d'absorption violette [61, 103]. Afin d'évaluer l'influence des corrections quantiques sur les spectres d'absorption théoriques, nous effectuons des simulations de dynamique moléculaire avec et sans potentiel quantique.

Pour inclure les effets d'énergie du point zéro, les simulations MD, qui ne comprennent

que le potentiel d'interaction classique, sont effectuées à une température effectif T^*, tandis que celles incluant le potentiel quantique, sont réalisées à la température physique $T = 10K$.

Dans la figure 8.6 nous montrons les résultats des spectres théoriques pour les deux systèmes, NaKr à gauche et NaAr à droite. Avec des lignes verticales discontinues, nous représentons les valeurs expérimentales rapportées pour les maxima du triplet [61]. Comme on peut voir, les spectres obtenus à partir des simulations avec le potentiel d'interaction classique (montré en bleu), reproduisent la structure triplet des spectres expérimentaux, mais ils sont décalés vers une région d'énergie inférieure par rapport aux résultats expérimentaux. Ce décalage vers le rouge des spectres d'absorption correspond au comportement observé par Ryan et ses collègues [61] pour les différents sites de piégeage de l'atome de Na dans les matrices de gaz rares, les spectres théoriques étaient situés dans la partie rouge du profil expérimental. Comme nous l'avons déjà mentionné, afin d'améliorer la correspondance entre les spectres théoriques et expérimentaux, Ryan et al. [61] ont modifié empiriquement dans leur travail le potentiel d'état excité pour être plus répulsif. Ici, nous montrons que l'ajout d'une expression approximative du potentiel quantique (obtenu en minimisant l'énergie de l'état fondamental) au potentiel d'interaction déplace la bande d'absorption simulée vers la bonne région énergétique (pour les matrices Ar et Kr dopées au Na).

Ces résultats corroborent la conclusion selon laquelle les écarts entre les simulations de température effective de la DM et l'expérience sont une conséquence de l'incapacité de l'approche de température effective à imiter les effets quantiques dans le voisinage de l'impureté, plutôt qu'une modification du potentiel d'interaction due aux effets de matrice. L'accord entre nos spectres théoriques et les spectres expérimentaux n'est que qualitatif, en raison des approximations introduites, principalement dans l'évaluation perturbatrice des énergies des états électroniques excités.

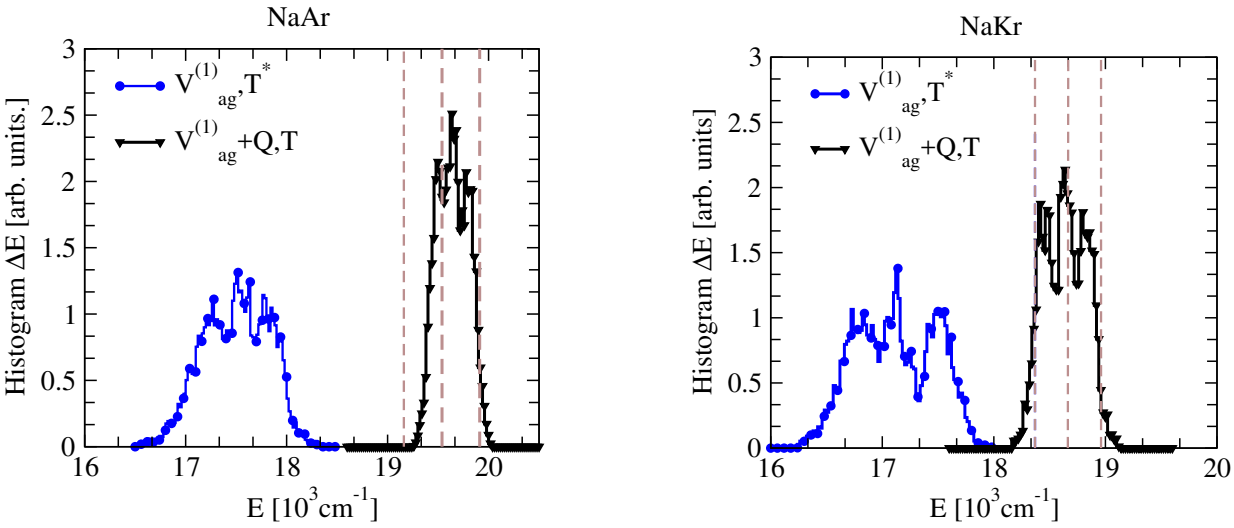

Figure 8.6: **Spectre d'absorption simulé obtenu comme histogramme de la superposition des différences d'énergie entre le sol et les états électroniques excités. Dans le panneau de gauche, les résultats de la matrice NaAr sont présentés et dans le panneau de droite, nous présentons les résultats de la matrice NaKr.**

Chapitre 6: Conclusions générales

L'un des problèmes majeures de la modélisation de la dynamique de processus atomiques et moléculaires a ce jour est d'être capable de considérer la totalité de la dimensionnalité du système. En général, les méthodes pour étudier des systèmes microscopiques peuvent être classifiés selon deux approches : Une approche purement quantique, qui est limité à la description de quelques atomes, ou une approche basée sur la mécanique classique, qui peuvent être appliqué a des systèmes comprenant un très grand nombre de particules. Néanmoins, dans cette dernière, des effets quantiques ne sont pas prises en compte.

Dans ce contexte se place le sujet de cette thèse, de développer des méthodes quantiques basées sur une description de la dynamique par trajectoires. Dans le futur, de tels méthodes peuvent ouvrir la voie vers une description quantique de systèmes à haute dimensionnalité. Le travail de cette thèse consistait à développer, implémenter et tester de tels méthodes pour des systèmes modèles, qui néanmoins présentent des aspects quantiques. Comme résultat principal, il est montré que ces méthodes, qui ne sont pas basées sur la fonction d'onde, mais sur un ensemble de trajectoires seulement, sont capable de décrire des effets quantiques comme l'énergie de point zéro, l'éffet tunnel, la dispersion

de paquets d'ondes ou des interférences quantiques. La méthodologie est basée sur la propagation de trajectoires qui interagissent entre eux par un potentiel d'interaction qui permet ainsi de décrire des effets quantiques. Comme point de départ, on considère une discrétisation de la densité quantique, a partir duquel un potentiel quantique peut être obtenu analytiquement, permettant ainsi d'effectuer un calcul de dynamique quantique par une propagation de trajectoires. Cette méthodologie est appliquée à plusieurs systèmes modèles, comme des oscillateurs harmoniques et anharmoniques, et à une barrière de potentiel de différents paramètres pour analyser la diffusion et l'effet tunnel. En intégrant le Lagrangien avec un potentiel supplémentaire, le potentiel quantique, il est possible de reconstruire la fonction d'onde et ainsi de calculer des spectres via des fonctions de corrélation. Par cette démarche, il est alors possible de décrire l'énergie de point zéro, ainsi que la discrétisation des niveaux d énergie pour des problèmes liées par l'ensemble des trajectoires. En ce qui concerne les calculs de transmission / réflexion, un accord avec des calculs quantiques standards de référence montrent un très bonne accord, montrant ainsi la validité de l'approche par trajectoires. En extension de ces résultats, la méthodologie est appliquée ensuite à des problèmes quantiques avec un Hamiltonien dépendent du temps. En particulier, l'ionisation de l'atome de hydrogène par des impulsions ultrabrèves et fortes a été considérée. Dans le domaine des paramètres choisi, ce système a la particularité que la dynamique électronique sous l'influence du champs s'étale sur un grand domaine spatiale, ce qui rend les méthodes standards, basées sur des grilles spatiaux ou des fonctions de bases très laborieux. Dans cette situation, une description par trajectoires est particulièrement avantageux, car elle évite des larges grilles ou fonctions de bases. La méthodologie proposée n'est pas seulement capable de reproduire quantitativement des résultats des calculs de référence, mais offre aussi la possibilité d'une interprétation de la dynamique sur la base des trajectoires. En plus de la méthode de trajectoires mentionnées ci-dessus, deux autres méthodes ont été développées et testées dans cette thèse. La première consiste en l'utilisation de la densité quantique développée dans une base de polynômes de Chebychev. L'avantage de cette approche est que les dérivées nécessaires de la densité pour la propagation peuvent être obtenues par les pro-

priétés de recursion des polynômes. Néanmoins, une extension à plusieurs dimensions de cette approche reste un défi majeur. Pour étendre la dynamique à des problèmes à haute dimensionnalité, une troisième approche a été développée. Sur la base d'un ansatz particulier pour la densité à plusieurs corps, une expression pour le potentiel quantique à haute dimension a été développée, qui s'ajoute au potentiel classique. Ainsi, des propagations de type dynamique moléculaire pour un grand nombre de particules est possible, en incluant des effets quantiques. Cette méthodologie a été appliquée à la spectroscopie d'atomes de gaz rare, incrustées dans des matrices cryogéniques. Comme résultat principale de cette axe de thématique, un meilleur accord avec des données expérimentales qu'une une approche purement classique a été obtenu, confirmant ainsi les capacités prometteuses de cette nouvelle approche.

Les perspectives qui se dégagent sur la base du travail proposé sont multiples : Au delà de l'utilisation des méthodes présentés pour les études de nombreux d'autres systèmes atomiques et moléculaires, l'utilisation de trajectoires pour effectuer une dynamique quantique présente un fondement théorique intéressant pour développer des méthodes mixtes quantique/classiques. En particulier, différentes régions dans l'espace de configurations peuvent être définis, qui sont traitées, soit par la dynamique quantique, soit par la dynamique classique, avec une transition continue. Comme exemple, on peut citer des problèmes de diffusion atomique ou moléculaire, avec des interactions à très longue portée, où la dynamique électronique à grande amplitude induit par l'interaction avec des impulsions lasers fortes, une domaine de recherche en plein développement expérimentalement.

Bibliography

[1] A. H. Zewail, Femtochemistry: ultrafast dynamics of the chemical bond, World Scientific 1 (1994).

[2] O. Kühn, L. Wöste, Analysis and control of ultrafast photoinduced reactions, Springer Science & Business Media, **87** (2007).

[3] M. H. Beck, A. Jäckle, GA Worth, H. D. Meyer, The multiconfigurational time-dependent Hartree (MCTDH) method: a highly efficient, Physics Report **324**, 1 (2000).

[4] C. Cerjan, Numerical grid methods and their application to Schrödinger's equation, Springer Science & Business Media, **412** (1993).

[5] J. C. Light, T. Carrington Jr, Discrete-variable represetations and their utilization, Advances in Chemical Physics, **114**, 263-301 (2000).

[6] L. de Broglie, Recherches sur la théorie des quanta. Thèse de Doctorant, Université de Paris, 1925.

[7] D. Bohm, A suggested interpretation of the quantum theory in terms of "hidden" variables, Physical Review, **85**, 166 (1952).

[8] C. L. Lopreore and R. E. Wyatt, Quantum wave packet dynamics with trajectories, Physics Review Letters, **82**, 5190 (1999).

[9] R. E. Wyatt, Quantum dynamics with trajectories, (Springer Science & Bussiness Media, 2006).

[10] R. E. Wyatt, Quantum wave packet dynamics with trajectories: Application to reactive scattering, The Journal of Chemical Physics, **111**, 4406 (1999).

[11] C. L. Lopreore and R. E. Wyatt, Quantum wave packet dynamics with trajectories: reflections on a downhill ramp potential, Chemical Physics Letters, **325**, 73 (2000).

[12] E. R. Bittner and R. E. Wyatt, Integrating the quantum Hamilton-Jacobi equations by wavefront expansion and phase space analysis, The Journal of Chemical Physics, **113**, 8888 (2000).

[13] R. E. Wyatt and E. R. Bittner, Quantum wave packet dynamics with trajectories: Implementation with adaptive Lagrangian grids, The Journal of Chemical Physics, **113**, 8898 (2000).

[14] K. H. Hughes and R. E. Wyatt, Wavepacket dynamics on dynamically adapting grids: application of the equidistribution principle, Chemical Physics Letters, **366**, 336 (2002).

[15] B. K. Dey, A. Askar and H. Rabitz, Multidimensional wave packet dynamics within the fluid dynamical formulation of the Schrödinger equation, The Journal of Chemical Physics, **109**, 8770 (1998).

[16] F. S. Mayor, A. Askar and H. A. Rabitz, Quantum fluid dynamics in the Lagrangian representation and applications to photodissociation problems, The Journal of Chemical Physics, **111**, 2423 (1999).

[17] B. K. Kendrick, A new method for solving the quantum hydrodynamic equations of motion, The Journal of Chemical Physics, **119**, 5805 (2003).

[18] L. Cruz-Rodríguez, J. C. Tremblay, A. Martínez-Mesa and Ll. Uranga-Piña, A Chebyshev expansion of hydrodynamical fields for ultrafast vibrational wave packet dynamics, Computational Theoretical Chemistry, **1078**, 104 (2016).

[19] C. J. Trahan, K. Hughes and R. E. Wyatt, A new method for wave packet dynamics: Derivative propagation along quantum trajectories, The Journal of Chemical Physics, **118**, 9911 (2003).

[20] C. J. Trahan, R. E. Wyatt and B. Poirier, Multidimensional quantum trajectories: Applications of the derivative propagation method, The Journal of Chemical Physics, **122**, 164104 (2005).

[21] R. E. Wyatt, Wave packet dynamics on adaptive moving grids, The Journal of Chemical Physics, **117**, 9569 (2002).

[22] R. E. Wyatt and E. R. Bittner, Using quantum trajectories and adaptive grids to solve quantum dynamical problems, Computing in Science & Engineering, **5**, 22 (2003).

[23] L. R. Pettey and R. E. Wyatt, Wave packet dynamics with adaptive grids: The moving boundary truncation method, Chemical Physics Letters, **424**, 443 (2006).

[24] K. H. Hughes and R. E. Wyatt, Wavepacket dynamics on arbitrary Lagrangian–Eulerian grids: Application to an Eckart barrier, Physical Chemistry Chemical Physics, **5**, 3905 (2003).

[25] C. J. Trahan and R. E. Wyatt, An arbitrary Lagrangian–Eulerian approach to solving the quantum hydrodynamic equations of motion: equidistribution with "smart" springs, The Journal of Chemical Physics, **118**, 4784 (2003).

[26] K. Park, B. Poirier and G. Parlant, Quantum trajectory calculations for bipolar wavepacket dynamics in one dimension, The Journal of Chemical Physics, **129**, 194112 (2008).

[27] Y. Goldfarb, I. Degani and D.J. Tannor, Bohmian mechanics with complex action: A new trajectory-based formulation of quantum mechanics, The Journal of Chemical Physics, **125**, 231103 (2006).

[28] C-C. Chou, Complex-valued derivative propagation method with approximate Bohmian trajectories for quantum barrier scattering, Chemical Physics, **457**, 160 (2015).

[29] W. Koch and D. J.Tannor, Wavepacket revivals via complex trajectory propagation, Chemical Physics Letters, **683**, 306 (2017).

[30] C-C Chou, Schrödinger-Langevin equation with quantum trajectories for photodissociation dynamics, Annals of Physics, **377**, 22 (2017).

[31] C-C Chou, Two-dimensional reactive scattering with transmitted quantum trajectories, International Journal of Quantum Chemistry, **115**, 419 (2015).

[32] S. Garashchuk, V. A. Rassolov, Quantum dynamics with Bohmian trajectories: energy conserving approximation to the quantum potential, Chemical Physics Letters, **376**, 358 (2003).

[33] S. Garashchuk and V. A. Rassolov, Energy conserving approximations to the quantum potential: Dynamics with linearized quantum force, The Journal of Chemical Physics, **120**, 1181 (2004).

[34] S. Garashchuk and V. A. Rassolov, Bohmian dynamics on subspaces using linearized quantum force, The Journal of Chemical Physics, **120**, 6815 (2004).

[35] S. Garashchuk, V. Rassolov and O. Prezhdo, 6 Semiclassical Bohmian Dynamics, Reviews in Computational Chemistry, **287**, 27 (2011).

[36] S. Garashchuk and M. V. Volkov, Incorporation of quantum effects for selected degrees of freedom into the trajectory-based dynamics using spatial domains, The Journal of Chemical Physics, **137**, 074115 (2012).

[37] S. Garashchuk, J. Jakowski and A. V. Rassolov, Approximate quantum trajectory dynamics for reactive processes in condensed phase, Molecular Simulation, **41**, 86 (2015).

[38] B. Poirier, Bohmian mechanics without pilot waves, Chemical Physics, **370**, 4 (2010).

[39] J. Schiff and B. Poirier, Communication: Quantum mechanics without wavefunctions, The Journal of Chemical Physics, **136**, 031102 (2012).

[40] B. Poirier, in Quantum Trajectories, edited by K.H. Hughes and G. Parlant, Trajectory-Based Derivation of Classical and Quantum Mechanics, p. 6 (CCP6, Daresbury Laboratory, Daresbury, UK, 2011)

[41] G. Parlant, Y. C. Ou, K. Park and B. Poirier, Classical-like trajectory simulations for accurate computation of quantum reactive scattering probabilities, Computational and Theoretical Chemistry, **990**, 3 (2012).

[42] Y. Scribano,G. Parlant and B. Poirier, Communication: Adiabatic quantum trajectory capture for cold and ultra-cold chemical reactions, The Journal of Chemical Physics **149**, 021101 (2018).

[43] M. J. Hall, D. A. Deckert and H. M. Wiseman, Quantum phenomena modeled by interactions between many classical worlds, Physical Review X, **4**, 041013 (2014).

[44] L. Cruz-Rodríguez, Ll. Uranga-Piña, A. Martínez-Mesa and C. Meier, Quantum dynamics modeled by interacting trajectories, Chemical Physics **503**, 39-49 (2018).

[45] B. Poirier, Phys. Rev. X **4**, 040002 (2014).

[46] A. S. Sanz, F. Borondo and S. Mirét-Artés, Causal trajectories description of atom diffraction by surfaces, Physical Review B, **61**, 7743 (2000).

[47] R. Guantes, A. S. Sanz, J. M. Roig and S. Mirét-Artés, Atom–surface diffraction: a trajectory description. Surface science reports, **53**, 199 (2004).

[48] A. S. Sanz and S. Miret-Artés, A trajectory-based understanding of quantum interference, Journal of Physics A: Mathematical and Theoretical, **41**, 435303 (2008).

[49] A. S. Sanz and S. Mirét-Artés, A trajectory description of quantum processes. II. Applications, (Springer, 2014).

[50] X.Y. Lai, Q.Y. Cai and M.S Zhan, From a quantum to a classical description of intense laser–atom physics with Bohmian trajectories. New Journal of Physics 11, 113035 (2009).

[51] N. Takemoto and A. Becker, Visualization and interpretation of attosecond electron dynamics in laser-driven hydrogen molecular ion using Bohmian trajectories, The Journal of Chemical Physics, **134**, 074309 (2011).

[52] Y. Song, F. M. Guo, S. Y. Li, J. G. Chen, S. L. Zeng and Y. J. Yang, Investigation of the generation of high-order harmonics through Bohmian trajectories. Physical Review A, **86**, 033424 (2012).

[53] S. S. Wei, Su-Yu Li, F-M. Guo, Yu-Jun Yang and B. Wang, Dynamic stabilization of ionization for an atom irradiated by high-frequency laser pulses studied with the Bohmian-trajectory scheme, Physical Review A, **87**, 063418 (2013).

[54] J. Wu, B. B. Augstein, and C. F. de Morisson Faria, Bohmian-trajectory analysis of high-order-harmonic generation: Ensemble averages, nonlocality, and quantitative aspects, Physical Review A, **88**, 063416 (2013).

[55] R. Sawada, T. Sato and K.. L. Ishikawa, Analysis of strong-field enhanced ionization of molecules using bohmian trajectories, Physical Review A, **90**, 023404 (2014).

[56] H. Z. Jooya, D. A. Telnov, P. C. Li and S-I. Chu, Exploration of subcycle multiphoton ionization and transient electron density structures with Bohmian trajectories, Physic Review A, **91**, 063412 (2015).

[57] H. Z. Jooya, A. D. Telnov and S.I Chu, Exploration of the electron multiple recollision dynamics in intense laser fields with Bohmian trajectories, Physical Review A, **93**, 063405 (2016).

[58] Y. Song, Y. Yang, F. Guo and S. Li, Revisiting the time-dependent ionization process through the Bohmian-mechanics method, Journal of Physics B: Atomic, Molecular and Optical Physics **50**, 095003 (2017).

[59] N. Douguet and K. Bartschat, Dynamics of tunneling ionization using Bohmian mechanics, Physical Review A, **97**, 013402, (2018).

[60] Y. Y. Huang, X. Y. Lai, and X. J. Liu, High-order harmonic generation in a two-color strong laser field with Bohmian trajectory theory, Chinese Physics B, **27**, 073204 (2018).

[61] M. Ryan, M. Collier, P. de Pujo, Claudine Crépin and John G. McCaffre, Investigations of the optical spectroscopy of atomic sodium isolated in solid argon and krypton: experiments and simulations. The Journal of Physical Chemistry A, **114**, 3011 (2010).

[62] P. R. Holland, The quantum theory of motion (Cambridge University Press, Cambridge, MA, 1993).

[63] V.E. Madelung, Quantentheorie in hydrodynamischer form,Z. Physik, 40, 322 (1926).

[64] C. Cohen-Tannoudji, B. Diu, F. Laloë, Quantum Mechanics, Hermann and John Wiley & Sons. Inc, France, 1995.

[65] R. E. Wyatt, Quantum wavepacket dynamics with trajectories: wavefunction synthesis along quantum paths, Chemical Physics Letters, **313**, 189 (1999).

[66] Z. S. Wang, G. R. Darling and S. Holloway, Dissociation dynamics from a de Broglie-Bohm perspective, The Journal of Chemical Physics, **115**, 10373 (2001).

[67] C. C. Chou, R. E. Wyatt, Computational method for the quantum Hamilton-Jacobi equation: Bound states in one dimension, The Journal of Chemical Physics, **125**, 174103 (2006).

[68] E. R. Bittner, Quantum tunneling dynamics using hydrodynamic trajectories, The Journal of Chemical Physics, **112**, 9703 (2000).

[69] H. Tal-Ezer, R. Kosloff, An accurate and efficient scheme for propagating the time-dependent Schrödinger equation, The Journal of Chemical Physics, **81**, 3967 (1984).

[70] R. Kosloff,H. Tal-Ezer, A direct relaxation method for calculating eigenfunctions and eigenvalues of the Schrödinger equation on a grid, Chemical Physics Letters, **127**, 223 (1986).

[71] D. Neuhauser, M. Baer, R. S. Judson, D. J. Kouri, The application of time-dependent wavepacket methods to reactive scattering, Computer Physics Communications, **63**, 460 (1991).

[72] D. J. Kouri, Y. Huang, W. Zhu, D. K. Hoffman, Variational principles for the time-independent wave packet Schrödinger and wave packet Lippmann-Schwinger equations, The Journal of Chemical Physics, **100**, 3662 (1994).

[73] R. Baer, M. Head-Gordon, Sparsity of the density matrix in Kohn-Sham density functional theory and an assessment of linear system-size scaling methods, Physical Review Letters, **79**, 3962 (1997).

[74] R. Peyret, Spectral Methods for Incompressible Viscous Flow, (Springer-Verlag New York, 2002).

[75] W. H. Press, S. A. Teukolsky, W. T. Vetterling, B. P. Flannery, Numerical recipes in Fortran 77 and Fortran 90, (Cambridge University Press Cambridge, 1996).

[76] R.L. Burden, J.Douglas Faires, Análisis Numérico (Grupo Editorial Iberoamericana, México, 1985).

[77] H. D. Meyer, F.Gatti, G. A. Worth, Multidimensional quantum dynamics, John Wiley and Sons (2009).

[78] D. J. Tannor, Introduction to quantum mechanics. A Time-Dependent Perspective, (University Science Books, 2007).

[79] H. F. Trotter, On the product of semi-groups of operators, Proceedings of the American Mathematical Society, **10**, 545 (1959).

[80] M. D. Feit. J. A. Fleck and A. Steiger, Solution of the Schrödinger equation by a spectral method, Journal of Computational Physics, **47**, 412 (1982).

[81] G. G. Paulus, F. Lindner, H. Walther, A. Baltuska, E. Gouliel-Makis, M. Lezius, and F. Krausz, Measurement of the phase of few-cycle laser pulses, Physical Review Letters, **91**, 253004 (2003).

[82] H. Li, B. Mignolet, G. Wachter, S. Skruszewicz, S. Zherebtsov, F. Süßmann, A. Kessel, S. A. Trushin, Nora G. Kling, M. Kübel, B. Ahn, D. Kim, I. Ben-Itzhak, C. L. Cocke, T. Fennel, J. Tiggesbäumker, K.-H. Meiwes-Broer, C. Lemell, J. Burgdörfer, R. D. Levine, F. Remacle, and M. F. Kling, Coherent electronic wave packet motion in C 60 controlled by the waveform and polarization of few-cycle laser fields, Physical Review Letters, **114**, 123004 (2015).

[83] C.-Z. Gao, P. M. Dinh, P.-G. Reinhard, E. Suraud, and C. Meier, Forward-backward asymmetry of photoemission in C 60 excited by few-cycle laser pulses, Physical Review A, **95**(3), 033427 (2017).

[84] P. G. Reinhard, E. Suraud and C. Meier, The impact of the carrier envelope phase-dependence on system and laser parameters, Journal of Physics B: Atomic, Molecular and Optical Physics, **51**(2), 024007 (2018).

[85] E. Haier, S. Norsett and G. Wanner, Solving Ordinary, Differential Equations I, Nonstiff problems, (Springer-Verlag, 2000).

[86] P. M. Morse, Diatomic molecules according to the wave mechanics. II. Vibrational levels, Physical Review, **34**, 57 (1929).

[87] R. Schinke, Photodissociattion Dynamics, Spectroscipy and Fragmentation of Small Polyatomic Molecules, (Cambridge University Press, 1993).

[88] B. J. Berne and D. Thirumalai, On the simulation of quantum systems: path integral methods, Annual Review of Physical Chemistry, **37**, 401 (1986).

[89] M. E. Tuckerman, B. J. Berne, G. J. Martyna and M. L. Klein, Efficient molecular dynamics and hybrid Monte Carlo algorithms for path integrals, The Journal of Chemical Physics, **99**, 2796 (1993).

[90] L. Cruz-Rodríguez, Ll. Uranga-Piña, A. Martínez-Mesa and C. Meier, Quantum trajectory study of laser-driven atomic ionization, accepted for publication in Chemical Physics Letter.

[91] R. Heather and H. Metiu, An efficient procedure for calculating the evolution of the wave function by fast Fourier transform methods for systems with spatially extended wave function and localized potential, The Journal of Chemical Physics, **86**, 5009 (1987).

[92] N. Takemoto, A. Shimshovitz, D. J. Tannor, Communication: Phase space approach to laser-driven electronic wavepacket propagation, The Journal of Chemical Physics, **137**, 011102 (2012).

[93] J. A. Boatz, M. E. Fajardo, Monte Carlo simulations of the structures and optical absorption spectra of Na atoms in Ar clusters, surfaces, and solids, The Journal of Chemical Physics, **101**, 3472 (1994).

[94] J. Douady, S. Awali, L. Poisson, B. Soep, J. M. Mestdagh, and B. Gervais, Spectroscopy and Dynamics of K Atoms on Argon Clusters, The Journal of Physical Chemistry A, **119**, 6074 (2015).

[95] S. Awali, L. Poisson, M. B. E. H. Rhouma and J. M. Mestdagh, Absorption Spectroscopy, a Tool for Probing Local Structures and the Onset of Large-Amplitude Motions in Small KArn Clusters at Increasing Temperatures, The Journal of Physical Chemistry A **119**, 9729 (2015).

[96] B. M. Davis and J. G. McCaffrey, Absorption spectroscopy of heavy alkaline earth metals Ba and Sr in rare gas matrices—CCSD (T) calculations and atomic site occupancies, The Journal of Chemical Physics, **144**, 044308 (2016).

[97] B. M. Davis, B. Gervais and J. G. McCaffrey, An investigation of the sites occupied by atomic barium in solid xenon—A 2D-EE luminescence spectroscopy and molecular dynamics study, The Journal of Chemical Physics, **148**, 124308 (2018).

[98] B. M. Davis and John G. McCaffrey, Luminescence of Atomic Barium in Rare Gas Matrices: A Two-Dimensional Excitation/Emission Spectroscopy Study, The Journal of Physical Chemistry A, Just Accepted Manuscript, (2018).

[99] L.C. Balling, M. D. Havey, J.F. Dawson, Absorption and emission spectra of Na atoms trapped in rare-gas matrices, The Journal of Chemical Physics, **69**, 1670 (1978).

[100] L.C. Balling, M.D. Havey, J. J. Wright, Absorption and emission spectra of K atoms trapped in rare-gas matrices, The Journal of Chemical Physics, **70**, 2404 (1979).

[101] J.J. Wright, L. C. Balling, Absorption and emission spectra of Li atoms trapped in rare gas matrices, The Journal of Chemical Physics, **73**(7), 3103 (1980).

[102] S. Tam, M.E. Fajardo, Matrix isolation spectroscopy of metal atoms generated by laser ablation. III. The Na/Ar, Na/Kr, and Na/Xe systems, The Journal of Chemical Physics, **99**, 854 (1993).

[103] E. Jacquet, D. Zanuttini, J. Douady, E. Giglio, and B. Gervais, Spectroscopic properties of alkali atoms embedded in Ar matrix, The Journal of Chemical Physics, **135**, 174503 (2011).

[104] M. P. Allen and D. J. Tildsley, Computer Simulation of liquids, (Clarendon Press-Oxford, 1987).

[105] L. Verlet, Computer "experiments" on classical fluids. I. Thermodynamical properties of Lennard-Jones molecules, Physical Review, **159**, 98 (1967).

[106] O.J. Buneman, Time-reversible difference procedures, Journal of Computational Physics, **1**, 517 (1967).

[107] W. C. Swope, H. C. Andersen P. H. Berens and K. R. Wilson, A computer simulation method for the calculation of equilibrium constants for the formation of physical

clusters of molecules: Application to small water clusters, The Journal of Chemical Physics, **76**, 637 (1982).

[108] G. Rojas-Lorenzo, Estructura y Dinámica de Matrices de Gases Nobles Dopadas, Tesis en Opción al Grado de Doctor en Ciencias Físicas, La Habana, 2003.

[109] J. P. Bergsma, P. H. Berens, K. R. Wilson, D. R. Fredkin and E. J. Heller, Electronic spectra from molecular dynamics: a simple approach, The Journal of Physical Chemistry, **88**, 612 (1994).

[110] G. Rojas-Lorenzo, J. Rubayo-Soneira, F. Vigliotti, and M. Chergui, Ultrafast structural dynamics in electronically excited solid neon. II. Molecular-dynamics simulations of the electronic bubble formation, Physical Review B **67**, 115119 (2003).

[111] G. Rojas-Lorenzo, J. Rubayo-Soneira, S.F. Alberti and M. Chergui, Nonadiabatic Dynamics of Excited Hg ($^3P^1$) in Ar Matrixes, The Journal of Physical Chemistry A, **107**, 8225 (2003).

[112] P. Pajón-Suárez, G. A. Rojas-Lorenzo, J. Rubayo-Soneira, R. Hernández-Lamoneda and P. Larrégaray, On the Local Relaxation of Solid Neon upon Rydberg Excitation of a NO Impurity: The Role of the NO (A)- Ne Interaction Potential and Zero-Point Quantum Delocalization. The Journal of Physical Chemistry A, **113**, 14399-14406 (2009).

[113] R. Lozada-García, G. Rojas-Lorenzo, C. Crépin, M. Ryan and J. G. McCaffrey, Hg–Xe Exciplex Formation in Mixed Xe/Ar Matrices: Molecular Dynamics and Luminescence Study. The Journal of Physical Chemistry A, **119**, 2307-2317 (2014).

[114] R. P. Saxon, R. E. Olson, B. Liu, A binitio calculations for the X 2Σ, A 2Π, and B 2Σ states of NaAr: Emission spectra and cross sections for fine-structure transitions in Na–Ar collisions, The Journal of Chemical Physics, **67**, 2692 (1977).

[115] A. Mushinski and M.P. Nightingale, Many-body trial wave functions for atomic systems and ground states of small noble gas clusters, The Journal of Chemical Physics, **101**, 8831 (1994).

[116] C. Tsoo, D.A. Estrin and S.J. Singer, Electronic energy shifts of a sodium atom in argon clusters by simulated annealing, The Journal of Chemical Physics, **93**, 7187 (1990).

[117] R. P. Feynman, A. R. Hibbs, D. F. Styer, Quantum mechanics and path integrals (Courier Corporation, 2010).

[118] S. W. Rick, D. L. Lynch and J. D. Doll, A variational Monte Carlo study of argon, neon, and helium clusters, The Journal of Chemical Physics, **95**, 3506 (1991).

[119] R. Car and M. Parrinello, Unified approach for molecular dynamics and density-functional theory, Physical Review Letters, **55**, 2471 (1985).

[120] M. E. Tuckerman and M. Parrinello, Integrating the Car–Parrinello equations. I. Basic integration techniques, The Journal of Chemical Physics, **101**, 1302 (1994).

[121] C FJ Walther, S. Patshkovskii and T. Heine, Grand-canonical quantized liquid density-functional theory in a Car-Parrinello implementation, Journal of Chemical Physics, **139**, 034110 (2013).

[122] L. C. Balling , J. J. Wright, J. Chem. Phys. **79**, 2941 (1983).

A PROPERTIES OF CHEBYSHEV POLYNOMIALS

The Chebyshev polynomial of first kind, $T_k(x)$, is the polynomial of degree k defined in the range $x \in [-1, 1]$ by the relation [74, 75]

$$T_k(x) = cos(k\, cos^{-1}(x)) \ . \tag{A.0.1}$$

Therefore, $-1 \leq T_k(x) \leq 1$. By setting $x = \cos z$, we have

$$T_k(z) = cos(kz) \ , \tag{A.0.2}$$

from which it is possible to deduce the expressions for the first Chebyshev polynomials:

$$T_0 = 1,\ T_1 = \cos z = x,\ \ T_2 = \cos 2z = 2cos^2 z - 1 = 2x^2 - 1...$$

From the trigonometric identity

$$\cos\,(k+1)z + \cos\,(k-1)z = 2\cos\ z \cos\ kz \ ,$$

it can be obtained the recurrence relationship

$$T_k(x) = 2xT_k(x) - T_{k-1}(x), \quad k \geq 1, \tag{A.0.3}$$

which allows to deduce, in particular, the expression of the polynomials T_k, $k \geq 2$ from the knowledge of T_0 and T_1.

The polynomial T_k has k zeros in the interval $[-1, 1]$, located at the points x_i (abscissas of Gauss quadrature)

$$x_i = \cos\left(i + \frac{1}{2}\right)\frac{\pi}{k} \ , \quad i = 0, ..., k-1 \ . \tag{A.0.4}$$

Another important property of the Chebyshev polynomials are the recurrence relations obtained for the derivatives T_k',

$$T_k^{'} = \frac{d}{dz}(\cos kz)\frac{dz}{dx} = k\frac{sinkz}{sinz} \ ,$$

from where it gets,

$$T_{k+1}^{'}(x) = 2(k+1)(k-1)T_k(x) - (k+1)T_{k-1}^{'}(x) \ , \quad k > 1 \ . \tag{A.0.5}$$

The Chebyshev polynomials constitute a complete basis of orthogonal polynomials in the interval $[-1, 1]$ with weight $(1 - x^2)^{-1/2}$,

$$\int_{-1}^{1} \frac{T_i(x)T_j(x)}{\sqrt{1-x^2}}dx = \frac{\pi}{2}a_i\delta_{ij} \ , \tag{A.0.6}$$

where δ_{ij} is the Kronecker delta and a_i is defined as $a_0 = 2$ and $a_i = 1$ for $i > 1$.

The completeness property tells us that in general any function $f(x)$ can be represented as a linear combination of Chebyshev polynomials,

$$f_M(x) = \sum_{m=0}^{M} c_m T_m(x) \ , \tag{A.0.7}$$

where the residual function $R_M(x) = f(x) - f_M(x)$ is canceled out when average is performed [74],

$$\int_{-1}^{1} \left(\frac{f(x)T_l(x)}{\sqrt{1-x^2}} - \frac{f_M(x)T_l(x)}{\sqrt{1-x^2}} \right) dx = 0 \ , \quad l = 0, ..., M \ . \tag{A.0.8}$$

Then, making use of the orthogonality of the Chebyshev polynomials Eq. (A.0.6) the expansion coefficients c_m can be evaluated from

$$c_m(x) = \frac{2}{\pi a_m} \int_{-1}^{1} \frac{f(x)T_m(x)}{\sqrt{1-x^2}} dx \ . \tag{A.0.9}$$

Among the main properties of the Chebyshev polynomials, those which make them attractive to describe the quantum dynamics of a system are the recurrence relations between the expansion coefficients of the function $f(x)$ and the expansion coefficients of its derivatives.

Suppose we have the function $f(x)$ for which the expansion in Chebyshev polynomials up to certain order M is known, and $f^{(p)}(x)$ is the derivative of order p of $f(x)$. In general we can express its Chebyshev expansion as

$$f_M^{(p)}(x) = \sum_{m=0}^{M} c_m^{(p)} T_m(x) \ . \tag{A.0.10}$$

Then for the expansion coefficients $c_m^{(p)}$ of $f^{(p)}(x)$ we can derive the following recurrence relation

$$a_{m-1} c_{m-1}^{(p)} = c_{m+1}^{(p)} + 2m c_m^{(p-1)}, \quad m \geq 1 \ , \tag{A.0.11}$$

which must be complemented by the initial values of the coefficients

$$c_M^{(1)} = 0, c_{M-1}^{(1)} = 2M c_m,$$

for the first derivative, and for the second derivative

$$c_M^{(2)} = c_{M-1}^{(2)} = 0 \ .$$

In the calculations developed in this work it is required to represent up to the third derivative of the hydrodynamic fields. The explicit expressions for the recurrence relations between the different coefficients are

$$a_{m-1} c_{m-1}^{(1)} = c_{m+1}^{(1)} + 2m c_m \ , \quad m \geq 1 \ , \tag{A.0.12}$$

$$a_{m-1} c_{m-1}^{(2)} = c_{m+1}^{(2)} + 2m c_m^{(1)}, \quad m \geq 1 \ . \tag{A.0.13}$$

$$a_{m-1}c^{(3)}_{m-1} = c^{(3)}_{m+1} + 2mc^{(2)}_m, \quad m \geq 1 \ . \tag{A.0.14}$$

A.0.1 Collocation methods used to find the Chebyshev expansion coefficients

Considering the Chebyshev expansion (A.0.10) we want to calculate the coefficients c_m by means of a collocation (or interpolation) technique. Here as collocation points we will use the zeros of the Chebyshev polynomials (A.0.4).

The Chebyshev polynomials satisfy also discrete orthogonality relations. If x_i, $i = 0, ..., m-1$, are the zeros of $T_m(x)$, and if $i, j < m$ then we have

$$\sum_{k=0}^{m-1} T_i(x_k)T_j(x_k) = m\delta_{ij}b_i, \quad b_0 = 1 \quad b_i = \frac{1}{2} \ , i > 0 \ . \tag{A.0.15}$$

Then, combining equations (A.0.1), (A.0.4) and (A.0.15), it can be obtained an expression for the expansion coefficients of a certain function $f(x)$ defined in the interval $[-1, 1]$. If we use N Chebyshev polynomials in order to evaluate each coefficient c_j, $j = 0, ..., N-1$ we have [75]

$$c_j = \frac{2}{N} \sum_{k=0}^{N-1} f(x_k)T_j(x_k) \ , \tag{A.0.16}$$

where x_i are the Gauss quadrature points defined in Eq. (A.0.4). In order to evaluate the expansion coefficients using this collocation method we need to know the values of the arbitrary function $f(x)$ at the zeros of the Chebyshev polynomials. Other set of points, such as the extrema of T_k can also be used as collocation points. Here we use the zeros of T_k for the interpolation.

B CHEBYSHEV EXPANSION OF THE FIELDS. NUMERICAL ALGORITHM

1. **Initialization**

   1.1 The initial ensemble of trajectories x_i, $i = 1, ..., N$, is built. The initial grid is chosen equally spaced between the interval $[x_{min}, x_{max}]$ which sample the region where the density is localized.

   1.2 We evaluate at each trajectory position x_i, $i = 1, ..., N$

   - the initial density $\rho(x_i, t_0)$,

   -the regularized density $\rho_{reg}(x_i, t_0)$ (Eq. (3.2.20)),

   - the logarithm of the regularized density $C(x_i, t_0) = \ln(\rho_{reg}(x_i, t_0))/2$,

   - the logarithm of the reference Gaussian $C_0(x_i, t_0)$ (Eq. (3.2.25)),

   -and the residual function $\phi(x_i, t_0)$ (Eq. (3.2.5)).

   1.3 The initial wave function is chosen with $S(x_i, t_0) = 0$, then the initial velocity of each trajectory is $v_i = \nabla S(x_i, t_0)/m = 0$ and $\nabla^2 S(x_i, t_0) = 0$.

   1.4 The expansion coefficients of $\phi(x_i, t_0)$, $\nabla\phi(x_i, t_0)$ and $\nabla^2\phi(x_i, t_0)$ are evaluated from Eqs. (3.2.19), (3.2.13) and (3.2.14), respectively.

   1.5 The initial quantum potential $Q(x_i, t_0)$ (Eq.(3.2.7)) is evaluated.

2. **Dynamics**

   2.1 The equations (3.2.2)-(3.2.4) are integrated using the four order Runge-Kutta method with a fixed $\Delta t = 0.1 a.u.$ and the trajectories positions, as well as S, C and ρ, are updated:

   $$x_i(t + \Delta t)\ , C(x_i, t + \Delta t)\ , S(x_i, t + \Delta t)\ , \rho(x_i, t + \Delta t) = e^{2C(x_i, t+\Delta t)}\ .$$

   2.2 The regularized density is calculated $\rho_{reg}(x_i, t + \Delta t)$ (Eq.(3.2.20)) and then C is evaluated from the regularized density $C(x_i, t + \Delta t) = \ln(\rho_{reg}(x_i, t + \Delta t))/2$.

   2.3 $\langle x \rangle$ and σ are calculated evaluating Eqs. (3.2.21) and (3.2.22).

   2.4 The reference function $C_0(x_i, t + \Delta t)$ is evaluated from Eq. (3.2.25) and then the residual function $\phi(x_i, t + \Delta t)$ (Eq. (3.2.5)) is updated.

   2.5 The Chebyshev expansion coefficients of S and ϕ are calculated (Eq. (3.2.19)).

   2.6 From the coefficients c_j and s_j, using Eq. (3.2.11)-(3.2.14), the coefficients $s_j^{(1)}$, $s_j^{(2)}$, $c_j^{(1)}$ and $c_j^{(2)}$ are evaluated. The derivatives of the fields: $\nabla S(x_i, t + \Delta t)$, $\nabla^2 S(x_i, t + \Delta t)$, $\nabla\phi(x_i, t + \Delta t)$ and $\nabla^2\phi(x_i, t + \Delta t)$ are expressed as a finite sum of Chebyshev polynomials using Eqs. (3.2.9) and (3.2.10).

   2.7 The quantum potential $Q(x_i, t + \Delta t)$ (Eq. (3.2.7)) is evaluated.

   2.8 Return to step 2.1.

C CALCULATION OF THE CORRELATION FUNCTION

The correlation function is defined as (atomic units are used unless specified):

$$C(t) = \langle \Psi(x,0) | \Psi(x,t) \rangle \ . \tag{C.0.1}$$

Hence, in order to evaluate the correlation function, we need the initial wave function $\Psi(x,0)$ and its value at each time $\Psi(x,t)$. The initial wave function at each trajectory is calculated as

$$\Psi(x_i,0) = \sqrt{\rho(x_i,0)} \ , i = 1, ..., N, \tag{C.0.2}$$

where $\rho(x_i,0)$ is evaluated from Eq. (4.2.5) using the final distribution of trajectories after the relaxation described in Sec. 4.3.1. The initial momentum and phase are fixed to zero.

In order to evaluate $\Psi(x_i,t)$ the wave function is reconstructed along each trajectory from:

$$\begin{aligned} \Psi(x_i,t) &= \Psi(x_i,0) \exp\left(-\frac{1}{2} \int_{t_0}^{t} \left(\frac{\partial v}{\partial x} \right)_{x_i(\tau)} d\tau \right) \\ &\times \exp\left(i \int_{t_0}^{t} \left[\frac{1}{2m} \left(\frac{\partial S}{\partial x} \right)^2 - V - Q \right]_{x_i(\tau)} d\tau \right) . \end{aligned} \tag{C.0.3}$$

The exponential terms in the equation displayed above are evaluated at each time step at the position of each trajectory by integrating simultaneously Eqs. (4.2.1)-(4.2.3). The integration of Eq. (4.2.3) is performed considering the quantum-like potential Q_0 given in Eq. (4.2.10) and the full quantum potential Q. The correlation functions are then evaluated from $\Psi(x_i,t)$ integrated using Q_0 and Q, and they are identified as $C_0(t)$ and $C(t)$ respectively. The results are presented and discussed in chapter four.

D QUANTUM THERMAL CORRECTION IN THE HARMONIC APPROXIMATION

The diagonal elements of the density matrix ρ_q of the one-dimensional quantum harmonic oscillator interacting with a reservoir at temperature T has the following form

$$\rho_q(x,T) \approx e^{-\frac{m\omega x^2}{\hbar}\tanh(\frac{\hbar\omega}{2k_bT})} \ , \tag{D.0.1}$$

where k_b is the Boltzman constant, $\hbar$ is the Planck constant divided by 2π, x is the position, m the mass, ω the frequency of the oscillator and T the temperature. By applying the classical correspondence principle $\hbar \to 0$ it can be obtained the corresponding classical density distribution ρ_c,

$$\rho_c(x,T^*) \approx e^{-\frac{m\omega^2x^2}{2k_bT^*}} = e^{-\frac{V(x)}{k_bT^*}} \ , \tag{D.0.2}$$

being $V(x) = \frac{m\omega^2x^2}{2}$ for the harmonic oscillator. By comparing (D.0.1) with (D.0.2) and considering an equivalent classical system with an effective temperature T^* such that its respective classical density distribution mimics the quantum density described above, the following relation can be obtained,

$$-\frac{m\omega^2x^2}{2k_bT^*} = -\frac{m\omega x^2}{\hbar}\tanh(\frac{\hbar\omega}{2k_bT}) \ , \tag{D.0.3}$$

or, writing explicitly the expression for the temperature at which the equality holds,

$$T^* = \frac{\hbar\omega}{2k_b}\tanh^{-1}(\frac{\hbar\omega}{2k_bT}) \ . \tag{D.0.4}$$

Then we arrive to an expression for the effective temperature at which classical molecular dynamics simulations should be carried out for harmonic sytems in order to account for zero-point energy effects. As the classical and the quantum system possess the same value of the density distributions at every point in space, the observables calculated using the equivalent classical system will be the same as the corresponding ones of the quantum systems, making this approximation very appealing to describe quantum effects. This effective temperature is used in chapter five to perform MD simulations of alkali metal doped rare gas matrices.

E EVALUATION OF THE ENERGIES OF THE EXCITED ELECTRONIC STATES OF THE DOPED RARE GAS MATRICES

Here we present the approximation developed by Balling *et al.* to calculate the energy of the excited states of alkali atoms trapped in rare gas matrices [122]. In particular, we are interested in the splitting of the first p state level, because transitions between the $s-p$ bands give the strongest absorption and emission bands for these systems. As we mentioned in section 5.2.2 of chapter five, the ground state and the excited p states of an alkali atom trapped in a rare gas matrix are calculated in terms of the two-body potentials corresponding to the electronic states $X^2\Sigma$, $A^2\Pi$, $B^2\Sigma$ of the alkali-rare gas dimers, which were denoted along chapter five as $V_{ag}^{(\alpha)}$ for $\alpha = 1, 2, 3$, respectively.

The calculation of the energy levels of the alkali atom trapped in the matrix, considering only pairwise interactions is a good approximation only for the ground state. This is due to the fact that the electronic density of the ground state of the alkali atom, as well as that of the ground state of the rare gas atoms are spherically symmetric. However, for the calculation of the p excited states, the interaction energy depends on the angles between the internuclear distances. In Ref. [93], the approximation developed by Balling et al. [122] was used to study the absorption spectra of Na atoms trapped in Ar clusters. In chapter five, we use the same approximation to study the absorption spectra of Na trapped in Ar and Kr matrices. Therefore, here we give some details related with the correction proposed in Ref. [122] for the calculation of the excited state energies.

The approach is based on the Borh-Oppenheimer approximation to separate the electronic structure of the atoms and the vibrational motion of the matrix. Assuming that the core electrons of the Na atom are not affected by the rare gas atoms, and only the valence electron is affected by the matrix, the Hamiltonian for the optically active electron of the Na atom is given by

$$H = H_A(\mathbf{r}_e) + \sum_{k=1}^{N} V(\mathbf{r}_e, \mathbf{r}_k) \ , \tag{E.0.1}$$

where $H_A(\mathbf{r}_e)$ is the Hamiltonian for the free valence electron, $V(\mathbf{r}_e, \mathbf{r}_k)$ is the perturbation caused by the rare gas atoms, with k running over all the rare gas atoms surrounding the sodium. The vectors $\mathbf{r}_e$ and $\mathbf{r}_k$ are the electron and rare gas atoms position vectors, respectively, for a coordinate system with origin at the center of mass of the alkali atom.

In Ref. [93], following the previous work of Balling and collaborators, the authors used the first order perturbation theory to calculate the energy leves of the total Hamiltonian H in Eq. (E.0.1). Identifying ϵ_i and ψ_i with the eigenvalues and eigenvectors of the unperturbed Hamiltonian H_A, the eigenvalues E of H, can be derived by solving,

$$det|V_{ij} - (\epsilon_i - E)\delta_{ij}| = 0 \ , \tag{E.0.2}$$

where,

$$V_{ij} = \sum_{k=1}^{N} \langle \psi_i | V(\mathbf{r}_e, \mathbf{r}_k) | \psi_j \rangle \ . \tag{E.0.3}$$

The matrix V_{ij} has the form [93],

$$V_{ij} = \sum_{k=1}^{N} \left[\frac{1}{3} \left(V_{ag}^{(3)}(r_{k0}) + 2V_{ag}^{(2)}(r_{k0}) \right) + \frac{1}{6} \left(V_{ag}^{(3)}(r_{k0}) - V_{ag}^{(2)}(r_{k0}) \right) A_{ij} \right] , \tag{E.0.4}$$

and the matrix elements A_{ij} are given by

$\mathbf{A} =$

$$\begin{bmatrix} -(3\cos^2\theta_k - 1) & -3\sqrt{2}\sin\theta_k\cos\theta_k e^{-i\phi_k} & -3sin^2\theta_k e^{-2i\phi_k} \\ -3\sqrt{2}\sin\theta_k\cos\theta_k e^{i\phi_k} & 2(3\cos^2\theta_k - 1) & 3\sqrt{2}\sin\theta_k\cos\theta_k e^{-i\phi_k} \\ -3sin^2\theta_k e^{2i\phi_k} & 3\sqrt{2}\sin\theta_k\cos\theta_k e^{i\phi_k} & -(3\cos^2\theta_k - 1) \end{bmatrix} ,$$

where r_{k0} is the radial distance of the $k-th$ rare gas atom to the Na impurity and θ_k, ϕ_k are the angles of this atom in a spherical coordinate system centered at the impurity.

Then, by solving equation (E.0.2) we obtain the three energy eigenvalues E representing the contribution to the total energy of the Na-Rg interaction in the excited states. The solutions of equation (E.0.2) for E, denoted by $E^{(\beta)}$ with $\beta = 1, 2, 3$ will be used in section 5.2.3 to calculate the total energy of the matrix when the Na atom is excited to its first p-state.

F DERIVATION OF THE APPROXIMATE QUANTUM POTENTIAL

The Hamiltonian of a system composed by N rare gas atoms and a Na impurity can be written as follows (we will use atomic units otherwise indicated, $\hbar = 1$)

$$\hat{H} = -\frac{1}{2}\sum_{k=0}^{N}\frac{1}{m_k}\nabla_k^2 + U_{gg} + U_{ag}^{(1)} \ , \tag{F.0.1}$$

$U_{ag}^{(1)}$ accounts for the Na-Rg interaction and U_{gg} is the contribution due to the Rg-Rg interactions.

The local energy of the system can be evaluated by solving:

$$\Psi(\mathbf{r}_0, \mathbf{r}_1, ..., \mathbf{r}_N)E_L = \hat{H}\Psi(\mathbf{r}_0, \mathbf{r}_1, ..., \mathbf{r}_N) \ . \tag{F.0.2}$$

From the *ansatz* for the ground state wave function proposed in chapter five,

$$\Psi(\mathbf{r}_0, \mathbf{r}_1, ..., \mathbf{r}_N) = exp\left(\sum_{i=1}^{N-1}\sum_{j>i} u_{gg}(r_{ij}) + \sum_{i=1}^{N} u_{ag}(r_{i0})\right), \quad r_{i0} = |\mathbf{r}_i - \mathbf{r}_0| \ , \quad i, j = 1, .., N, \tag{F.0.3}$$

we can write (the dependence of Ψ on $\mathbf{r}_i$ has been omitted in order to simplify the notation)

$$\log\Psi = \sum_{i=1}^{N-1}\sum_{j>i} u_{gg}(r_{ij}) + \sum_{i=1}^{N} u_{ag}(r_{i0}) \ , \tag{F.0.4}$$

by applying $\hat{H}$ on Ψ we obtain for the right hand side of equation (F.0.2)

$$\Psi E_L = -\frac{1}{2}\Psi\sum_{k=0}^{N}\frac{1}{m_k}[\nabla_k^2\log\Psi + (\nabla_k\log\Psi)^2] + U_{gg}\Psi + U_{ag}^{(1)}\Psi \ . \tag{F.0.5}$$

or from Eq. (F.0.4)

$$\Psi E_L = -\frac{1}{2}\Psi\sum_{k=0}^{N}\frac{1}{m_k}\left[\nabla_k^2\left(\sum_{i=1}^{N-1}\sum_{j>i}^{N} u_{gg}(r_{ij}) + \sum_{i=1}^{N} u_{ag}(r_{i0})\right) + \left[\nabla_k\left(\sum_{i=1}^{N-1}\sum_{j>i}^{N} u_{gg}(r_{ij}) + \sum_{i=1}^{N} u_{ag}(r_{i0})\right)\right]^2\right] + U_{gg}\Psi + U_{ag}^{(1)}\Psi \ . \tag{F.0.6}$$

Then, dividing by Ψ which is assumed to have no nodes, as it represents the ground state

wave function of the rare gas matrix, we arrive to Eq. (5.3.5) of chapter five

$$E_L = -\frac{1}{2}\sum_{k=0}^{N}\frac{1}{m_k}\Bigg[\nabla_k^2\Bigg(\sum_{i=1}^{N-1}\sum_{j>i}^{N}u_{gg}(r_{ij})+\sum_{i=1}^{N}u_{ag}(r_{i0})\Bigg) + \Bigg(\nabla_k\Bigg(\sum_{i=1}^{N-1}\sum_{j>i}^{N}u_{gg}(r_{ij})+\sum_{i=1}^{N}u_{ag}(r_{i0})\Bigg)\Bigg)^2\Bigg] + U_{gg}+U_{ag}^{(1)}\ . \quad \text{(F.0.7)}$$

Analyzing the terms involving ∇_k^2 the local energy takes the form

$$E_L = -\frac{\mu}{2}\Bigg[\sum_{k=1}^{N}u_{ag}^{''}(r_{k0})+2\frac{u_{ag}^{'}(r_{k0})}{r_{k0}}\Bigg]-\frac{1}{m_g}\Bigg[\sum_{k=1}^{N-1}\sum_{j>k}^{N}u_{gg}^{''}(r_{kj})+2\frac{u_{gg}^{'}(r_{kj})}{r_{kj}}\Bigg] - \frac{1}{2}\sum_{k=0}^{N}\frac{1}{m_k}\Bigg[\Bigg(\nabla_k\Bigg(\sum_{i=1}^{N-1}\sum_{j>i}^{N}u_{gg}(r_{ij})+\sum_{i=1}^{N}u_{ag}(r_{i0})\Bigg)\Bigg)^2\Bigg]+U_{gg}+U_{ag}^{(1)}\ , \quad \text{(F.0.8)}$$

where $u^{''}$ and $u^{'}$ stands for the first and second derivatives of the function u and μ is the reduced mass. Thus, by expanding the term containing ∇_k we get several crossed terms which we will neglect as a first approximation, keeping only the terms of the type $u^{'2}(r_ij)$, obtaining the following approximation for the local energy,

$$E_L \approx -\frac{\mu}{2}\Bigg[\sum_{k=1}^{N}u_{ag}^{''}(r_{k0})+2\frac{u_{ag}^{'}(r_{k0})}{r_{k0}}\Bigg]-\frac{1}{m_g}\Bigg[\sum_{k=1}^{N-1}\sum_{j>k}^{N}u_{gg}^{''}(r_{kj})+2\frac{u_{gg}^{'}(r_{kj})}{r_{kj}}\Bigg] - \frac{1}{m_g}\sum_{k=1}^{N-1}\sum_{j>k}^{N}u_{gg}^{'2}(r_{kj})-\frac{\mu}{2}\sum_{k=1}^{N}u_{ag}^{'2}(r_{k0})+U_{gg}+U_{ag}^{(1)}\ . \quad \text{(F.0.9)}$$

Hence, grouping together the terms involving u_{gg} and the terms involving u_{ag} we arrive to the for of the effective energies U_{ag}^{eff} and U_{gg}^{eff} used in chapter five:

$$U_{ag}^{eff} = -\frac{\mu}{2}\sum_{k=1}^{N}\Bigg(u_{ag}^{''}(r_{k0})+2\frac{u_{ag}^{'}(r_{k0})}{r_{k0}}+u_{ag}^{'2}(r_{k0})\Bigg)+U_{ag}^{(1)}=Q+U_{ag}^{(1)}\ , \quad \text{(F.0.10)}$$

$$U_{gg}^{eff} = -\frac{1}{m_g}\sum_{k=1}^{N}\sum_{j>k}^{N}\Bigg(u_{gg}^{''}(r_{jk})+2\frac{u_{gg}^{'}(r_{kj})}{r_{kj}}+u_{gg}^{'2}(r_{kj})\Bigg)+U_{gg}=Q+U_{gg} \quad \text{(F.0.11)}$$

List of publications of the author related to this Thesis

1. L. Cruz-Rodríguez, J. C. Tremblay, A. Martínez-Mesa and Ll. Uranga-Piña, A Chebyshev expansion of hydrodynamical fields for ultrafast vibrational wave packet dynamics, Computational Theoretical Chemistry, **1078**, 104 (2016).
2. L. Cruz-Rodríguez, Ll. Uranga-Piña, A. Martínez-Mesa and C. Meier, Quantum dynamics modeled by interacting trajectories, Chemical Physics **503**, 39-49 (2018).
3. L. Cruz-Rodríguez, Ll. Uranga-Piña, A. Martínez-Mesa and C. Meier, Quantum trajectory study of laser-driven atomic ionization, resubmitted after referees report for publication to Chemical Physics Letter.

Other publications

- L. Cruz, N.Figueroa, R. Mulet y J. Piñero, Efecto del ruido intrínseco en la dinámica del módulo p53-Mdm2" (Intrinsic noise in the p53-Mdm2 system.), Revista Cubana de Física, 28, No.1,0253 9268, (2011).
- L. Cruz, N.Figueroa and R. Mulet, On the role of intrinsic noise on the response of the p53-Mdm2 module, JSTAT, 2015.
- L. Cruz Rodríguez, A. Pérez Martínez, Faraday Effect, astrophysical implications, Proceedings of the International Workshop on Astronomy and Relativistic Astrophysics, SLAC eConf (2013).
- L. Cruz Rodríguez, A. Pérez Martínez, H. Pérez Rojas and E. Rodríguez Querts, Quantized Faraday effect in (3+1)-dimensional and (2+1)-dimensional systems, Physical Review A 88, 052126 (2013).
- L. Cruz Rodríguez, A. Pérez Martínez, H. Pérez Rojas and E. Rodríguez Querts, Astrophysical implications on the quantized Faraday effect, Astronomische Nachrichten, 335, 635–640, (2014).
- L. Cruz Rodríguez, A. Pérez Martínez, H. Pérez Rojas and E. Rodríguez, On propagation of photons in a magnetized medium, AN 336, No. 8/9, 905–909 (2015).
- L. Cruz Rodríguez, A. Pérez Martínez, Gabriella Piccinelli and E. Rodríguez Querts, Quantum Faraday Effect in the Universe, 7th International Workshop on Astronomy and Relativistic Astrophysics (IWARA 2016) International Journal of Modern Physics: Conference Series 45 1760046 (2017).

Acknowledgements

A mi familia, a todos, por su amor incondicional siempre, muchas gracias. En especial a mis padres y al flaco, por soportar mi mal humor, mis tristezas y por siempre responder a mis tareas urgentes. Es imposible expresar mi gratitud por las incontables horas que han pasado apoyándome de todas las maneras posibles, que han ido desde leerse un capítulo de la tesis, discutir sobre el trabajo, hasta crear en menos de 24 horas un trabajo de la mecánica cuántica y la sociedad!! Los quiero mucho.

Thank you Llinersy and Aliezer, for all your effort, for finding the time to help me, in spite of your multiple responsibilities and the new little members of the family. Thank you for your advices and for giving me the chance of working with you. Thank you for giving me the opportunity to do my Phd under the co-supervision of professor Christoph Meier. Thank you Chris!! Working with you has been an amazing experience, thank you for all your help, your time, and for all the things I have learned with you. You have all my gratitude and admiration.

To JC, thank you for receiving me in Berlin. I still remember when I arrived completely lost at the beginning of my PhD, thank you for your patience and for the very nice time I spent in Berlin.

A mis amigos, a Yana por ser simplemente tu, gracias por tu amistad incondicional después de todos estos años. A la pequeña, por tu cariño, tu alegria siempre, adoptándome como tu hermana mayor. Al Fermi y Patri, por todos los momentos que hemos compartido juntos a lo largo de esta larga carrera. A Ele, por pasar de ser mi estudiante a convertirse en mi amiga. A Andrés, por todo lo que vivimos juntos, los buenos y los malos momentos, a Gise por su cariño, muchas gracias.

Thank you to the group from LCAR, Alex, François, Patricia, Evgeny, Nadine, Bruno, Didier, Ettienne, the secretaries, Christine and Carole, for make me feel like home in Toulouse. Thank you also to the young part of the group for the beers and all the moments we shared outside the lab. Thank you Patri for taking care of me and for being always present. Thank you François and Anna for your cooking! Thank you Alex for introducing me to the night life in Toulouse, a German in Puerto Habana!

Of course, thank you to the other part of my Toulouse family, not related with physics, Sergio, Raquel and Antonio, the Spanish gang! Thank you for being always present. Thank you Raquel for the Sundays we spent working together and the nights we spent dancing. Thank you Sergio for being an unconditional friend. Thank you Juancito and Berta, the new members of the Spanish gang, for all the nice moments we shared at the alliance and at the bars. Thank you Sofia, for showing me the frapuchino and helped me with the hard process of writing a thesis.

Merci Barbara, Oceana et Eva de m'accueillir au sein de votre famille, a été une expérience incroyable de partager l'appartement avec vous.

Thank you Camila, for being a real friend, always there for me, thank you for your

love.

Vielen Dank, Bine, dass du mich bei dir zu Hause hast und mich eine tolle Frau kennenlernen lässt.

Thank you Matze, for our coffees and our jogging together, learning Spanish and German.

Gracias Adis por tus deliciosos frijoles haciendo que Berlin se sintiera un poco como casa.

Gracias a todos los que de una forma u otra se preocuparon por mi y me apoyaron.

Finalmente a Juan José, por confiar en mi, por "aparecer" en mi vida en un momento difícil y a pesar de todo quedarte a mi lado. Gracias por darme tu amor. Te quiero mucho.

Abstract of the Thesis

In this thesis different trajectory-based methods for the study of quantum mechanical phenomena are developed. The first approach is based on a global expansion of the hydrodynamic fields in Chebyshev polynomials. The scheme is used for the study of one-dimensional vibrational dynamics of bound wave packets in harmonic and anharmonic potentials.

Furthermore, a different methodology is developed, which, starting from a parametrization previously proposed for the density, allows the construction of effective interaction potentials between the pseudo-particles representing the density. Within this approach several model problems are studied and important quantum mechanical effects such as, zero point energy, tunneling, barrier scattering and over barrier reflection are founded to be correctly described by the ensemble of interacting trajectories. The same approximation is used for study the laser-driven atom ionization.

A third approach considered in this work consists in the derivation of an approximate many-body quantum potential for cryogenic Ar and Kr matrices with an embedded Na impurity. To this end, a suitable *ansatz* for the ground state wave function of the solid is proposed. This allows to construct an approximate quantum potential which is employed in molecular dynamics simulations to obtain the absorption spectra of the Na impurity isolated in the rare gas matrix.

Keywords: Quantum Dynamics, Molecules, Ultrafast processes

Résumé de thèse

Dans cette thèse, différentes méthodes de dynamique quantique basées sur la propagation de trajectoires sont développées. La première approche consiste en une développer global des champs hydrodynamiques sur une base de polynômes de Chebyshev. Ce schéma est utilisé pour étudier la dynamique vibrationnelle unidimensionnelle de paquets d'ondes dans des potentiels harmoniques et anharmoniques.

Par la suite, une méthodologie différente est développée, qui, à partir d'un paramétrage précédemment proposé pour la densité quantique, permet de construire des potentiels d'interaction effectifs entre les pseudo-particules représentant la densité. Dans le cadre de cette approche, plusieurs problèmes de modélisation sont étudiés et des effets quantiques importants sont décrits, tels que l'énergie de point zéro, l'effet tunnel, la diffusion et la réflexion sur une barrière. La même approximation est utilisée pour l'étude de l'ionisation des atomes par laser.

Dans une troisième approche, un potentiel quantique approximatif à plusieurs corps est dérivé pour décrire des matrices d'argon et de krypton contenant une impureté de sodium. Il est obtenu en proposant un *ansatz* approprié pour la fonction d'onde de l'état fondamental du solide. Le potentiel est utilisé dans les simulations de dynamique moléculaire pour obtenir les spectres d'absorption de l'atome de Na isolé dans les matrices cryogéniques.

Mots-clés: Dynamique quantique, Molécules, Processus ultrarapides

Discipline: Sciences de la matière